

**TRIP STEELS: CONSTITUTIVE MODELING AND
COMPUTATIONAL ISSUES**

by

IOANNIS CHRISTOU PAPATRIANTAFILLOU

Submitted to the Department of Mechanical & Industrial Engineering of

UNIVERSITY OF THESSALY

In Partial Fulfillment of the Requirements for the Degree of

DOCTOR OF PHILOSOPHY

UNIVERSITY OF THESSALY

JUNE 2005



**ΠΑΝΕΠΙΣΤΗΜΙΟ ΘΕΣΣΑΛΙΑΣ
ΒΙΒΛΙΟΘΗΚΗ & ΚΕΝΤΡΟ ΠΛΗΡΟΦΟΡΗΣΗΣ
ΕΙΔΙΚΗ ΣΥΛΛΟΓΗ «ΓΚΡΙΖΑ ΒΙΒΛΙΟΓΡΑΦΙΑ»**

Αριθ. Εισ.: 4549/1
Ημερ. Εισ.: 20-07-2005
Δωρεά: Συγγραφέα
Ταξιθετικός Κωδικός: Δ
669.961 42
ΠΑΠ

**TRIP STEELS: CONSTITUTIVE MODELING AND
COMPUTATIONAL ISSUES**

by

IOANNIS CHRISTOU PAPTIRIANTAFILLOU

Submitted to the Department of Mechanical & Industrial Engineering of
UNIVERSITY OF THESSALY

In Partial Fulfillment of the Requirements for the Degree of

DOCTOR OF PHILOSOPHY

UNIVERSITY OF THESSALY

JUNE 2005

Abstract

TRIP (TRansformation Induced Plasticity) of multi-phase steels is a new generation of low-alloy steels that exhibit an enhanced combination of strength and ductility. These steels make use of the TRIP phenomenon, i.e., the transformation of retained austenite to martensite with plastic deformation, which is responsible for the remarkable enhancement of properties.

A constitutive model for the mechanical behavior of steels exhibiting “Transformation Induced Plasticity” during martensitic transformation is presented in the Thesis.

Two categories of multiphase TRIP steels are examined. The first category is the two-phase TRIP steels, in which particles of martensite are isotropically dispersed in an austenitic matrix; the second includes the four-phase TRIP steels, in which particles of retained austenite, martensite and bainite are isotropically dispersed in a ferritic matrix. In both cases the retained austenite is metastable at room temperature and, under the effect of plastic deformation, transforms to martensite.

TRIP steels are essentially composite materials with evolving volume fractions of the individual phases. The total strain is assumed to be the sum of elastic, plastic and transformation parts. No restriction is placed on the magnitude of the strains and appropriate “finite strain” constitutive equations are developed. Standard isotropic linear hypoelasticity of homogeneous solids is used in order to describe the elastic behavior of TRIP steels since the elastic properties of all individual phases are essentially the same. The plastic part is determined by using homogenization techniques for non-linear composites that have been developed recently by Ponte-Castañeda, Suquet, and co-workers (Ponte-Castañeda 1996, Suquet 1996a, Ponte-Castañeda and Suquet 1998). The constitutive equation for the plastic deformation rate is estimated in terms of the plastic properties of the individual phases. The transformation strain rate has both deviatoric and volumetric parts and is proportional to the rate of change of the volume fraction of martensite. The evolution of martensite due to martensitic transformation is described by a kinetic model, which takes into account temperature, plastic strain and stress state.

A methodology for the numerical integration of the resulting non-linear constitutive equations for TRIP steels in the context of the finite element method is developed and the constitutive model is implemented in a general-purpose finite element program. A methodology for the

numerical integration of the constitutive model under plane stress conditions is also developed.

The constitutive model for the four-phase TRIP steels is calibrated by using experimental data of uniaxial tension tests of a specific TRIP steel. The model predictions fit the data reasonably well. The dependence on temperature and stress state is examined.

The constitutive model is used for the simulation of necking in a uniaxial tension test using the finite element method. TRIP effect hardens the material and increases substantially the range of uniform elongation. The constitutive model is used also for the calculation of “forming limit diagrams” for sheets made of TRIP steel; it is found that the TRIP phenomenon increases the strain at which local necking results from a gradual localization of the strains at an initial thickness imperfection in the sheet.

Acknowledgments

I wish to express my sincere thanks to my supervisor, Professor Nikolao Arava, for his guidance and support throughout the course of this research. His continuous and well-targeted advices were determinant in the completion of my Thesis. It was a real challenge and a great experience to work close to a scientist like him. His knowledge and personality was a source of inspiration for me all these years. I am grateful to him because as an excellent teacher he is, he managed not only to widen my scientific knowledge but also to influence my way of thinking.

I would also like to thank Professor Gregory Haidemenopoulo, one of the three-member advisory committee, for his significant help and well-aimed advices over the years of the dissertation. Especially, I thank him for the plenty of time he devoted in many helpful discussions about TRIP steels.

Furthermore, I thank the Assistant Professor Sp. Karamano, one of the three-member advisory committee, for his sincere interest and encouragement.

The author is also grateful to the other members of the committee Professor A. Giannakopoulo, Professor K. Papadimitriou, Professor V. Kostopoulo and Assistant Professor G. Petropoulo for their sincere interest and useful advices.

Moreover, I would like to thank ECSC and GSRT (ΓΤΕΤ) for their financial support through the projects “Optimization of microstructure in multiphase steels containing retained austenite” (ECSC, contract No 7210-PR/161), “Control and exploitation of the bake-hardening effect in multi-phase high-strength steels”, (ECSC, contract No 7210-PR/370) and “Materials with Microstructure: Constitutive Modeling and Computational Issues” (ΓΤΕΤ/ΠΕΝΕΔ 1999).

Many thanks to my colleagues Dr. A. Vasilako and Dr. A. Katsama for the excellent collaboration during the two ECSC research programs and the helpful conversations we had. Furthermore, I would like to thank M. Agoras for the use of his program concerning the

solution of the forming limit diagrams problem and my colleagues K. Christodoulou and S. Houliara for their encouragement.

Moreover, thanks to Mrs. M. Karanika, the secretary of the Laboratory of Mechanics and Strength of Materials, for her secretarial support.

I would also like to thank Natassa for her patience, continuous support and encouragement during the years of the course.

Finally, I would like to express my gratitude to my family; my brother Dimitri and my parents Christo and Evagellia for their unfailing support and continuous encouragement all over the years of my studies. They made the best they could for making my work much more easy. I am very grateful to them and the least I can do is to devote them this Thesis.

IOANNIS CHRISTOU PAPTANTAFILLOU

UNIVERSITY OF THESSALY

JUNE 2005

TABLE OF CONTENTS

LIST OF FIGURES	5
LIST OF TABLES	16
1. INTRODUCTION	17
2. HISTORICAL PERSPECTIVE	22
2.1. Introduction.....	23
2.2. General aspects of martensitic transformation.....	24
2.3. Driving force for martensitic transformation.....	26
2.4. Transformation Plasticity.....	27
2.5. Heat treatment of TRIP steels.....	29
2.6. Modeling of the mechanical constitutive behavior.....	30
3. VISCOPLASTICITY	34
3.1. Introduction.....	35
3.2. Constitutive model of viscoplasticity.....	35
3.3. Numerical Integration of constitutive equations-Solution method.....	36
3.4. Linearization moduli.....	38
3.5. Use of viscoplasticity for describing rate independent plasticity.....	39
3.6. Implementation of a viscoplastic model into FEM.....	40
3.7. Results.....	41
3.8. Conclusions.....	49
4. HOMOGENIZATION THEORY-DETERMINATION OF PLASTIC STRAIN	50
4.1. Introduction.....	51
4.2. Homogenization method for non-linear viscous solids.....	51
4.2.1. A description of various “secant methods”.....	53
4.2.2. The Hashin Shtrikman bounds.....	55

4.3. Application to non-linear composites	57
4.3.1. Homogenization method for a two-phase non-linear composite.....	57
4.3.2. Homogenization method for a four-phase non-linear composite.....	60
4.4. A summary of the constitutive equations used for \mathbf{D}^p in TRIP steels.....	62
5. UNIT CELL CALCULATIONS.....	64
5.1. Introduction.....	65
5.2. Modeling the microstructure of the two-phase TRIP steel	65
5.3. The unit cell problem-uniaxial tension.....	65
5.4. Comparison of the predictions of the homogenization theory with the unit cell calculations.....	70
6. CONSTITUTIVE MODELING OF TRIP STEELS.....	74
6.1. Introduction.....	75
6.2. A brief geometric definition of the deformation rate tensor.....	75
6.3. Constitutive formulation.....	77
6.3.1. The elastic part of the deformation rate \mathbf{D}^e	78
6.3.2. The plastic part of the deformation rate \mathbf{D}^p	78
6.3.2.1. Hardening of the phases	
6.3.2.2. Accounting for the inherited dislocation structure of newly formed martensite	
6.3.3. The transformation part of the deformation rate \mathbf{D}^{TRIP} and the evolution of the volume fraction of the phases.....	82
6.3.3.1. A transformation kinetics model for the determinant of \hat{f}	
6.3.3.2. Remarks on the transformation kinetics model	
6.4. Evolution of volume fraction of phases in two-phase TRIP steels.....	90
6.5. Evolution of volume fraction of phases in four-phase TRIP steels.....	91
6.6. Summary of Constitutive equations.....	91

7. COMPUTATIONAL ISSUES - IMPLEMENTATION INTO FEM.....	94
7.1. Introduction.....	95
7.2. Numerical Integration of the Constitutive Equations.....	95
7.2.1. Four-phase TRIP steel.....	96
7.2.1.1. Integration using the backward Euler method	
7.2.1.2. Integration using a combination of backward and the forward Euler schemes	
7.2.2. Two-phase TRIP steel.....	100
7.3. The linearization moduli.....	100
7.4. The role of UMAT (User MATerial subroutine).....	101
7.5. Integral formulation of the problem – The “weak” solution.....	101
7.6. Finite element formulation.....	103
7.7. Calculation of Jacobian – Linearization of equations.....	105
8. COMPUTATIONAL MODEL FOR PLANE STRESS.....	109
8.1. Introduction.....	110
8.2. Integration of constitutive equations under plane stress conditions.....	111
8.3. The linearization moduli.....	113
9. FINITE ELEMENT RESULTS FOR TWO-PHASE TRIP STEELS.....	115
9.1. Introduction.....	116
9.2. Effect of temperature on martensitic transformation in uniaxial tension.....	116
9.3. Simple shear.....	122
9.4. Plane strain tension.....	125
10. FINITE ELEMENT RESULTS FOR FOUR-PHASE TRIP STEELS.....	128
10.1. Introduction.....	129
10.2. Experimental data used for the calibration of the model.....	129
10.3. A note on the integration scheme: backward vs. forward-backward Euler.....	133
10.4. Calibration of the model.....	135
10.4.1. Uniaxial versus plane-strain tension.....	138

11. FINITE ELEMENT RESULTS OF NECKING PROBLEM FOR FOUR-PHASE TRIP STEELS	142
11.1. Introduction.....	143
11.2. Simulation of necking in a uniaxial tension test.....	143
11.3. Simulation of necking in a plane strain tension test.....	153
11.4. Comparison of neck formation in uniaxial and plane strain tension.....	155
11.5. Summary of necking analysis	158
12. FINITE ELEMENT RESULTS OF A MODE-I CRACK PROBLEM FOR FOUR-PHASE TRIP STEELS	160
12.1. Introduction.....	161
12.2. FEM simulation of crack.....	161
13. FORMING LIMIT DIAGRAMS FOR TRIP STEELS	170
13.1. Introduction.....	171
13.2. Problem formulation.....	171
13.3. Results.....	175
14. PROPOSALS FOR FUTURE RESEARCH ON TRIP STEELS	179
REFERENCES	181
APPENDICES	186
APPENDIX A.....	187
APPENDIX B.....	189
APPENDIX C.....	190
APPENDIX D.....	195
APPENDIX E.....	197

LIST OF FIGURES

Figure 2.1: Total elongation and tensile strength of TRIP steels in comparison with conventional high strength steels; IF-HS:high strength interstitial free steel, DP: dualphase steel, HSLA: high strength low alloy steel.

Figure 2.2: Lattice distortion and correspondence proposed by BAIN for the FCC→BCC (BCT) martensitic transformation in iron alloys. The correspondence related cell in the parent phase (indicated by bold lines) becomes a unit cell in martensite as a consequence of Bainstrain.

Figure 2.3: Schematic illustration of homogenous lattice deformation (a) and shuffles (b).

Figure 2.4: Schematic diagram showing the free energy change for a martensitic transformation.

Figure 2.5: Schematic representation of the interrelationships between stress-assisted and strain-induced martensitic transformation.

Figure 2.6: Schematic representation of the heat treatment performed for TRIP steels (A: austenite, B: bainite, F: ferrite).

Figure 2.7: Microstructure of TRIP steel.

Figure 2.8: Schematic representation of tensile flow properties and transformation behavior for high-strength TRIP steel. Dotted lines represent σ - ϵ behavior of stable austenite (σ_A) and martensite (σ_M). Solid curves show experimental shape of σ - ϵ and f - ϵ curves of metastable austenite. Dashed curve shows predicted σ - ϵ curve from “rule of mixtures”, based on shape of associated f - ϵ curve. (a) Behavior of material at temperatures above M_s^σ , (b) behavior below M_s^σ .

Figure 2.9: Comparison of experimental and calculated stress strain curves for 14Ni-7Cr stainless steel studied by Naturani, et al. (1982).

Figure 2.10: Comparison of model predictions for equivalent shear stress vs equivalent plastic strain. Experimental points represent data measured in simple tension tests for a 14Cr-7Ni SITP alloy.

Figure 3.1: Hardening curves $\sigma_y(\bar{\epsilon}^p)/\sigma_0$ vs. $\bar{\epsilon}^p$ for $n=5, 10$ and 15 .

Figure 3.2: Variation of σ_{eq}/σ_0 with $\bar{\epsilon}^p$ in plane strain tension for $n=5, m=10$, $\dot{\epsilon}_o = 10^{-4} s^{-1}$ and strain rates $0.1\dot{\epsilon}_o, \dot{\epsilon}_o$ and $10\dot{\epsilon}_o$, together with the flow stress $\sigma_y(\bar{\epsilon}^p)$.

Figure 3.3: Variation of σ_{eq}/σ_0 with $\bar{\epsilon}^p$ in plane strain tension for $n=5, m=60$, $\dot{\epsilon}_o = 10^{-4} s^{-1}$ and strain rates $0.1\dot{\epsilon}_o, \dot{\epsilon}_o$ and $10\dot{\epsilon}_o$, together with the flow stress $\sigma_y(\bar{\epsilon}^p)$.

Figure 3.4: Variation of σ_{eq}/σ_0 with $\bar{\epsilon}^p$ in plane strain tension for $n=5, m=100$, $\dot{\epsilon}_o = 10^{-4} s^{-1}$ and strain rates $0.1\dot{\epsilon}_o, \dot{\epsilon}_o$ and $10\dot{\epsilon}_o$, together with the flow stress $\sigma_y(\bar{\epsilon}^p)$.

Figure 3.5: Variation of σ_{eq}/σ_0 with $\bar{\epsilon}^p$ in plane strain tension for $n=5, m=1000$, $\dot{\epsilon}_o = 10^{-4} s^{-1}$ and strain rates $0.1\dot{\epsilon}_o, \dot{\epsilon}_o$ and $10\dot{\epsilon}_o$, together with the flow stress $\sigma_y(\bar{\epsilon}^p)$.

Figure 3.6: Variation of σ_{eq}/σ_0 with $\bar{\epsilon}^p$ in plane strain tension for $n=10, m=10$, $\dot{\epsilon}_o = 10^{-4} s^{-1}$ and strain rates $0.1\dot{\epsilon}_o, \dot{\epsilon}_o$ and $10\dot{\epsilon}_o$, together with the flow stress $\sigma_y(\bar{\epsilon}^p)$.

Figure 3.7: Variation of σ_{eq}/σ_0 with $\bar{\epsilon}^p$ in plane strain tension for $n=10, m=60$, $\dot{\epsilon}_o = 10^{-4} s^{-1}$ and strain rates $0.1\dot{\epsilon}_o, \dot{\epsilon}_o$ and $10\dot{\epsilon}_o$, together with the flow stress $\sigma_y(\bar{\epsilon}^p)$.

Figure 3.8: Variation of σ_{eq}/σ_0 with $\bar{\epsilon}^p$ in plane strain tension for $n=10, m=100$, $\dot{\epsilon}_o = 10^{-4} s^{-1}$ and strain rates $0.1\dot{\epsilon}_o, \dot{\epsilon}_o$ and $10\dot{\epsilon}_o$, together with the flow stress $\sigma_y(\bar{\epsilon}^p)$.

Figure 3.9: Variation of σ_{eq}/σ_0 with $\bar{\varepsilon}^p$ in plane strain tension for $n=10$, $m=1000$, $\dot{\varepsilon}_o = 10^{-4} s^{-1}$ and strain rates $0.1\dot{\varepsilon}_o$, $\dot{\varepsilon}_o$ and $10\dot{\varepsilon}_o$, together with the flow stress $\sigma_y(\bar{\varepsilon}^p)$.

Figure 3.10: Variation of σ_{eq}/σ_0 with $\bar{\varepsilon}^p$ in plane strain tension for $n=15$, $m=10$, $\dot{\varepsilon}_o = 10^{-4} s^{-1}$ and strain rates $0.1\dot{\varepsilon}_o$, $\dot{\varepsilon}_o$ and $10\dot{\varepsilon}_o$, together with the flow stress $\sigma_y(\bar{\varepsilon}^p)$.

Figure 3.11: Variation of σ_{eq}/σ_0 with $\bar{\varepsilon}^p$ in plane strain tension for $n=15$, $m=60$, $\dot{\varepsilon}_o = 10^{-4} s^{-1}$ and strain rates $0.1\dot{\varepsilon}_o$, $\dot{\varepsilon}_o$ and $10\dot{\varepsilon}_o$, together with the flow stress $\sigma_y(\bar{\varepsilon}^p)$.

Figure 3.12: Variation of σ_{eq}/σ_0 with $\bar{\varepsilon}^p$ in plane strain tension for $n=15$, $m=100$, $\dot{\varepsilon}_o = 10^{-4} s^{-1}$ and strain rates $0.1\dot{\varepsilon}_o$, $\dot{\varepsilon}_o$ and $10\dot{\varepsilon}_o$, together with the flow stress $\sigma_y(\bar{\varepsilon}^p)$.

Figure 3.13: Variation of σ_{eq}/σ_0 with $\bar{\varepsilon}^p$ in plane strain tension for $n=15$, $m=1000$, $\dot{\varepsilon}_o = 10^{-4} s^{-1}$ and strain rates $0.1\dot{\varepsilon}_o$, $\dot{\varepsilon}_o$ and $10\dot{\varepsilon}_o$, together with the flow stress $\sigma_y(\bar{\varepsilon}^p)$.

Figure 5.1: Three-dimensional periodic array of prismatic cells.

Figure 5.2: Prismatic cell approximated by cylindrical cell.

Figure 5.3: Dimensions of the cylindrical cell.

Figure 5.4: FEM modeling of Unit Cell.

Figure 5.5: Finite element mesh that corresponds to the case with $f=0.20$, i.e., 20% of martensite volume. The blue elements correspond to the martensitic particles and the red elements are the austenitic matrix.

Figure 5.6: Schematic depiction of the idea of unit cell modeling.

Figure 5.7: Schematic description of the problem with the boundary conditions.

Figure 5.8: Variation of flow stress in austenite and martensite.

Figure 5.9: Deformed finite element meshes at the final elongation for $f=7.5\%$, $f=20\%$, $f=30\%$ and $f=50\%$. The blue elements correspond to the martensitic particles and the red elements are the austenitic matrix.

Figure 5.10: Comparison of stress-strain curves for $f=7.5\%$.

Figure 5.11: Comparison of stress-strain curves for $f=20\%$.

Figure 5.12: Comparison of stress-strain curves for $f=30\%$.

Figure 5.13: Comparison of stress-strain curves for $f=50\%$.

Figure 6.1: Displacement, stretch, and rotation of material vector $d\mathbf{X}$ to new position $d\mathbf{x}$.

Figure 6.2: Hardening behavior of individual phases for the four-phase TRIP steel.

Figure 6.3: Hardening behavior of individual phases for the two-phase TRIP steel.

Figure 6.4: Probability function P and its derivative with respect to a normalized driving force, $(g - \bar{g})/s_g$, illustrating the effect of normalized temperature Θ and triaxiality Σ on the driving force for transformation. Figure taken from Stringfellow *et. al.* (1992).

Figure 7.1: Body deformation.

Figure 7.2: Discretization.

Figure 9.1: Schematic description of the uniaxial tension problem.

Figure 9.2: Volume fraction of martensite formed versus nominal strain for different temperatures in uniaxial tension.

Figure 9.3: Stress-strain curves of austenite and martensite at different temperatures.

Figure 9.4: Equivalent plastic strain $\bar{\varepsilon}^p = \int \sqrt{\frac{2}{3} \mathbf{D}^p : \mathbf{D}^p} dt$ versus nominal strain for different temperatures in uniaxial tension.

Figure 9.5: Variation of the TRIP “equivalent strains” ε_q^{TRIP} (DEV) and ε_p^{TRIP} (VOL) with the nominal strain for different temperatures in uniaxial tension.

Figure 9.6: Plastic strain $\bar{\varepsilon}^{p(a)}$ in austenite versus nominal strain for different temperatures in uniaxial tension.

Figure 9.7: Plastic strain $\bar{\varepsilon}^{p(m)}$ in martensite versus nominal strain for different temperatures in uniaxial tension.

Figure 9.8: Variation of $\bar{\varepsilon}^p$, $\bar{\varepsilon}^{p(a)}$ and $\bar{\varepsilon}^{p(m)}$ with nominal strain for $T_1 = -50^\circ C$.

Figure 9.9: Schematic representation of the simple shear problem.

Figure 9.10: Volume fraction of martensite formed versus equivalent strain $\bar{\varepsilon} = \int \sqrt{\frac{2}{3} \mathbf{D}' : \mathbf{D}'} dt$ in simple shear at room temperature ($T = 23^\circ C$).

Figure 9.11: Hydrostatic pressure and shear component versus equivalent strain $\bar{\varepsilon} = \int \sqrt{\frac{2}{3} \mathbf{D}' : \mathbf{D}'} dt$ in simple shear at room temperature ($T = 23^\circ C$).

Figure 9.12: Volume fraction of martensite formed versus equivalent strain $\bar{\varepsilon} = \int \sqrt{\frac{2}{3} \mathbf{D}' : \mathbf{D}'} dt$ for the three problems considered at room temperature ($T = 23^\circ C$).

Figures 9.13: Triaxiality ratio Σ versus equivalent strain $\bar{\varepsilon} = \int \sqrt{\frac{2}{3} \mathbf{D}' : \mathbf{D}' } dt$ for plane strain tension (a) and simple shear (b) at room temperature ($T_3 = 23^\circ\text{C}$).

Figure 9.14: Equivalent stress versus equivalent strain $\bar{\varepsilon} = \int \sqrt{\frac{2}{3} \mathbf{D}' : \mathbf{D}' } dt$ for different stress states in room temperature ($T_3 = 23^\circ\text{C}$).

Figure 9.15: Equivalent plastic strain in the composite versus equivalent strain for different stress states in room temperature ($T_3 = 23^\circ\text{C}$).

Figure 10.1: Tensile test specimen according to DIN EN 10002.

Figure 10.2: Schematic representation of the heat treatment performed for TRIP steel 52122 (A: austenite, B: bainite, F: ferrite).

Figure 10.3: Microstructure of TRIP steel 52122.

Figure 10.4: Experimental results for the $f - \varepsilon$ curve in TRIP steel 52122.

Figure 10.5: Experimental results for the $\sigma - \varepsilon$ curve of TRIP steel 52122.

Figure 10.6: Comparison of $f - \varepsilon$ curves for BE and FBE integration schemes.

Figure 10.7: $f - \varepsilon$ curves in uniaxial tension for room temperature and 50°C .

Figure 10.8: Stress-strain curves in uniaxial tension.

Figure 10.9: Equivalent plastic strain in the individual phases $\bar{\varepsilon}^{p(r)}$ together with equivalent plastic strain in the TRIP steel $\bar{\varepsilon}^p = \int \sqrt{\frac{2}{3} \mathbf{D}^p : \mathbf{D}^p } dt$.

Figure 10.10: Evolution of volume fractions $c^{(r)}$ at room temperature.

Figure 10.11: Comparison of model predictions for $f - \varepsilon$ curves in uniaxial and plane strain tension at room temperature.

Figure 10.12: Comparison of model predictions for $f - \varepsilon$ curves in uniaxial and plane strain tension at 50°C .

Figure 10.13: Comparison of model predictions for stress-strain curve in uniaxial and plane strain tension at room temperature.

Figure 10.14: Comparison of model predictions for stress-strain curves in uniaxial and plane strain tension at 50°C .

Figure 10.15: Comparison of model predictions for equivalent stress vs. nominal strain in uniaxial and plane strain tension at room temperature.

Figure 10.16: Comparison of model predictions for hydrostatic pressure vs. nominal strain tension in uniaxial and plane strain tension at room temperature.

Figure 11.1: The cylindrical specimen analyzed.

Figure 11.2: The finite element model used for the analysis and a schematic representation of the boundary conditions imposed.

Figure 11.3: Schematic representation of the geometric imperfection.

Figure 11.4: Stress-strain curves for the transforming TRIP steel predicted by a necking analysis and the corresponding uniform solution at room temperature.

Figure 11.5: 3D representation of the specimen during the evolution of necking for a TRIP steel at room temperature: a) undeformed, b) 40%, c) 50%, d) 57% nominal strain.

Figure 11.6: Stress-strain curves for a TRIP steel and a “non-transforming” steel at room temperature. Arrows indicate maximum-load position.

Figure 11.7: Deformed configurations for a nominal strain of 50% at room temperature: (a,c) transforming, (b,d) non-transforming steel.

Figure 11.8: Contours of hydrostatic stress $p = \sigma_{kk}/3$ (in Pa) for a nominal strain of 50% at room temperature: a) transforming, b) non-transforming steel.

Figure 11.9: Contours of triaxiality ratio $\Sigma = p/\sigma_{eq}$ for a nominal strain of 50% at room temperature: a) transforming, b) non-transforming steel.

Figure 11.10: Contours of volume fraction of phases for a nominal strain of 50% at room temperature: a) martensite f , b) austenite $c^{(a)}$, c) bainite $c^{(3)}$, d) ferrite $c^{(4)}$.

Figure 11.11: Contours of equivalent plastic strain of the phases $\bar{\varepsilon}^{p(r)}$ for a nominal strain of 50% at room temperature: a) martensite, b) austenite, c) bainite, d) ferrite.

Figure 11.12: Stress-strain curves for room temperature and 50°C in uniaxial tension.

Figure 11.13: Deformed configurations of TRIP specimens for a nominal strain of 57% at (a,c) room temperature, (b,d) 50°C.

Figure 11.14: Contours of triaxiality ratio for nominal strain of 57% at: a) room temperature, b) 50°C.

Figure 11.15: Contours of volume fraction f of martensite for a nominal strain of 57% at: a) room temperature, b) 50°C.

Figure 11.16: Contours of equivalent plastic strain $\bar{\varepsilon}^p = \int \sqrt{\frac{2}{3} \mathbf{D}^p : \mathbf{D}^p} dt$ for a nominal strain of 57% at: a) room temperature, b) 50°C.

Figure 11.17: Plastic zones (yellow regions) for different strain levels: (a,b,c) room temperature, and (d,e,f) 50°C.

Figure 11.18: The rectangular specimen analyzed.

Figure 11.19: Stress-strain curves for a TRIP steel and a “non-transforming” steel in plane strain tension at room temperature.

Figure 11.20: Stress-strain curves for room temperature and 50°C in plane strain tension.

Figure 11.21: Deformed and undeformed configurations for a nominal strain of 50% at room temperature: a) uniaxial tension, b) plane strain tension.

Figure 11.22: Contours of triaxiality ratio Σ for a nominal strain of 57% at room temperature: a) uniaxial tension, b) plane strain tension.

Figure 11.23: Contours of volume fraction of martensite f for a nominal strain of 57% at room temperature: a) uniaxial tension, b) plane strain tension.

Figure 11.24: Contours of von Mises equivalent stress (in Pa) for a nominal strain of 57% at room temperature: a) uniaxial tension, b) plane strain tension.

Figure 11.25: Contours of hydrostatic stress (in Pa) for a nominal strain of 57% at room temperature: a) uniaxial tension, b) plane strain tension.

Figure 11.26: Contours of equivalent plastic strain $\bar{\epsilon}^p = \int \sqrt{\frac{2}{3} \mathbf{D}^p : \mathbf{D}^p} dt$ for a nominal strain of 57% at room temperature: a) uniaxial tension, b) plane strain tension.

Figure 12.1: Schematic description of the crack blunting problem: (a) the circular near-tip region modeled, (b) schematic representation of the near-tip small-scale-yielding boundary value problem.

Figure 12.2: The finite element mesh used in the calculations.

Figure 12.3: The finite element mesh in the region near the crack tip.

Figure 12.4: Deformed finite element mesh superposed on the undeformed mesh (green lines) in the region near the blunt crack tip at a load level $K_I \equiv K_I / (\sigma_0 \sqrt{b_0}) = 50$ for the transforming steel at room temperature.

Figure 12.5: Opening stress ahead of the crack tip at different load levels for a TRIP steel and a non-transforming steel at room temperature.

Figure 12.6: Variation of the hydrostatic pressure ahead of the crack tip at different load levels for a TRIP steel and a non-transforming steel at room temperature.

Figure 12.7: Variation of the triaxiality ratio ahead of the crack tip at different load levels for a TRIP steel and a non-transforming steel at room temperature.

Figure 12.8: Variation of equivalent plastic strain $\bar{\epsilon}^p = \int \sqrt{\frac{2}{3} \mathbf{D}^p : \mathbf{D}^p} dt$ ahead of the crack tip at different load levels for a TRIP steel and a non-transforming steel at room temperature.

Figure 12.9: Contour of equivalent plastic strain $\bar{\epsilon}^p = \int \sqrt{\frac{2}{3} \mathbf{D}^p : \mathbf{D}^p} dt$ ahead of the crack tip at a load level of $K_I \equiv K_I / (\sigma_0 \sqrt{b_0}) = 50$ for a TRIP steel at room temperature.

Figure 12.10: Contour of equivalent plastic strain $\bar{\epsilon}^p = \int \sqrt{\frac{2}{3} \mathbf{D}^p : \mathbf{D}^p} dt$ ahead of the crack tip at a load level of $K_I \equiv K_I / (\sigma_0 \sqrt{b_0}) = 50$ for the non-transforming steel at room temperature.

Figure 12.11: Distribution of volume fraction of martensite ahead of the crack tip at different load levels for room temperature and 50°C.

Figure 12.12: Normal stress distribution ahead of the crack tip at different load levels for room temperature and 50⁰C.

Figure 12.13: Variation of equivalent plastic strain $\bar{\varepsilon}^p = \int \sqrt{\frac{2}{3} \mathbf{D}^p : \mathbf{D}^p} dt$ ahead of the crack tip at different load levels for room temperature and 50⁰C.

Figure 13.1: Narrow band in biaxially stretched sheet.

Figure 13.2: Forming limit curves for two different values of initial thickness inhomogeneities $H^b/H = 0.999$ and 0.99 . The solid lines correspond to the TRIP steel, whereas the dashed lines are for a non-transforming steel. The dark triangles are experimental data.

Figure 13.3: Growth of maximum principal logarithmic strain inside the band ε_l^b for the TRIP steel and $\rho = 0$.

Figure 13.4: Evolution of band thickness h^b for the TRIP steel and $\rho = 0$.

Figure 13.5: Forming limit curves for three different values of m ($m = 50, 60, 70$) for initial thickness inhomogeneity $H^b/H = 0.99$. The solid line corresponds to the value of m we use in the calculations for TRIP steel, whereas the dashed lines are for the comparison curves.

LIST OF TABLES

Table 5.1: f and R/R_C for the FEM models examined

Table 6.1: Chemical compositions of steels DOCOL 1400 and DOCOL 600, contents in mass %.

Table 9.1: Values used in the kinetics model.

Table 9.2: Values used in the kinetics model.

Table 10.1: Chemical composition of TRIP steel 52122.

Table 10.2: Results of retained austenite measurements for TRIP steel 52122.

Table 10.3: CPU time required for the one-element uniaxial tension test.

Table 10.4: Values used in the kinetics model.

Table 10.5: Values used in the kinetics model.

CHAPTER ONE

INTRODUCTION

The strict requirements set by automotive industry for passive safety, weight reduction and energy saving has led to the development of new group of steels with improved properties. Recently, various kinds of high-strength steels have been developed to satisfy the requirements set by automotive industry. The main problem of these steels are the manifold defects associated with their inferior formability so as the enhancement of strength without deteriorating the formability remains one of the most important targets of material development.

The introduction of a new group of high-strength steels with a microstructure consisting of at least two different components has led to an enlargement of the strength level without a deterioration of ductility. These multiphase steels offer very attractive combinations of strength and ductility, which are due to the coexistence of phases the different microstructures, their different mechanical properties and their mutual interactions.

TRIP (TRansformation Induced Plasticity) multi-phase steels are a new generation of low-alloy steels that exhibit an enhanced combination of strength and ductility satisfying the requirements of automotive industry. These steels make use of the TRIP phenomenon, which is known as the transformation of retained austenite to martensite with plastic deformation and is responsible for the remarkable properties that exhibit.

The basic aim of this Thesis is the development of a constitutive model that simulates the mechanical behavior of multiphase TRIP steels.

In this research we examine two categories of multiphase TRIP steels. The first category is the two-phase TRIP steels in which particles of martensite are isotropically dispersed in austenitic matrix; the second includes the four-phase TRIP steels in which particles of retained austenite, martensite and bainite are isotropically dispersed in ferritic matrix. In both cases the retained austenite is metastable at room temperature and, under the effect of stress and/or plastic deformation, transforms to martensite. In particular, at temperatures just above the so-called M_s temperature, transformation can be induced via stress-assisted nucleation on the same sites which trigger the spontaneous transformation on cooling, but now assisted by the thermodynamic effect of applied stress (Olson and Cohen (1982)). Above a temperature M_s^σ , the transformation stress exceeds the flow stress of the parent phase and transformation is preceded by significant plastic deformation; this is known as strain-induced nucleation and involves the production of new nucleation sites by plastic deformation (Olson and Cohen (1975)). Finally, above a temperature M_d , no transformation is observed prior to fracture. In

our research we focus our attention to the temperature range above M_s^σ and below M_d , where the dominant nucleation mechanism is strain-induced.

TRIP steels are essentially composite materials with evolving volume fractions of the individual phases. The total strain is assumed to be the sum of elastic, plastic and transformation parts. No restriction is placed on the magnitude of the strains and appropriate “finite strain” constitutive equations are developed. The elastic properties of all individual phases are essentially the same. Therefore, standard isotropic linear hypoelasticity of homogeneous solids is used in order to describe the elastic behavior of TRIP steels. The individual phases of the composite exhibit different hardening behavior during the deformation process. The hardening behavior of the individual phases influences not only the mechanical behavior of TRIP steels but also the evolution of martensite. Experimental data are used for the determination of the hardening properties of the constituent phases. Viscoplasticity is used to model the mechanical behavior of the individual phases in plastic region. The overall viscoplastic behavior of the composite (TRIP steel) is determined by using homogenization techniques for non-linear composites that have been developed recently by Ponte-Castañeda, Suquet, and co-workers (Ponte-Castañeda 1996, Suquet 1996a, Ponte-Castañeda and Suquet 1998) and the constitutive equation for the plastic deformation rate is estimated in terms of the plastic properties of the individual phases. The constitutive model proposed considers the apportionment of stress between the individual phases and estimates the different levels of strain accumulated in the constituent phases. A critical aspect of the transformation process is the strain softening which occurs as a result of the transformation strain. The strain softening has been incorporated into the model by considering an additional deformation rate contribution to the total deformation rate, proportional to the rate of increase of the martensite volume fraction. The transformation strain rate consists of a dilatational term accounting for the positive transformation volume change and of a deviatoric term that models the transformation shape strain.

The evolution of martensite due to martensitic transformation is described by a kinetic model, which takes into account temperature, plastic strain and stress state. The modified OC model proposed by Stringfellow et al. (1992) is used to describe the evolution of martensite during transformation.

A methodology for the numerical integration of the resulting non-linear constitutive equations for TRIP steels in the context of the finite element method is presented. The implementation of the constitutive model in a general-purpose finite element program (ABAQUS) and the

procedure of solving the problem with finite elements in the context of finite strains are presented. The ABAQUS finite element code provides a general interface so that a particular constitutive model can be introduced via a “user subroutine” named UMAT (User MATerial). A methodology is also developed for the numerical integration of the constitutive model under plane stress conditions. In such problems, the out-of-plane component of the deformation gradient is not defined kinematically and some modifications to the general method are needed.

The constitutive model developed for the two-phase TRIP steel is implemented in ABAQUS through the subroutine UMAT and is used for the analysis of model problems. In particular the problems of uniaxial tension at different temperatures, finite simple shear, and plane strain tension are studied in detail. The dependence on temperature and stress state is examined.

The constitutive model developed for the four-phase TRIP steel is also implemented in ABAQUS through the subroutine UMAT and is used for the calibration of the model. Experimental data from interrupted tensile tests in a specific TRIP steel are used for the calibration.

The calibrated model is used together with the finite element method for the analysis of necking in a tension specimen. Simulations are carried out for uniaxial and plane strain tension and the temperature dependence is also examined. Comparisons are made with the corresponding problems in which martensitic transformation is suppressed.

The calibrated model for four-phase TRIP steels is used also for the simulation of a plane strain mode-I blunt crack under small scale yielding conditions. The problem of crack is solved for two temperatures and comparisons are made with corresponding problems in which martensitic transformation is suppressed.

Finally, the constitutive model developed for the four-phase TRIP steel is used to calculate ‘forming limit diagrams’ for sheets made of TRIP steels. Experimental data from the same TRIP steel used for the calibration are compared with the predictions of the analysis and comparisons are made with corresponding problems in which martensitic transformation is suppressed.

The Thesis proceeds with Chapter 2, where we review some of the relevant research that has been performed and we present a description of martensitic transformations, followed by a more specific discussion of the transformation plasticity phenomenon.

In the constitutive model developed, plastic strain is modelled using a viscoplastic constitutive equation instead of the classical rate-independent plasticity. In Chapter 3, we examine the validity of using viscoplasticity for the description of rate-independent plasticity.

In Chapter 4, we develop a methodology for the determination of the plastic part of the deformation rate \mathbf{D}^p in TRIP steels. We present a description of the homogenization techniques for non-linear materials that have been developed recently by Ponte-Castañeda, Suquet, and co-workers. The homogenization techniques are then applied to a two-phase and a four-phase TRIP steel.

In Chapter 5, the results of the homogenization theory for the two-phase composite are compared to corresponding results of unit cell calculations.

In Chapter 6, a constitutive model that describes the mechanical behavior of steels exhibiting the “Transformation Induced Plasticity” (TRIP) phenomenon during martensitic transformation is presented. Two- and four-phase TRIP steels are considered. No restriction is placed on the magnitude of the strains and appropriate “finite strain” constitutive equations are developed.

In Chapter 7, a methodology for the numerical integration of the resulting non-linear constitutive equations for TRIP steels in the context of the finite element method is presented. The implementation of the constitutive model in a finite element program and the procedure of solving the problem with finite elements in the context of finite strains are presented. The corresponding methodology under plane stress conditions is presented in Chapter 8.

In Chapter 9, the constitutive model for the two-phase TRIP steel is implemented in ABAQUS through the subroutine UMAT and is used for the analysis of model problems. In particular the problems of: i) uniaxial tension at different temperatures, ii) finite simple shear, and iii) plane strain tension are studied in detail.

In Chapter 10, the constitutive model for the four-phase TRIP steel is implemented in ABAQUS and is used for the calibration of the model with available experimental data. The calibrated model is used then to analyze the problems of uniaxial and plane-strain tension.

In Chapter 11, the calibrated model for the four-phase TRIP steel is used to study the development of a neck in a tension specimen.

In Chapter 12, is the problem of a plane strain mode-I blunt crack under small scale yielding conditions in a four-phase TRIP steel is studied in detail.

In Chapter 13, the calibrated model for the four-phase TRIP steel is used to calculate ‘forming limit diagrams’ for sheets made of TRIP steels. Experimental data from the same TRIP steel used for the calibration are compared with the predictions of the analytical model.

Finally, in Chapter 14 we present aspects of future research on TRIP steels.

CHAPTER TWO

HISTORICAL PERSPECTIVE

2.1 Introduction

Multiphase steels such as dual-phase steels show a very good combination of strength and formability so that the applicable region of high-strength steels has been widely enlarged. Especially the new developed TRIP-aided multiphase steels, which make use of the TRIP-effect (TRansformation Induced Plasticity), can further improve formability as well as strength due to the transformation of the metastable at room temperature retained austenite to martensite during the deformation.

TRIP steels offer very attractive combination of elongation and tensile strength as can be seen in Figure 2.1. A comparison of different steel families can be made by the product $R_m \times A_{80}$ (R_m stands for tensile strength and A_{80} for total % elongation) which can be above 20.000 MPa \times % for TRIP steels. The absolute elongation values can be as high as the values of the high-strength IF steels, which present the best formable high-strength steels developed so far. The tensile strength range of TRIP steels is 650 to 950 MPa and is much higher than today's tensile strength range of cold formable steels.

Therefore, TRIP-aided multiphase steels have the best strength-ductility balance among the formable high-strength steels developed so far. Furthermore, they can be used in structural and safety parts and can compete with other materials such as aluminium and composites in the future car light-weight design.

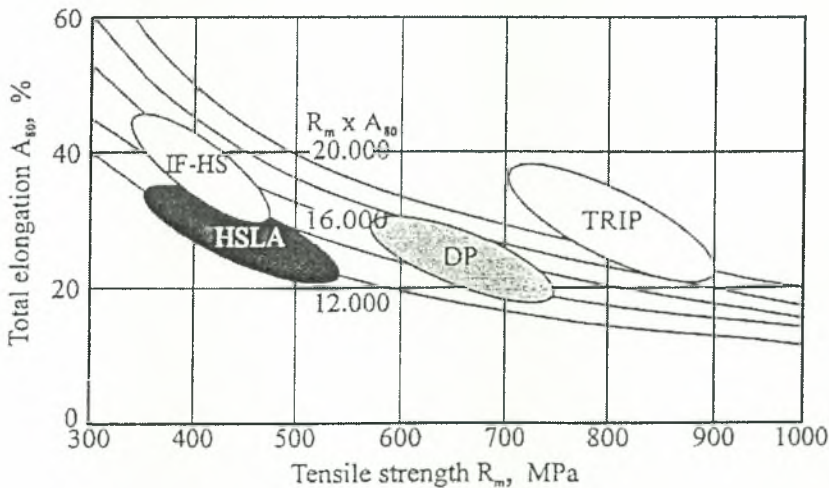


Figure 2.1: Total elongation and tensile strength of TRIP steels in comparison with conventional high strength steels; IF-HS: high strength interstitial free steel, DP: dual-phase steel, HSLA: high strength low alloy steel.

We present next a description of martensitic transformations, followed by a more specific discussion of the transformation plasticity phenomenon. A description of the heat treatment for the TRIP steels we examine is also presented. Finally, we review some of the relevant research that has been performed in this field.

2.2 General aspects of martensitic transformation

The strengthening of steel through quenching is a process that has been used for thousand of years. It has been only in relatively recent years, however, that this strengthening has been shown to be the result of a structural change called a martensitic transformation. The martensitic transformation is a widely observed phenomenon which has been observed in many metallic as well as ceramic systems.

The phenomenological features which distinguish martensitic transformations have been reviewed by Wayman (1983). A martensitic reaction can be considered to be a first-order solid-state structural change, which is (a) displacive, (b) diffusionless, and (c) dominated in kinetics and morphology by the strain energy arising from shear-like displacements. This set of three characteristics is regarded as both necessary and sufficient to define a martensitic transformation.

Martensitic transformation represents a subset of a more general classification of displacive (diffusionless) phase transformations, which are characterized by high speeds of transformation during which atoms move over distances less than the atomic spacing. In a displacive structural change, there is a coordinated shift of atoms, sometimes referred to descriptively as a “military” transformation. It is presumed that the atoms move in organized ways relative to their neighbors. In general, these displacements can be described as a combination of a homogenous lattice deformation and shuffles. In a lattice deformation or lattice-distortive strain, the coordinated shift of atoms converts one Bravais lattice homogeneously to another, and also involves whatever rigid-body rotation may occur because of the coupling between the transforming region and the adjacent parent matrix. The part of the lattice deformation which accomplishes the change in crystal structure, is a pure deformation, and is usually called the Bain distortion or Bain strain, the term originally adopted for the FCC→BCC (BCT) martensitic transformation in ferrous alloys. The transformation produces a shear strain as well as a volume expansion, which can vary from 0 to 5 percent, depending upon the chemical composition of the alloy. The Bain distortion, which helps visualize the lattice correspondence between the parent and product phases is presented in Figure 2.2. On the other hand, a shuffle is a coordinated shift of atoms within a

unit cell, which may change the structure but, in itself, does not produce a homogenous lattice-distortive strain. Figure 2.3 illustrates, in simple form, the distinction between lattice-distortive and shuffle displacements. Even though displacive phase transformations may generally comprise various combinations of lattice deformations and shuffles, martensitic transformation is typically dominated by lattice deformations rather than by shuffles, although shuffles are not excluded.

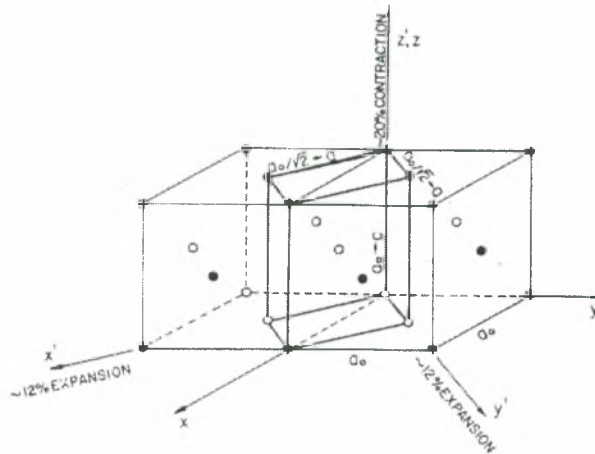


Figure 2.2: Lattice distortion and correspondence proposed by BAIN for the FCC→BCC (BCT) martensitic transformation in iron alloys. The correspondence related cell in the parent phase (indicated by bold lines) becomes a unit cell in martensite as a consequence of Bain strain.

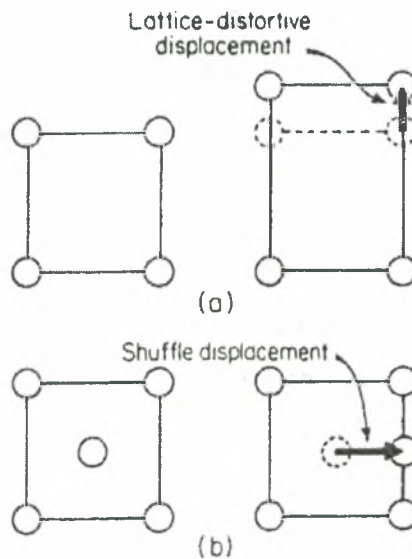


Figure 2.3: Schematic illustration of homogenous lattice deformation (a) and shuffles (b).

2.3 Driving force for martensitic transformation

At any given temperature, there exists one preferential crystallographic structure corresponding to the lowest energy level. The martensite phase has the thermodynamically preferred crystal structure at relatively low temperatures, so that when the steel is quenched, the original austenite structure, stable at high temperatures, tends to transform into martensite. Figure 2.4 shows schematically the change in chemical free energies of martensite and austenite (parent phase) with temperature.

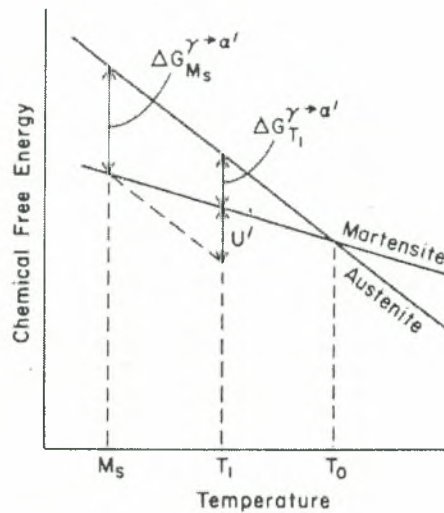


Figure 2.4: Schematic diagram showing the free energy change for a martensitic transformation.

The difference in free energy of austenite and martensite represents the chemical driving force $\Delta G^{\gamma \rightarrow \alpha'}$ available for martensitic transformation. For the transformation to occur, an energy barrier must be overcome, since, during transformation, crystal atoms will temporarily assume configurations corresponding to higher energy levels. If the driving force for transformation is not high enough, the energy barrier cannot be overcome: the parent state (austenite) cannot transform into the thermodynamically favorable product phase (martensite), and is said to be metastable. In temperature T_0 the free energy of austenite and martensite are in equilibrium and as the temperature decreases ($T_1 < T_0$) the chemical driving force $\Delta G_{T_1}^{\gamma \rightarrow \alpha'}$ increases so that, when austenite is rapidly cooled below a sufficiently low temperature, M_s , a spontaneous transformation to martensite occurs. The difference in free energies between austenite (γ) and martensite (α') at the M_s temperature is the critical chemical driving force

$\Delta G_{M_s}^{\gamma \rightarrow \alpha'}$ for the onset of the martensitic transformation. Martensitic transformation continues with further cooling beyond M_s until the temperature of M_f where no transformation can be observed and the amount of untransformed austenite is called retained austenite.

Another means of altering the driving force for transformation is by supplying mechanical work in the form of an applied stress. In this manner, the transformation of austenite to martensite can occur at temperatures higher than that for spontaneous transformation. Transformation at temperatures above M_s is said to be mechanically induced.

2.4 Transformation Plasticity

The shear-like displacive nature of martensitic transformations is responsible for the appearance of special interactions when external stresses are applied. The martensitic shape change itself contributes a mode of deformation, called Transformation Induced Plasticity (TRIP), which can influence stress-strain behavior in important ways.

The transformation plasticity that accompanies martensitic transformation in the presence of an applied stress provides substantial alteration of the mechanical properties of the material. This unique process allows for the design of materials which take advantage of the transformation itself, not simply the properties of transformation product. The notion of exploiting the properties of such a structural change is quite novel with respect to the classical view of the relationships between a material's structure and its properties.

It is useful to distinguish between the roles of elastic stress and plastic strain in influencing the martensitic nucleation process. As indicated schematically in Figure 2.5, the application of a stress at a temperature not far above M_s can include nucleation even though the stress may be well below the normal yield strength of the parent phase. This transformation is called stress-assisted (S.A.T.) because the existing nucleation sites are simply aided mechanically by the thermodynamic contribution of the applied stress. In other words, the critical driving force for nucleating the sites that normally operate without any external stress at M_s can be attained at temperatures above M_s since the mechanical driving force makes up for the reduced chemical driving force at such higher temperatures. Due to this interrelationship, stress-induced nucleation requires higher stresses, the higher the temperature, in accordance with the slope of line AC in Figure 2.5. It may be mentioned that the transformational-mechanical interactions described above are representative of athermal kinetics. For isothermal kinetics the corresponding effects of elastic stress and plastic strain are described by line A'B.

At a temperature designated as M_s^σ , the stress required for nucleation reaches the yield strength of the parent phase. Above M_s^σ significant plastic flow precedes the transformation, and an additional contribution to transformation can arise from the production of new and more potent nucleating sites by plastic deformation. This transformation is defined as strain-induced (S.I.T.). Under these conditions, the nucleating stresses at temperatures above M_s^σ do not fall on the extension of line AC, but rather along the line CD. The temperature M_s^σ thus defines an approximate boundary between the temperature regimes where the two modes of nucleation dominate; near M_s^σ both modes will operate. M_d is the temperature above which the chemical driving force becomes so small that nucleation cannot be mechanically induced, even in the plastic strain regime. Macroscopic yielding follows the line ACD in Figure 2.5. Often there is an overlap between the stress-assisted and strain-induced temperature ranges, and so the temperature may not be defined sharply. The line ACD designates the stress temperature conditions where the TRIP phenomenon sets in.

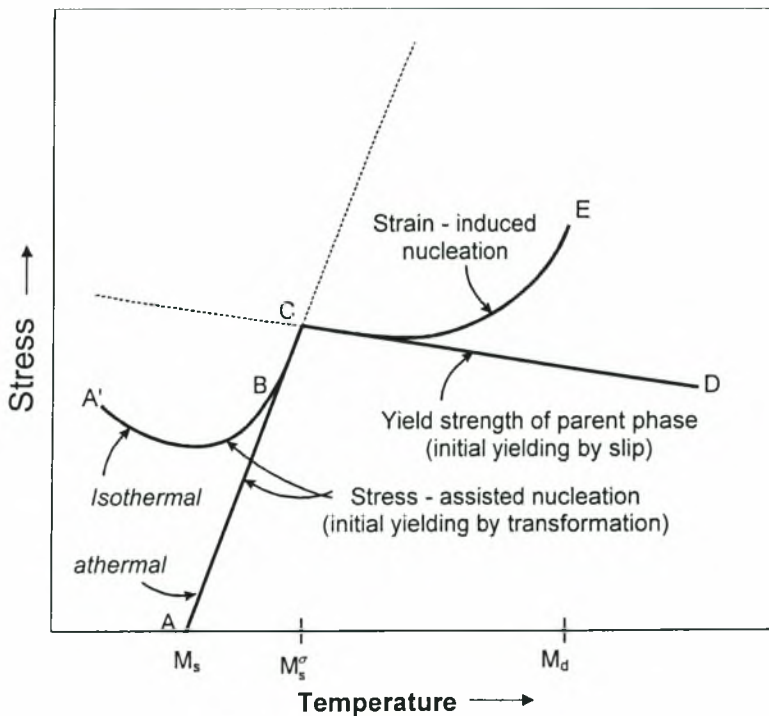


Figure 2.5: Schematic representation of the interrelationships between stress-assisted and strain-induced martensitic transformation.

At temperatures below M_s^σ , increasing the applied stress above the stress assisted transformation start line AB in Figure 2.5 causes further transformation and the concomitant

plastic flow is a consequence of the transformation plasticity. Under these conditions, the volume fraction of martensite formed is found to be a linear function of the plastic strain for a substantial part of the transformation. The resulting morphology is about the same as observed for the spontaneous transformation, which takes place without applied stress on cooling below M_s . At temperatures above M_s^σ , there is a sigmoidal relationship between the volume fraction of martensite and plastic strain as the stress is raised above the strain-induced transformation start line BC in Figure 2.5. In this case, the morphology depends on the new nucleation sites introduced by the slip-yielding of the parent phase along the line BC of Figure 2.5.

2.5 Heat treatment of TRIP steels

There are two categories of TRIP steels. The fully austenitic steels and the steels that contain dispersed particles of retained austenite. Our interest is focused in the latter category of TRIP steels and especially to those that retained austenite is dispersed in a matrix of ferrite and bainite. These steels are known as four-phase TRIP steels because retained austenite is metastable at room temperature and will be transformed to martensite during straining.

TRIP steel obtain the triple-phase microstructure following a specific procedure of heat treatment presented in Figure 2.6. The specimen of steel is first heated until a temperature of 700-900°C where intercritical annealing takes place. The temperature and time (almost 3 minutes) of intercritical annealing are chosen in a way that a microstructure of 50% ferrite and 50% austenite to be formed. Quenching after intercritical annealing is performed to an intermediate temperature above the martensite start temperature, which allows the bainite transformation to occur during isothermal holding. Bainite isothermal transformation takes place at temperatures 350-450°C and times 200-600 seconds and leads to the transformation of a part of austenite to bainite. The amount of austenite transformed to bainite depends on the temperature and time of the bainite isothermal transformation. Therefore, after bainite isothermal transformation the steel obtains a microstructure of 50% ferrite, 35-45% bainite and 15-5% austenite. In this step, the remaining austenite is further enriched with carbon, which shifts the martensite start temperature below room temperature. Finally, the specimen of steel is quenched in room temperature without austenite transformed to martensite and the desirable microstructure of 50% ferrite, 35-45% bainite and 15-5% austenite is retained. An electron microscopy picture of a typical TRIP microstructure is shown in Figure 2.7.

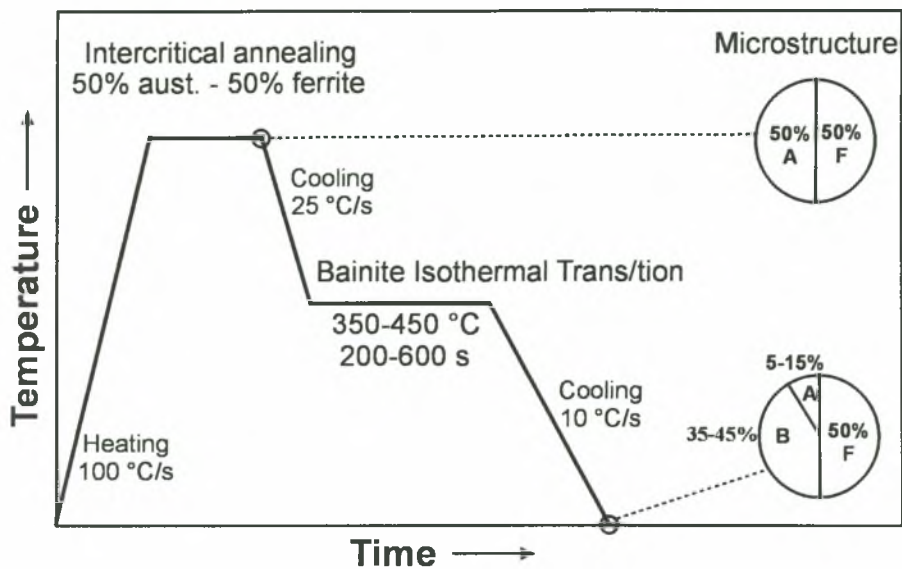


Figure 2.6: Schematic representation of the heat treatment performed for TRIP steels (A: austenite, B: bainite, F: ferrite).

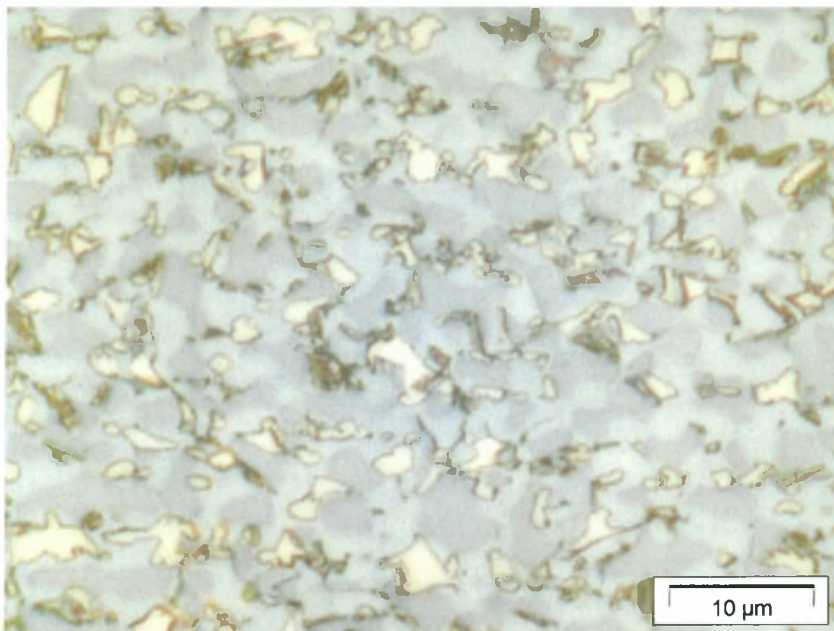


Figure 2.7: Microstructure of TRIP steel

2.6 Modeling of the mechanical constitutive behavior

A constitutive model for TRIP steels should predict the rate of martensitic formation ($f - \varepsilon$ curve) and how the evolution of martensite affects the stress-strain curve. The model should take into consideration the complicated nature of the interactions between stress,

strain, and transformation kinetics. Several modeling efforts have been undertaken in the past mainly focused on homogeneous austenitic steels.

One of the first attempts was made by Olson and Azrin (1978). They proposed a model that makes use of the "rule of mixtures" relation in order to relate the flow stress of TRIP steels to the deformation induced martensite content:

$$\sigma = \sigma_A + f \Delta\sigma$$

where σ_A is the austenite flow stress, and $\Delta\sigma$ is the strength difference between austenite and martensite. The dotted lines labelled σ_A and σ_M in Figure 2.8 represent the flow properties of stable austenite and martensite, respectively. The transformation curves observed at temperatures above and below M_s^σ and their associated σ - ϵ curves are denoted by the solid curves in Figure 2.8(a) and (b) respectively. The dashed σ - ϵ curves are the predictions of the proposed equation in each case. As the figures suggest, the curve measured above M_s^σ are in qualitative agreement with the rule of mixtures while the corresponding curve for temperature below M_s^σ differs significantly because of the "dynamic softening" effect.

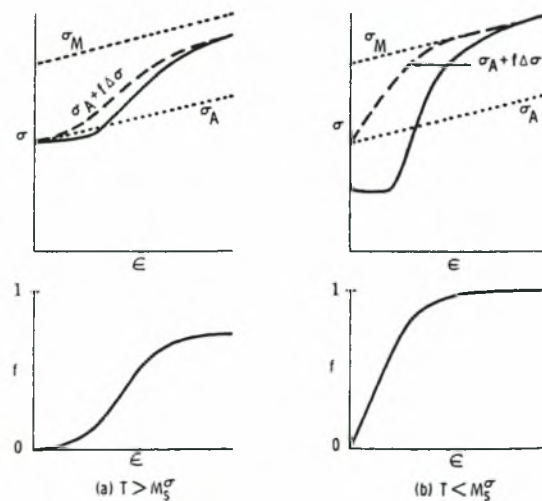


Figure 2.8: Schematic representation of tensile flow properties and transformation behavior for high-strength TRIP steel. Dotted lines represent σ - ϵ behavior of stable austenite (σ_A) and martensite (σ_M). Solid curves show experimental shape of σ - ϵ and f - ϵ curves of metastable austenite. Dashed curve shows predicted σ - ϵ curve from "rule of mixtures", based on shape of associated f - ϵ curve. (a) Behavior of material at temperatures above M_s^σ , (b) behavior below

M_s^σ .

A simple model was proposed also by Narutani *et al.* (1982). They derive a constitutive relation that predicts the flow behavior of metastable austenite from the strain-induced transformation kinetics and the flow properties of the two separate phases. Its principal feature is the use of the rule of mixture based on the assumption that the strain in both phases is equal to the macroscopic plastic strain. Due to the typically large difference in strength between martensite and austenite, this model, unaugmented, significantly overestimates the plastic stiffness, and does not correctly predict the strain levels in the individual phases. Naturani *et al.* proposed that, since some of the macroscopic plastic strain arises from martensitic transformation and does not correspond to the strain-hardening of either phase, the state of the plastic strain of each phase would correspond to the total strain minus a transformation strain proportional to the volume fraction of martensite. This is known as the strain-corrected rules of mixtures. Therefore, in calculating the respective phase contributions to the total flow stress, a “shape strain” contribution to the total strain is subtracted. Furthermore, this estimate is then scaled to match experimental data by subtracting a “dynamic softening” factor proportional to the rate of martensite formation. The functional form used in this model yields reasonable agreement with experimental data from uniaxial tension tests, as shown in Figure 2.9 but according to Stringfellow (1990) leads to numerical problems when introduced into computer codes for study of boundary value problems.

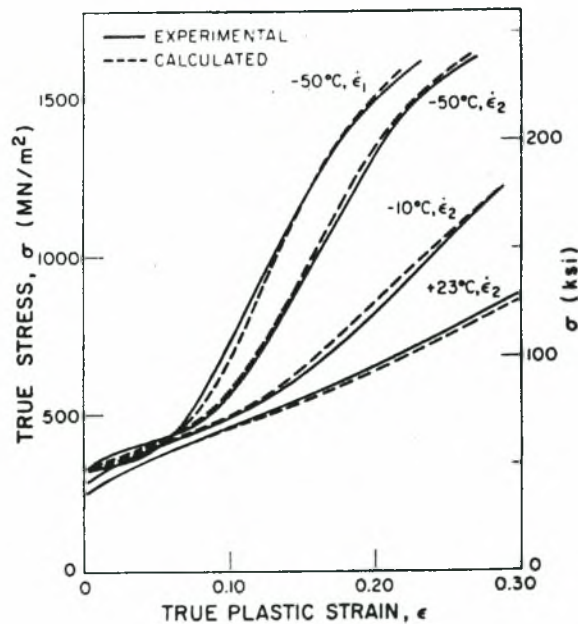


Figure 2.9: Comparison of experimental and calculated stress strain curves for 14Ni-7Cr stainless steel studied by Naturani, et al. (1982).

One of the first attempts to simulate with finite elements the mechanical behavior of steels that exhibit the transformation plasticity phenomenon was made by Stringfellow et al. (1992). They proposed a constitutive model that describes the transformation plasticity accompanying strain-induced martensitic transformation in metastable austenitic steels. The model proposed, considers the evolution of the volume fraction of martensite using a transformation kinetics law and defines the flow strength of the evolving two-phase composite using a constitutive law. The transformation kinetics model used is an updated form of the Olson and Cohen model (1975) for strain induced martensitic transformation kinetics, in which stress state sensitivity of the transformation process has been incorporated. A self-consistent method is used for predicting the resultant stress-strain behavior of the two-phase composite. The predicted results for both martensite evolution vs strain and stress vs strain are in good agreement with experimental data as can be seen in Figure 2.10.

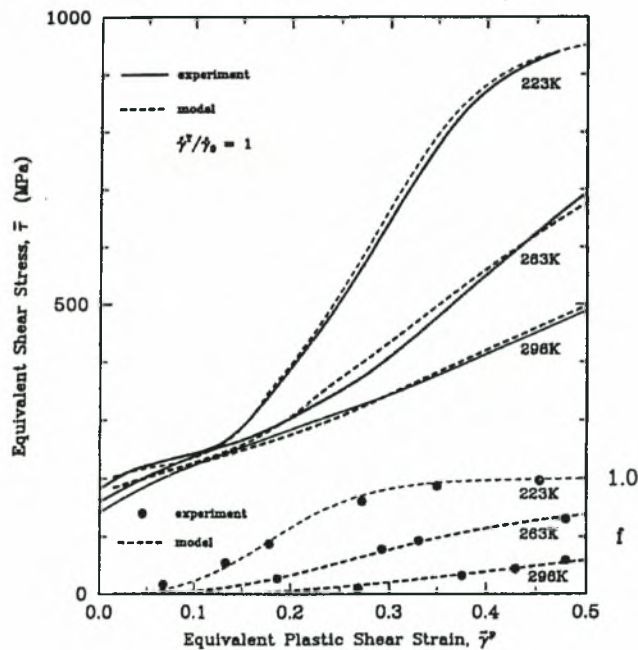


Figure 2.10: Comparison of model predictions for equivalent shear stress vs equivalent plastic strain. Experimental points represent data measured in simple tension tests for a 14Cr-7Ni SITP alloy.

CHAPTER THREE

VISCOPLASTICITY

3.1 Introduction

In the constitutive model developed, plastic strain is modeled using a viscoplastic constitutive equation instead of rate independent plasticity. The use of viscoplasticity leads to a more simplified system of constitutive equations and favors the application of the homogenization theory we use. In this chapter we examine the validity of using viscoplasticity for describing the plastic strain and we set the requirements that should be satisfied.

3.2 Constitutive model of viscoplasticity

In a small-strain plasticity problem the total strain $\boldsymbol{\varepsilon}$ can be decomposed into elastic and plastic parts:

$$\boldsymbol{\varepsilon} = \boldsymbol{\varepsilon}^e + \boldsymbol{\varepsilon}^p \quad (3.1)$$

Isotropic linear elasticity is assumed and the elastic strain tensor $\boldsymbol{\varepsilon}^e$ is related to the Cauchy stress tensor $\boldsymbol{\sigma}$ as follows

$$\boldsymbol{\varepsilon}^e = \mathbf{M}^e : \boldsymbol{\sigma} \quad \text{or} \quad \boldsymbol{\sigma} = \mathbf{L}^e : \boldsymbol{\varepsilon}^e \quad (3.2)$$

where \mathbf{M}^e and \mathbf{L}^e are the fourth-order compliance and stiffness tensors defined as

$$\mathbf{M}^e = \frac{1}{2G} \mathbf{K} + \frac{1}{3K} \mathbf{J} \quad \text{and} \quad \mathbf{L}^e = 2G \mathbf{K} + 3K \mathbf{J} \quad (3.3)$$

where G , K are the elastic shear and bulk modulus respectively, and \mathbf{K} , \mathbf{J} are fourth order tensors with Cartesian components:

$$K_{ijkl} = I_{ijkl} - J_{ijkl}, \quad I_{ijkl} = \frac{1}{2} (\delta_{ik} \delta_{jl} + \delta_{il} \delta_{jk}), \quad J_{ijkl} = \frac{1}{3} \delta_{ij} \delta_{kl}, \quad (3.4)$$

with δ_{ij} being the Kronecker delta.

The rate of the plastic strain using tensor $\boldsymbol{\varepsilon}^p$ is given by the form:

$$\dot{\boldsymbol{\varepsilon}}^p = \dot{\bar{\boldsymbol{\varepsilon}}}^p \mathbf{N} \quad \text{with} \quad \dot{\bar{\boldsymbol{\varepsilon}}}^p = \dot{\varepsilon}_0 \left[\frac{\sigma_{eq}}{\sigma_y(\bar{\boldsymbol{\varepsilon}}^p)} \right]^m \quad \text{and} \quad \mathbf{N} = \frac{3}{2} \frac{\mathbf{s}}{\sigma_{eq}} \quad (3.5)$$

where $\dot{\varepsilon}_0$ is a reference value for strain rate, m is the strain-rate-sensitivity exponent of the

material, $\sigma_{eq} = \sqrt{\frac{3}{2} \mathbf{s} : \mathbf{s}}$ is the von Mises equivalent stress, \mathbf{s} is the deviatoric stress tensor, and

$\sigma_y(\bar{\boldsymbol{\varepsilon}}^p)$ is the yield stress of the material at the reference strain rate $\dot{\varepsilon}_0$. The yield stress of the

material exhibits hardening during straining and it is considered as a function of equivalent plastic strain $\bar{\boldsymbol{\varepsilon}}^p$ through:

$$\sigma_y(\bar{\varepsilon}^P) = \sigma_0 \left(1 + \frac{\bar{\varepsilon}^P}{\varepsilon_0} \right)^{1/n} \quad (3.6)$$

where σ_0, ε_0 are reference values for yield stress and strain respectively with $\sigma_0 = E \varepsilon_0$ (E is the Young modulus), n is the hardening exponent, and $\bar{\varepsilon}^P = \int_0^t \dot{\varepsilon}^P dt$ is the equivalent plastic strain.

It can be shown easily that the following equations hold

$$\mathbf{N} : \mathbf{N} = \frac{3}{2}, \quad \boldsymbol{\sigma} : \mathbf{N} = \sigma_{eq}, \quad \mathbf{L}^e : \mathbf{N} = \mathbf{N} : \mathbf{L}^e = 2G\mathbf{N} \quad \text{and} \quad \sqrt{\frac{2}{3} \dot{\boldsymbol{\varepsilon}}^P : \dot{\boldsymbol{\varepsilon}}^P} = \dot{\bar{\varepsilon}}^P \quad (3.7)$$

3.3 Numerical Integration of constitutive equations-Solution method

In a finite element environment, the solution is developed incrementally and the constitutive equations are integrated numerically at the element Gauss points. In a displacement based finite element formulation the solution is deformation driven. At a given Gauss point, the solution $(\boldsymbol{\sigma}_n, \boldsymbol{\varepsilon}_n, \bar{\varepsilon}_n^P)$ at time t_n as well as the strain $\boldsymbol{\varepsilon}_{n+1}$ at time t_{n+1} are known and the problem is to determine $(\boldsymbol{\sigma}_{n+1}, \bar{\varepsilon}_{n+1}^P)$. The numerical calculation of $\boldsymbol{\sigma}_{n+1}$ and $\bar{\varepsilon}_{n+1}^P$ is described in the following.

The constitutive equation of elasticity gives:

$$\boldsymbol{\sigma}_{n+1} = \mathbf{L}^e : \boldsymbol{\varepsilon}_{n+1}^e = \mathbf{L}^e : (\boldsymbol{\varepsilon}_n^e + \Delta\boldsymbol{\varepsilon} - \Delta\boldsymbol{\varepsilon}^P) = \boldsymbol{\sigma}^e - \mathbf{L}^e : \Delta\boldsymbol{\varepsilon}^P \quad (3.8)$$

where $\Delta\boldsymbol{\varepsilon} = \boldsymbol{\varepsilon}_{n+1} - \boldsymbol{\varepsilon}_n$ and $\Delta\boldsymbol{\varepsilon}^P = \boldsymbol{\varepsilon}_{n+1}^P - \boldsymbol{\varepsilon}_n^P$ are the total and plastic strain increments, and $\boldsymbol{\sigma}^e = \mathbf{L}^e : (\boldsymbol{\varepsilon}_n^e + \Delta\boldsymbol{\varepsilon})$ is the known “elastic predictor”.

The plastic constitutive equations are integrated using the backward Euler scheme. Equation (3.5) implies that

$$\Delta\boldsymbol{\varepsilon}^P = \Delta\bar{\varepsilon}^P \mathbf{N}_{n+1} \quad \text{with} \quad \Delta\bar{\varepsilon}^P = \dot{\varepsilon}_\sigma \left[\frac{\sigma_{eq}|_{n+1}}{\sigma_y(\bar{\varepsilon}_{n+1}^P)} \right]^m \Delta t \quad (3.9)$$

We substitute (3.9) into the elasticity equation (3.8) and take into account that $\mathbf{L}^e : \mathbf{N} = 2G\mathbf{N}$ to find:

$$\boldsymbol{\sigma}_{n+1} = \boldsymbol{\sigma}^e - 2G \Delta\bar{\varepsilon}^P \mathbf{N}_{n+1} \quad (3.10)$$

Next, we calculate the deviatoric part of $\boldsymbol{\sigma}_{n+1}$:

$$\mathbf{s}_{n+1} = \mathbf{s}^e - 2G \Delta\bar{\varepsilon}^P \mathbf{N}_{n+1} \quad (3.11)$$

In the last equation we use the definition of $\mathbf{N}_{n+1} = \frac{3}{2\sigma_{eq}|_{n+1}} \mathbf{s}_{n+1}$ to find:

$$\mathbf{s}_{n+1} = \mathbf{s}^e - \frac{3G\Delta\bar{\varepsilon}^p}{\sigma_{eq}|_{n+1}} \mathbf{s}_{n+1} \quad \text{or} \quad \mathbf{s}_{n+1} = c \mathbf{s}^e \quad (3.12)$$

where $c = \left(1 + \frac{3G\Delta\bar{\varepsilon}^p}{\sigma_{eq}|_{n+1}}\right)^{-1}$. The last equation shows that the tensors σ'_{n+1} and $(\sigma^e)'$ are co-linear. Therefore \mathbf{N}_{n+1} can be determined as follows

$$\mathbf{N}_{n+1} = \frac{3}{2} \frac{\mathbf{s}_{n+1}}{\sqrt{\frac{3}{2} \mathbf{s}_{n+1} : \mathbf{s}_{n+1}}} = \frac{3}{2} \frac{\mathbf{s}^e}{\sqrt{\frac{3}{2} \mathbf{s}^e : \mathbf{s}^e}} = \mathbf{N}^e = \text{known} \quad (3.13)$$

Projecting the stress tensor in (3.10) onto the deviatoric plane and the pressure axis (i.e., calculating $\sigma_{n+1} : \mathbf{N}_{n+1} = \sigma_{eq}|_{n+1}$ and $\sigma_{n+1} : \delta/3 = p_{n+1}$) we find

$$\sigma_{eq}|_{n+1} = \sigma_{eq}^e - 3G\Delta\bar{\varepsilon}^p \quad \text{and} \quad p_{n+1} = p^e = \text{known} \quad (3.14)$$

where $p = \sigma : \delta/3 = \sigma_{kk}/3$ is the hydrostatic stress, and the relationship $\mathbf{N} : \mathbf{N} = 3/2$ have been used. Next, we solve equation (3.9) for the equivalent stress $\sigma_{eq}|_{n+1}$:

$$\sigma_{eq}|_{n+1} = \sigma_y(\bar{\varepsilon}_{n+1}^p) \left(\frac{\Delta\bar{\varepsilon}^p}{\dot{\varepsilon}_o \Delta t} \right)^{1/m} \quad (3.15)$$

Substituting (3.15) into (3.14), we obtain the basic equation of the problem:

$$F(\Delta\bar{\varepsilon}^p) = \sigma_y(\bar{\varepsilon}_n^p + \Delta\bar{\varepsilon}^p) \left(\frac{\Delta\bar{\varepsilon}^p}{\dot{\varepsilon}_o \Delta t} \right)^{1/m} - \sigma_{eq}^e + 3G\Delta\bar{\varepsilon}^p = 0 \quad (3.16)$$

We choose the increment of equivalent plastic strain $\Delta\bar{\varepsilon}^p$ as the primary unknown and we develop a numerical method for solving the above non-linear equation. The solution is obtained by using Newton's method. The derivative of $F(\Delta\bar{\varepsilon}^p)$ with respect to $\Delta\bar{\varepsilon}^p$ have to be defined for the solution of the non-linear equation:

$$F'(\Delta\bar{\varepsilon}^p) = \left(\frac{\Delta\bar{\varepsilon}^p}{\dot{\varepsilon}_o \Delta t} \right)^{1/m} \left(h_{n+1} + \frac{\sigma_y}{m\Delta\bar{\varepsilon}^p} \right) + 3G \quad (3.17)$$

where $h_{n+1} = \frac{d\sigma_y}{d\bar{\varepsilon}^p}|_{n+1}$. Equation (3.16) is solved iteratively until a fixed point is reached. The first estimate for $\Delta\bar{\varepsilon}^p$ used to start the Newton loop is obtained by using a forward Euler scheme, i.e.,

$$\left(\Delta\bar{\varepsilon}^p\right)_{est} = \dot{\varepsilon}_o \left[\frac{\sigma_{eq}|_n}{\sigma_y(\bar{\varepsilon}_n^p)} \right]^m \Delta t \quad (3.18)$$

Once $\Delta\bar{\varepsilon}^p$ has been found, (3.10) defines σ_{n+1} . Finally $\bar{\varepsilon}_{n+1}^p = \bar{\varepsilon}_n^p + \Delta\bar{\varepsilon}^p$, which completes the integration process.

3.4 Linearization moduli

In an implicit finite element code, the overall discretized equilibrium equations are written at the end of the increment, resulting in a set of non-linear equations for the nodal unknowns. If a full Newton scheme is used to solve the global non-linear equations, one needs to calculate the linearization moduli $\bar{\mathbf{C}}$ defined:

$$\bar{\mathbf{C}} = \frac{\partial \sigma_{n+1}}{\partial \varepsilon_{n+1}} \quad (3.19)$$

For simplicity, we drop the subscript $n+1$ with the understanding that all quantities are evaluated at the end of the increment, unless otherwise indicated. In general, $\bar{\mathbf{C}}$ depends on both the constitutive model and the algorithm used for the numerical integration of the constitutive equations. Starting with the derivative of the elasticity equation (3.10) we find:

$$\sigma_{n+1} = \sigma_n + \mathbf{L}^e : \Delta \varepsilon - 2G \Delta\bar{\varepsilon}^p \mathbf{N}_{n+1} \quad \Rightarrow \quad d\sigma = \mathbf{L}^e : d\varepsilon - 2G(d\bar{\varepsilon}^p \mathbf{N} + \Delta\bar{\varepsilon}^p d\mathbf{N}) \quad (3.20)$$

In order to determine $\bar{\mathbf{C}}$ we need to express the terms $d\bar{\varepsilon}^p$, $d\mathbf{N}$ as functions of $d\varepsilon$. The term

$d\mathbf{N}$ is equal to $d\mathbf{N}^e = \frac{3}{2}d\left(\frac{1}{\sigma_{eq}^e} \mathbf{s}^e\right)$, which, after some simple algebra, it found to be

$$d\mathbf{N} = \frac{2G}{\sigma_{eq}^e} \left(\frac{3}{2} \mathbf{K} - \mathbf{N} \mathbf{N} \right) : d\varepsilon \quad (3.21)$$

We define $d\bar{\varepsilon}^p$ from equation (3.9):

$$\Delta\bar{\varepsilon}^p = \dot{\varepsilon}_o \left[\frac{\sigma_{eq}}{\sigma_y(\bar{\varepsilon}^p)} \right]^m \Delta t \quad \Rightarrow \quad d\bar{\varepsilon}^p = \frac{\partial \Delta\bar{\varepsilon}^p}{\partial \sigma_{eq}} \frac{\partial \sigma_{eq}}{\partial \sigma} : d\sigma + \frac{\partial \Delta\bar{\varepsilon}^p}{\partial \sigma_y} \frac{d\sigma_y}{d\bar{\varepsilon}^p} d\bar{\varepsilon}^p \quad (3.22)$$

Also, we can show easily that

$$\frac{\partial \Delta\bar{\varepsilon}^p}{\partial \sigma_{eq}} = \dot{\varepsilon}_o m \left(\frac{\sigma_{eq}}{\sigma_y} \right)^{m-1} \frac{\Delta t}{\sigma_y} \quad \Rightarrow \quad \frac{\partial \Delta\bar{\varepsilon}^p}{\partial \sigma_{eq}} = m \frac{\Delta\bar{\varepsilon}^p}{\sigma_{eq}} \quad (3.23)$$

$$\frac{\partial \sigma_{eq}}{\partial \sigma} = \mathbf{N} \quad (3.24)$$

$$\frac{\partial \Delta \bar{\varepsilon}^p}{\partial \sigma_y} = \dot{\varepsilon}_e m \left(\frac{\sigma_{eq}}{\sigma_y} \right)^{m-1} \left(-\frac{\Delta t \sigma_{eq}}{\sigma_y^2} \right) \Rightarrow \frac{\partial \Delta \bar{\varepsilon}^p}{\partial \sigma_y} = -m \frac{\Delta \bar{\varepsilon}^p}{\sigma_y} \quad (3.25)$$

$$\frac{d\sigma_y}{d\bar{\varepsilon}^p} = h \quad (3.26)$$

We substitute (3.23)-(3.26) into (3.22) to find

$$d\bar{\varepsilon}^p = m \frac{\Delta \bar{\varepsilon}^p}{\sigma_{eq}} \mathbf{N} : d\boldsymbol{\sigma} - m \frac{\Delta \bar{\varepsilon}^p}{\sigma_y} h d\bar{\varepsilon}^p \quad (3.27)$$

Next, we substitute $d\boldsymbol{\sigma}$ from (3.20) into (3.27):

$$d\bar{\varepsilon}^p = m \frac{\Delta \bar{\varepsilon}^p}{\sigma_{eq}} \mathbf{N} : \left[\mathbf{L}^e : d\boldsymbol{\varepsilon} - 2G \left(d\bar{\varepsilon}^p \mathbf{N} + \Delta \bar{\varepsilon}^p d\mathbf{N} \right) \right] - m \frac{\Delta \bar{\varepsilon}^p}{\sigma_y} h d\bar{\varepsilon}^p \quad (3.28)$$

Taking into account that $\mathbf{N} : \mathbf{L}^e = 2G \mathbf{N}$, $\mathbf{N} : \mathbf{N} = 3/2$ and $\mathbf{N} : d\mathbf{N} = 0$, we conclude that

$$d\bar{\varepsilon}^p = m \Delta \bar{\varepsilon}^p \left[\frac{2G}{\sigma_{eq}} \mathbf{N} : d\boldsymbol{\varepsilon} - \left(\frac{3G}{\sigma_{eq}} + \frac{h}{\sigma_y} \right) d\bar{\varepsilon}^p \right]$$

which implies that

$$d\bar{\varepsilon}^p = \frac{2G}{3G + \sigma_{eq} \left(\frac{h}{\sigma_y} + \frac{1}{m \Delta \bar{\varepsilon}^p} \right)} \mathbf{N} : d\boldsymbol{\varepsilon} \quad (3.29)$$

Finally, we substitute (3.21) and (3.29) into (3.20) to find:

$$d\boldsymbol{\sigma} = \mathbf{L}^e : d\boldsymbol{\varepsilon} - 2G \left[\frac{2G}{3G + \sigma_{eq} \left(\frac{h}{\sigma_y} + \frac{1}{m \Delta \bar{\varepsilon}^p} \right)} (\mathbf{N} : d\boldsymbol{\varepsilon}) \mathbf{N} + \frac{2G \Delta \bar{\varepsilon}^p}{\sigma_{eq}^e} \left(\frac{3}{2} \mathbf{K} - \mathbf{N} \mathbf{N} \right) : d\boldsymbol{\varepsilon} \right]$$

or

$$d\boldsymbol{\sigma} = \bar{\mathbf{C}} : d\boldsymbol{\varepsilon} \quad (3.30)$$

where

$$\bar{\mathbf{C}} = \frac{\partial \boldsymbol{\sigma}_{n+1}}{\partial \boldsymbol{\varepsilon}_{n+1}} = \mathbf{L}^e - \frac{4G^2}{3G + \sigma_{eq} \left(\frac{h}{\sigma_y} + \frac{1}{m \Delta \bar{\varepsilon}^p} \right)} \mathbf{N} \mathbf{N} - \frac{4G^2 \Delta \bar{\varepsilon}^p}{\sigma_{eq}^e} \left(\frac{3}{2} \mathbf{K} - \mathbf{N} \mathbf{N} \right) \quad (3.31)$$

3.5 Use of viscoplasticity for describing rate independent plasticity

The viscoplastic model developed can be used for the description of rate independent plasticity in limit $m \rightarrow \infty$ as described in the following. The plastic strain rate is determined from the viscoplastic relation (3.5):

$$\dot{\bar{\epsilon}}^p = \dot{\bar{\epsilon}}^p N \quad \text{with} \quad \dot{\bar{\epsilon}}^p = \dot{\epsilon}_0 \left[\frac{\sigma_{eq}}{\sigma_y(\bar{\epsilon}^p)} \right]^m \quad (3.32)$$

- In equation (3.32) if $\sigma_{eq} < \sigma_y$ and $m \rightarrow \infty$, the rate of plastic strain tends to zero ($\dot{\bar{\epsilon}}^p \rightarrow 0$). Therefore, as $m \rightarrow \infty$, equation (3.32) predicts a vanishing plastic strain rate for stress states inside the “yield surface” defined by the relationship $\sigma_{eq} = \sigma_y$.
- Equation (3.32) implies that

$$\sigma_{eq} = \sigma_y(\bar{\epsilon}^p) \left(\frac{\dot{\bar{\epsilon}}^p}{\dot{\epsilon}_0 \Delta t} \right)^{1/m} \quad (3.33)$$

If $m \rightarrow \infty$ then $1/m \rightarrow 0$ and (3.33) implies that, when $\dot{\bar{\epsilon}}^p \neq 0$, $\sigma_{eq} \rightarrow \sigma_y(\bar{\epsilon}^p)$.

Therefore, if $\dot{\bar{\epsilon}}^p \neq 0$, the yield criterion $\sigma_{eq} = \sigma_y$ is satisfied asymptotically as $m \rightarrow \infty$.

- If we consider the limit of $F(\Delta\bar{\epsilon}^p)$ in equation (3.16) with $m \rightarrow \infty$ ($1/m \rightarrow 0$), we obtain the following equation:

$$F(\Delta\bar{\epsilon}^p) \approx \sigma_y(\bar{\epsilon}_n^p + \Delta\bar{\epsilon}^p) - \sigma_{eq}^e + 3G \Delta\bar{\epsilon}^p = 0 \quad (3.34)$$

Equation (3.34) is the same as that of the von Mises yielding criterion in rate independent plasticity. Similarly, as $m \rightarrow \infty$, the expression for the derivative $F'(\Delta\bar{\epsilon}^p)$ is the same as that of the rate independent von Mises plasticity, i.e.,

$$F'(\Delta\bar{\epsilon}^p) \xrightarrow{m \rightarrow \infty} h_{n+1} + 3G \quad (3.35)$$

Therefore, a viscoplastic model with a high value exponent m can be used for the description of rate independent plasticity. The level of the exponent m for which the above observations are valid is of great interest and has to be examined.

3.6 Implementation of a viscoplastic model into FEM

The procedure described in section 3.3 for the numerical integration of the elastoplastic constitutive equations is implemented in the ABAQUS general-purpose finite element program. This program provides a general interface so that the viscoplastic constitutive model can be introduced as a “user subroutine” through UMAT.

In order to avoid numerical difficulties for large values of the strain-rate sensitivity exponent m , equation (3.16) that determines $\Delta\bar{\epsilon}^p$ is written in the form

$$\left(\frac{\Delta \bar{\epsilon}^p}{\dot{\epsilon}_o \Delta t} \right)^{1/m} = \frac{\sigma_{eq}^e - 3G \Delta \bar{\epsilon}^p}{\sigma_y (\bar{\epsilon}_n^p + \Delta \bar{\epsilon}^p)} \quad \text{or} \quad G(\Delta \bar{\epsilon}^p) = \frac{1}{m} \ln \left(\frac{\Delta \bar{\epsilon}^p}{\dot{\epsilon}_o \Delta t} \right) - \ln \left[\frac{\sigma_{eq}^e - 3G \Delta \bar{\epsilon}^p}{\sigma_y (\bar{\epsilon}_n^p + \Delta \bar{\epsilon}^p)} \right] = 0$$

and the last equation $G(\Delta \bar{\epsilon}^p) = 0$ is solved for $\Delta \bar{\epsilon}^p$ in the computations.

3.7 Results

The use of an exponent m with a high value is a basic requirement for the description of rate independent plasticity using a viscoplastic model. The proposed model should be essentially independent of the rate of loading.

“One element” tests for $m = 10, 60, 100$ and 1000 are carried out in ABAQUS in order to simulate plane strain tension. Four node isoparametric plane strain elements are used in the computations. A final elongation of 30% deformation is imposed in all cases. A value of $\dot{\epsilon}_o = 10^{-4} \text{ s}^{-1}$ is used for the “reference strain rate” and calculations are carried out for imposed strain rates of $0.1\dot{\epsilon}_o$, $\dot{\epsilon}_o$ and $10\dot{\epsilon}_o$.

The effect of the hardening exponent n on the viscoplastic model is also examined. The series of “one element” tests described above have been performed for three different hardening exponents, namely $n = 5, 10$ and 15 .

In all cases analyzed, the values of $E = 300\sigma_o$ and $\nu = 0.3$ are used for Young’s modulus and Poisson ratio.

In addition to the calculations with the viscoplastic model, “one element” tests are carried out in ABAQUS using the classical rate independent von Mises plasticity model; the flow stress varies with plastic strain according to equation (3.6), which is implemented via the UHARD “user subroutine” (ABAQUS 2003). The variation of the normalized yield stress σ_y/σ_o with the equivalent plastic strain $\bar{\epsilon}^p$ is shown in Figure 3.1 for three different values of the hardening exponent, namely $n = 5, 10$ and 15 .

Figures 3.2-3.5 show the variation of the normalized equivalent stress σ_{eq}/σ_o in plane strain tension with the equivalent plastic strain $\bar{\epsilon}^p$ for a hardening exponent $n = 5$, for different values of the exponent ($m = 10, 60, 100$ and 1000) and for different imposed strain rates ($0.1\dot{\epsilon}_o$, $\dot{\epsilon}_o$ and $10\dot{\epsilon}_o$). The curves marked “ σ_y ” on the figures corresponds to the rate independent von Mises model.

The corresponding curves for $n = 10$ and 15 are shown in Figures 3.6-3.9 and 3.10-3.13.

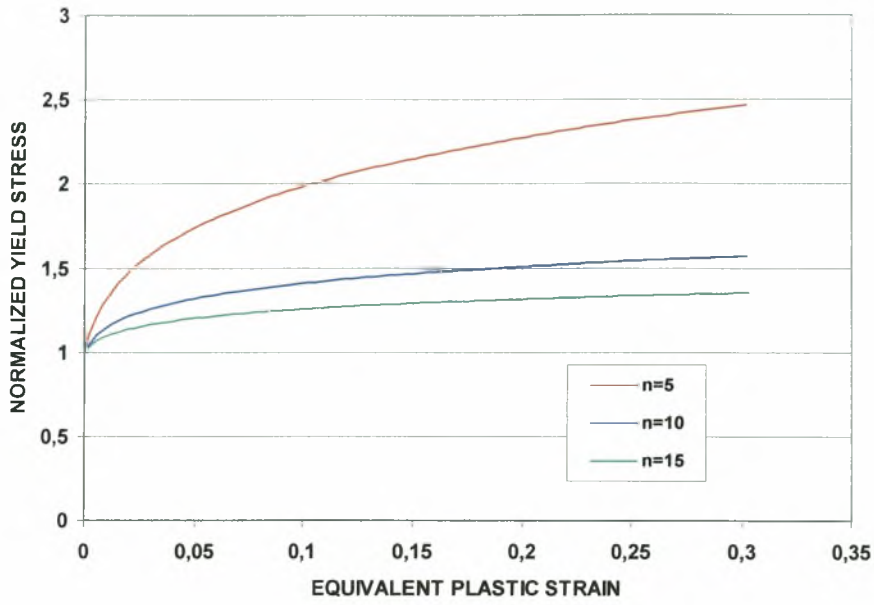


Figure 3.1: Hardening curves $\sigma_y(\bar{\epsilon}^p)/\sigma_0$ vs. $\bar{\epsilon}^p$ for $n=5, 10$ and 15 .

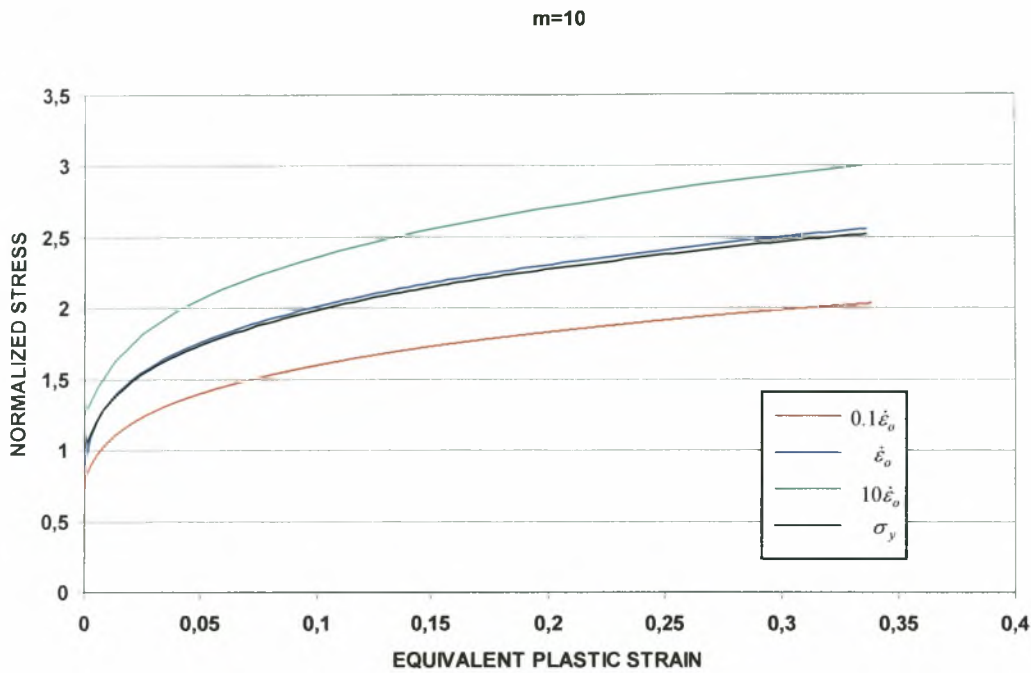
Material with hardening exponent $n = 5$ 

Figure 3.2: Variation of σ_{eq}/σ_0 with $\bar{\varepsilon}^P$ in plane strain tension for $n = 5$, $m = 10$, $\dot{\varepsilon}_0 = 10^{-4} s^{-1}$ and strain rates $0.1\dot{\varepsilon}_0$, $\dot{\varepsilon}_0$ and $10\dot{\varepsilon}_0$, together with the flow stress $\sigma_y(\bar{\varepsilon}^P)$.

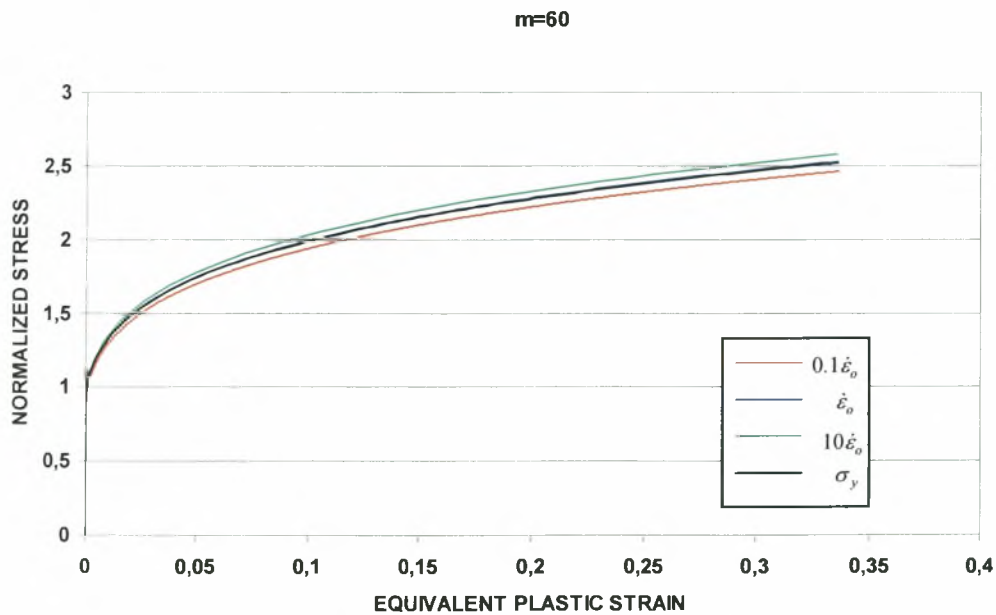


Figure 3.3: Variation of σ_{eq}/σ_0 with $\bar{\varepsilon}^P$ in plane strain tension for $n = 5$, $m = 60$, $\dot{\varepsilon}_0 = 10^{-4} s^{-1}$ and strain rates $0.1\dot{\varepsilon}_0$, $\dot{\varepsilon}_0$ and $10\dot{\varepsilon}_0$, together with the flow stress $\sigma_y(\bar{\varepsilon}^P)$.

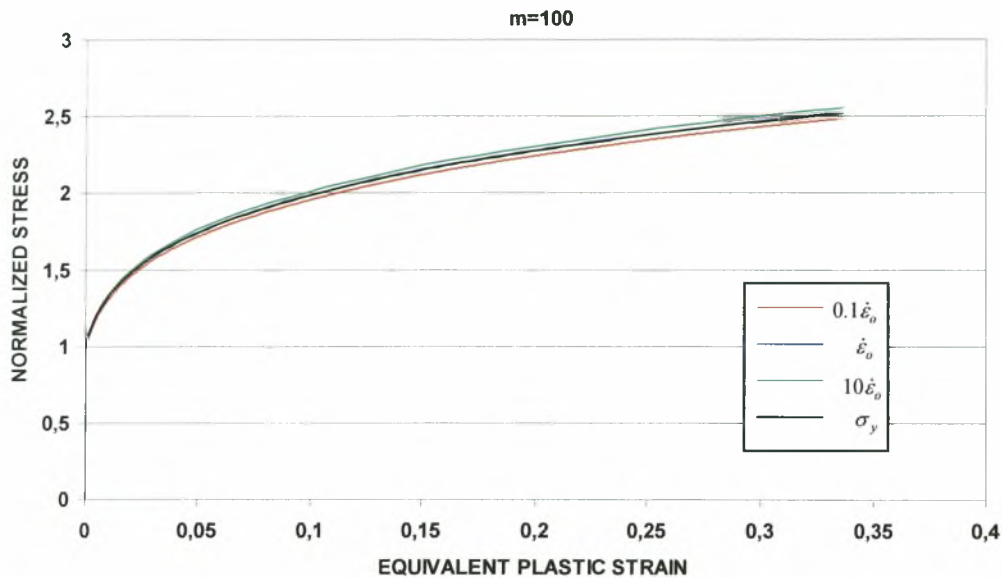


Figure 3.4: Variation of σ_{eq}/σ_0 with $\bar{\epsilon}^P$ in plane strain tension for $n = 5$, $m = 100$, $\dot{\epsilon}_0 = 10^{-4} \text{ s}^{-1}$ and strain rates $0.1\dot{\epsilon}_0$, $\dot{\epsilon}_0$ and $10\dot{\epsilon}_0$, together with the flow stress $\sigma_y(\bar{\epsilon}^P)$.

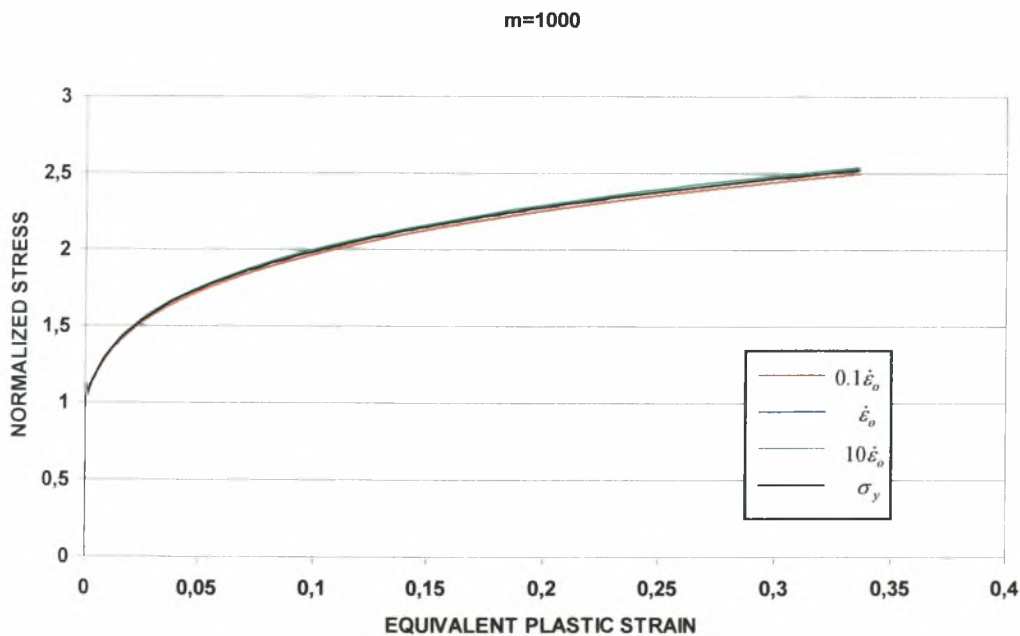


Figure 3.5: Variation of σ_{eq}/σ_0 with $\bar{\epsilon}^P$ in plane strain tension for $n = 5$, $m = 1000$, $\dot{\epsilon}_0 = 10^{-4} \text{ s}^{-1}$ and strain rates $0.1\dot{\epsilon}_0$, $\dot{\epsilon}_0$ and $10\dot{\epsilon}_0$, together with the flow stress $\sigma_y(\bar{\epsilon}^P)$.

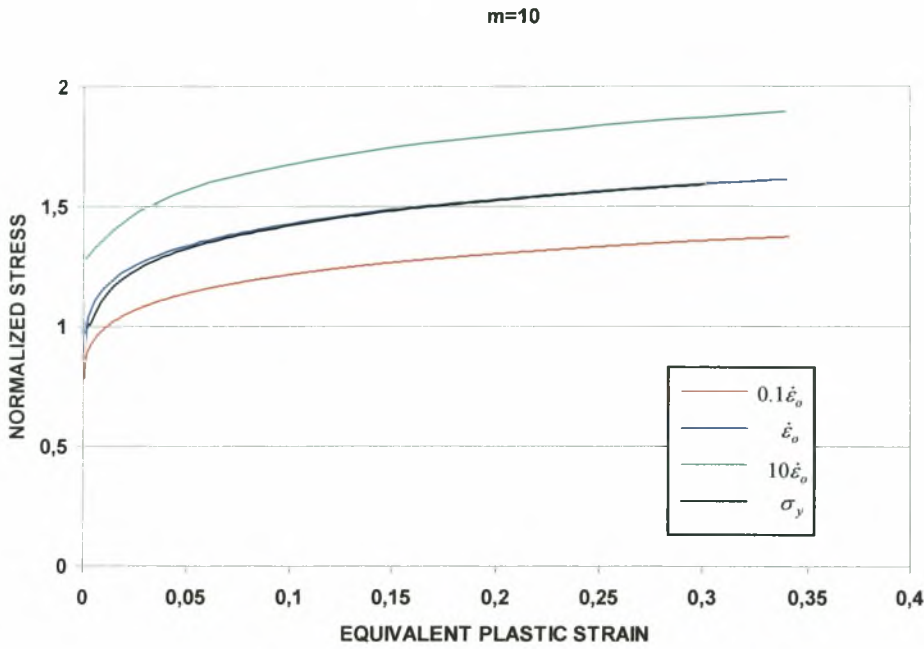
Material with hardening exponent $n = 10$ 

Figure 3.6: Variation of σ_{eq}/σ_0 with $\bar{\epsilon}^p$ in plane strain tension for $n = 10$, $m = 10$, $\dot{\epsilon}_0 = 10^{-4} s^{-1}$ and strain rates $0.1\dot{\epsilon}_0$, $\dot{\epsilon}_0$ and $10\dot{\epsilon}_0$, together with the flow stress $\sigma_y(\bar{\epsilon}^p)$.

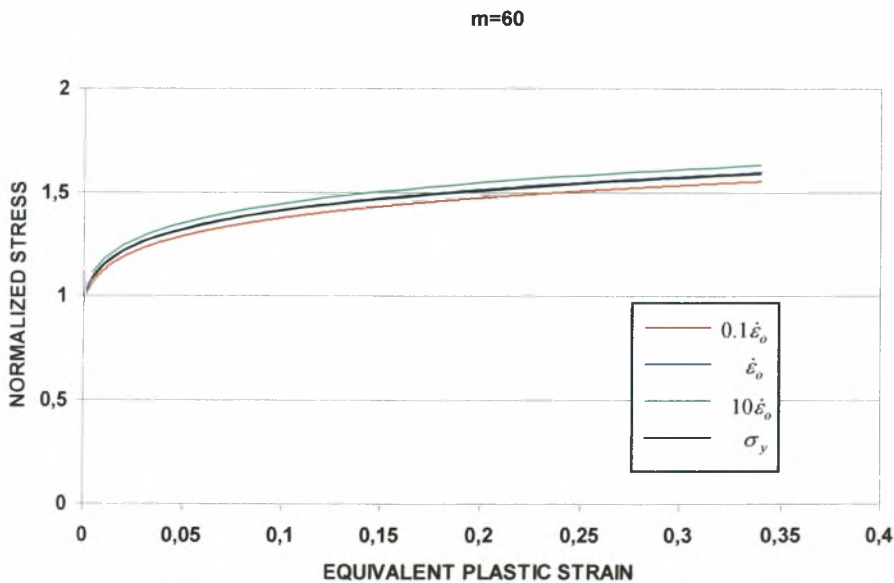


Figure 3.7: Variation of σ_{eq}/σ_0 with $\bar{\epsilon}^p$ in plane strain tension for $n = 10$, $m = 60$, $\dot{\epsilon}_0 = 10^{-4} s^{-1}$ and strain rates $0.1\dot{\epsilon}_0$, $\dot{\epsilon}_0$ and $10\dot{\epsilon}_0$, together with the flow stress $\sigma_y(\bar{\epsilon}^p)$.

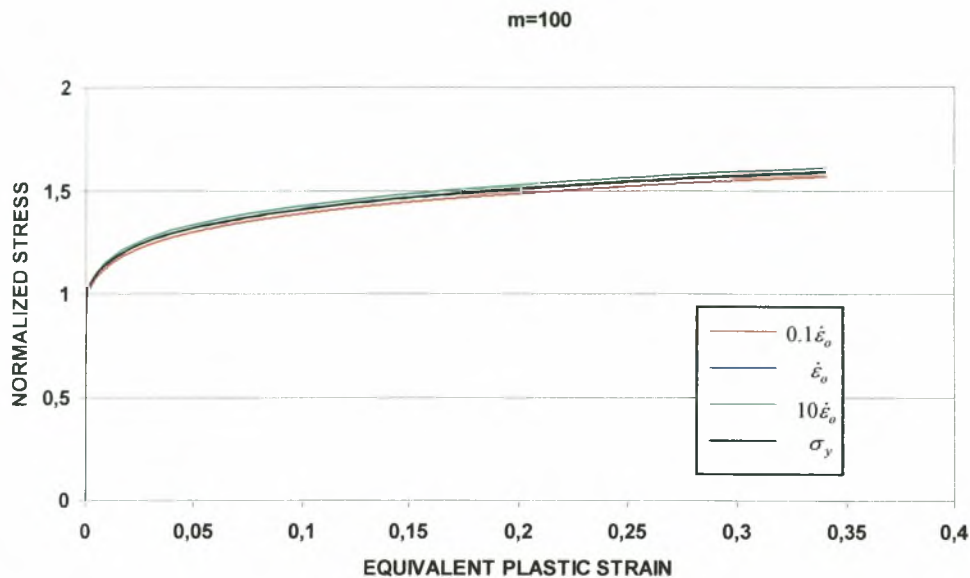


Figure 3.8: Variation of σ_{eq}/σ_0 with $\bar{\epsilon}^P$ in plane strain tension for $n=10$, $m=100$, $\dot{\epsilon}_0 = 10^{-4} s^{-1}$ and strain rates $0.1\dot{\epsilon}_0$, $\dot{\epsilon}_0$ and $10\dot{\epsilon}_0$, together with the flow stress $\sigma_y(\bar{\epsilon}^P)$.

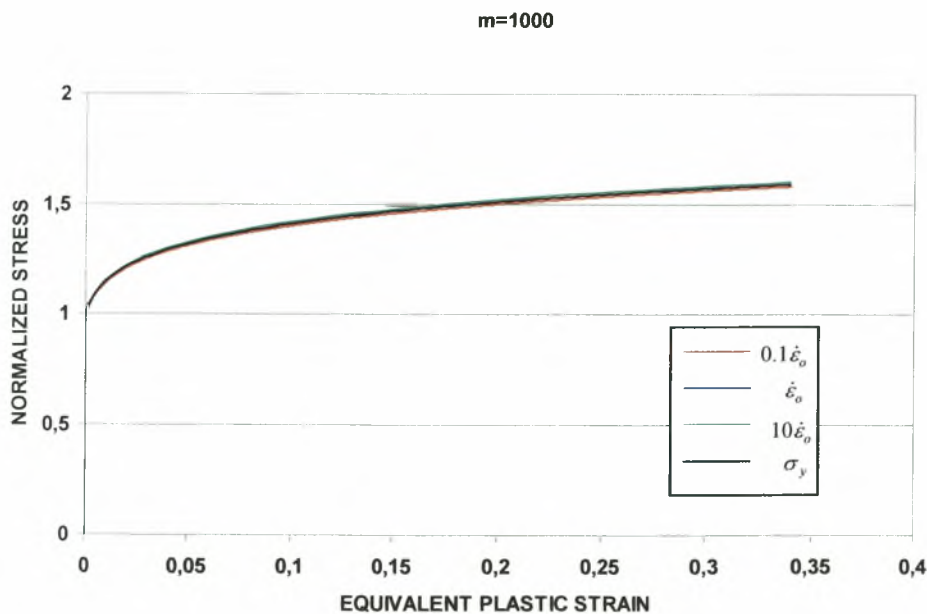


Figure 3.9: Variation of σ_{eq}/σ_0 with $\bar{\epsilon}^P$ in plane strain tension for $n=10$, $m=1000$, $\dot{\epsilon}_0 = 10^{-4} s^{-1}$ and strain rates $0.1\dot{\epsilon}_0$, $\dot{\epsilon}_0$ and $10\dot{\epsilon}_0$, together with the flow stress $\sigma_y(\bar{\epsilon}^P)$.

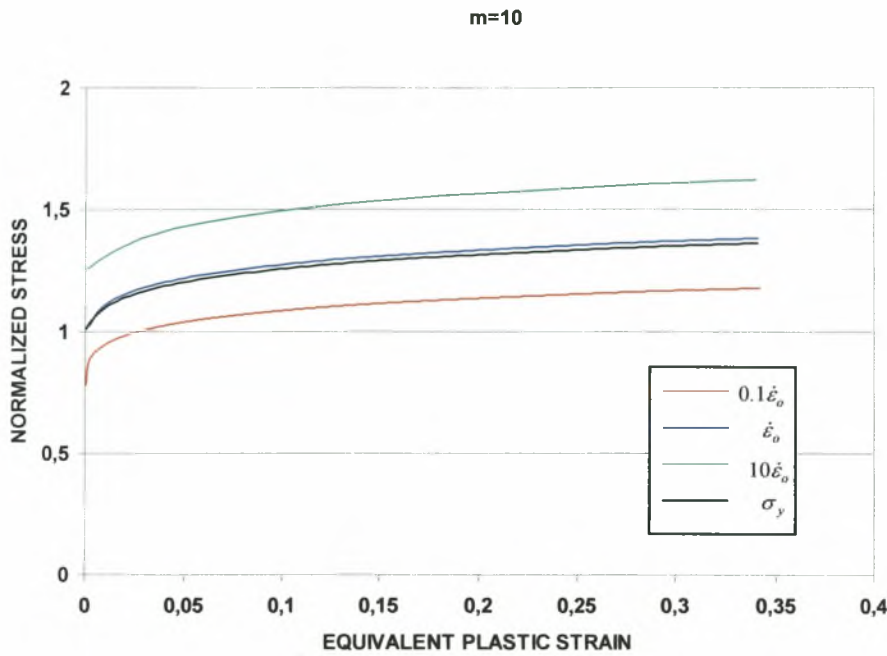
Material with hardening exponent $n = 15$ 

Figure 3.10: Variation of σ_{eq}/σ_0 with $\bar{\epsilon}^P$ in plane strain tension for $n = 15$, $m = 10$, $\dot{\epsilon}_0 = 10^{-4} \text{ s}^{-1}$ and strain rates $0.1\dot{\epsilon}_0$, $\dot{\epsilon}_0$ and $10\dot{\epsilon}_0$, together with the flow stress $\sigma_y(\bar{\epsilon}^P)$.

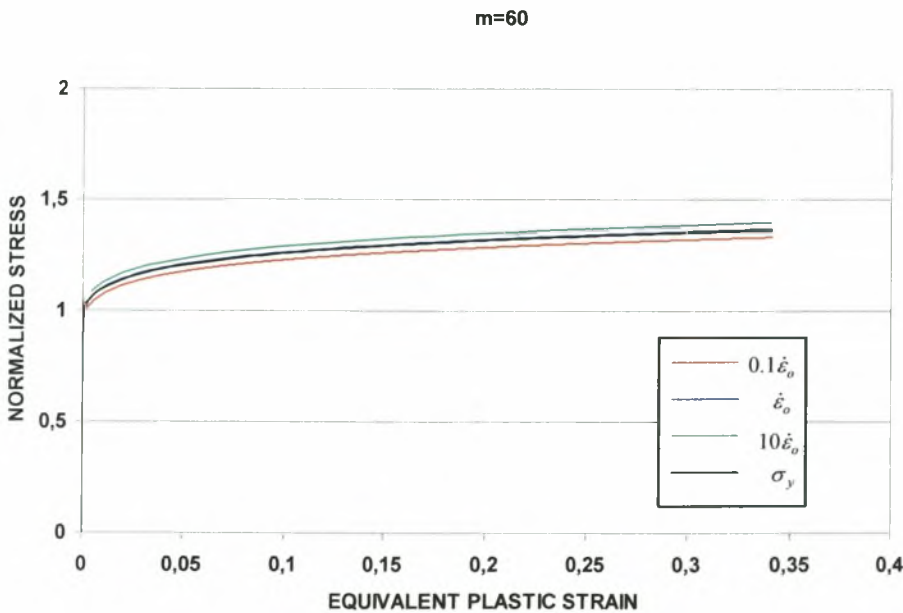


Figure 3.11: Variation of σ_{eq}/σ_0 with $\bar{\epsilon}^P$ in plane strain tension for $n = 15$, $m = 60$, $\dot{\epsilon}_0 = 10^{-4} \text{ s}^{-1}$ and strain rates $0.1\dot{\epsilon}_0$, $\dot{\epsilon}_0$ and $10\dot{\epsilon}_0$, together with the flow stress $\sigma_y(\bar{\epsilon}^P)$.

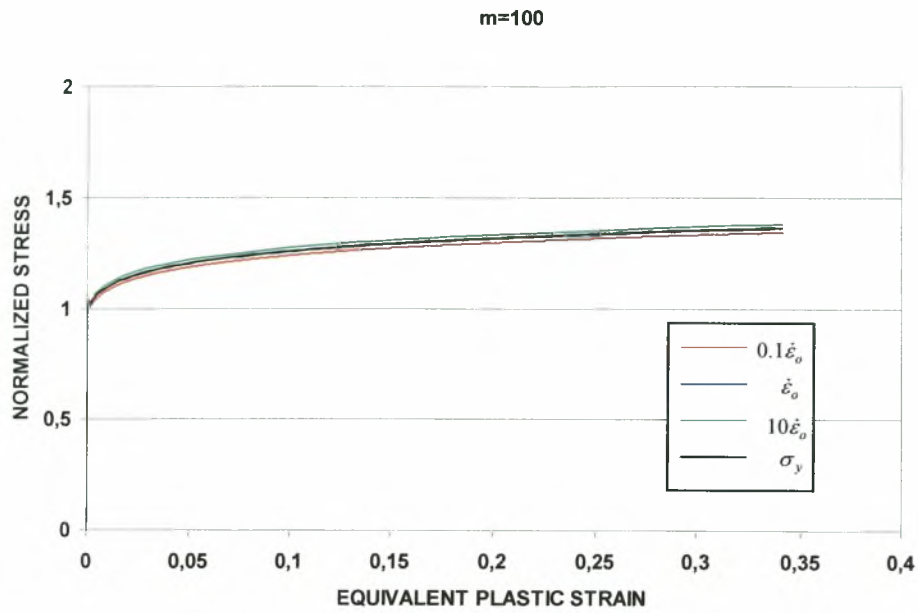


Figure 3.12: Variation of σ_{eq}/σ_0 with $\bar{\epsilon}^p$ in plane strain tension for $n = 15$, $m = 100$, $\dot{\epsilon}_0 = 10^{-4} s^{-1}$ and strain rates $0.1\dot{\epsilon}_0$, $\dot{\epsilon}_0$ and $10\dot{\epsilon}_0$, together with the flow stress $\sigma_y(\bar{\epsilon}^p)$.

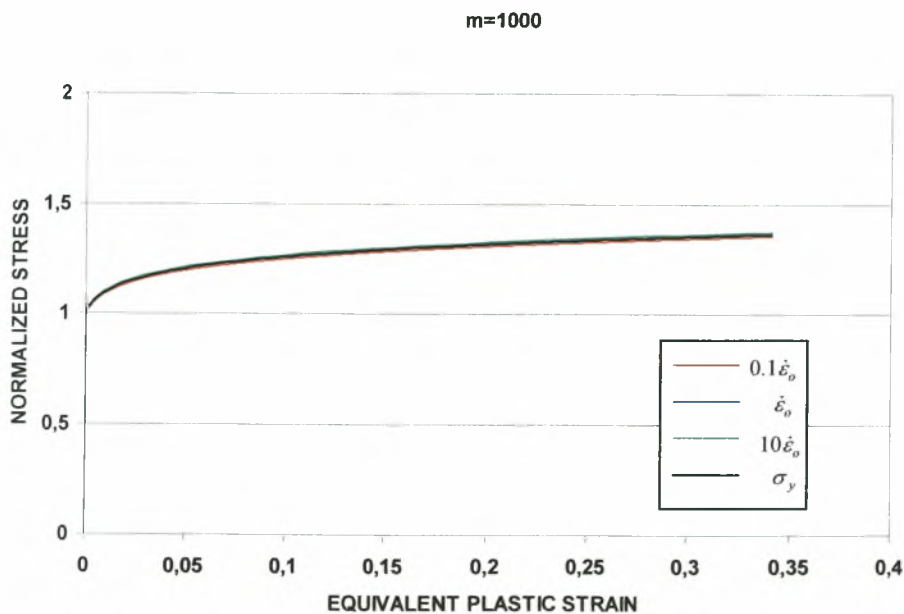


Figure 3.13: Variation of σ_{eq}/σ_0 with $\bar{\epsilon}^p$ in plane strain tension for $n = 15$, $m = 1000$, $\dot{\epsilon}_0 = 10^{-4} s^{-1}$ and strain rates $0.1\dot{\epsilon}_0$, $\dot{\epsilon}_0$ and $10\dot{\epsilon}_0$, together with the flow stress $\sigma_y(\bar{\epsilon}^p)$.

3.8 Conclusions

The results shown in Figures 3.2-3.13 make it clear that, for all values of the hardening exponent considered ($n = 5, 10$ and 15), the response of the viscoplastic model is essentially rate independent for values of the strain rate exponent $m > 60$.

CHAPTER FOUR

HOMOGENIZATION THEORY - DETERMINATION OF PLASTIC STRAIN

4.1 Introduction

As mentioned in the introduction, the total deformation rate \mathbf{D} is written as the sum of an elastic, a plastic and a transformation part. In this chapter, we develop a methodology for the determination of the plastic part of the deformation rate \mathbf{D}^p in TRIP steels.

TRIP steels are essentially composite materials with evolving volume fractions of the individual phases. For the purposes of this chapter, we assume that all phases exhibit purely viscoplastic behavior, i.e., they behave as non-linear viscous solids. The overall viscoplastic behavior of the “composite” (TRIP steel) is then determined by using homogenization techniques for non-linear materials that have been developed recently by Ponte-Castañeda (1996), Suquet (1996a) and Ponte-Castañeda and Suquet (1998).

In this chapter, we present briefly a description of the homogenization technique, which we then apply to a two-phase TRIP steel. The homogenization technique is then used in order to determine the plastic part of the deformation rate \mathbf{D}^p of the actual four-phase TRIP steel. The results of the homogenization for the two-phase composite are compared to those of unit cell calculations in Chapter 5.

4.2 Homogenization method for non-linear viscous solids

We consider a composite material comprised of N isotropic, viscoplastic and incompressible phases distributed statistically uniformly and isotropically. The mechanical behavior of each phase “ r ” is described by a viscoplastic potential of the form $\Psi^{(r)} = \Psi^{(r)}(\sigma_{eq})$:

$$\mathbf{D}^{p(r)} = \frac{\partial \Psi^{(r)}}{\partial \boldsymbol{\sigma}} = \dot{\bar{\epsilon}}^{p(r)} \mathbf{N} = \frac{1}{2} \theta^{(r)} \mathbf{s} \quad (4.1)$$

with

$$\mathbf{N} = \frac{3}{2\sigma_{eq}} \mathbf{s}, \quad \dot{\bar{\epsilon}}^{p(r)} = \frac{\partial \Psi^{(r)}}{\partial \sigma_{eq}} = \sqrt{\frac{2}{3}} \mathbf{D}^p : \mathbf{D}^p, \quad \theta^{(r)} = \frac{3\dot{\bar{\epsilon}}^{p(r)}}{\sigma_{eq}} = \frac{3}{\sigma_{eq}} \frac{\partial \Psi^{(r)}}{\partial \sigma_{eq}} \quad (4.2)$$

where $\mathbf{D}^{p(r)}$ is the plastic part of the deformation rate of phase r , \mathbf{s} the deviatoric part of the stress tensor $\boldsymbol{\sigma}$, $\theta^{(r)} = 1/\mu^{(r)}$ the viscous shear compliance that depends on the von mises equivalent stress $\sigma_{eq} = \sqrt{\frac{3}{2} \mathbf{s} : \mathbf{s}}$, $\mu^{(r)}$ is the viscous shear modulus, and $\bar{\epsilon}^{p(r)}$ is the equivalent plastic strain. We note that

$$\mathbf{N} : \mathbf{N} = \frac{3}{2}. \quad (4.3)$$

Our goal is to determine the corresponding viscoplastic constitutive equation for the “composite” TRIP steel.

A brief description of the homogenization technique used is given in the following. Consider a “representative volume element” (rve) V of the composite material where the size of the inhomogeneities is small compared to that of V . The composite is made up of N homogenous phases $V^{(r)}$, $r = 1, \dots, N$ with volume fraction $c^{(r)}$:

$$\sum_{r=1}^N c^{(r)} = 1. \quad (4.4)$$

The local constitutive behavior of the individual phases derives from a viscous potential $\Psi^{(r)} = \Psi^{(r)}(\sigma_{eq}^{(r)})$:

$$\mathbf{D}^{p(r)} = \frac{\partial \Psi^{(r)}(\sigma_{eq}^{(r)})}{\partial \boldsymbol{\sigma}^{(r)}}, \quad (4.5)$$

where $\boldsymbol{\sigma}^{(r)}$ is the stress tensor in phase r . The local stress and strain fields within the rve solve a boundary value problem consisting of (4.5), compatibility conditions met by \mathbf{D}^p and equilibrium equations satisfied by $\boldsymbol{\sigma}$, i.e.,

$$\mathbf{D}^p = \frac{1}{2}(\nabla \mathbf{v} + \mathbf{v} \nabla) \quad (4.6)$$

$$\text{with } \boldsymbol{\sigma} \in S(\boldsymbol{\Sigma}) = \{\boldsymbol{\tau}, \nabla \cdot \boldsymbol{\tau} = 0, \boldsymbol{\tau} \cdot \mathbf{n} = \boldsymbol{\Sigma} \cdot \mathbf{n} \text{ on } \partial V\}, \quad (4.7)$$

where $\boldsymbol{\Sigma}$ is the macroscopic stress applied on the boundary ∂V of the rve, and \mathbf{n} is the outward unit normal to ∂V .

In general the nonlinear boundary value problem (4.5), (4.6) and (4.7) cannot be solved analytically and approximations have to be introduced. All the approximations known, aim at reducing this nonlinear problem to a sequence of linear ones. Two methods are classically used to predict the overall response of nonlinear composites, the “secant” and “tangent” formulations. Recently a third class of methods based on variational properties of the potential governing the overall behavior of the composite has been proposed by Ponte Castañeda (1992) and Suquet (1993). The various “secant” and “tangent” methods are relatively straightforward but are based on arbitrary approximations, whereas the variational methods appear to be more complicated but provide rigorous bounds to the solution of the problem. Interestingly, Suquet (1995, 1996b) showed that a certain variation of the secant method (the

so called “modified secant method”) is identical to the variational procedure of Ponte Castañeda (1991, 1992). Therefore, we choose to work with the “modified secant method” described below, which gives the same results as the rigorous variational procedure.

In the following we give a brief description of the family of secant methods and emphasize its “modified” variation.

4.2.1 A description of various “secant methods”

In this first class of methods, the constitutive law for each phase (4.5) is written in the form

$$\mathbf{D}^p = \mathbf{M}_s(\boldsymbol{\sigma}) : \boldsymbol{\sigma}, \quad \mathbf{M}_s = \frac{1}{2\mu_s} \mathbf{K}, \quad (4.8)$$

where the local secant moduli μ_s are given by

$$\frac{1}{\mu_s(\mathbf{x})} = \frac{3}{\sigma_{eq}(\mathbf{x})} \frac{\partial \Psi(\mathbf{x}, \sigma_{eq}(\mathbf{x}))}{\partial \sigma_{eq}}, \quad (4.9)$$

and \mathbf{K} is a fourth-order tensor with Cartesian components

$$K_{ijkl} = I_{ijkl} - J_{ijkl}, \quad I_{ijkl} = \frac{1}{2}(\delta_{ik}\delta_{jl} + \delta_{il}\delta_{jk}), \quad J_{ijkl} = \frac{1}{3}\delta_{ij}\delta_{kl}.$$

An approximation is introduced by considering that these secant moduli are constant within each phase

$$\mu_s(\mathbf{x}) = \mu_s^{(r)} \quad \text{in phase } r \quad \text{with} \quad \frac{1}{\mu_s^{(r)}} = \frac{3}{\sigma_{eq}^{(r)}} \frac{\partial \Psi^{(r)}(\sigma_{eq}^{(r)})}{\partial \sigma_{eq}^{(r)}}, \quad (4.10)$$

where the “effective stress” of phase r , $\sigma_{eq}^{(r)}$, is constant on phase r and has to be specified.

Equations (4.8)-(4.10) replace now (4.5) in the original problem, i.e., the (approximate) secant problem consists now of (4.8)-(4.10), (4.6) and (4.7), where now the secant tensors $\mathbf{M}_s^{(r)}$ are

constant within each phase. The specification of $\sigma_{eq}^{(r)}$ is now the “heart” of the problem; different choices for the definition of $\sigma_{eq}^{(r)}$ lead to several variations of the secant method.

The *classical secant method* is based on the assumption that the effective stress $\sigma_{eq}^{(r)}$ in each phase is equal to the von Mises equivalent stress $\Sigma_{eq}^{(r)}$ associated with the average stress $\boldsymbol{\Sigma}^{(r)}$ over that phase, i.e.,

$$\sigma_{eq}^{(r)} = \Sigma_{eq}^{(r)} = \sqrt{\frac{3}{2} \mathbf{S}^{(r)} : \mathbf{S}^{(r)}} \quad \text{with} \quad \boldsymbol{\Sigma}^{(r)} = \langle \boldsymbol{\sigma} \rangle_{(r)}, \quad (4.11)$$

where the symbol $\langle \cdot \rangle_{(r)}$ denotes spatial averaging over $V^{(r)}$, and $\mathbf{S}^{(r)}$ is the deviatoric part of $\boldsymbol{\Sigma}^{(r)}$. This choice has serious limitations as pointed out by Qiu and Weng (1992).

The *modified secant method* proposed by Suquet (1996a) is motivated by the observation that the field $\boldsymbol{\sigma}$ in phase r oscillates in each individual phase about its average $\boldsymbol{\Sigma}^{(r)}$ but that nonlinear functions of this field (e.g. σ_{eq} or $\mu(\sigma_{eq})$) do not oscillate about the same nonlinear function applied to $\mathbf{S}^{(r)}$. It is therefore proposed to evaluate nonlinear functions of the stress field by means of the second moment of the stress field:

$$\sigma_{eq}^{(r)} = \sqrt{\langle \sigma_{eq}^2 \rangle_{(r)}}. \quad (4.12)$$

We consider now the special case in which all phases are incompressible. Then, consider a linear composite comprised of N incompressible phases with viscous shear moduli $\mu^{(r)}$ occupying the subdomains $V^{(r)}$. Set $\theta^{(r)} = \frac{1}{\mu^{(r)}}$, $\theta = (\theta^{(1)}, \dots, \theta^{(N)})$ and let

$$\mathbf{M}^{\text{hom}}(\theta) = \frac{1}{2\mu^{\text{hom}}(\theta)} \mathbf{K} = \frac{\theta^{\text{hom}}(\theta)}{2} \mathbf{K} \quad (4.13)$$

be the overall viscous compliance tensor of this linear composite¹. Then denoting by $\boldsymbol{\sigma}$ the stress field in this linear composite, one has:

$$\sigma_{eq}^{(r)} = \sqrt{\langle \sigma_{eq}^2 \rangle_{(r)}} = \sqrt{\frac{3}{c^{(r)}} \boldsymbol{\sigma} : \frac{\partial \mathbf{M}^{\text{hom}}(\theta)}{\partial \theta^{(r)}} : \boldsymbol{\sigma}} \quad (4.14)$$

$$\text{with } \boldsymbol{\sigma} \in S(\boldsymbol{\Sigma}) = \{ \boldsymbol{\tau}, \nabla \cdot \boldsymbol{\tau} = 0, \boldsymbol{\tau} \cdot \mathbf{n} = \boldsymbol{\Sigma} \cdot \mathbf{n} \text{ on } \partial V \}. \quad (4.15)$$

A detailed proof of this result can be found in Kreher (1990) or Suquet (1995). This result applies to the solution of the secant problem as well, although it is not a linear problem. Indeed, once the solution of the secant problem is known, the secant moduli $\mu_s^{(r)}$ are known. Then a linear problem with these specific viscous moduli can be posed and its solution is precisely the solution of the secant nonlinear problem. Therefore the “effective stress” of each individual nonlinear phase can be computed from a linear theory.

Substituting (4.13) into (4.14) we find

$$\sigma_{eq}^{(r)} = \sqrt{\frac{3}{c^{(r)}} \boldsymbol{\sigma} : \left(\frac{1}{2} \frac{\partial \theta^{\text{hom}}}{\partial \theta^{(r)}} \mathbf{K} \right) : \boldsymbol{\sigma}} = \sigma_{eq} \sqrt{\frac{1}{c^{(r)}} \frac{\partial \theta^{\text{hom}}}{\partial \theta^{(r)}}}. \quad (4.16)$$

¹ At this point it is assumed that a method for the determination of $\mathbf{M}^{\text{hom}}(\theta)$ is available for the linear composite.

In conclusion, for a given stress state $\boldsymbol{\sigma}$, the proposed modified secant moduli approach involves three steps:

1. A linear theory providing an expression for $\mathbf{M}^{\text{hom}}(\theta) = \frac{\theta^{\text{hom}}(\theta)}{2} \mathbf{K}$ and its partial derivatives with respect to $\theta^{(r)}$.
2. The resolution of $2N$ nonlinear problems for the $2N$ unknowns $(\theta^{(r)}, \sigma_{eq}^{(r)})$:

$$\theta^{(r)} = \frac{3}{\sigma_{eq}^{(r)}} \frac{\partial \Psi^{(r)}(\sigma_{eq}^{(r)})}{\partial \sigma_{eq}^{(r)}}, \quad \sigma_{eq}^{(r)} = \sigma_{eq} \sqrt{\frac{1}{c^{(r)}} \frac{\partial \theta^{\text{hom}}}{\partial \theta^{(r)}}} \equiv \bar{b}^{(r)}(\theta) \sigma_{eq}. \quad (4.17)$$

3. Once the $2N$ nonlinear problems (4.17) are solved and $(\theta^{(r)}, \sigma_{eq}^{(r)})$ are found, $\mathbf{M}^{\text{hom}}(\theta)$ is evaluated and the overall deformation rate is finally given by:

$$\mathbf{D}^p = \mathbf{M}^{\text{hom}}(\theta) : \boldsymbol{\sigma} = \frac{\theta^{\text{hom}}(\theta)}{2} \mathbf{s}. \quad (4.18)$$

As mentioned earlier, we choose to work with the modified secant method proposed by Suquet (1996a), the results of which coincide with those of the rigorous variational procedure of Ponte Castañeda (1991, 1992).

We conclude this section with a brief description of the Hashin-Strickman estimates, found in Willis (1980), that are used for the determination of $\mathbf{M}^{\text{hom}}(\theta) = \frac{\theta^{\text{hom}}(\theta)}{2} \mathbf{K}$ in the linear composite.

4.2.2 The Hashin Shtrikman bounds

Consider a composite material comprised of N isotropic phases distributed statistically uniformly and isotropically with volume fractions $c^{(r)}$ ($r = 1, \dots, N$), shear modulus (viscosity) $\mu^{(r)}$, and bulk modulus $\kappa^{(r)}$. The viscous stiffness and compliance tensors $\mathbf{L}^{(r)}$ and $\mathbf{M}^{(r)}$ of every phase r have the form

$$\mathbf{L}^{(r)} = 2\mu^{(r)} \mathbf{K} + 3\kappa^{(r)} \mathbf{J} \quad \text{and} \quad \mathbf{M}^{(r)} = (\mathbf{L}^{(r)})^{-1} = \frac{1}{2\mu^{(r)}} \mathbf{K} + \frac{1}{3\kappa^{(r)}} \mathbf{J}. \quad (4.19)$$

We choose one of the N phases as the “comparison material”, denoted by

$$\hat{\mathbf{L}}_o = 2\hat{\mu}_o \mathbf{K} + 3\hat{\kappa}_o \mathbf{J}. \quad (4.20)$$

According to the Hashin-Shtrikman theory, the overall viscous stiffness tensor of the composite \mathbf{L}^{hom} is given by the form:

$$\mathbf{L}^{\text{hom}} = \left\{ \sum_{r=1}^N c^{(r)} \left[\mathbf{I} + (\mathbf{L}^{(r)} - \hat{\mathbf{L}}_o) : \mathbf{P} \right]^{-1} \right\}^{-1} : \left\{ \sum_{r=1}^N c^{(r)} \mathbf{L}^{(r)} : \left[\mathbf{I} + (\mathbf{L}^{(r)} - \hat{\mathbf{L}}_o) : \mathbf{P} \right]^{-1} \right\}, \quad (4.21)$$

where \mathbf{I} the the fourth-order identity tensor, and

$$\mathbf{P} = 2\mu_p \mathbf{K} + 3\kappa_p \mathbf{J}, \quad 2\mu_p = \frac{3(\hat{\kappa}_o + 2\hat{\mu}_o)}{5\hat{\mu}_o(3\hat{\kappa}_o + 4\hat{\mu}_o)}, \quad 3\kappa_p = \frac{1}{3\hat{\kappa}_o + 4\hat{\mu}_o}. \quad (4.22)$$

Carrying out the algebra in (4.21) we conclude that the overall viscous stiffness tensor \mathbf{L}^{hom} can be written as

$$\mathbf{L}^{\text{hom}} = 2\mu^{\text{hom}} \mathbf{K} + 3\kappa^{\text{hom}} \mathbf{J}, \quad (4.23)$$

where

$$\mu^{\text{hom}} = \left\{ \sum_{r=1}^N c^{(r)} \frac{5\hat{\mu}_o(3\hat{\kappa}_o + 4\hat{\mu}_o)}{6\mu^{(r)}(\hat{\kappa}_o + 2\hat{\mu}_o) + \hat{\mu}_o(9\hat{\kappa}_o + 8\hat{\mu}_o)} \right\}^{-1} \sum_{r=1}^N c^{(r)} \frac{5\hat{\mu}_o(3\hat{\kappa}_o + 4\hat{\mu}_o)\mu^{(r)}}{6\mu^{(r)}(\hat{\kappa}_o + 2\hat{\mu}_o) + \hat{\mu}_o(9\hat{\kappa}_o + 8\hat{\mu}_o)} \quad (4.24)$$

and

$$\kappa^{\text{hom}} = \left\{ \sum_{r=1}^N c^{(r)} \frac{(3\hat{\kappa}_o + 4\hat{\mu}_o)}{(3\kappa^{(r)} + 4\hat{\mu}_o)} \right\}^{-1} \sum_{r=1}^N c^{(r)} \frac{(3\hat{\kappa}_o + 4\hat{\mu}_o)\kappa^{(r)}}{(3\kappa^{(r)} + 4\hat{\mu}_o)}. \quad (4.25)$$

The corresponding compliance tensor is

$$\mathbf{M}^{\text{hom}} = (\mathbf{L}^{\text{hom}})^{-1} = \frac{1}{2\mu^{\text{hom}}} \mathbf{K} + \frac{1}{3\kappa^{\text{hom}}} \mathbf{J}. \quad (4.26)$$

Equations (4.24) and (4.25) yield upper bounds for μ^{hom} , κ^{hom} whenever $\hat{\mu}_o$, $\hat{\kappa}_o$ are chosen larger than $\mu^{(r)}$, $\kappa^{(r)}$ for each r and the smallest upper bounds are obtained by setting $\hat{\mu}_o = \hat{\mu}_{o/g} = \max(\mu^{(r)})$ and $\hat{\kappa}_o = \hat{\kappa}_{o/g} = \max(\kappa^{(r)})$. Similarly, the greatest lower bounds are found by setting $\hat{\mu}_o = \hat{\mu}_{o/l} = \min(\mu^{(r)})$ and $\hat{\kappa}_o = \hat{\kappa}_{o/l} = \min(\kappa^{(r)})$. These bounds were given by Hashin and Shtrikman (Willis (1980)), with the implicit restriction that $\hat{\mu}_{o/g}$, $\hat{\kappa}_{o/g}$ has both to be obtained from the same phase, and $\hat{\mu}_{o/l}$, $\hat{\kappa}_{o/l}$ similarly. This restriction was removed by Walpole (1996).

For the case that the N isotropic phases are incompressible ($\kappa^{(r)} \rightarrow \infty$) the composite will also be incompressible ($\kappa^{\text{hom}} \rightarrow \infty$) and the expression for μ^{hom} is simplified to

$$\mu^{\text{hom}} = \left(\sum_{r=1}^N \frac{c^{(r)} \mu^{(r)}}{\mu^{(r)} + \frac{3}{2} \hat{\mu}_o} \right) \bigg/ \left(\sum_{r=1}^N \frac{c^{(r)}}{\mu^{(r)} + \frac{3}{2} \hat{\mu}_o} \right). \quad (4.27)$$

Setting $\theta^{\text{hom}} = 1/\mu^{\text{hom}}$, $\theta^{(r)} = 1/\mu^{(r)}$ and $\hat{\theta}_o = 1/\hat{\mu}_o$ we obtain the following expression for θ^{hom}

$$\frac{1}{\theta^{\text{hom}}} = \left(\sum_{r=1}^N \frac{\frac{c^{(r)}}{\theta^{(r)}}}{\frac{1}{\theta^{(r)}} + \frac{3}{2\hat{\theta}_o}} \right) \bigg/ \left(\sum_{r=1}^N \frac{c^{(r)}}{\frac{1}{\theta^{(r)}} + \frac{3}{2\hat{\theta}_o}} \right). \quad (4.28)$$

4.3 Application to non-linear composites

In this section we apply the “modified secant method” to a multi-phase (two- or four-phase) composite. The viscous potential of each phase is of the form

$$\Psi^{(r)}(\sigma_{eq}) = \frac{\sigma_y^{(r)} \dot{\varepsilon}_o^{(r)}}{m+1} \left(\frac{\sigma_{eq}}{\sigma_y^{(r)}} \right)^{m+1}, \quad (4.29)$$

where $\sigma_y^{(r)}$ is a reference stress, $\dot{\varepsilon}_o^{(r)}$ is a reference strain rate, and m is the common for all phases strain rate sensitivity exponent. Equation (4.1) takes now the form

$$\mathbf{D}^{p(r)} = \dot{\varepsilon}^{p(r)} \mathbf{N} = \frac{1}{2} \theta^{(r)} \mathbf{s}, \quad (4.30)$$

where now the equivalent plastic strain rate $\dot{\varepsilon}^{p(r)}$ depends on the von Mises equivalent stress σ_{eq} though the well known “power law creep” relationship

$$\dot{\varepsilon}^{p(r)} = \dot{\varepsilon}_o^{(r)} \left(\frac{\sigma_{eq}}{\sigma_y^{(r)}} \right)^m. \quad (4.31)$$

Also

$$\theta^{(r)} = \frac{3 \dot{\varepsilon}_o^{(r)}}{\sigma_{eq}} \left(\frac{\sigma_{eq}}{\sigma_y^{(r)}} \right)^m \quad (4.32)$$

in this case.

4.3.1 Homogenization method for a two-phase non-linear composite

The two-phase TRIP steel we examine consists of particles of martensite isotropically dispersed in austenitic matrix. The behavior of each phase is described in terms of viscous potentials of the form of equation (4.29). We denote the martensitic and austenitic phases with

the numbers 1,2 respectively and we choose the austenitic matrix as the comparison material ($\hat{\mu}_o = \mu_o^{(2)} = 1/\theta^{(2)}$). The use of the austenitic phase, which is the “softer” of the two phases, as the comparison material (4.27) provides the corresponding Hashin-Shtrikman lower bound.

The volume fractions of the individual phases $c^{(r)}$ together with the parameters $\dot{\varepsilon}_o^{(r)}$, $\sigma_y^{(r)}$ and the macroscopic σ_{eq} are assumed to be known. In the following, we discuss the determination of θ^{hom} .

Equations (4.17) are written as

$$\sigma_{eq}^{(r)} = \sigma_{eq} \sqrt{\frac{1}{c^{(r)}} \frac{\partial \theta^{\text{hom}}}{\partial \theta^{(r)}}} \equiv \bar{b}^{(r)}(\theta) \sigma_{eq}, \quad \theta^{(r)} = \frac{3 \dot{\varepsilon}_o^{(r)} \left(\frac{\sigma_{eq}^{(r)}}{\sigma_y^{(r)}} \right)^{m-1}}{\sigma_y^{(r)}}, \quad (4.33)$$

where

$$\frac{1}{\theta^{\text{hom}}} = \left(\sum_{r=1}^2 \frac{\frac{c^{(r)}}{\theta^{(r)}}}{\frac{1}{\theta^{(r)}} + \frac{3}{2\theta^{(2)}}} \right) \bigg/ \left(\sum_{r=1}^2 \frac{c^{(r)}}{\frac{1}{\theta^{(r)}} + \frac{3}{2\theta^{(2)}}} \right). \quad (4.34)$$

Equations (4.33) for $r=1,2$ provide four non-linear equations for the determination of $(\theta^{(1)}, \theta^{(2)}, \sigma_{eq}^{(1)}, \sigma_{eq}^{(2)})$.

Next, we discuss the solution of this system and reduce the problem to the solution of a single non-linear equation. We define the ratio $x \equiv \frac{\theta^{(1)}}{\theta^{(2)}}$ and use equation (4.33) to find

$$x = \frac{\theta^{(1)}}{\theta^{(2)}} = D \left(\frac{\bar{b}^{(1)}}{\bar{b}^{(2)}} \right)^{m-1} \quad \text{where} \quad D = \frac{\dot{\varepsilon}_o^{(1)} \left(\frac{\sigma_y^{(2)}}{\sigma_y^{(1)}} \right)^m}{\dot{\varepsilon}_o^{(2)} \left(\frac{\sigma_y^{(1)}}{\sigma_y^{(2)}} \right)^m}. \quad (4.35)$$

Using the definitions of $\bar{b}^{(r)}$, namely $\bar{b}^{(r)} = \sqrt{\frac{1}{c^{(r)}} \frac{\partial \theta^{\text{hom}}}{\partial \theta^{(r)}}}$, we can express the factors $\bar{b}^{(1)}$ and $\bar{b}^{(2)}$ in terms of x as follows

$$\bar{b}^{(1)}(x) = \frac{5}{5 + 3c^{(2)}(x-1)}, \quad \bar{b}^{(2)}(x) = \frac{\sqrt{10 + 15x^2 - 6c^{(2)}(x-1)^2}}{5 + 3c^{(2)}(x-1)}. \quad (4.36)$$

Now, we consider x as the basic unknown, and note that (4.36) defines $\bar{b}^{(1)}$ and $\bar{b}^{(2)}$ in terms of x . The basic equation that defines x is (4.35), which is written as

$$H(x) \equiv x - D \left[\frac{\bar{b}^{(1)}(x)}{\bar{b}^{(2)}(x)} \right]^{m-1} = 0. \quad (4.37)$$

The above equation is solved numerically for x by using a Newton-Raphson scheme. Once x is found, $\bar{b}^{(1)}$ and $\bar{b}^{(2)}$ are determined from (4.36), $(\theta^{(1)}, \theta^{(2)}, \sigma_{eq}^{(1)}, \sigma_{eq}^{(2)})$ from (4.33), and θ^{hom} from (4.34).

The corresponding macroscopic equation for the homogenized two-phase composite is

$$\mathbf{D}^p = \mathbf{M}^{\text{hom}} : \boldsymbol{\sigma} = \frac{\theta^{\text{hom}}}{2} \mathbf{s} = \dot{\boldsymbol{\varepsilon}}^p \mathbf{N}, \quad \mathbf{N} = \frac{3}{2\sigma_{eq}} \mathbf{s}, \quad (4.38)$$

where

$$\dot{\boldsymbol{\varepsilon}}^p = \sqrt{\frac{2}{3} \mathbf{D}^p : \mathbf{D}^p} = \frac{1}{3} \sigma_{eq} \theta^{\text{hom}}. \quad (4.39)$$

We conclude this section with a discussion of the consequences of the fact that the strain rate exponents are the same for both phases, i.e., $m^{(1)} = m^{(2)} \equiv m$. Because of that, the value of x in (4.35) or, equivalently, the solution of (4.37) is independent of the applied stress $\boldsymbol{\sigma}$; this is not the case if $m^{(1)} \neq m^{(2)}$, because then

$$x = \frac{\theta^{(1)}}{\theta^{(2)}} = \frac{\dot{\varepsilon}_o^{(1)} (\sigma_y^{(2)})^{m^{(2)}} (\bar{b}^{(1)})^{m^{(1)}-1}}{\dot{\varepsilon}_o^{(2)} (\sigma_y^{(1)})^{m^{(1)}} (\bar{b}^{(2)})^{m^{(2)}-1}} (\sigma_{eq})^{m^{(1)}-m^{(2)}} = \text{function of } \sigma_{eq}. \quad (4.40)$$

Therefore, when $m^{(1)} = m^{(2)} \equiv m$, the quantities $(x, \bar{b}^{(1)}, \bar{b}^{(2)})$ are independent of $\boldsymbol{\sigma}$, $(\sigma_{eq}^{(1)}, \sigma_{eq}^{(2)})$ are proportional to σ_{eq} , and $(\theta^{(1)}, \theta^{(2)}, \theta^{\text{hom}})$ are proportional to σ_{eq}^{m-1} , i.e.,

$$\theta^{\text{hom}} = C \sigma_{eq}^{m-1}, \quad (4.41)$$

where C is a function of the parameters $(c^{(1)}, c^{(2)}, \dot{\varepsilon}_o^{(1)}, \dot{\varepsilon}_o^{(2)}, \sigma_y^{(1)}, \sigma_y^{(2)})$. Then

$$\dot{\boldsymbol{\varepsilon}}^p = \sqrt{\frac{2}{3} \mathbf{D}^p : \mathbf{D}^p} = \frac{1}{3} \sigma_{eq} \theta^{\text{hom}} \Rightarrow \dot{\boldsymbol{\varepsilon}}^p = B \sigma_{eq}^m \quad \text{where} \quad B = \frac{1}{3} C, \quad (4.42)$$

i.e., according to the modified secant method, the constitutive equation of the homogenized two-phase composite maintains the ‘‘power law creep’’ form with the same strain rate exponent m . Practically speaking, when $m^{(1)} = m^{(2)} \equiv m$, a single application of the modified secant method is sufficient for the complete characterization of the composite, i.e., the calculation of the C constant.

4.3.2 Homogenization method for a four-phase non-linear composite (four-phase TRIP steel)

The multiphase TRIP steel is considered as a composite material with a ferritic matrix containing bainite and retained austenite, which gradually transforms into martensite. We denote the martensitic, austenitic, bainitic and ferritic phases with the numbers 1, 2, 3 and 4 respectively and choose the ferritic matrix as the comparison material ($\hat{\mu}_o = \mu^{(4)} = 1/\theta^{(4)}$).

The constitutive behavior of all four phases is described by the power law type of constitutive equations given by (4.30)-(4.32).

In the following, we discuss the determination of θ^{hom} for the four-phase composite for a given composition $c^{(r)}$ and macroscopic stress σ .

Equations (4.17) are written as

$$\sigma_{eq}^{(r)} = \sigma_{eq} \sqrt{\frac{1}{c^{(r)}} \frac{\partial \theta^{\text{hom}}}{\partial \theta^{(r)}}} \equiv \bar{b}^{(r)}(\theta) \sigma_{eq}, \quad \theta^{(r)} = \frac{3 \dot{\epsilon}_o^{(r)}}{\sigma_y^{(r)}} \left(\frac{\sigma_{eq}^{(r)}}{\sigma_y^{(r)}} \right)^{m-1}, \quad (4.43)$$

where

$$\frac{1}{\theta^{\text{hom}}} = \left(\sum_{r=1}^4 \frac{\frac{c^{(r)}}{\theta^{(r)}}}{\frac{1}{\theta^{(r)}} + \frac{3}{2\theta^{(4)}}} \right) / \left(\sum_{r=1}^4 \frac{c^{(r)}}{\frac{1}{\theta^{(r)}} + \frac{3}{2\theta^{(4)}}} \right). \quad (4.44)$$

Equations (4.43) for $r=1,2,3,4$ provide eight non-linear equations for the determination of $(\theta^{(r)}, \sigma_{eq}^{(r)})$.

Next, we discuss the solution of this system and reduce the problem to the solution of a system of three non-linear equations. We define the ratios $x^{(r)} \equiv \frac{\theta^{(r)}}{\theta^{(4)}}$ for $r=1,2,3$ and use

equation (4.33) to find

$$x^{(r)} = \frac{\theta^{(r)}}{\theta^{(4)}} = D^{(r)} \left(\frac{\bar{b}^{(r)}}{\bar{b}^{(4)}} \right)^{m-1} \quad \text{where} \quad D^{(r)} = \frac{\dot{\epsilon}_o^{(r)}}{\dot{\epsilon}_o^{(4)}} \left(\frac{\sigma_y^{(4)}}{\sigma_y^{(r)}} \right)^m, \quad r=1,2,3. \quad (4.45)$$

Using the definitions of $\bar{b}^{(r)}$, namely $\bar{b}^{(r)} = \sqrt{\frac{1}{c^{(r)}} \frac{\partial \theta^{\text{hom}}}{\partial \theta^{(r)}}}$, we can express the factors $\bar{b}^{(r)}$ in terms of \mathbf{x} as follows

$$\bar{b}^{(r)}(\mathbf{x}) = \left[\frac{1}{(2+3x^{(r)})^2} \frac{4\Pi(\mathbf{x})+6A(\mathbf{x})}{[\Pi(\mathbf{x})]^2} \right]^{1/2} \quad \text{for} \quad r=1,2,3, \quad (4.46)$$

$$\text{and } \bar{b}^{(4)}(\mathbf{x}) = \left[\frac{1}{c^{(4)}} \frac{B(\mathbf{x})\Pi(\mathbf{x}) - A(\mathbf{x})C(\mathbf{x})}{[\Pi(\mathbf{x})]^2} \right]^{1/2}, \quad (4.47)$$

where \mathbf{x} is the collection $\mathbf{x} = (x^{(1)}, x^{(2)}, x^{(3)})$, $x^{(4)} = 1$, and

$$A(\mathbf{x}) = \sum_{r=1}^4 \frac{2c^{(r)} x^{(r)}}{2 + 3x^{(r)}}, \quad \Pi(\mathbf{x}) = \sum_{r=1}^4 \frac{2c^{(r)}}{2 + 3x^{(r)}}, \quad (4.48)$$

$$B(\mathbf{x}) = -\sum_{r=1}^3 \frac{4c^{(r)} x^{(r)}}{(2 + 3x^{(r)})^2}, \quad C(\mathbf{x}) = -\frac{2c^{(4)}}{5} - \sum_{r=1}^3 \frac{4c^{(r)}}{(2 + 3x^{(r)})^2}. \quad (4.49)$$

Now, we consider $\mathbf{x} = (x^{(1)}, x^{(2)}, x^{(3)})$ as the basic unknowns, and note that (4.46) and (4.47)

define the $\bar{b}^{(r)}$'s in terms of \mathbf{x} . The basic equations that define \mathbf{x} are (4.45), which can be written as

$$H^{(r)}(\mathbf{x}) \equiv x^{(r)} - D^{(r)} \left[\frac{\bar{b}^{(r)}(\mathbf{x})}{\bar{b}^{(4)}(\mathbf{x})} \right]^{m-1} = 0, \quad r = 1, 2, 3. \quad (4.50)$$

The above system is solved numerically for $\mathbf{x} = (x^{(1)}, x^{(2)}, x^{(3)})$ by using a Newton-Raphson scheme. Details of the solution procedure are presented in Appendix A. Once \mathbf{x} is found, the $\bar{b}^{(r)}$'s are determined from (4.46) and (4.47), $(\theta^{(r)}, \sigma_{eq}^{(r)})$ from (4.43), and θ^{hom} from (4.44).

The corresponding macroscopic equation for the homogenized four-phase composite is

$$\mathbf{D}^p = \mathbf{M}^{\text{hom}} : \boldsymbol{\sigma} = \frac{\theta^{\text{hom}}}{2} \mathbf{s} = \dot{\boldsymbol{\varepsilon}}^p \mathbf{N}, \quad \mathbf{N} = \frac{3}{2\sigma_{eq}} \mathbf{s}, \quad (4.51)$$

where

$$\dot{\boldsymbol{\varepsilon}}^p = \sqrt{\frac{2}{3}} \mathbf{D}^p : \mathbf{D}^p = \frac{1}{3} \sigma_{eq} \theta^{\text{hom}}. \quad (4.52)$$

In way similar to that of the two-phase composite, we can show that, since the strain rate exponents are the same for all phases, i.e., $m^{(1)} = m^{(2)} = m^{(3)} = m^{(4)} \equiv m$, \mathbf{x} and $\bar{b}^{(r)}$ are independent of $\boldsymbol{\sigma}$, the $\sigma_{eq}^{(r)}$ are proportional to σ_{eq} , and the $\theta^{(r)}$ and θ^{hom} are proportional to σ_{eq}^{m-1} . Therefore, according to the modified secant method, the constitutive equation of the homogenized four-phase composite maintains the ‘‘power law creep’’ form with the same strain rate exponent m .

It should be noted also that the sequence of steps used above for the four-phase composite can be used easily for an N -phase composite in order to reduce the homogenization problem to

the solution of a system of $N-1$ non-linear equations with unknowns the quantities

$$\left(\frac{\theta^{(1)}}{\theta^{(N)}}, \frac{\theta^{(2)}}{\theta^{(N)}}, \dots, \frac{\theta^{(N-1)}}{\theta^{(N)}} \right).$$

4.4 A summary of the constitutive equation used for \mathbf{D}^p in TRIP steels

The results of the previous section are used for the description of the plastic deformation rate \mathbf{D}^p of four-phase TRIP steels as follows.

Each of the four phases is viscoplastic and obeys a constitutive equation of the form

$$\mathbf{D}^{p(r)} = \dot{\bar{\varepsilon}}^{p(r)} \mathbf{N} = \frac{1}{2} \theta^{(r)} \mathbf{s}, \quad \mathbf{N} = \frac{3}{2 \sigma_{eq}} \mathbf{s} \quad r = 1, 2, 3, 4, \quad (4.53)$$

where

$$\dot{\bar{\varepsilon}}^{p(r)} = \dot{\varepsilon}_o^{(r)} \left[\frac{\sigma_{eq}}{\sigma_y^{(r)}(\bar{\varepsilon}^{p(r)})} \right]^m, \quad \theta^{(r)} = \frac{3 \dot{\varepsilon}_o^{(r)}}{\sigma_{eq}} \left[\frac{\sigma_{eq}}{\sigma_y^{(r)}(\bar{\varepsilon}^{p(r)})} \right]^m, \quad (4.54)$$

and $\sigma_y^{(r)}(\bar{\varepsilon}^{p(r)})$ are known functions describing the hardening behavior of the phases.

The behavior of the homogenized four-phase TRIP steel is written as

$$\mathbf{D}^p = \mathbf{M}^{\text{hom}} : \boldsymbol{\sigma} = \frac{\theta^{\text{hom}}}{2} \mathbf{s} = \dot{\bar{\varepsilon}}^p \mathbf{N}, \quad (4.55)$$

where

$$\dot{\bar{\varepsilon}}^p = \sqrt{\frac{2}{3} \mathbf{D}^p : \mathbf{D}^p} = \frac{1}{3} \sigma_{eq} \theta^{\text{hom}}. \quad (4.56)$$

The effective modulus θ^{hom} is determined by using the modified secant method described in the previous section, for given values of the material properties $\dot{\varepsilon}_o^{(r)}$, m and the equivalent plastic strain in each phase $\bar{\varepsilon}^{p(r)}$, which define the $\sigma_y^{(r)}$'s.

These equations are used in a finite element environment and the calculations are carried out incrementally. Within each increment the value of the $\sigma_y^{(r)}$'s are assumed to take constant values, as assumed in the previous section; these constant values are either those at the start or at the end of the increment, depending on whether a forward or a backward Euler scheme is used for the numerical integration of the elastoplastic equations. The modified secant method described in the previous section provides, among other things, the values of $\dot{\bar{\varepsilon}}^{p(r)}$ for each phase, which are then used to update the value of $\bar{\varepsilon}^{p(r)}$ at the end of the increment:

$$\bar{\varepsilon}_{n+1}^{p(r)} = \bar{\varepsilon}_n^{p(r)} + \dot{\bar{\varepsilon}}^{p(r)} \Delta t$$

where Δt is the corresponding time increment.

Also, in the finite element calculations a value of $m > 60$ is used, so that the behavior of the phases and the TRIP steel obey essentially a rate-independent von Mises plasticity law, where now the functions $\sigma_y^{(r)}(\bar{\varepsilon}^{p(r)})$ define the variation of the flow stress of the phases with the corresponding equivalent plastic strain $\bar{\varepsilon}^{p(r)}$.

CHAPTER FIVE

UNIT CELL CALCULATIONS

5.1 Introduction

In this chapter we consider a two-phase TRIP steel made of an austenitic matrix that contains dispersed martensite. The volume fractions of the two phases are assumed to remain constant as the “composite” material deforms and the homogenization technique (i.e., the modified secant method) is used to determine the overall behavior of the two-phase TRIP steel.

The corresponding “unit cell” for the two-phase TRIP steel is also defined. Then, unit cell calculations for the corresponding problem of uniaxial tension are carried out and the results are compared with those of the homogenization theory.

5.2 Modeling the microstructure of the two-phase TRIP steel

The two-phase composite we examine consists of particles of martensite isotropically and homogeneously dispersed in the matrix phase of austenite. The microstructure of the composite material can be described approximately by a three-dimensional periodic array of identical prismatic cells. Every cell models the two phases of the composite and consists of a martensitic spherical inclusion embedded in the center of a hexagonal prism simulating the austenitic matrix. Figure 5.1 shows a schematic representation of the three-dimensional periodic array of prismatic cells. The periodic array of prismatic cells shown in Figure 5.1 is extended in all three directions. In order to minimize the calculations, we replace the prismatic cells with the corresponding cylindrical cells as shown in Figures 5.2 and 5.3.

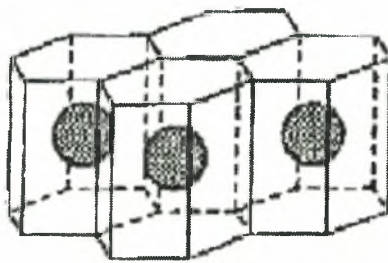


Figure 5.1: Three-dimensional periodic array of prismatic cells

5.3 The unit cell problem – uniaxial tension

In this section we use the ABAQUS general purpose finite element program in order to solve the corresponding cylindrical unit cell problem with the appropriate periodic boundary conditions for the problem of uniaxial tension.

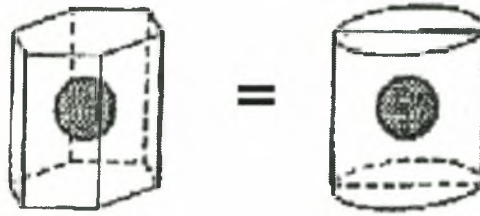


Figure 5.2: Prismatic cell approximated by cylindrical cell

The spherical inclusion embedded in the center of the cylinder shown in Figure 5.3 models the martensitic particles and its radius R is related with the volume fraction of martensite f according to the equation:

$$f = \frac{V_{\text{mart}}}{V_{\text{TRIP}}} = \frac{V_{\text{sphere}}}{V_{\text{total}}} = \frac{\frac{4}{3} \pi R^3}{\pi R_c^2 h} \Rightarrow R = \left(\frac{3}{4} f R_c^2 h \right)^{1/3} \quad (5.1)$$

where R_c is the radius of the cylindrical cell and h its height. The height h is assumed equal to $2R_c$, so that the last equation implies that

$$\frac{R}{R_c} = \left(\frac{3f}{2} \right)^{1/3}. \quad (5.2)$$

The axisymmetric problem is symmetric about the midplane at $z=0$; therefore we need to model one-quarter of the cross-section on the $z-r$ plane as show in Figure 5.4, where the dark area represents the martensitic phase.

A typical finite element mesh used in the calculations is shown in Figure 5.5.

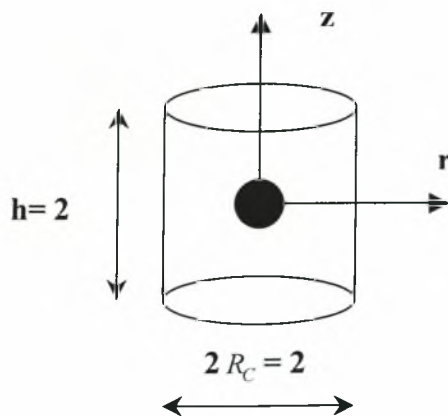


Figure 5.3: Dimensions of the cylindrical cell

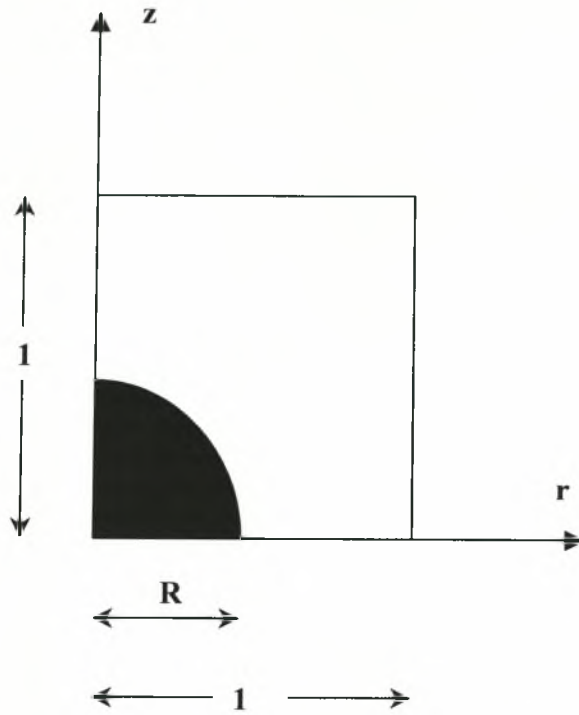


Figure 5.4: FEM modeling of Unit Cell

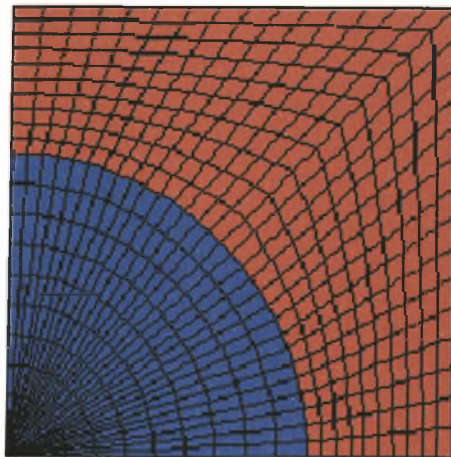


Figure 5.5: Finite element mesh that corresponds to the case with $f = 0.20$, i.e., 20% of martensite volume. The blue elements correspond to the martensitic particles and the red elements are the austenitic matrix.

Figure 5.6 shows schematically the aforementioned successive geometric approximations involved in the modeling, i.e., the steps that lead from the actual three-dimensional prismatic unit cells to the axisymmetric finite element modeling of the unit cell.

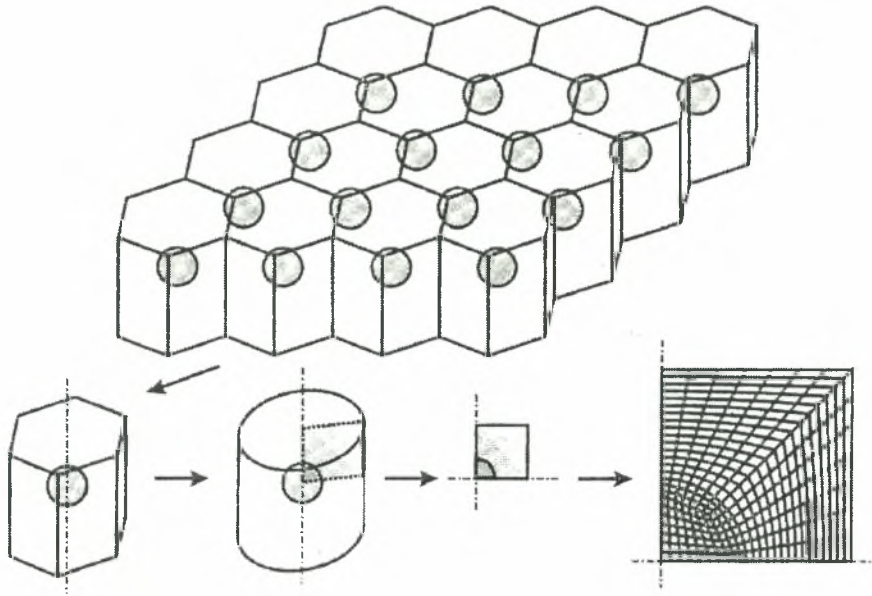


Figure 5.6: Schematic depiction of the idea of unit cell modeling

Four different volume fractions are analyzed, namely $f = 0.075, 0.20, 0.30, 0.50$. The corresponding values of the ratio R/R_C are shown in Table 5.1.

MODEL	f (%)	R/R_C
I	7.5	0.483
II	20	0.670
III	30	0.766
IV	50	0.910

Table 5.1: f and R/R_C for the FEM models examined

The finite element used in the calculations are four-node axisymmetric, isoparametric “B-bar” elements (CAX4H in ABAQUS). A “finite strain” analysis is carried out. In order to model a uniaxial tension test, we impose a uniform displacement on the top side of the mesh until a final elongation of 35% is reached.

Boundary conditions along the other three sides of the model provide the necessary symmetry and periodicity conditions for modeling the infinite series of stacked cells in uniaxial tension. All nodes along the midplane are constrained to move only in the radial direction, and all nodes along the pole (z -axis) are constrained to have zero radial displacement. Also, all nodes on the outer edge of the cell are constrained to have equal radial displacements. A schematic representation of the boundary conditions is shown in Figure 5.7.

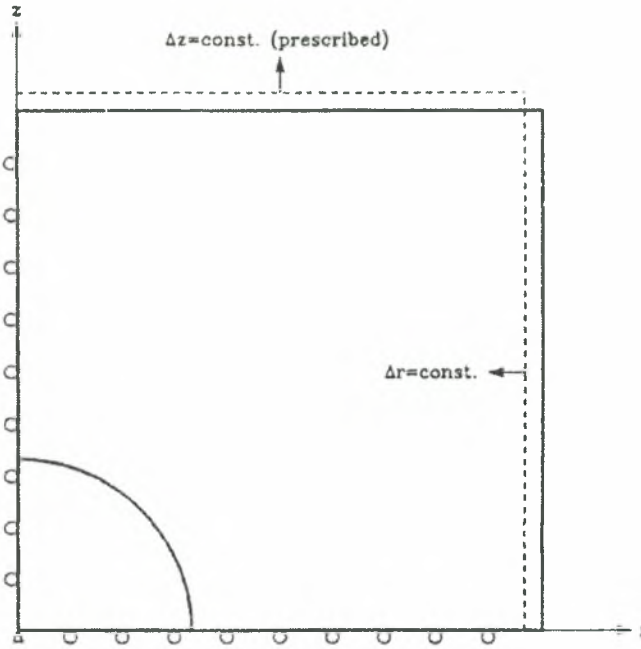


Figure 5.7: Schematic description of the problem with the boundary conditions.

The two phases involved (austenite and martensite) are modeled as elastic-plastic materials that obey the classical von Mises yield criterion with the associated flow rule. The hardening behavior of the two phases is described by the following equations

$$\text{austenite: } \sigma_y^{(a)}(\bar{\varepsilon}^{p(a)}) = 323 + 2163 \bar{\varepsilon}^{p(a)} \text{ (MPa)} \quad \text{for } \bar{\varepsilon}^{p(a)} \leq 0.24365, \quad (5.3)$$

$$\sigma_y^{(a)}(\bar{\varepsilon}^{p(a)}) = 850 \text{ (MPa)} \quad \text{for } \bar{\varepsilon}^{p(a)} \geq 0.24365, \quad (5.4)$$

$$\text{martensite: } \sigma_y^{(m)}(\bar{\varepsilon}^{p(m)}) = 920 + 1000 \left[\bar{\varepsilon}^{p(m)} \right]^{0.15} \text{ (MPa)}, \quad (5.5)$$

where the superscripts (a) and (m) denote austenite and martensite respectively. The variation of $\sigma_y^{(a)}$ and $\sigma_y^{(m)}$ with $\bar{\varepsilon}^{p(a)}$ and $\bar{\varepsilon}^{p(m)}$ respectively is shown in Figure 5.8. The elastic behavior of both phases is assumed to be isotropic and linear; the elastic strains that

develop are very small compared to the plastic ones and do not influence substantially the results.

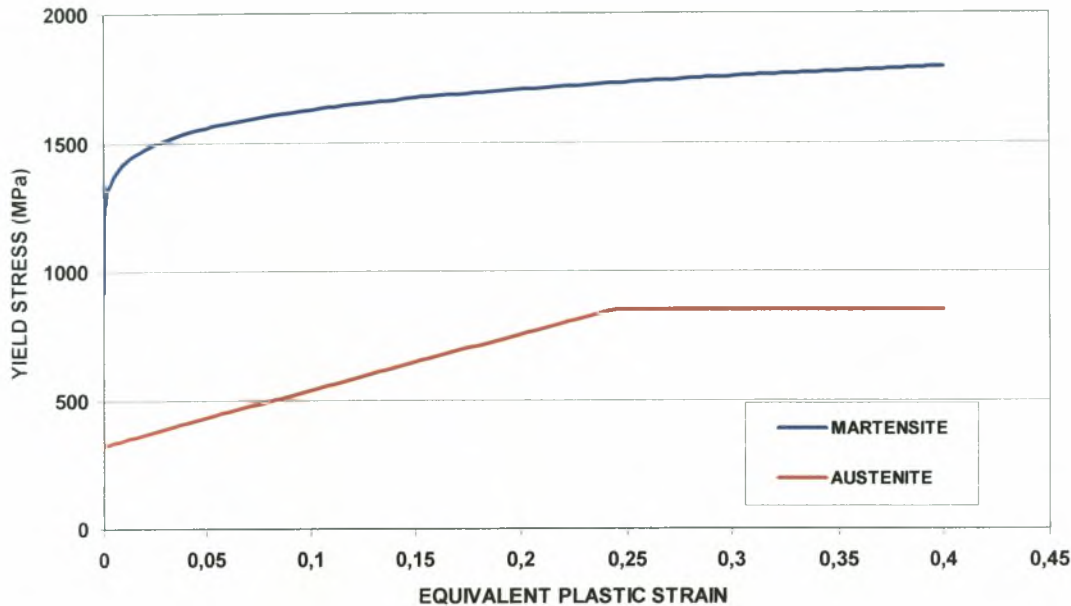


Figure 5.8: Variation of flow stress in austenite and martensite

5.4 Comparison of the predictions of the homogenization theory with the unit cell calculations

The unit cell problem is solved with ABAQUS for the four cases shown in Table 5.1. The deformed finite element meshes at the final elongation of 35% are shown in Figure 5.9.

The modified secant method described in Chapter 4 is also used for the analysis of the problem of uniaxial tension of the homogenized two-phase composite. In this case the response of the phase and the composite is purely viscoplastic, i.e., there no elastic strains present. Equations (4.32)-(4.33) are used to describe the behavior of each phase. The calculations are carried out incrementally by gradually increasing the imposed macroscopic uniaxial stress, and equations (5.3)-(5.5) are used for $\sigma_y^{(a)}$ and $\sigma_y^{(m)}$ in (4.32), which are assumed to take constant values over each increment. The values $\dot{\epsilon}_0^{(a)} = \dot{\epsilon}_0^{(m)} = 10^{-4} \text{ s}^{-1}$ and $m = 100$ are used in the calculations. The relatively large value of m makes the response of the phases and the two-phase composite essentially rate independent; the phases are almost rigid plastic solids that obey the von Mises yield criterion with the associated flow rule, and

$\sigma_y^{(a)}$ and $\sigma_y^{(m)}$ define now the variation of the flow stresses in the von Mises model. The applied stress is increased gradually at a rate such that the corresponding macroscopic strain rate is approximately 10^{-4} s^{-1} .

The results of the two methods are compared in Figures 5.10-5.13. It is found that the predictions of the two methods agree reasonably well in all four cases considered.

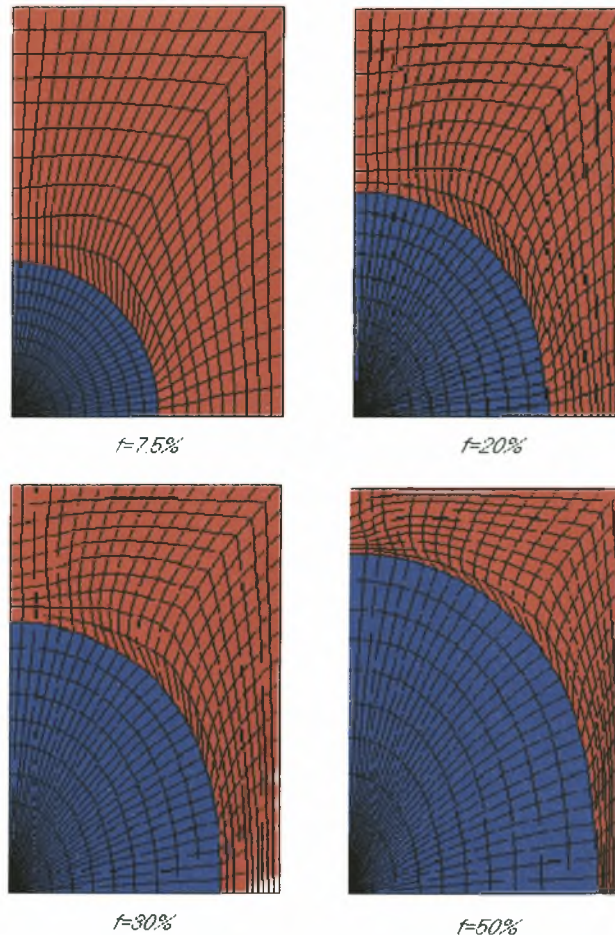


Figure 5.9: Deformed finite element meshes at the final elongation for $f=7.5\%$, $f=20\%$, $f=30\%$ and $f=50\%$. The blue elements correspond to the martensitic particles and the red elements are the austenitic matrix.

- **Model I ($f=7,5\%$)**

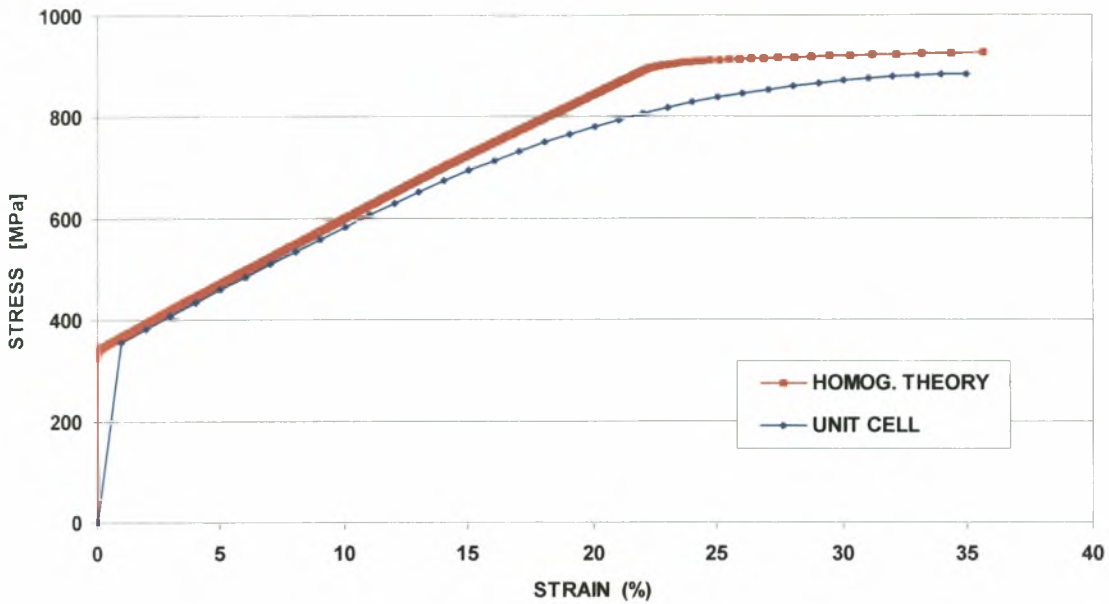


Figure 5.10: Comparison of stress-strain curves for $f=7.5\%$

- **Model II ($f=20\%$)**

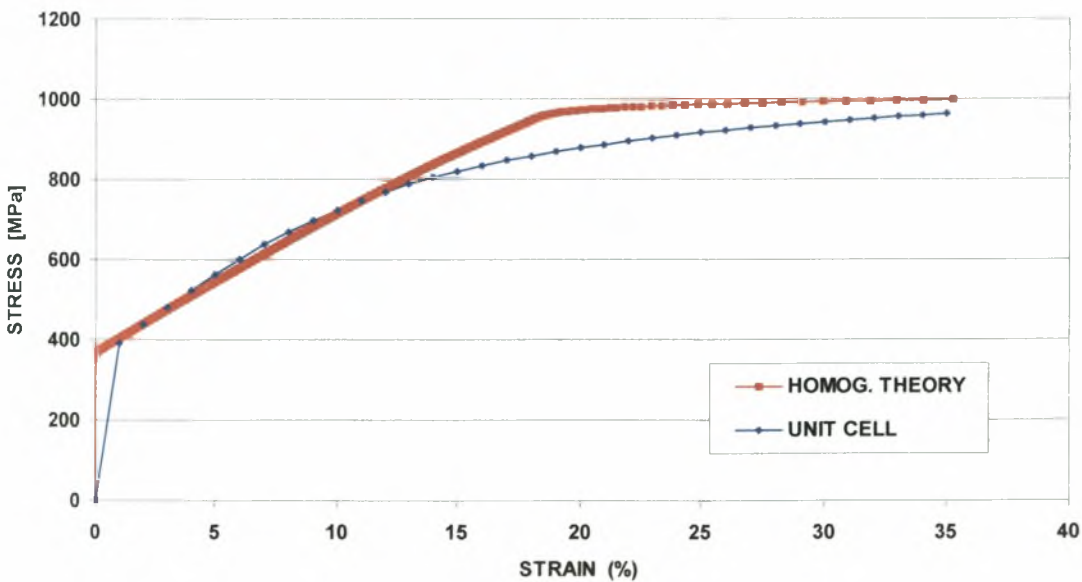


Figure 5.11: Comparison of stress-strain curves for $f=20\%$

- **Model III ($f=30\%$)**

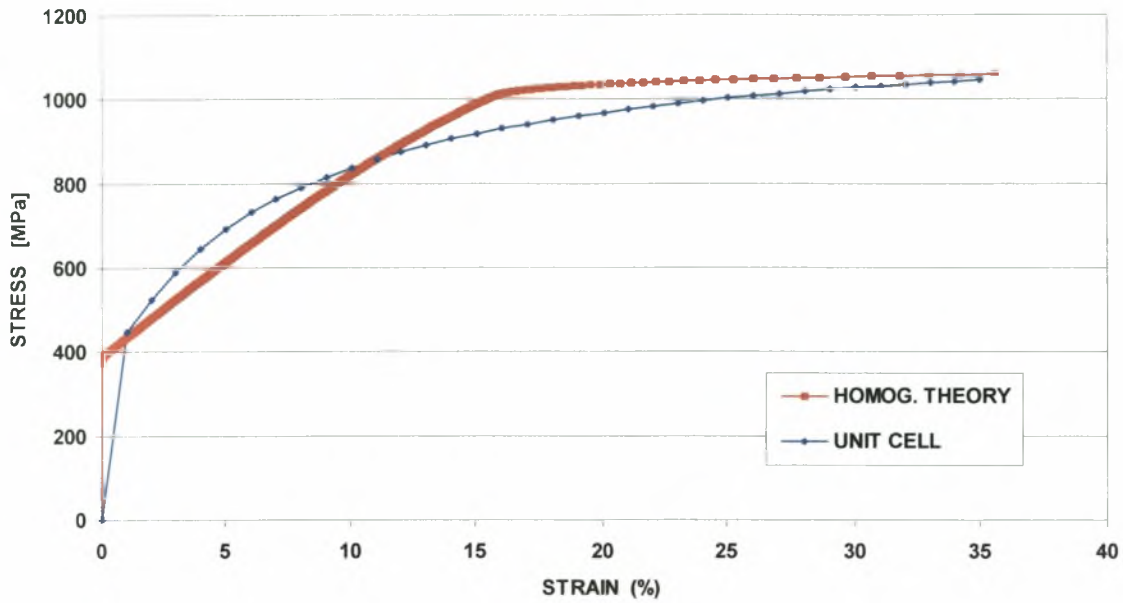


Figure 5.12: Comparison of stress-strain curves for $f=30\%$

- **Model IV ($f=50\%$)**

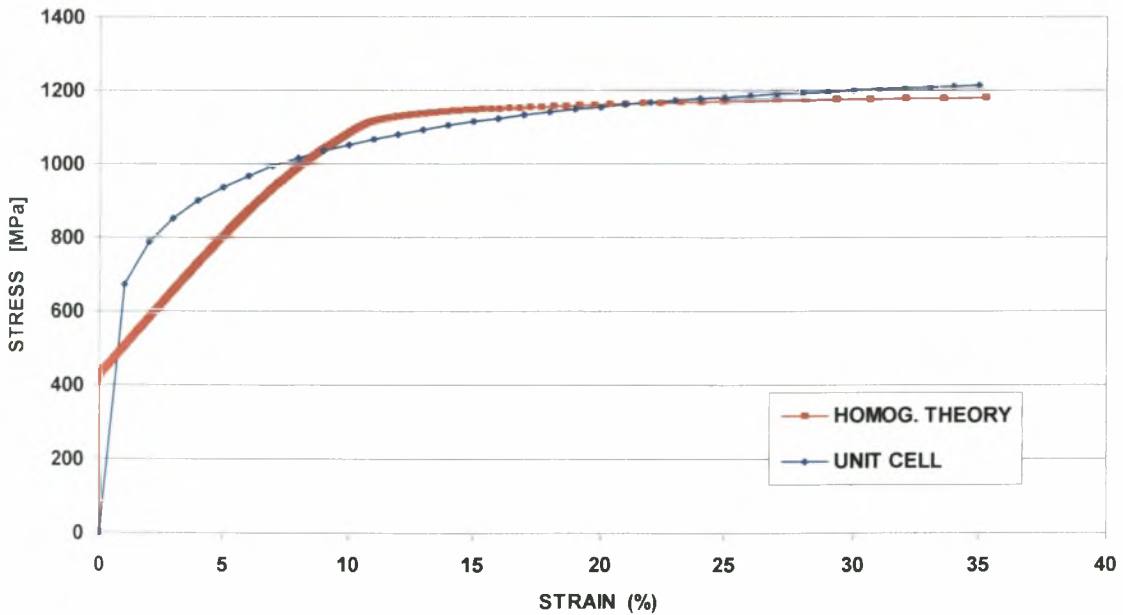


Figure 5.13: Comparison of stress-strain curves for $f=50\%$

CHAPTER SIX

CONSTITUTIVE MODELING OF TRIP STEELS

6.1 Introduction

In this chapter, a constitutive model that describes the mechanical behavior of steels exhibiting the “Transformation Induced Plasticity” (TRIP) phenomenon during martensitic transformation is presented. Two- and four-phase TRIP steels are considered.

TRIP steels are essentially composite materials with evolving volume fractions of the individual phases. The total deformation rate is written as the sum of elastic, plastic and transformation parts:

$$\mathbf{D} = \mathbf{D}^e + \mathbf{D}^p + \mathbf{D}^{TRIP} . \quad (6.1)$$

The elastic properties of all phases are essentially the same. Therefore, standard isotropic linear hypoelasticity of homogeneous solids is used in order to describe the elastic behavior of the TRIP steels. The constitutive equation of the plastic part \mathbf{D}^p is determined by using the homogenization technique described in Chapter 4. The transformation part \mathbf{D}^{TRIP} has both deviatoric and volumetric parts and is proportional to the rate of change of the volume fraction of martensite. Finally, the evolution of martensite due to martensitic transformation is described by a transformation kinetics model, which takes into account temperature, plastic strain and stress state.

No restriction is placed on the magnitude of the strains and appropriate “finite strain” constitutive equations are developed.

6.2 A brief geometric definition of the deformation rate tensor

In any structural problem the analyst describes the initial configuration of the structure and is interested in its deformation throughout the history of loading. We use the Lagrangian description of motion where we examine the motion of a material particle with respect to its initial configuration. Using this description the independent variables are the position \mathbf{X} of the particle at $t = 0$, and the time t . Figure 6.1 shows the displacement of a material particle initially located at some position \mathbf{X} in space to a new position \mathbf{x} .

Since we assume that material cannot appear or disappear, there will be a one-to-one correspondence between \mathbf{x} and \mathbf{X} , so that we can always write the history of the location of the particle as:

$$\mathbf{x} = \mathbf{x}(\mathbf{X}, t) \quad (6.2)$$

This relationship can be inverted:

$$\mathbf{x} = \mathbf{x}(\mathbf{X}, t) \quad \Leftrightarrow \quad \mathbf{X} = \mathbf{X}(\mathbf{x}, t) \quad (6.3)$$

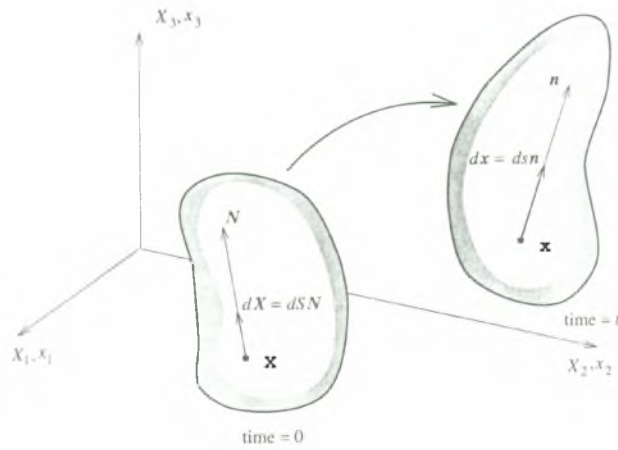


Figure 6.1: Displacement, stretch, and rotation of material vector $d\mathbf{X}$ to new position $d\mathbf{x}$

Now consider two neighbouring particles, located at \mathbf{X} and at $\mathbf{X} + d\mathbf{X}$ in the initial (reference) configuration. Let \mathbf{x} and $\mathbf{x} + d\mathbf{x}$ be the positions of the same particles in the current (deformed) configuration. Then

$$d\mathbf{x} = \mathbf{x}(\mathbf{X} + d\mathbf{X}, t) - \mathbf{x}(\mathbf{X}, t) = \frac{\partial \mathbf{x}(\mathbf{X}, t)}{\partial \mathbf{X}} \cdot d\mathbf{X} \quad \text{or} \quad d\mathbf{x} = \mathbf{F} \cdot d\mathbf{X} = d\mathbf{X} \cdot \mathbf{F}^T \quad (6.4)$$

where

$$\mathbf{F}(\mathbf{X}, t) = \frac{\partial \mathbf{x}(\mathbf{X}, t)}{\partial \mathbf{X}} = \mathbf{x} \nabla_{\mathbf{X}} \quad (6.5)$$

is the “deformation gradient” tensor, and $\nabla_{\mathbf{X}} = \frac{\partial}{\partial \mathbf{X}}$ is the gradient operator on the current configuration.

Many of the materials we need to model are path dependent, their constitutive equations are written in the deformed configuration, and require the use of quantities which are strain-rate-like. The velocity \mathbf{v} of a material particle is defined as

$$\mathbf{v}(\mathbf{X}, t) = \frac{\partial \mathbf{x}(\mathbf{X}, t)}{\partial t}. \quad (6.6)$$

The last equation provides a “Lagrangian” description of the velocity field. Using the relationship $\mathbf{X} = \mathbf{X}(\mathbf{x}, t)$ in $\mathbf{v}(\mathbf{X}, t)$ we can find the Eulerian description of the velocity field: $\mathbf{v}(\mathbf{x}, t)$.

We define as “ $d\mathbf{v}$ ” the difference in velocity of two neighbouring material points with positions \mathbf{X} and $\mathbf{X} + d\mathbf{X}$ in the reference configurations and \mathbf{x} and $\mathbf{x} + d\mathbf{x}$ in the deformed

configuration. In the following, we derive two alternative expressions for $d\mathbf{v}$. Using the Lagrangian description of \mathbf{v} , we find

$$\begin{aligned} d\mathbf{v} &= \mathbf{v}(\mathbf{X} + d\mathbf{X}, t) - \mathbf{v}(\mathbf{X}, t) = \frac{\partial \mathbf{v}(\mathbf{X} + d\mathbf{X}, t)}{\partial t} - \frac{\partial \mathbf{v}(\mathbf{X}, t)}{\partial t} = \\ &= \frac{\partial}{\partial t} [\mathbf{v}(\mathbf{X} + d\mathbf{X}, t) - \mathbf{v}(\mathbf{X}, t)] = \frac{\partial}{\partial t} (d\mathbf{v}) = \frac{\partial}{\partial t} (\mathbf{F} \cdot d\mathbf{X}) = \dot{\mathbf{F}} \cdot d\mathbf{X}. \end{aligned} \quad (6.7)$$

The corresponding Eulerian description gives

$$d\mathbf{v} = \mathbf{v}(\mathbf{x} + d\mathbf{x}, t) - \mathbf{v}(\mathbf{x}, t) = \frac{\partial \mathbf{v}(\mathbf{x}, t)}{\partial \mathbf{x}} \cdot d\mathbf{x} = \mathbf{L}(\mathbf{x}, t) \cdot d\mathbf{x}, \quad (6.8)$$

where

$$\mathbf{L}(\mathbf{x}, t) = \frac{\partial \mathbf{v}(\mathbf{x}, t)}{\partial \mathbf{x}} = \mathbf{v} \nabla \quad (6.9)$$

is the velocity gradient tensor in the current configuration, and $\nabla = \frac{\partial}{\partial \mathbf{x}}$ is the gradient operator on the current configuration. Combining (6.7) and (6.8), we find

$$\dot{\mathbf{F}} \cdot d\mathbf{X} = \mathbf{L} \cdot d\mathbf{x}. \quad (6.10)$$

Setting $d\mathbf{x} = \mathbf{F} \cdot d\mathbf{X}$ in the last equation, we find that

$$\dot{\mathbf{F}} \cdot d\mathbf{X} = \mathbf{L} \cdot \mathbf{F} \cdot d\mathbf{X}. \quad (6.11)$$

Since the last equation holds for arbitrary $d\mathbf{X}$, we conclude that $\dot{\mathbf{F}} = \mathbf{L} \cdot \mathbf{F}$ or

$$\mathbf{L} = \dot{\mathbf{F}} \cdot \mathbf{F}^{-1}. \quad (6.12)$$

The velocity gradient tensor \mathbf{L} can be written as the sum of a symmetric tensor \mathbf{D} , called the rate of deformation tensor, and a skew-symmetric tensor \mathbf{W} , called the spin tensor or the vorticity tensor:

$$\mathbf{D} = \frac{1}{2}(\mathbf{L} + \mathbf{L}^T) = \frac{1}{2} \left[\frac{\partial \mathbf{v}}{\partial \mathbf{x}} + \left(\frac{\partial \mathbf{v}}{\partial \mathbf{x}} \right)^T \right] = \frac{1}{2}(\mathbf{v} \nabla + \nabla \mathbf{v}). \quad (6.13)$$

The skew-symmetric part (spin tensor) of the decomposition is:

$$\mathbf{W} = \frac{1}{2}(\mathbf{L} - \mathbf{L}^T) = \frac{1}{2} \left[\frac{\partial \mathbf{v}}{\partial \mathbf{x}} - \left(\frac{\partial \mathbf{v}}{\partial \mathbf{x}} \right)^T \right] = \frac{1}{2}(\mathbf{v} \nabla - \nabla \mathbf{v}). \quad (6.14)$$

6.3 Constitutive formulation

As mentioned earlier, the total deformation rate is written as the sum of elastic, plastic and transformation parts:

$$\mathbf{D} = \mathbf{D}^e + \mathbf{D}^p + \mathbf{D}^{TRIP} \quad (6.15)$$

the following we derive detailed constitutive equations for the individual parts of \mathbf{D} .

6.3.1 The elastic part of the deformation rate \mathbf{D}^e

The elastic properties of the individual phases in TRIP steels are almost identical and the composite material can be viewed as homogenous in the elastic region. Isotropic linear hypoelasticity is assumed and the constitutive equation for \mathbf{D}^e is written as

$$\mathbf{D}^e = \mathbf{M}^e : \overset{\nabla}{\boldsymbol{\sigma}} \quad \text{or} \quad \overset{\nabla}{\boldsymbol{\sigma}} = \mathbf{L}^e : \mathbf{D}^e \quad (6.16)$$

where $\overset{\nabla}{\boldsymbol{\sigma}} = \dot{\boldsymbol{\sigma}} + \boldsymbol{\sigma} \cdot \mathbf{W} - \mathbf{W} \cdot \boldsymbol{\sigma}$ is the Jaumann or co-rotational stress rate, and \mathbf{M}^e and $\mathbf{L}^e = \mathbf{M}^{e-1}$ are the elastic compliance and stiffness tensors respectively, which can be written as

$$\mathbf{L}^e = 2\mu \mathbf{K} + 3\kappa \mathbf{J} \quad \text{and} \quad \mathbf{M}^e = \frac{1}{2\mu} \mathbf{K} + \frac{1}{3\kappa} \mathbf{J}. \quad (6.17)$$

μ and κ being the elastic shear and bulk moduli of the material.

Use of \mathbf{D}^e and $\overset{\nabla}{\boldsymbol{\sigma}}$, instead of the usual strain and stress rates, in (6.16) renders the constitutive equation “objective”, i.e., observer-independent. Also, it is now well known that, when the elastic strains are small, the hypoelastic constitutive equation (6.16) is consistent to leading order with hyperelasticity (Needleman 1985).

6.3.2 The plastic part of the deformation rate \mathbf{D}^p

The plastic part of the deformation rate \mathbf{D}^p is determined in terms of the plastic properties of the individual phases by using the modified secant method described in Chapter 4. The corresponding constitutive equation is of the form

$$\mathbf{D}^p = \frac{1}{2} \theta^{\text{hom}} \mathbf{s} = \dot{\boldsymbol{\varepsilon}}^p \mathbf{N}, \quad \mathbf{N} = \frac{3}{2\sigma_{eq}} \mathbf{s}, \quad \sigma_{eq} = \sqrt{\frac{3}{2} \mathbf{s} : \mathbf{s}}, \quad \dot{\boldsymbol{\varepsilon}}^p = \sqrt{\frac{2}{3} \mathbf{D}^p : \mathbf{D}^p} = \frac{1}{3} \sigma_{eq} \theta^{\text{hom}}, \quad (6.18)$$

where θ^{hom} is determined from the homogenization theory described in Chapter 4.

Each of the phases is viscoplastic and obeys a constitutive equation of the form

$$\mathbf{D}^p = \dot{\boldsymbol{\varepsilon}}^{p(r)} \mathbf{N} = \frac{1}{2} \theta^{(r)} \mathbf{s}, \quad \mathbf{N} = \frac{3}{2\sigma_{eq}} \mathbf{s} \quad r = 1, 2, 3, 4, \quad (6.19)$$

where

$$\dot{\bar{\varepsilon}}^{p(r)} = \dot{\varepsilon}_p^{(r)} \left[\frac{\sigma_{eq}}{\sigma_y^{(r)}(\bar{\varepsilon}^{p(r)})} \right]^m, \quad \theta^{(r)} = \frac{3\dot{\varepsilon}_o^{(r)}}{\sigma_{eq}} \left[\frac{\sigma_{eq}}{\sigma_y^{(r)}(\bar{\varepsilon}^{p(r)})} \right]^m, \quad (6.20)$$

and $\sigma_y^{(r)}(\bar{\varepsilon}^{p(r)})$ are known functions describing the hardening behavior of the phases.

6.3.2.1 Hardening of the phases

The individual phases of the composite material exhibit different hardening behavior during the deformation process. The hardening behavior of the individual phases influences not only the mechanical behavior of TRIP steels but also the $f - \varepsilon$ behavior. The evolution of martensite is strongly affected by the plastic strain of retained austenite. Higher level of plastic strain accumulated by austenite leads to a greater amount of austenite transformed to martensite. In order to determine the hardening behavior of the phases a detailed bibliographic search has been made. The hardening behavior of the phases is modeled with expressions of the form:

$$\sigma_y^{(r)} = H^{(r)}(\bar{\varepsilon}^{p(r)}) \quad (6.21)$$

where for each phase r , $\sigma_y^{(r)}$ is the yield stress, $\bar{\varepsilon}^{p(r)}$ is the equivalent plastic strain and $H^{(r)}(\bar{\varepsilon}^{p(r)})$ is the hardening expression. The hardening behavior of the phases is strongly affected by the thermal treatment applied, especially for the four-phase TRIP steel. Therefore, the determination of the hardening properties of the constituent phases is a very difficult task and experimental data accounting for similar but not identical conditions of thermal treatment are used.

In the following, the selected hardening behavior of the phases for the four-phase TRIP steel is presented. The hardening behavior of martensite was obtained from experimental data of the partly martensitic steel DOCOL 1400 (volume fraction of martensite $\approx 95\%$) presented in Technical steel research (2002). Input data for the hardening behavior of the ferritic phase were obtained from experimental results for the annealed ferritic steel DOCOL 600, also presented in Technical Steel Research (2002). The chemical composition of DOCOL 1400 and DOCOL 600 is given in Table 6.1. The hardening behavior of bainite was obtained from tensile tests performed in a 0.5% C steel subjected to thermal treatment in the range of bainite formation (coiling temperature of 950°C , bainite isothermal transformation at 400°C for 300sec) and presented in Technical Steel Research (2002). The hardening curve for austenite was obtained from experimental data of Naturani et al. (1982). Furthermore temperature

dependence of the hardening curves has been taken into consideration. The selected hardening expressions accounting for the hardening behavior of the four phases (the following labels are used: retained austenite=(a), martensite=(m), bainite=(3), ferrite=(4)) for two different temperatures (23°C , 50°C) are ($\sigma_y^{(r)}$ in MPa):

For Temperature 23°C :

$$\sigma_y^{(a)} = 300 + 500(\bar{\varepsilon}^{p(a)})^{0.25} \quad (6.22) \quad \sigma_y^{(m)} = 1200 + 1025(\bar{\varepsilon}^{p(m)})^{0.13} \quad (6.23)$$

$$\sigma_y^{(3)} = 810 + 753(\bar{\varepsilon}^{p(3)})^{0.25} \quad (6.24) \quad \sigma_y^{(4)} = 290 + 690(\bar{\varepsilon}^{p(4)})^{0.47} \quad (6.25)$$

For Temperature 50°C :

$$\sigma_y^{(a)} = 290 + 500(\bar{\varepsilon}^{p(a)})^{0.25} \quad (6.26) \quad \sigma_y^{(m)} = 1200 + 1025(\bar{\varepsilon}^{p(m)})^{0.13} \quad (6.27)$$

$$\sigma_y^{(3)} = 800 + 733(\bar{\varepsilon}^{p(3)})^{0.25} \quad (6.28) \quad \sigma_y^{(4)} = 265 + 590(\bar{\varepsilon}^{p(4)})^{0.47} \quad (6.29)$$

We present the above hardening curves for the individual phases of the four-phase TRIP steel for the temperatures of 23°C and 50°C because the experimental data used for the comparison with the FEM model are obtained in those two temperatures. The hardening curves accounting for the hardening expressions of the four phases are presented in Figure 6.2.

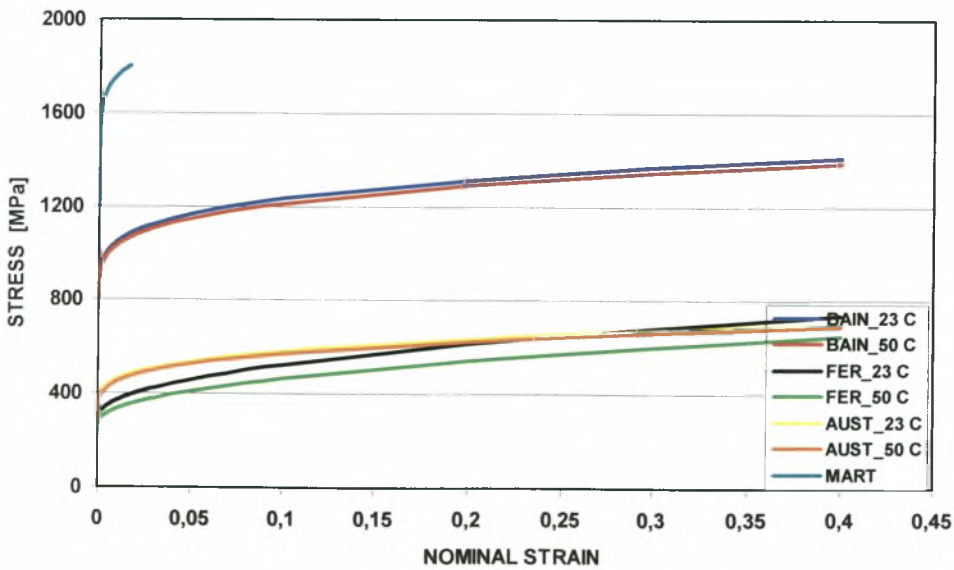


Figure 6.2: Hardening behavior of individual phases for the four-phase TRIP steel

The hardening behavior of the constituents for the two-phase TRIP steel has been incorporated to our model using experimental data from Naturani et al. (1982) for the flow stress of austenite and martensite. Analytical expressions for the hardening models were obtained from a fit to the presented curves. For the austenitic phase the hardening behavior was assumed linear, whereas a power-law fit was used for the martensitic phase:

Retained Austenite:

$$\sigma_y^{(a)} = 323 + 2163 \bar{\varepsilon}^{p(a)} \quad (\text{MPa}) \quad \text{for } \bar{\varepsilon}^{p(a)} \leq 0.24365 \quad (6.30)$$

$$\sigma_y^{(a)} = 850 \quad (\text{MPa}) \quad \text{for } \bar{\varepsilon}^{p(a)} \geq 0.24365 \quad (6.31)$$

Martensite:

$$\sigma_y^{(m)} = 920 + 1000 \left(\bar{\varepsilon}^{p(m)} \right)^{0.15} \quad (\text{MPa}) \quad (6.32)$$

The hardening behavior of the two phases is presented in Figure 6.3.

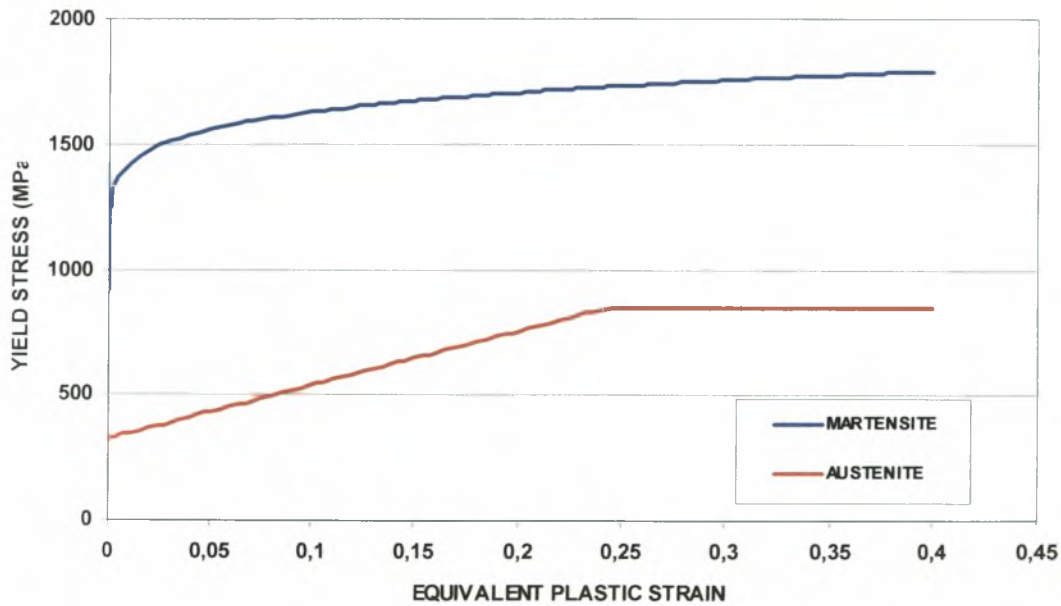


Figure 6.3: Hardening behavior of individual phases for the two-phase TRIP steel

Steel	C	Mn	Si	Al	P	S	N	Cu	V
DOCOL 1400	0.170	1.590	0.5	0.046	0.010	0.001	0.006	0.01	0.01
DOCOL 600	0.148	0.746	0.196	0.045	0.052	0.003			

Table 6.1: Chemical compositions of steels DOCOL 1400 and DOCOL 600, contents in mass %.

6.3.2.2 Accounting for the inherited dislocation structure of newly-formed martensite

A unit of martensite that forms at a given austenite plastic strain inherits the strain-hardened dislocation structure of its parent austenite. Thus, each incrementally-formed unit of martensite is initially harder than the initial hardness of any previously-formed martensite, and is substantially harder than the initial hardness of undeformed martensite. This feature is accounted for in the model by keeping a running average of the hardness levels of previously formed martensite as proposed by Stringfellow et al. (1992). Each incremental unit of martensite is assumed to have an initial hardness, which is a function of the plastic strain in the austenite from which it was instantaneously produced. Therefore, the average hardness of the martensite continues to increase as initially harder martensite is added, even though (at first) negligible deformation is occurring in the martensite because of its already high hardness. Considering the hardening expression for martensite of equation (6.23) the average hardness is expressed by the form:

$$\sigma_y^{(m)} = \frac{f_n}{f_{n+1}} H^{(m)}(\bar{\varepsilon}_{n+1}^{p(m)}) + \frac{\Delta f}{f_{n+1}} H^{(m)}(\bar{\varepsilon}_n^{p(a)}) \quad (6.33)$$

where f_n and $f_{n+1} = f_n + \Delta f$ is the volume fraction of martensite at the beginning and at the end of the strain increment respectively, and $H^{(m)}$ is the function on the right hand side of (6.23). Stringfellow et al. (1992) made the assumption that at each increment, all of the prior-formed martensite is assumed to have been exposed to the same "average" strain history, despite the fact that each unit of this group has actually seen a different strain history. The error introduced by this assumption is second order.

6.3.3 The transformation part of the deformation rate D^{TRIP} and the evolution of the volume fraction of the phases

A critical aspect of the transformation process is the strain softening which occurs as a result of the transformation strain. The strain softening has been incorporated into the model by considering an additional deformation rate contribution to the total deformation rate, proportional to the rate of increase of the martensite volume fraction \dot{f} . This consideration was first used for transformation strain by Stringfellow et al. (1992) in a manner similar to that used by Hutchinson and Tvergaard (1989) for modeling softening due to void nucleation. In their constitutive model, the softening effects of void nucleation are accounted for by considering an additive strain rate term proportional to the rate of increase of the void volume

fraction. Similarly, Stringfellow et al. (1992) proposed the following form to account for the plastic softening due to martensitic nucleation:

$$\mathbf{D}^{TRIP} = A(\sigma_{eq}) \dot{f} \mathbf{N} + \frac{1}{3} \dot{\varepsilon}_v^p \boldsymbol{\delta} \quad \text{with} \quad \mathbf{N} = \frac{3}{2\sigma_{eq}} \mathbf{s}, \quad \sigma_{eq} = \sqrt{\frac{3}{2} \mathbf{s} : \mathbf{s}} \quad (6.34)$$

where σ_{eq} is the von Mises equivalent stress, \mathbf{s} is the deviatoric stress tensor, $\boldsymbol{\delta}$ is the second-order identity tensor, $A(\sigma_{eq})$ is a dimensionless function to be defined in the following, and $\dot{\varepsilon}_v^p = D_{kk}^{TRIP}$ is the transformation dilatation rate, the value of which is also defined later in this section.

The transformation strain rate as presented in equation (6.34) consists of a dilatational term accounting for the positive transformation volume change and of a deviatoric term that models the transformation shape strain. The dimensionless coefficient A reflects an ensemble effect of the shape strains over an isotropic, orientational distribution of nucleation sites as considered by Olson, Tzuzaki and Cohen (1987). Some sites will generate local shape strains in the direction of \mathbf{N} while others will generate shape strains orthogonal to \mathbf{N} . The factor A in equation (6.34) is used because the net shape strains not aligned with \mathbf{N} will tend to cancel themselves, leaving a net shape strain in the \mathbf{N} direction which is much less than the total number of transforming sites per unit volume times the shape strain associated with each site. Consistent with experimental data presented in Olson and Azrin (1978), A is taken to depend on the stress level:

$$A(\sigma_{eq}) = A_0 + A_1 \frac{\sigma_{eq}}{s_\alpha^*} \quad (6.35)$$

where A_0, A_1 are dimensionless constants and s_α^* is a reference austenite stress.

The dilatation rate $\dot{\varepsilon}_v^p = D_{kk}^{TRIP}$ is determined by taking into account the volume change associated with the martensitic transformation. During martensitic transformation, the volume of austenite changes by an amount $dV^{(a)} < 0$; the corresponding volume change of austenite is $dV^{(m)} > 0$. Put in other words, a volume $(-dV^{(a)})$ of austenite transforms into a volume $dV^{(m)}$ of martensite. The relative volume change Δ_v associated with the transformation is

$$\Delta_v = \frac{dV^{(m)} - (-dV^{(a)})}{(-dV^{(a)})} = -\frac{dV^{(m)} + dV^{(a)}}{dV^{(a)}} \quad \text{or} \quad dV^{(m)} = -(1 + \Delta_v) dV^{(a)} \quad (6.36)$$

Leal (1984) found experimentally that $\Delta_v \cong 0.02$ to 0.05 in austenitic steels, depending upon alloy composition. Equation (6.36) implies that

$$\dot{V}^{(m)} = -(1 + \Delta_v) \dot{V}^{(a)} \quad \text{or} \quad \dot{V}^{(a)} = -\frac{\dot{V}^{(m)}}{1 + \Delta_v} \quad (6.37)$$

For the two-phase composite the relation between the volumes of retained austenite $V^{(a)}$ and martensite $V^{(m)}$ is:

$$V = V^{(m)} + V^{(a)} \quad (6.38)$$

and in a rate form:

$$\dot{V} = \dot{V}^{(m)} + \dot{V}^{(a)} \quad (6.39)$$

For the four-phase TRIP steel the relation for the volumes of retained austenite $V^{(a)}$, martensite $V^{(m)}$, bainite $V^{(3)}$ and ferrite $V^{(4)}$ is:

$$V = V^{(m)} + V^{(a)} + V^{(3)} + V^{(4)} \quad (6.40)$$

Since the volumes of bainite and ferrite remain constant ($\dot{V}^{(3)} = \dot{V}^{(4)} = 0$), the last equation implies that

$$\dot{V} = \dot{V}^{(m)} + \dot{V}^{(a)} \quad (6.41)$$

Therefore, the expression accounting for the total volume change \dot{V} is the same in both the two- and four-phase material. In the expression for \dot{V} we replace $\dot{V}^{(a)}$ from equation (6.37) to find:

$$\dot{V} = \dot{V}^{(m)} + \dot{V}^{(a)} = \dot{V}^{(m)} - \frac{1}{1 + \Delta_v} \dot{V}^{(m)} = \frac{\Delta_v}{1 + \Delta_v} \dot{V}^{(m)} \quad (6.42)$$

Since changes in volume due to elastic strains are small and fully recoverable, it is assumed that changes in dilatations are due to volumetric plastic deformation rates only. Therefore, $\dot{\epsilon}_v^p$ is given by the form:

$$\dot{\epsilon}_v^p = \frac{\dot{V}}{V} \quad (6.43)$$

Using equations (6.42) and (6.43) we have:

$$\dot{\epsilon}_v^p = \frac{\dot{V}}{V} = \frac{\Delta_v}{1 + \Delta_v} \frac{\dot{V}^{(m)}}{V} \quad \text{or} \quad \frac{\dot{V}^{(m)}}{V} = \frac{1 + \Delta_v}{\Delta_v} \dot{\epsilon}_v^p \quad (6.44)$$

The volume fraction of martensite f is defined as the ratio of its volume to the total volume:

$$f = \frac{V^{(m)}}{V} \quad \Rightarrow \quad \dot{f} = \frac{\dot{V}^{(m)}}{V} - \frac{V^{(m)}}{V^2} \dot{V} = \frac{\dot{V}^{(m)}}{V} - f \frac{\dot{V}}{V} \quad (6.45)$$

In the above equation we set $\frac{\dot{V}^{(m)}}{V} = \frac{1 + \Delta_v}{\Delta_v} \dot{\epsilon}_v^p$ and $\frac{\dot{V}}{V} = \dot{\epsilon}_v^p$ to find

$$\dot{f} = \frac{1 + \Delta_v}{\Delta_v} \dot{\epsilon}_v^p - f \dot{\epsilon}_v^p = \frac{1 + \Delta_v - f \Delta_v}{\Delta_v} \dot{\epsilon}_v^p \Rightarrow \dot{f} = \frac{1 + (1 - f) \Delta_v}{\Delta_v} \dot{\epsilon}_v^p \quad (6.46)$$

or

$$\dot{\epsilon}_v^p = \frac{\Delta_v}{1 + (1 - f) \Delta_v} \dot{f} \quad (6.47)$$

As stated earlier, Leal (1984) found experimentally that $\Delta_v \cong 0.02$ to 0.05 . Therefore, the last equation can be written as

$$\dot{\epsilon}_v^p \cong \Delta_v \dot{f} \quad (6.48)$$

It is noted that for $\Delta_v = 0$ the volumetric part vanishes ($\dot{\epsilon}_v^p = 0$).

Finally, substituting the expression $\dot{\epsilon}_v^p \cong \Delta_v \dot{f}$ in (6.34), we conclude that the constitutive equation for \mathbf{D}^{TRIP} can be written as:

$$\mathbf{D}^{TRIP} = \left[A(\sigma_{eq}) \mathbf{N} + \frac{1}{3} \Delta_v \boldsymbol{\delta} \right] \dot{f} \quad (6.49)$$

6.3.3.1 A transformation kinetics model for the determination of \dot{f}

In previous studies, Olson and Cohen (1975, 1976) argued that intersections of shear bands in metastable austenites could be very effective nucleation sites for strain-induced martensitic transformation. They proposed an expression for the volume fraction of martensite vs plastic strain assuming that shear-band intersection is the dominant mechanism of strain-induced nucleation. The known as the OC (Olson-Cohen) model considered temperature and plastic strain as the only parameters controlling the evolution of martensite. The stress state sensitivity of the transformation kinetics was not explicitly considered in the OC model suggesting that for isothermal conditions the volume fraction of martensite formed becomes a function of plastic strain only. Therefore, Stringfellow et al. (1992) modified the OC model in a rate form so as to incorporate pressure sensitivity into the model. The modified OC model proposed by Stringfellow et al. (1992) for two-phase steels is used in our model to describe the evolution of martensite during transformation.

The rate of increase in the volume fraction of martensite \dot{f} is proportional to the rate of increase in the number of martensitic embryos per unit austenite volume \dot{N}_m :

$$\dot{f} = c^{(a)} \bar{v}_m \dot{N}_m \quad (6.50)$$

where \bar{v}_m is the average volume per martensitic unit. The factor $c^{(a)}$ reflects the decreasing volume fraction of austenite available for transformation; in the two-phase material $c^{(a)} = 1 - f$.

The Olson and Cohen model is based on the experimental observation that strain-induced nucleation of martensite occurs predominantly at shear band intersections within austenite. The number of operational nucleation sites, N_m , is taken to be equal to the number of shear-band intersections per unit volume, N_I , multiplied by the probability, P , that a shear band intersection will act as a nucleation site. Therefore, \dot{N}_m is given as:

$$\dot{N}_m = P \dot{N}_I + N_I \dot{P} H(\dot{P}), \quad (6.51)$$

where $H(\dot{P})$ is the Heaviside step function, reflecting the fact that the transformation is irreversible. The N_I is defined as:

$$N_I = \frac{f_I}{\bar{v}_I} \quad (6.52)$$

where f_I is the volume fraction of shear-band intersections, and \bar{v}_I is the average volume of a shear-band intersection. The parameter f_I is assumed to be related to the volume fraction of austenite occupied by shear-bands, f_{sb} , through a power-law expression of the form:

$$f_I = C (f_{sb})^r \quad (6.53)$$

where C is a geometric constant, and the exponent r models the orientation of shear-bands ($r=2$ for random orientation, $r=4$ for initially parallel shear bands). Olson and Cohen pointed out that shear bands will not be randomly oriented, but will tend to be initially parallel until secondary shear systems begin to operate. Thus, the number of intersections is expected to be initially low and then increase more rapidly. This behavior can be approximated by a value for the exponent r greater than 2.

Consistent with available data for the special case where the shear bands consist of hcp ε -martensite, the remaining austenite volume fraction of shear-bands, f_{sb} , is taken to depend on plastic strain in the austenite:

$$\dot{f}_{sb} = (1 - f_{sb}) \alpha \dot{\varepsilon}^{p(a)} \quad (6.54)$$

Equation (6.54) is based on the assumption of a constant rate of shear-band production. The factor $(1 - f_{sb})$ accounts for the diminishing austenite volume available to produce new shear-bands and $\dot{\bar{\epsilon}}^{p(a)}$ is the rate of the equivalent plastic strain in austenite. The parameter α represents the rate of shear band formation at low strains. It is dependent upon stacking fault energy, and since lower levels of stacking-fault energy promote shear-band deformation modes, α generally increases with decreasing stacking fault energy. The α -parameter is temperature dependent through the variation of stacking fault energy with temperature.

Integrating equation (6.54) under isothermal conditions we obtain:

$$f_{sb}(\bar{\epsilon}^{p(a)}) = 1 - e^{-\alpha \bar{\epsilon}^{p(a)}} \quad (6.55)$$

Substituting for f_{sb} in equation (6.53) and using (6.52) we obtain for N_I :

$$N_I = \frac{C}{\bar{v}_I} \left(1 - e^{-\alpha \bar{\epsilon}^{p(a)}}\right)^r \quad (6.56)$$

and differentiating:

$$\dot{N}_I = \frac{\alpha r C}{\bar{v}_I} e^{-\alpha \bar{\epsilon}^{p(a)}} \left(1 - e^{-\alpha \bar{\epsilon}^{p(a)}}\right)^{r-1} \dot{\bar{\epsilon}}^{p(a)} \quad (6.57)$$

or using equation (6.55):

$$\dot{N}_I = \frac{\alpha r C}{\bar{v}_I} (1 - f_{sb})(f_{sb})^{r-1} \dot{\bar{\epsilon}}^{p(a)} \quad (6.58)$$

Consistent with available strain-induced transformation kinetics data, the probability parameter, P , is determined assuming that there exists a Gaussian distribution of shear band intersection potencies (where ‘‘potency’’ is defined to be the minimum thermodynamic driving force at which a given nucleation site can be activated). Therefore, P is determined by a cumulative probability distribution function:

$$P(g) = \frac{1}{\sqrt{2\pi} s_g} \int_{-\infty}^g \exp\left[-\frac{1}{2} \left(\frac{g' - \bar{g}}{s_g}\right)^2\right] dg' \quad (6.59)$$

where \bar{g} and s_g are the dimensionless mean and the standard deviation of the probability distribution function. A method for the numerical calculation of the integral in (6.59) is presented in Appendix B. The probability, P , is taken to be a function of temperature and stress state through the argument of the distribution function g . The parameter g is a normalized net thermodynamic driving force, defined as:

$$g(\Theta, \Sigma) = g_0 - g_1 \Theta + g_2 \Sigma \quad (6.60)$$

where g_0 , g_1 and g_2 are dimensionless non-negative constants and Θ is a normalized temperature which is related to the absolute temperature T according to:

$$\Theta(T) = \frac{T - M_{s,ut}^{\sigma}}{M_{d,ut} - M_{s,ut}^{\sigma}} \quad (6.61)$$

where $M_{d,ut}$, $M_{s,ut}^{\sigma}$ are the absolute M_d (where no transformation is observed), M_s^{σ} (where strain-induced transformation is first observed) temperatures for uniaxial tension. The parameter Σ represents the ratio of the volumetric (pressure $p = \sigma_{kk}/3$) to the deviatoric stress invariants (equivalent stress σ_{eq}) and is a measure of the ‘‘triaxiality’’ of the stress state:

$$\Sigma = \frac{p}{\sigma_{eq}} \quad (6.62)$$

The rate of change of the probability function \dot{P} under isothermal conditions ($\dot{\Theta} = 0$) is given by the form:

$$\dot{P} = \frac{g_2}{\sqrt{2\pi} s_g} \exp\left[-\frac{1}{2}\left(\frac{g - \bar{g}}{s_g}\right)^2\right] \dot{\Sigma} \quad (6.63)$$

We differentiate Σ from equation (6.62):

$$\dot{\Sigma} = \Sigma \left(\frac{\dot{p}}{p} - \frac{\dot{\sigma}_{eq}}{\sigma_{eq}} \right) \quad (6.64)$$

The proposed kinetic model for the evolution of martensitic volume fraction, f , is obtained by substituting \dot{N}_m in equations (6.50) using (6.51), (6.58) and (6.59):

$$\dot{f} = c^{(a)} \left(A_f \dot{\bar{\epsilon}}^{p(a)} + B_f \dot{\Sigma} \right) \quad (6.65)$$

The coefficients A_f, B_f are functions of stress state and plastic strain for constant temperature:

$$A_f \left(\bar{\epsilon}^{p(a)}, \Sigma, T \right) = \alpha \beta_0 r (1 - f_{sb}) (f_{sb})^{r-1} P, \quad (6.66)$$

$$\text{with } \beta_0 = C \bar{v}_m / \bar{v}_l, \quad P = P(g(\Sigma, T)), \quad f_{sb} = f_{sb}(\bar{\epsilon}^{p(a)}) \quad (6.67)$$

$$B_f \left(\bar{\epsilon}^{p(a)}, \Sigma, T \right) = \frac{g_2}{\sqrt{2\pi} s_g} \beta_0 (f_{sb})^r \exp\left[-\frac{1}{2}\left(\frac{g - \bar{g}}{s_g}\right)^2\right] \quad \text{if } \dot{\Sigma} > 0 \quad (6.68)$$

$$B_f = 0 \quad \text{if } \dot{\Sigma} \leq 0 \quad (6.69)$$

6.3.3.2 Remarks on the transformation kinetics model

In the model presented the evolution of martensite due to martensitic transformation is viewed as a function of temperature, plastic strain and stress state. Temperature affects both the number of shear-band intersections produced, through the rate of shear band formation $a(T)$, and the probability of nucleation P , through equation (6.60) for g . Furthermore, plastic strain affects only the number of intersections, through (6.55) and stress state affects only the probability function, through (6.60). The thermodynamic driving force variable g of the probability function is a critical parameter determining the extent of transformation under different conditions. It decreases with increasing temperature but increases with increasing triaxiality. Thus, at fixed temperature, as the triaxiality increases, so does the probability that martensite will nucleate at a potential site. Figure 6.4 depicts P and \dot{P} as functions of g and the dependence of P on temperature and stress state. The variation of P with stress is seen as one of the most important features of the transformation.

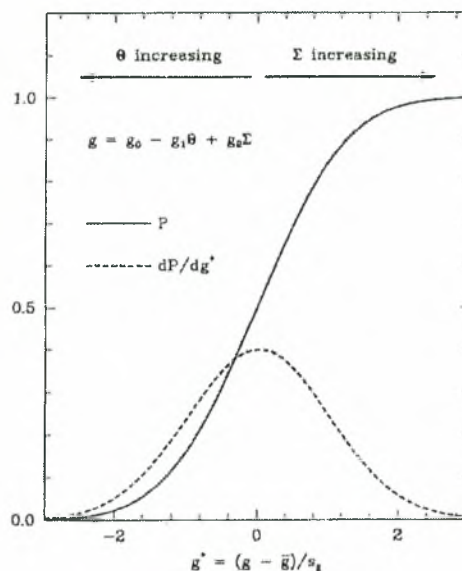


Figure 6.4: Probability function P and its derivative with respect to a normalized driving force, $(g - \bar{g})/s_g$, illustrating the effect of normalized temperature Θ and triaxiality Σ on the driving force for transformation. Figure taken from Stringfellow *et al.* (1992).

After thermal treatment, a four-phase TRIP steel obtains a substructure consisting of a dispersion of retained austenite islands and bainite in a ferritic matrix. The dispersed islands of retained austenite transform, with straining, into martensite leading to a substructure of martensitic islands dispersed in the matrix of TRIP steel. It is believed, that the transformation

of the dispersed austenitic islands affects the kinetics behavior and creates the need of the implementation of the grain size of the initially austenitic islands as an important parameter to the model.

Transformation can occur by two distinct mechanisms, i.e. stress-assisted and strain-induced transformation of retained austenite to martensite. The stress-assisted mechanism dominates at stresses lower than the yield strength of the retained austenite, whereas the strain-induced mechanism prevails after the yield strength has been surpassed. Experiments show that, in uniaxial tension, some amount of martensite appears before yielding takes place originating from the stress-assisted transformation. In order to account for this effect since our model considers strain-induced transformation only, we modify the initial values of f considering that they have a value different from zero.

6.4 Evolution of volume fraction of phases in two-phase TRIP steels

The two-phase composite consists of retained austenite and martensite. As stated earlier, the volume fraction of a phase is defined as the ratio of its volume to the total volume of the composite. The volume fraction of retained austenite is denoted by $c^{(2)}$ or $c^{(a)}$ while the martensitic volume fraction is denoted by $c^{(1)}$ or f :

$$f = c^{(1)} = \frac{V^{(m)}}{V} \quad (6.70)$$

$$c^{(a)} = c^{(2)} = 1 - f = \frac{V^{(a)}}{V} \quad (6.71)$$

Note that

$$V = V^{(m)} + V^{(a)} \quad \Rightarrow \quad f + c^{(a)} = 1 \quad (6.72)$$

and

$$\dot{f} + \dot{c}^{(a)} = 0 \quad (6.73)$$

Summarizing, we note that the evolution equations for the volume fractions of the individual phases are given by:

$$\text{Martensite:} \quad \dot{f} = c^{(a)} \left(A_f \dot{\varepsilon}^{p(a)} + B_f \dot{\Sigma} \right) \quad (6.74)$$

$$\text{Retained Austenite:} \quad (6.73) \Rightarrow \quad \dot{c}^{(a)} = -\dot{f} \quad (6.75)$$

6.5 Evolution of volume fraction of phases in four-phase TRIP steels

The four-phase TRIP steel we examine is considered as a composite material with a ferritic matrix containing bainite and retained austenite, which gradually transforms into martensite. We denote the volume fractions of martensite, austenite, bainite and ferrite with f , $c^{(a)}$, $c^{(3)}$, $c^{(4)}$ respectively and the correspondent volumes with $V^{(m)}$, $V^{(a)}$, $V^{(3)}$, $V^{(4)}$. From the relation between the volumes we obtain a relation for the volume fractions f , $c^{(a)}$, $c^{(3)}$, $c^{(4)}$:

$$V = V^{(m)} + V^{(a)} + V^{(3)} + V^{(4)} \quad \Rightarrow \quad f + c^{(a)} + c^{(3)} + c^{(4)} = 1 \quad (6.76)$$

and

$$\dot{f} + \dot{c}^{(a)} + \dot{c}^{(3)} + \dot{c}^{(4)} = 0 \quad (6.77)$$

Taking into account that $\frac{\dot{V}}{V} = \dot{\varepsilon}_v^p \cong \Delta_v \dot{f}$, we determine the evolution of the volume fraction of the phases as follows:

$$\text{Martensite:} \quad \dot{f} = c^{(a)} \left(A_f \dot{\varepsilon}^{p(a)} + B_f \dot{\Sigma} \right) \quad (6.78)$$

$$\text{Bainite:} \quad c^{(3)} = \frac{V^{(3)}}{V} \quad \Rightarrow \quad \dot{c}^{(3)} = -c^{(3)} \frac{\dot{V}}{V} \cong -c^{(3)} \Delta_v \dot{f} \quad (6.79)$$

$$\text{Ferrite:} \quad c^{(4)} = \frac{V^{(4)}}{V} \quad \Rightarrow \quad \dot{c}^{(4)} = -c^{(4)} \frac{\dot{V}}{V} \cong -c^{(4)} \Delta_v \dot{f} \quad (6.80)$$

$$\text{Retained Austenite:} \quad (6.77) \Rightarrow \dot{c}^{(a)} = -(\dot{f} + \dot{c}^{(3)} + \dot{c}^{(4)}) \cong -\left[1 - (c^{(3)} + c^{(4)})\right] \Delta_v \dot{f} \quad (6.81)$$

Summarizing, we note that the evolution equations for the volume fractions of the individual phases are given by:

$$\text{Martensite:} \quad \dot{f} = c^{(a)} \left(A_f \dot{\varepsilon}^{p(a)} + B_f \dot{\Sigma} \right) \quad (6.82)$$

$$\text{Retained Austenite:} \quad \dot{c}^{(a)} = -\left[1 - (c^{(3)} + c^{(4)})\right] \Delta_v \dot{f} \quad (6.83)$$

$$\text{Bainite:} \quad \dot{c}^{(3)} = -c^{(3)} \Delta_v \dot{f} \quad (6.84)$$

$$\text{Ferrite:} \quad \dot{c}^{(4)} = -c^{(4)} \Delta_v \dot{f} \quad (6.85)$$

6.6 Summary of Constitutive equations

The final form of the constitutive model that describes the mechanical behavior of TRIP steels consists of a system of equations accounting for both the cases of steels we examine (two-phase steel with $r = 1, 2$ and four-phase steel with $r = 1, 2, 3, 4$):

$$\text{Constitutive Formulation:} \quad \mathbf{D} = \mathbf{D}^e + \mathbf{D}^p + \mathbf{D}^{TRIP} \quad (6.86)$$

$$\text{Elastic behavior:} \quad \overset{\nabla}{\boldsymbol{\sigma}} = \mathbf{L}^e : \mathbf{D}^e \quad (6.87)$$

$$\text{Plastic Strain of the composite:} \quad \mathbf{D}^p = \dot{\bar{\boldsymbol{\varepsilon}}}^p \mathbf{N}, \quad \dot{\bar{\boldsymbol{\varepsilon}}}^p = \frac{1}{3} \sigma_{eq} \theta^{\text{hom}}(\sigma_{eq}) \quad (6.88)$$

$$\text{Plastic Strain of the phases:} \quad \mathbf{D}^{p(r)} = \dot{\bar{\boldsymbol{\varepsilon}}}^{p(r)} \mathbf{N}^{(r)}, \quad \dot{\bar{\boldsymbol{\varepsilon}}}^{p(r)} = \dot{\bar{\boldsymbol{\varepsilon}}}_o^{(r)} \left[\frac{\sigma_{eq}^{(r)}}{\sigma_y^{(r)}(\bar{\boldsymbol{\varepsilon}}^{p(r)})} \right]^m \quad (6.89)$$

$$\text{Transformation Deformation rate:} \quad \mathbf{D}^{TRIP} = \left[A(\sigma_{eq}) \mathbf{N} + \frac{1}{3} A_v \boldsymbol{\delta} \right] \dot{f} \quad (6.90)$$

The constitutive model is completed with the evolution equations of the volume fractions, which take the following form

Two-phase TRIP steel

$$\text{Martensite:} \quad \dot{f} = c^{(a)} \left(A_f \dot{\bar{\boldsymbol{\varepsilon}}}^{p(a)} + B_f \dot{\Sigma} \right) \quad (6.91)$$

$$\text{Retained Austenite:} \quad \dot{c}^{(a)} = -\dot{f} \quad (6.92)$$

For the case of the four-phase composite the constitutive equations are:

Four-phase TRIP steel

$$\text{Martensite:} \quad \dot{f} = c^{(a)} \left(A_f \dot{\bar{\boldsymbol{\varepsilon}}}^{p(a)} + B_f \dot{\Sigma} \right) \quad (6.93)$$

$$\text{Retained Austenite:} \quad \dot{c}^{(a)} = -\left[1 - (c^{(3)} + c^{(4)}) A_v \right] \dot{f} \quad (6.94)$$

$$\text{Bainite:} \quad \dot{c}^{(3)} = -c^{(3)} A_v \dot{f} \quad (6.95)$$

$$\text{Ferrite:} \quad \dot{c}^{(4)} = -c^{(4)} A_v \dot{f} \quad (6.96)$$

We note also that equations (6.86), (6.88) and (6.90) can be written also as

$$\mathbf{D} = \mathbf{D}^e + \mathbf{D}^{in} \quad (6.97)$$

$$\mathbf{D}^{in} = \mathbf{D}^p + \mathbf{D}^{TRIP} = \frac{1}{3} \dot{\bar{\boldsymbol{\varepsilon}}}_v^p \boldsymbol{\delta} + \dot{\bar{\boldsymbol{\varepsilon}}}_q \mathbf{N}, \quad \mathbf{N} = \frac{3}{2 \sigma_{eq}} \mathbf{s} \quad (6.98)$$

where

$$\dot{\bar{\boldsymbol{\varepsilon}}}_v^p = A_v \dot{f} \quad \text{and} \quad \dot{\bar{\boldsymbol{\varepsilon}}}_q = \frac{1}{3} \sigma_{eq} \theta^{\text{hom}}(\sigma_{eq}) + A(\sigma_{eq}) \dot{f} \quad (6.99)$$

We conclude this section with an alternative presentation of the constitutive model. We note that

$$\begin{aligned} \mathbf{D}^e &= \mathbf{M}^e : \overset{\nabla}{\boldsymbol{\sigma}} \\ \mathbf{D}^p &= \dot{\boldsymbol{\varepsilon}}^p(\sigma_{eq}) \mathbf{N} \\ \mathbf{D}^{TRIP} &= \dot{f} \left(A\mathbf{N} + \frac{1}{3} \Delta_v \boldsymbol{\delta} \right) = c^{(a)} \left(A_f \dot{\boldsymbol{\varepsilon}}^{p(a)} + B_f \dot{\Sigma} \right) \left(A\mathbf{N} + \frac{1}{3} \Delta_v \boldsymbol{\delta} \right) = \mathbf{S} + \mathbf{T} \dot{\Sigma} \end{aligned} \quad (6.100)$$

where

$$\mathbf{S}(\boldsymbol{\sigma}) = c^{(a)} A_f \dot{\boldsymbol{\varepsilon}}^{p(a)} \left(A\mathbf{N} + \frac{1}{3} \Delta_v \boldsymbol{\delta} \right), \quad \mathbf{T}(\boldsymbol{\sigma}) = c^{(a)} B_f \left(A\mathbf{N} + \frac{1}{3} \Delta_v \boldsymbol{\delta} \right).$$

Now

$$\Sigma = \frac{p}{\sigma_{eq}} \quad \Rightarrow \quad \dot{\Sigma} = \frac{\dot{p}}{\sigma_{eq}} - \frac{p}{\sigma_{eq}^2} \dot{\sigma}_{eq} = \frac{\boldsymbol{\delta} : \overset{\nabla}{\boldsymbol{\sigma}}}{\sigma_{eq}} - \frac{\Sigma}{\sigma_{eq}} \mathbf{N} : \overset{\nabla}{\boldsymbol{\sigma}} = \frac{1}{\sigma_{eq}} (\boldsymbol{\delta} - \Sigma \mathbf{N}) : \overset{\nabla}{\boldsymbol{\sigma}}.$$

Therefore, (6.100) can be written as

$$\mathbf{D}^{TRIP} = \mathbf{S} + \frac{1}{\sigma_{eq}} \mathbf{T} (\boldsymbol{\delta} - \Sigma \mathbf{N}) : \overset{\nabla}{\boldsymbol{\sigma}}.$$

Finally, $\mathbf{D} = \mathbf{D}^e + \mathbf{D}^p + \mathbf{D}^{TRIP} \Rightarrow$

$$\boxed{\mathbf{D} = \mathbf{M} : \overset{\nabla}{\boldsymbol{\sigma}} + \mathbf{Q}} \quad \text{or} \quad \boxed{\overset{\nabla}{\boldsymbol{\sigma}} = \mathbf{L} : \mathbf{D} + \mathbf{P}} \quad (6.101)$$

where

$$\mathbf{M} = \mathbf{M}^e + \frac{1}{\sigma_{eq}} \mathbf{T} (\boldsymbol{\delta} - \Sigma \mathbf{N}), \quad \mathbf{Q}(\boldsymbol{\sigma}) = \dot{\boldsymbol{\varepsilon}}^p \mathbf{N} + \mathbf{S}, \quad \text{and} \quad \mathbf{L} = \mathbf{M}^{-1}, \quad \mathbf{P}(\boldsymbol{\sigma}) = -\mathbf{M}^{-1} : \mathbf{Q}.$$

The quantity \mathbf{P} on the right hand side of (6.101) is an “initial stress”-type term that arises in the constitutive equations of rate-dependent solids.

CHAPTER SEVEN

COMPUTATIONAL ISSUES - IMPLEMENTATION INTO FEM

7.1 Introduction

In this chapter, a methodology for the numerical integration of the resulting non-linear constitutive equations for TRIP steels in the context of the finite element method is presented. The implementation of the constitutive model in a finite element program and the procedure of solving the problem with finite elements in the context of finite strains are presented.

7.2 Numerical Integration of the Constitutive Equations

In a finite element environment, the solution is developed incrementally and the constitutive equations are integrated numerically at the element Gauss integration points. In a displacement based finite element formulation the solution is deformation driven. Let \mathbf{F} denote the deformation gradient tensor. At a given Gauss point, the solution $(\mathbf{F}_n, \boldsymbol{\sigma}_n, c_n^{(r)})$ at time t_n as well as the deformation gradient \mathbf{F}_{n+1} at time $t_{n+1} = t_n + \Delta t$ are known and the problem is to determine $(\boldsymbol{\sigma}_{n+1}, c_{n+1}^{(r)})$.

The time variation of the deformation gradient \mathbf{F} during the time increment $[t_n, t_{n+1}]$ can be written as:

$$\mathbf{F}(t) = \Delta\mathbf{F}(t) \cdot \mathbf{F}_n = \mathbf{R}(t) \cdot \mathbf{U}(t) \cdot \mathbf{F}_n, \quad t_n \leq t \leq t_{n+1} \quad (7.1)$$

where $\mathbf{R}(t)$ and $\mathbf{U}(t)$ are the rotation and right stretch tensors associated with $\Delta\mathbf{F}(t)$. The corresponding deformation rate $\mathbf{D}(t)$ tensor can be written as:

$$\mathbf{D}(t) \equiv [\dot{\mathbf{F}}(t) \cdot \mathbf{F}^{-1}(t)]_s = [\Delta\dot{\mathbf{F}}(t) \cdot \Delta\mathbf{F}^{-1}(t)]_s \quad (7.2)$$

where the subscripts s and a denote the symmetric and antisymmetric parts respectively of a tensor.

If it is assumed that the Lagrangian triad associated with $\Delta\mathbf{F}(t)$ (i.e. the eigenvectors of $\mathbf{U}(t)$) remains fixed in the time interval $[t_n, t_{n+1}]$, it can readily be shown that:

$$\mathbf{D}(t) = \mathbf{R}(t) \cdot \dot{\mathbf{E}}(t) \cdot \mathbf{R}^T(t), \quad \mathbf{W}(t) = \dot{\mathbf{R}}(t) \cdot \mathbf{R}^T(t) \quad (7.3)$$

and

$$\overset{\nabla}{\boldsymbol{\sigma}}(t) = \mathbf{R}(t) \cdot \dot{\hat{\boldsymbol{\sigma}}}(t) \cdot \mathbf{R}^T(t) \quad (7.4)$$

where $\mathbf{E}(t) = \ln \mathbf{U}(t)$ is the logarithmic strain associated with the increment, and

$$\hat{\boldsymbol{\sigma}}(t) = \mathbf{R}^T(t) \cdot \boldsymbol{\sigma}(t) \cdot \mathbf{R}(t) \quad (7.5)$$

It is noted that at the start of the increment ($t = t_n$):



$$\Delta \mathbf{F}_n = \mathbf{R}_n = \mathbf{U}_n = \delta, \quad \hat{\boldsymbol{\sigma}}_n = \boldsymbol{\sigma}_n \quad \text{and} \quad \mathbf{E}_n = \mathbf{0} \quad (7.6)$$

whereas at the end of the increment ($t = t_{n+1}$):

$$\Delta \mathbf{F}_{n+1} = \mathbf{F}_{n+1} \cdot \mathbf{F}_n^{-1} = \mathbf{R}_{n+1} \cdot \mathbf{U}_{n+1} = \text{known} \quad \mathbf{E}_{n+1} = \ln \mathbf{U}_{n+1} = \text{known} \quad (7.7)$$

The constitutive equations accounting for both the cases of steels we examine (two-phase steel with $r = 1, 2$ and four-phase steel with $r = 1, 2, 3, 4$) can be written in the form:

$$\mathbf{D} = \mathbf{D}^e + \mathbf{D}^{in} \quad \Rightarrow \quad \dot{\mathbf{E}} = \dot{\mathbf{E}}^e + \dot{\mathbf{E}}^{in} \quad (7.8)$$

$$\overset{\vee}{\boldsymbol{\sigma}} = \mathbf{L}^e : \mathbf{D}^e \quad \Rightarrow \quad \dot{\hat{\boldsymbol{\sigma}}} = \mathbf{L}^e : \dot{\mathbf{E}}^e \quad (7.9)$$

$$\mathbf{D}^{in} = \frac{1}{3} \dot{\varepsilon}_v^p \delta + \dot{\varepsilon}_q \mathbf{N} \quad \Rightarrow \quad \dot{\mathbf{E}}^{in} = \frac{1}{3} \dot{\varepsilon}_v^p \delta + \dot{\varepsilon}_q \hat{\mathbf{N}} \quad (7.10)$$

$$\text{with} \quad \hat{\mathbf{N}} = \frac{3}{2\sigma_{eq}} \hat{\mathbf{s}}, \quad \dot{\varepsilon}_v^p = \Delta_v \dot{f}, \quad \dot{\varepsilon}_q = \frac{1}{3} \sigma_{eq} \theta^{\text{hom}}(\sigma_{eq}) + A(\sigma_{eq}) \dot{f} \quad (7.11)$$

For the four-phase composite the constitutive equations accounting for the volume fractions of the individual phases can be written in the form:

$$\dot{f} = c^{(a)} \left(A_f \dot{\bar{\varepsilon}}^{p(a)} + B_f \dot{\Sigma} \right) \quad (7.12)$$

$$\dot{c}^{(a)} \cong - \left[1 - (c^{(3)} + c^{(4)}) \Delta_v \right] \dot{f} \quad (7.13)$$

$$\dot{c}^{(3)} = -c^{(3)} \Delta_v \dot{f} \quad (7.14)$$

$$\dot{c}^{(4)} = -c^{(4)} \Delta_v \dot{f} \quad (7.15)$$

and for the two-phase composite:

$$\dot{f} = c^{(a)} \left(A_f \dot{\bar{\varepsilon}}^{p(a)} + B_f \dot{\Sigma} \right) \quad (7.16)$$

$$\dot{c}^{(a)} = -\dot{f} \quad (7.17)$$

As discussed in Chapter 6, A_f and B_f depend on $(\bar{\varepsilon}^{p(a)}, \Sigma, T)$.

The transformed constitutive equations (7.8) to (7.17) are similar to those of the usual “small strain” formulations in the sense that there are no co-rotational rates involved.

7.2.1 Four-phase TRIP Steel

It is interesting to note that equations (7.10) that defines the inelastic deformation rate $\dot{\mathbf{E}}^{in}$ and (7.12) that defines the evolution of f require numerical integration. The rest of the equations can be integrated exactly as follows:

$$(7.8) \quad \Rightarrow \quad \Delta \mathbf{E} = \Delta \mathbf{E}^e + \Delta \mathbf{E}^{in} \quad \Rightarrow \quad \Delta \mathbf{E}^e = \Delta \mathbf{E} - \Delta \mathbf{E}^{in} \quad (7.18)$$

$$(7.9) \Rightarrow \hat{\boldsymbol{\sigma}}_{n+1} = \boldsymbol{\sigma}_n + \mathbf{L}^e : \Delta \mathbf{E}^e = \boldsymbol{\sigma}_n + \mathbf{L}^e : (\Delta \mathbf{E} - \Delta \mathbf{E}^{in}) = \hat{\boldsymbol{\sigma}}^e - \mathbf{L}^e : \Delta \mathbf{E}^{in} \quad (7.19)$$

$$(7.14) \Rightarrow c_{n+1}^{(3)} = c_n^{(3)} e^{-\Delta_v \Delta f} \quad (7.20)$$

$$(7.15) \Rightarrow c_{n+1}^{(4)} = c_n^{(4)} e^{-\Delta_v \Delta f} \quad (7.21)$$

$$(7.13) \Rightarrow c_{n+1}^{(a)} = 1 - (f_{n+1} + c_{n+1}^{(3)} + c_{n+1}^{(4)}) \quad (7.22)$$

where $\hat{\boldsymbol{\sigma}}^e = \boldsymbol{\sigma}_n + \mathbf{L}^e : \Delta \mathbf{E}$ known in (7.19) is the “elastic predictor” and the notation $\Delta A = A_{n+1} - A_n$ is used.

The remaining equations are

$$\dot{\mathbf{E}}^{in} = \frac{1}{3} \dot{\varepsilon}_v^p \hat{\boldsymbol{\delta}} + \dot{\varepsilon}_q \hat{\mathbf{N}}, \quad \hat{\mathbf{N}} = \frac{3}{2\sigma_{eq}} \hat{\mathbf{s}}, \quad \dot{\varepsilon}_v^p = \Delta_v \dot{f}, \quad \dot{\varepsilon}_q = \frac{1}{3} \sigma_{eq} \theta^{\text{hom}}(\sigma_{eq}) + A(\sigma_{eq}) \dot{f} \quad (7.23)$$

and

$$\dot{f} = c^{(a)} (A_f \dot{\bar{\varepsilon}}^{p(a)} + B_f \dot{\Sigma}) \quad (7.24)$$

where $A_f = A_f(\bar{\varepsilon}^{p(a)}, \Sigma, T)$ and $B_f = B_f(\bar{\varepsilon}^{p(a)}, \Sigma, T)$.

Previous experience (Aravas and Ponte Castañeda, 2004) shows that it is essential to use a backward Euler scheme for the numerical integration of the “plastic flow” equation (7.23) in order to be able to use increments of reasonable size (i.e., several times the flow strain), whereas either the forward or the backward Euler method can be used in (7.24).

In the following, we use two different ways for the integration of the aforementioned constitutive equations. In the first, we use the backward Euler method for the integration of both (7.23) and (7.24); in the second, the backward Euler method is used for the numerical integration of (7.23), and the forward Euler method for (7.24). As will be discussed later, the computational model of the latter case is simpler but less accurate.

7.2.1.1 Integration using the backward Euler method

We use an algorithm similar to that proposed by Aravas (1987) for the numerical integration of pressure-dependent plasticity models.

Equations (7.23) and (7.24) are integrated using the backward Euler scheme:

$$\Delta \mathbf{E}^{in} = \frac{1}{3} \Delta \varepsilon_v^p \boldsymbol{\delta} + \Delta \varepsilon_q \hat{\mathbf{N}}_{n+1}, \quad (7.25)$$

$$\text{with } \Delta \varepsilon_v^p = \Delta_v \Delta f \quad (7.26)$$

$$\Delta \varepsilon_q = \frac{1}{3} \sigma_{eq} \Big|_{n+1} \theta^{\text{hom}} \left(\sigma_{eq} \Big|_{n+1} \right) + A \left(\sigma_{eq} \Big|_{n+1} \right) \Delta f \quad (7.27)$$

$$\Delta f = c_{n+1}^{(a)} \left(A_f \Big|_{n+1} \dot{\varepsilon}_{n+1}^{p(a)} \Delta t + B_f \Big|_{n+1} \Delta \Sigma \right), \quad (7.28)$$

$$\Delta \Sigma = \Sigma_{n+1} - \Sigma_n = \left(\frac{p}{\sigma_{eq}} \right)_{n+1} - \left(\frac{p}{\sigma_{eq}} \right)_n \quad (7.29)$$

where $A_f = A_f(\bar{\varepsilon}^{p(a)}, \Sigma, T)$ and $B_f = B_f(\bar{\varepsilon}^{p(a)}, \Sigma, T)$, and $\theta_{n+1}^{\text{hom}}$ and $\dot{\varepsilon}_{n+1}^{p(a)}$ are determined in terms of $\sigma_{eq} \Big|_{n+1}$ and $c_{n+1}^{(r)}$ by using the homogenization technique described in Chapter 4.

Next, we substitute (7.25) in (7.19) and set $\mathbf{L}^e = 2\mu\mathbf{K} + 3\kappa\mathbf{J}$ to find

$$\hat{\boldsymbol{\sigma}}_{n+1} = \hat{\boldsymbol{\sigma}}^e - 2\mu \Delta \varepsilon_q \hat{\mathbf{N}}_{n+1} - \kappa \Delta \varepsilon_v^p \boldsymbol{\delta} \quad (7.30)$$

The deviatoric part of $\hat{\boldsymbol{\sigma}}_{n+1}$ is

$$\hat{\mathbf{s}}_{n+1} = \hat{\mathbf{s}}^e - 2\mu \Delta \varepsilon_q \hat{\mathbf{N}}_{n+1} \quad (7.31)$$

Then, we set $\hat{\mathbf{N}}_{n+1} = \frac{3}{2\sigma_{eq} \Big|_{n+1}} \hat{\mathbf{s}}_{n+1}$ to find

$$\hat{\mathbf{s}}_{n+1} = \hat{\mathbf{s}}^e - \frac{3\mu \Delta \varepsilon_q}{\sigma_{eq} \Big|_{n+1}} \hat{\mathbf{s}}_{n+1} \Rightarrow \hat{\mathbf{s}}_{n+1} = c \hat{\mathbf{s}}^e \quad \text{where } c = \frac{1}{1 + 3\Delta \varepsilon_q (\mu / \sigma_{eq} \Big|_{n+1})} \quad (7.32)$$

The last equation shows that $\hat{\mathbf{s}}_{n+1}$ and $\hat{\mathbf{s}}^e$ are co-linear. Therefore

$$\hat{\mathbf{N}}_{n+1} = \frac{3}{2\sigma_{eq} \Big|_{n+1}} \hat{\mathbf{s}}_{n+1} = \frac{3}{2} \frac{1}{\sqrt{\frac{3}{2} \hat{\mathbf{s}}_{n+1} : \hat{\mathbf{s}}_{n+1}}} \hat{\mathbf{s}}_{n+1} = \frac{3}{2} \frac{1}{\sqrt{\frac{3}{2} \hat{\mathbf{s}}^e : \hat{\mathbf{s}}^e}} \hat{\mathbf{s}}^e = \hat{\mathbf{N}}^e = \text{known}$$

Next, we project the stress tensor defined in (7.30) onto the deviatoric plane ($\sigma_{eq} = \hat{\boldsymbol{\sigma}} : \hat{\mathbf{N}} = \boldsymbol{\sigma} : \mathbf{N}$) and the pressure axis ($p = (1/3)\hat{\boldsymbol{\sigma}} : \boldsymbol{\delta} = (1/3)\boldsymbol{\sigma} : \boldsymbol{\delta}$) to find:

$$\sigma_{eq} \Big|_{n+1} = \sigma_{eq}^e - 3\mu \Delta \varepsilon_q \quad (7.33)$$

$$\text{and } p_{n+1} = p^e - \kappa \Delta \varepsilon_v^p \quad (7.34)$$

where μ , κ are the elastic shear and bulk modulus respectively and $\sigma_{eq}^e = \hat{\boldsymbol{\sigma}}^e : \hat{\mathbf{N}}^e$, $p^e = (1/3)\hat{\boldsymbol{\sigma}}^e : \boldsymbol{\delta}$ are the equivalent stress and the hydrostatic pressure of the elastic predictor tensor $\hat{\boldsymbol{\sigma}}^e$ respectively.

We choose $\Delta\varepsilon_q$ and Δf as the primary unknowns and treat (7.27) and (7.28) as the basic equations in which $\sigma_{eq}|_{n+1}$, p_{n+1} , $\Delta\varepsilon_v^p$, $c_{n+1}^{(3)}$, $c_{n+1}^{(4)}$ and $c_{n+1}^{(a)}$ are defined by equations (7.33), (7.34), (7.26), (7.20), (7.21) and (7.22). The numerical evaluation of the probability distribution function $P(g)$ defined in (6.59) is discussed in detail in Appendix A. Also, $\theta_{n+1}^{\text{hom}}$ and $\dot{\varepsilon}_{n+1}^{p(a)}$ are determined by using the homogenization technique described in Chapter 4. Newton's method is used for the solution of (7.27) and (7.28). It turns out that a good initial estimate for $\Delta\varepsilon_q$ and Δf is required for the Newton iterations to converge; the first estimate used in the iterations is the solution of the equations in which a backward Euler scheme is used in (7.23) and a forward Euler scheme in (7.24), as described in the following section.

Once $\Delta\varepsilon_q$ and Δf are found, $\sigma_{eq}|_{n+1}$, p_{n+1} , $\Delta\varepsilon_v^p$, $c_{n+1}^{(3)}$, $c_{n+1}^{(4)}$, $c_{n+1}^{(a)}$ and $\hat{\sigma}_{n+1}$ are determined from (7.33), (7.34), (7.26), (7.20), (7.21), (7.22), and (7.30). Finally, σ_{n+1} is computed from:

$$\sigma_{n+1} = \mathbf{R}_{n+1} \cdot \hat{\sigma}_{n+1} \cdot \mathbf{R}_{n+1}^T \quad (7.35)$$

which completes the integration process.

7.2.1.2 Integration using a combination of backward and the forward Euler schemes

We use now the forward Euler scheme for the numerical integration of (7.24):

$$\Delta f = c_n^{(a)} \left(A_f \Big|_n \dot{\varepsilon}_n^{p(a)} \Delta t + B_f \Big|_n \Delta \Sigma \right) \quad (7.36)$$

with

$$\Delta \Sigma = \Sigma_{n+1} - \Sigma_n = \left(\frac{P}{\sigma_{eq}} \right)_{n+1} - \left(\frac{P}{\sigma_{eq}} \right)_n \quad (7.37)$$

Note that Δf cannot be determined from the known quantities at the start of the increment alone, since $\Delta \Sigma$ depends on the stress state at the end of the increment.

We choose $\Delta\varepsilon_q$ as the primary unknown and treat (7.27) as the basic equation for its determination:

$$\Delta\varepsilon_q = \frac{1}{3} \sigma_{eq}|_{n+1} \theta_{n+1}^{\text{hom}} \Delta t + A \left(\sigma_{eq}|_{n+1} \right) \Delta f \quad (7.38)$$

The solution procedure is similar to that described in the previous section, where now Δf is defined by equation (7.36). Newton's method is used for the solution of (7.38). the first estimate for $\Delta\varepsilon_q$ in the Newton iterations is determined as follows:

$$\Delta\varepsilon_q|_{\text{guess}} = \frac{1}{3} \sigma_{eq}|_n \theta_n^{\text{hom}} \Delta t + A \left(\sigma_{eq}|_n \right) \Delta f|_{\text{guess}} \quad (7.39)$$

with
$$\Delta f|_n^{guess} = c_n^{(a)} A_f|_n \dot{\bar{\varepsilon}}_n^{p(a)} \Delta t \quad (7.40)$$

7.2.2 Two-phase TRIP steels

For the integration of the constitutive equations accounting for the two-phase TRIP steel, we use the backward Euler method. The resulting system of equations is similar to of the four-phase TRIP steel, with a smaller number of evolution equations for the volume fractions of the constituent phases. The non-linear system equations with unknowns Δf and $\Delta \varepsilon_q$ is

$$\Delta f = c_{n+1}^{(a)} \left(A_f|_{n+1} \Delta \bar{\varepsilon}_{n+1}^{p(a)} + B_f|_{n+1} \Delta \Sigma \right) \quad (7.41)$$

$$\Delta \varepsilon_q = \frac{1}{3} \sigma_{eq}|_{n+1} \theta_{n+1}^{hom} \Delta t + A \left(\sigma_{eq}|_{n+1} \right) \Delta f \quad (7.42)$$

The volume fraction of austenite $c_{n+1}^{(a)}$ is given by:

$$c_{n+1}^{(a)} = 1 - f_{n+1} \quad (7.43)$$

A solution method similar to that of the four-phase steel is used.

7.3 The linearization moduli

As will be discussed in section 7.7 that follows the so-called “linearization moduli” are required, when the finite element method is used for the solution to the problem. They are defined as

$$\hat{\mathbf{C}} = \frac{\partial \hat{\boldsymbol{\sigma}}_{n+1}}{\partial \mathbf{E}_{n+1}} \quad (7.44)$$

In general, $\hat{\mathbf{C}}$ depends on both the constitutive model **and** the algorithm used for the numerical integration of the constitutive equations. The derivation of $\hat{\mathbf{C}}$ is presented in Appendix C, where it is shown that $\hat{\mathbf{C}}$ is of the form

$$\hat{\mathbf{C}} = \frac{\partial \hat{\boldsymbol{\sigma}}_{n+1}}{\partial \mathbf{E}_{n+1}} = \mathbf{L}^\varepsilon - g_1 \mathbf{K} + g_2 \hat{\mathbf{N}} \hat{\mathbf{N}} - g_3 \hat{\mathbf{N}} \hat{\boldsymbol{\delta}} - g_4 \hat{\boldsymbol{\delta}} \hat{\mathbf{N}} - g_5 \hat{\boldsymbol{\delta}} \hat{\boldsymbol{\delta}} \quad (7.45)$$

where g_1 , g_2 , g_3 , g_4 and g_5 are constants.

We also calculate for later use the quantity \mathbf{C} defined as $C_{ijkl} = R_{im} R_{jn} R_{kp} R_{lq} \hat{C}_{mnpq}$:

$$\mathbf{C} = \mathbf{L}^\varepsilon - g_1 \mathbf{K} + g_2 \mathbf{N} \mathbf{N} - g_3 \mathbf{N} \boldsymbol{\delta} - g_4 \boldsymbol{\delta} \mathbf{N} - g_5 \boldsymbol{\delta} \boldsymbol{\delta} \quad (7.46)$$

7.4 The role of UMAT (User MATerial subroutine)

The constitutive model for TRIP steels is implemented into the ABAQUS general purpose finite element code. This code provides a general interface so that a particular constitutive model can be introduced via a “user subroutine” named UMAT (User MATerial).

The subroutine UMAT passes in all the information at the start of the increment, i.e., \mathbf{F}_n , $\boldsymbol{\sigma}_n$, $c_n^{(r)}$, $\bar{\varepsilon}_n^{p(r)}$, as well as \mathbf{F}_{n+1} , and the user has to calculate the values of the corresponding quantities at the end of the increment, i.e., $\boldsymbol{\sigma}_{n+1}$, $c_{n+1}^{(r)}$, and $\bar{\varepsilon}_n^{p(r)}$.

In addition, the so-called “linearization moduli” should be calculated in UMAT.

7.5 Integral formulation of the problem – The “weak” solution

In this section we present a brief description of the finite element formulation of the problem. We consider the spatial configuration of a general deformable body of initial volume V_0 at time $t=0$. At time t the body is deformed to a volume V surrounded by a surface S as shown in Figure 7.3. The body is loaded by body forces \mathbf{b} per unit mass and traction forces \mathbf{T} per unit area on the part S_σ of S , and imposed displacements $\hat{\mathbf{u}}$ on the remainder of S_u of S .

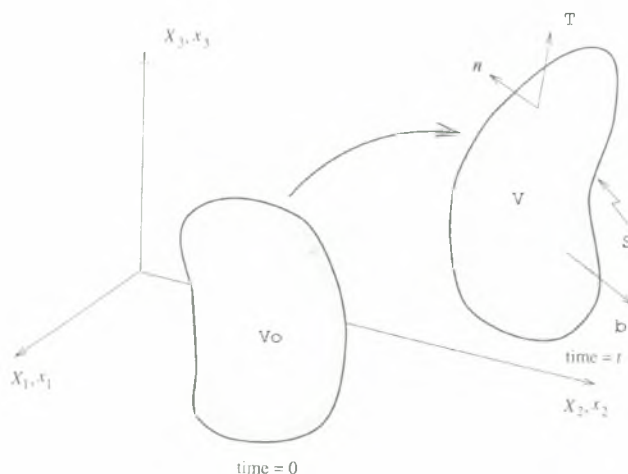


Figure 7.1: Body deformation

The equations of equilibrium are

$$\frac{\partial \sigma_{ij}}{\partial x_j} + \rho b_i = 0 \quad (7.47)$$

where σ_{ij} is the Cauchy stress tensor, and ρ is the mass density. The problem is completed by the kinematical relationships

$$D_{ij} = \frac{1}{2} \left(\frac{\partial v_i}{\partial x_j} + \frac{\partial v_j}{\partial x_i} \right) \quad (7.48)$$

where \mathbf{v} is the velocity field, and the constitutive equations as defined in Chapter 6.

We consider that the displacement vector \mathbf{u} is known on part of the boundary S_u :

$$\mathbf{u} = \hat{\mathbf{u}} \equiv \text{known on } S_u \quad (7.49)$$

On the remaining boundary S_σ the applied tractions are known:

$$\mathbf{n} \cdot \boldsymbol{\sigma} = \mathbf{T} \equiv \text{known on } S_\sigma \quad (7.50)$$

The problem can be formulated in an integral form as follows:

Find a displacement field $\mathbf{u}(\mathbf{x})$ such that $\mathbf{u} = \hat{\mathbf{u}}$ on S_u and

$$\int_V \left[\frac{\partial \sigma_{ij}(\mathbf{u})}{\partial x_j} + \rho b_i \right] v_i^* dV + \int_{S_\sigma} [T_i - n_j \sigma_{ij}(\mathbf{u})] v_i^* dS = 0 \quad (7.51)$$

for all continuous and differentiable fields $\mathbf{v}^*(\mathbf{x})$ that satisfy the condition $\mathbf{v}^* = \mathbf{0}$ on S_u . The stress field $\boldsymbol{\sigma}(\mathbf{u})$ is determined for given \mathbf{u} via the constitutive equations.

Using Green's theorem in (7.51) we reach the alternative formulation:

Find a displacement field $\mathbf{u}(\mathbf{x})$ such that $\mathbf{u} = \hat{\mathbf{u}}$ on S_u and

$$G(\mathbf{u}(\mathbf{x})) \equiv \int_V \boldsymbol{\sigma}(\mathbf{u}(\mathbf{x})) : \mathbf{D}^* dV - \int_V \rho \mathbf{b} \cdot \mathbf{v}^* dV - \int_S \mathbf{T} \cdot \mathbf{v}^* dS = 0 \quad (7.52)$$

for all continuous and differentiable fields $\mathbf{v}^*(\mathbf{x})$ that satisfy the condition $\mathbf{v}^* = \mathbf{0}$ on S_u . In the above equation

$$D_{ij}^* = \frac{1}{2} \left(\frac{\partial v_i^*}{\partial x_j} + \frac{\partial v_j^*}{\partial x_i} \right) \quad (7.53)$$

The vanishing of the non-linear functional $G(\mathbf{u})$ for all "virtual" velocity fields $\mathbf{v}^*(\mathbf{x})$ defines the "weak" solution $\mathbf{u}(\mathbf{x})$ of the problem.

The integral statement (7.52) provides the basis for the finite element formulation as described in the following section.

We conclude this section mentioning that, in view of the symmetry of $\boldsymbol{\sigma}$, equation (7.52) can be written as

$$G(\mathbf{u}(\mathbf{x})) \equiv \int_V \boldsymbol{\sigma}(\mathbf{u}(\mathbf{x})) : \mathbf{L}^* dV - \int_V \rho \mathbf{b} \cdot \mathbf{v}^* dV - \int_S \mathbf{T} \cdot \mathbf{v}^* dS = 0 \quad (7.54)$$

where

$$L_{ij}^* = \frac{\partial v_i^*}{\partial x_j} \quad (7.55)$$

7.6 Finite element formulation

In a finite element setting, the problem is solved incrementally and the primary unknown is the displacement increment $\Delta \mathbf{u}(\mathbf{x})$ that defines the position of the body at the end of the increment:

$$\mathbf{u}_{n+1}(\mathbf{x}) = \mathbf{u}_n(\mathbf{x}) + \Delta \mathbf{u}(\mathbf{x}), \quad \mathbf{x}_{n+1}(\mathbf{x}) = \mathbf{x}_n(\mathbf{x}) + \Delta \mathbf{u}(\mathbf{x}) = \mathbf{X} + \mathbf{u}_{n+1}(\mathbf{x}) \quad (7.56)$$

Next, we introduce the finite element interpolation, which, at the element level, can be written as

$$\{\Delta \mathbf{u}(\mathbf{x})\} = [N(\mathbf{x})] \{\Delta \mathbf{u}_e^N\} \quad (7.57)$$

where $[N(\mathbf{x})]$ is the interpolation matrix, and $\{\Delta \mathbf{u}_e^N\}$ the vector of nodal unknowns of the element. In the above equation and for the rest of this chapter, the following notation is used:

$\{ \}$ denotes a column, $[\]$ denotes a row, $[\]$ denotes a matrix.

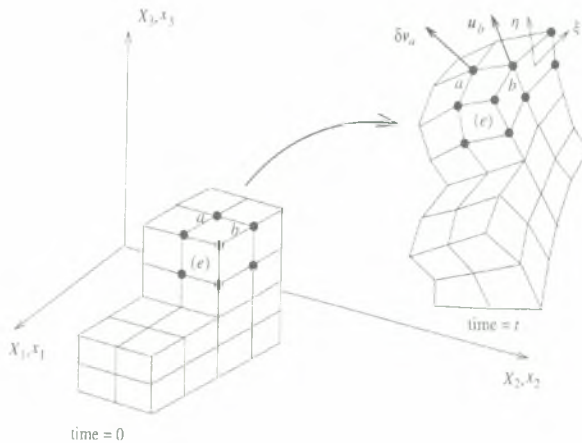


Figure 7.2: Discretization

We also define $\Delta \mathbf{L} \equiv \frac{\partial(\Delta \mathbf{u})}{\partial \mathbf{x}_{n+1}}$, which is written in matrix form as

$$\{\Delta L(\mathbf{x})\} = [B_L(\mathbf{x})] \{\Delta u_e^N\} \quad (7.58)$$

Similarly, for the virtual velocity vector \mathbf{v}^* and for the corresponding velocity gradient

$\mathbf{L}^* = \frac{\partial \mathbf{v}^*}{\partial \mathbf{x}_{n+1}}$ are written as

$$\{\mathbf{v}^*(\mathbf{x})\} = [N(\mathbf{x})] \{\mathbf{v}_e^{*N}\} \quad (7.59)$$

$$\text{and} \quad \{L^*(\mathbf{x})\} = [B_L(\mathbf{x})] \{\mathbf{v}_e^{*N}\} \quad (7.60)$$

Substituting the above fields in (7.54) we find

$$G = [\mathbf{v}^{*N}] \mathbf{A}_e \left(\int_{V_{n+1}^e} [B_L]_{n+1}^T \{\sigma\}_{n+1} dV - \int_{V_{n+1}^e} [N]_{n+1}^T \rho \{b\}_{n+1} dV - \int_{S_{n+1}^e} [N]_{n+1}^T \{T\}_{n+1} dS \right) = 0 \quad (7.61)$$

where $[\mathbf{v}^{*N}]$ is the global row of nodal virtual velocities, and \mathbf{A}_e is the ‘‘assembly operator’’.

Since last equation must hold for arbitrary values of $[\mathbf{v}^{*N}]$, we have that

$$\boxed{\mathbf{A}_e \int_{V_{n+1}^e} [B_L]_{n+1}^T \{\sigma\}_{n+1} dV = \{F\}_{n+1}} \quad (7.62)$$

where

$$\{F\}_{n+1} = \mathbf{A}_e \left(\int_{V_{n+1}^e} [N]_{n+1}^T \rho \{b\}_{n+1} dV + \int_{S_{n+1}^e} [N]_{n+1}^T \{T\}_{n+1} dS \right) \quad (7.63)$$

is the global vector of applied loads. The quantity $\{\sigma\}_{n+1}$ in (7.62) is a non-linear function of the unknown nodal displacement increments $\{\Delta u^N\}$. Equation (7.62) provides the set of non-linear equations that determine $\{\Delta u^N\}$. In fact, (7.62) can be written as

$$\boxed{\{R(\Delta u^N)\}_{n+1} \equiv \mathbf{A}_e \int_{V_{n+1}^e} [B_L]_{n+1}^T \{\sigma(\Delta u^N)\}_{n+1} dV - \{F\}_{n+1} = \{0\}} \quad (7.64)$$

where $\{R(\Delta u^N)\}_{n+1}$ is the global ‘‘residual’’ force vector, i.e., the difference between the forces required to maintain $\{\sigma\}_{n+1}$ in the body and the applied forces $\{F\}_{n+1}$.

The non-linear system (7.64) is solved for $\{\Delta u^N\}$ by using Newton's method. The corresponding Jacobian matrix, which plays the role of the "stiffness matrix" now, is determined by using (7.61) as follows. We write (7.61) in the form

$$G = [v^{*N}] \{R\}_{n+1} = 0 \quad (7.65)$$

and calculate

$$dG = [v^{*N}] \frac{\partial \{R(\Delta u^N)\}_{n+1}}{\partial \{\Delta u^N\}} d\{\Delta u^N\} = [v^{*N}] [K] d\{\Delta u^N\} \quad (7.66)$$

where $[K]$ now is the required Jacobian.

7.7 Calculation of Jacobian – Linearization of equations

The easiest way to calculate the Jacobian $[K]$ is to start with the continuum form of G , calculate the differential dG , and then introduce the finite element discretization; the resulting equation compared to (7.66) identifies $[K]$. The procedure is as follows.

We write $G(\Delta u)$ in the form

$$G(\Delta u) = \int_V \text{tr} \left(\boldsymbol{\sigma} \cdot \frac{\partial \mathbf{v}^*}{\partial \mathbf{x}} \right) dV - \int_{V_0} \rho_0 \mathbf{b} \cdot \mathbf{v}^* dV_0 - \int_{S_0^0} \mathbf{T}^0 \cdot \mathbf{v}^* dS_0 \quad (7.67)$$

where \mathbf{T}^0 is the nominal traction vector and ρ_0 the initial density. In (7.67) and for the rest of this section all quantities are evaluated at the end of the increment, unless indicated otherwise.

We note also that

$$d\mathbf{x} = d\mathbf{x}_{n+1} = d(\mathbf{x}_n + \Delta \mathbf{u}) = d(\Delta \mathbf{u}) \quad (7.68)$$

Next, we note that

$$\int_V \text{tr} \left(\boldsymbol{\sigma} \cdot \frac{\partial \mathbf{v}^*}{\partial \mathbf{x}} \right) dV = \int_{V_0} \text{tr} \left(\boldsymbol{\sigma} \cdot \frac{\partial \mathbf{v}^*}{\partial \mathbf{X}} \cdot \frac{\partial \mathbf{X}}{\partial \mathbf{x}} \right) J dV_0 = \int_{V_0} \text{tr} \left(\boldsymbol{\sigma} \cdot \frac{\partial \mathbf{v}^*}{\partial \mathbf{X}} \cdot \mathbf{F}^{-1} \right) J dV_0$$

so that (7.67) can be written as

$$G(\Delta u) = \int_{V_0} \text{tr} \left(\frac{\partial \mathbf{v}^*}{\partial \mathbf{X}} \cdot \mathbf{F}^{-1} \cdot \boldsymbol{\sigma} \right) J dV_0 - \int_{V_0} \rho_0 \mathbf{b} \cdot \mathbf{v}^* dV_0 - \int_{S_0^0} \mathbf{T}^0 \cdot \mathbf{v}^* dS_0 \quad (7.69)$$

We assume now that the applied loads are independent of the motion of the body, i.e., we exclude "follower forces". Then

$$dG = \int_{V_0} \text{tr} \left[\frac{\partial \mathbf{v}^*}{\partial \mathbf{X}} \cdot \left(d(\mathbf{F}^{-1}) \cdot \boldsymbol{\sigma} + \mathbf{F}^{-1} \cdot d\boldsymbol{\sigma} + \mathbf{F}^{-1} \cdot \boldsymbol{\sigma} \frac{dJ}{J} \right) \right] J dV_0 \quad (7.70)$$

where $J = \det(\mathbf{F})$. But $\frac{\partial \mathbf{v}^*}{\partial \mathbf{X}} = \frac{\partial \mathbf{v}^*}{\partial \mathbf{x}} \cdot \frac{\partial \mathbf{x}}{\partial \mathbf{X}} = \mathbf{L}^* \cdot \mathbf{F}$, so that the last equation becomes

$$dG = \int_V \left[\text{tr} \left[\mathbf{L}^* \cdot \left(\mathbf{F} \cdot d(\mathbf{F}^{-1}) \cdot \boldsymbol{\sigma} + d\boldsymbol{\sigma} + \frac{dJ}{J} \boldsymbol{\sigma} \right) \right] \right] dV \quad (7.71)$$

Next, we evaluate $\mathbf{F} \cdot d(\mathbf{F}^{-1})$, $d\boldsymbol{\sigma}$ and dJ/J .

Evaluation of $\mathbf{F} \cdot d(\mathbf{F}^{-1})$

$$\mathbf{F} \cdot \mathbf{F}^{-1} = \boldsymbol{\delta} \quad \Rightarrow \quad d\mathbf{F} \cdot \mathbf{F}^{-1} + \mathbf{F} \cdot d(\mathbf{F}^{-1}) = \mathbf{0} \quad \Rightarrow \quad \mathbf{F} \cdot d(\mathbf{F}^{-1}) = -d\mathbf{F} \cdot \mathbf{F}^{-1} \quad (7.72)$$

$$\text{Also } \mathbf{F} = \frac{\partial \mathbf{x}}{\partial \mathbf{X}} \quad \Rightarrow \quad d\mathbf{F} = \frac{\partial(d\mathbf{x})}{\partial \mathbf{X}} \quad \text{or} \quad \boxed{d\mathbf{F} = \frac{\partial(d(\Delta \mathbf{u}))}{\partial \mathbf{X}}} \quad (7.73)$$

Therefore,

$$(7.72) \Rightarrow \mathbf{F} \cdot d(\mathbf{F}^{-1}) = -\frac{\partial(d(\Delta \mathbf{u}))}{\partial \mathbf{X}} \cdot \frac{\partial \mathbf{X}}{\partial \mathbf{x}} = -\frac{\partial(d(\Delta \mathbf{u}))}{\partial \mathbf{x}} \quad \Rightarrow \quad \boxed{\mathbf{F} \cdot d(\mathbf{F}^{-1}) = -d\mathbf{L}} \quad (7.74)$$

$$\text{where } \boxed{d\mathbf{L} = \frac{\partial(d(\Delta \mathbf{u}))}{\partial \mathbf{x}}}$$

Evaluation of dJ

We recall the result $\frac{\partial J}{\partial F_{ki}} = J(\mathbf{F}^{-1})_{ik}$, which implies that

$$\begin{aligned} dJ &= J(\mathbf{F}^{-1})_{ik} dF_{ki} = J(\mathbf{F}^{-1} \cdot d\mathbf{F})_{ii} = J \text{tr}(\mathbf{F}^{-1} \cdot d\mathbf{F}) = \\ &= J \text{tr} \left(\frac{\partial \mathbf{X}}{\partial \mathbf{x}} \cdot \frac{\partial(d\Delta \mathbf{u})}{\partial \mathbf{X}} \right) = J \text{tr} \left(\frac{\partial(d\Delta \mathbf{u})}{\partial \mathbf{x}} \right) = J \text{tr}(d\mathbf{L}) \end{aligned} \quad (7.75)$$

$$\text{or} \quad \boxed{\frac{dJ}{J} = dL_{kk}} \quad (7.76)$$

Before we proceed to the evaluation of $d\boldsymbol{\sigma}$, we substitute $\mathbf{F} \cdot d(\mathbf{F}^{-1})$ and dJ/J in (7.71) to find

$$dG = \int_V \left[\text{tr} \left[\mathbf{L}^* \cdot (-d\mathbf{L} \cdot \boldsymbol{\sigma} + d\boldsymbol{\sigma} + \boldsymbol{\sigma} dL_{kk}) \right] \right] dV \quad \text{or} \quad dG = \int_V \mathbf{L}^* : (d\boldsymbol{\sigma} - \boldsymbol{\sigma} \cdot d\mathbf{L}^T + \boldsymbol{\sigma} dL_{kk}) dV \quad (7.77)$$

where we took into account that $\text{tr}(\mathbf{A} \cdot \mathbf{B}) = A_{ik} B_{ki} = \mathbf{A} : \mathbf{B}^T$.

Evaluation of $d\boldsymbol{\sigma}$

We note that $d\boldsymbol{\sigma}$ denotes the variation of $\boldsymbol{\sigma}$ with respect to the displacement increment $\Delta\mathbf{u}$. In general, $d\boldsymbol{\sigma}$ depends on the constitutive model **and** the algorithm used for the numerical integration of the constitutive equations. The exact evaluation of $d\boldsymbol{\sigma}$ in finite strain problems is always very involved. In order to simplify the calculation, we use the following approximate technique.

As mentioned in section 7.2, the assumption is made that the Lagrangian triad associated with $\Delta\mathbf{F}(t)$ (i.e., the eigenvectors of $\mathbf{U}(t)$) remains fixed in the time interval $[t_n, t_{n+1}]$. Then, it follows that

$$\dot{\mathbf{E}} = \mathbf{R}^T \cdot \mathbf{D} \cdot \mathbf{R}, \quad \mathbf{W} = \dot{\mathbf{R}} \cdot \mathbf{R}^T, \quad \overset{\nabla}{\boldsymbol{\sigma}} = \mathbf{R} \cdot \dot{\hat{\boldsymbol{\sigma}}} \cdot \mathbf{R}^T \quad (7.78)$$

where $\hat{\boldsymbol{\sigma}} = \mathbf{R}^T \cdot \boldsymbol{\sigma} \cdot \mathbf{R}$.

We note that

$$\dot{\hat{\boldsymbol{\sigma}}} = \frac{\partial \hat{\boldsymbol{\sigma}}}{\partial \mathbf{E}} : \dot{\mathbf{E}} = \hat{\mathbf{C}} : \dot{\mathbf{E}} = \hat{\mathbf{C}} : (\mathbf{R}^T \cdot \mathbf{D} \cdot \mathbf{R}) \quad (7.79)$$

so that

$$\overset{\nabla}{\boldsymbol{\sigma}} = \mathbf{R} \cdot \dot{\hat{\boldsymbol{\sigma}}} \cdot \mathbf{R}^T = \mathbf{R} \cdot \left[\hat{\mathbf{C}} : (\mathbf{R}^T \cdot \mathbf{D} \cdot \mathbf{R}) \right] \cdot \mathbf{R}^T = \mathbf{C} : \mathbf{D} = \mathbf{C} : \mathbf{L} \quad (7.80)$$

where $C_{ijkl} = R_{im} R_{jn} R_{kp} R_{lq} \hat{C}_{mnpq}$. Then

$$\dot{\boldsymbol{\sigma}} = \overset{\nabla}{\boldsymbol{\sigma}} - \boldsymbol{\sigma} \cdot \mathbf{W} + \mathbf{W} \cdot \boldsymbol{\sigma} = \mathbf{C} : \mathbf{L} - \frac{1}{2} \boldsymbol{\sigma} \cdot (\mathbf{L} - \mathbf{L}^T) + \frac{1}{2} (\mathbf{L} - \mathbf{L}^T) \cdot \boldsymbol{\sigma} \quad (7.81)$$

Based on equation (7.81), we introduce the *approximation* that

$$\boxed{d\boldsymbol{\sigma} \equiv \mathbf{C} : d\mathbf{L} - \frac{1}{2} \boldsymbol{\sigma} \cdot (d\mathbf{L} - d\mathbf{L}^T) + \frac{1}{2} (d\mathbf{L} - d\mathbf{L}^T) \cdot \boldsymbol{\sigma}} \quad (7.82)$$

Now, we substitute $d\boldsymbol{\sigma}$ from (7.82) in (7.77) to find

$$dG = \int_V \mathbf{L}^* : \left(\mathbf{C} : d\mathbf{L} - \frac{1}{2} \boldsymbol{\sigma} \cdot (d\mathbf{L} + d\mathbf{L}^T) + \frac{1}{2} (d\mathbf{L} - d\mathbf{L}^T) \cdot \boldsymbol{\sigma} + dL_{kk} \boldsymbol{\sigma} \right) dV \quad (7.83)$$

or

$$\boxed{dG = \int_V \mathbf{L}^* : (\mathbf{C} + \boldsymbol{\Sigma} + \boldsymbol{\sigma} \boldsymbol{\delta}) : d\mathbf{L} dV} \quad (7.84)$$

where $\Sigma_{ijkl} = \frac{1}{2} (\delta_{ik} \sigma_{jl} - \delta_{il} \sigma_{jk} - \sigma_{ik} \delta_{jl} + \sigma_{il} \delta_{jk})$.

Next, we introduce the finite element discretization

$$\{L^*\} = [B_L] \{v_e^{*N}\} \quad \text{and} \quad \{dL\} = [B_L] d\{u_e^N\} \quad (7.85)$$

in (7.84) to find

$$dG = [v^{*N}] \left(\mathbf{A} \int_{V^e} [B_L]^T ([C] + [\mathcal{L}] + \{\sigma\}[\delta]) [B_L] dV \right) d\{\Delta u^N\} \quad (7.86)$$

where $\{\sigma\}$ and $\{\delta\}$ are the vector representation of the stress tensor and the second order identity tensor, and $[C]$ and $[\mathcal{L}]$ are the matrix form of the fourth-order tensors \mathbf{C} and Σ . The detailed form of $[\mathcal{L}]$ is given in Appendix D.

Referring now to equation (7.66), we conclude that

$$[K] = \mathbf{A} [k^e] \quad (7.87)$$

where $[k^e]$ is the “element stiffness matrix” defined as

$$[k^e] = \int_{V^e} [B_L]^T ([C] + [\mathcal{L}] + \{\sigma\}[\delta]) [B_L] dV \quad (7.88)$$

It should be noted that, because of the approximation involved in (7.82), the expression for the Jacobian given in (7.88) is approximate as well. However, this approximation influences only the rate of convergence of the overall equilibrium iterations for the solution of (7.64) and not the accuracy of the solution, which depends on the “tolerance” used in (7.64). The exact Jacobian is more involved and is discussed in detail in Ramaswamy and Aravas (1998).

It should be noted also that $[\mathcal{L}]$ is a symmetric matrix, whereas the product $\{\sigma\}[\delta]$ results in a non-symmetric matrix. In our model $[C]$ is non-symmetric as well. Therefore, the corresponding $[k^e]$ is non-symmetric. ABAQUS is based on the formulation outlined above and uses (7.88) for the calculation of the Jacobian; the $[\mathcal{L}]$ matrix is included automatically in finite-strain analyses and the user has to provide the sum $[C] + \{\sigma\}[\delta]$ via UMAT. Our experience indicates that, when $[k^e]$ in (7.88) is replaced by its symmetric part, the required solution time decreases whereas the overall rate of convergence is not affected substantially.

CHAPTER EIGHT

COMPUTATIONAL MODEL FOR PLANE STRESS

8.1 Introduction

In this chapter we analyze the behavior of TRIP steels under plane stress conditions. In such problems, one considers a thin plane disc of uniform thickness loaded in its plane. The plane $X_3 = 0$ is taken to coincide with the mean plane of the disc. The in-plane displacement field is assumed to be of the form

$$u_1 = u_1(X_1, X_2) \quad \text{and} \quad u_2 = u_2(X_1, X_2). \quad (8.1)$$

In isotropic materials, it is also assumed that the deformation gradient and the stress tensor are of the form

$$[F] = \begin{bmatrix} F_{11} & F_{12} & 0 \\ F_{21} & F_{22} & 0 \\ 0 & 0 & F_{33} \end{bmatrix} \quad \text{and} \quad [\sigma] = \begin{bmatrix} \sigma_{11} & \sigma_{12} & 0 \\ \sigma_{12} & \sigma_{22} & 0 \\ 0 & 0 & 0 \end{bmatrix} \quad (8.2)$$

Equations (8.1) and the expression for $[F]$ given in (8.2) are consistent provided that $u_3 = u_3(X_3)$. However, in finite strain problems, when the in-plane displacement field is inhomogeneous, the out-of-plane displacement and the corresponding thickness variation will be functions of (X_1, X_2) . Then, the question arises as to whether the plane stress conditions are maintained as the disc deforms. The conditions under which the plane stress assumption is accurate for certain problems have been studied in detail by Hutchinson *et al.* (1978), Tvergaard (1978) and Needleman and Tvergaard (1984).

For the rest of this chapter we assume that, as the material deforms, the resulting thickness variation is insignificant, so that the plane stress assumption is valid and equations (8.1) and (8.2) hold.

In the following we discuss the application of the backward Euler method to problems of plane stress for TRIP steels. In such problems, the out-of-plane component of the deformation gradient F_{33} is not defined kinematically and some modifications to the method described in Chapter 7 are needed. Referring to the methodology described in section 7.2 we note that the deformation gradient associated with the increment under consideration can be written as

$$[\Delta F_{n+1}] = \begin{bmatrix} \Delta \bar{F}_{11} & \Delta \bar{F}_{12} & 0 \\ \Delta \bar{F}_{21} & \Delta \bar{F}_{22} & 0 \\ 0 & 0 & \lambda_3 \end{bmatrix} \quad (8.3)$$

where $\Delta \bar{F}_{\alpha\beta}$, $\alpha, \beta = (1, 2)$ are the known in-plane components, and λ_3 is the unknown out-of-plane component, which is determined from the condition $\sigma_{33}|_{n+1} = 0$. The corresponding $[U_{n+1}]$, $[R_{n+1}]$ and $[\Delta E]$ are of the form

$$[U_{n+1}] = \begin{bmatrix} \bar{U}_{11} & \bar{U}_{12} & 0 \\ \bar{U}_{12} & \bar{U}_{22} & 0 \\ 0 & 0 & \lambda_3 \end{bmatrix}, [R_{n+1}] = \begin{bmatrix} \cos \bar{\theta} & -\sin \bar{\theta} & 0 \\ \sin \bar{\theta} & \cos \bar{\theta} & 0 \\ 0 & 0 & 1 \end{bmatrix}, [\Delta E] = \begin{bmatrix} \Delta \bar{E}_{11} & \Delta \bar{E}_{12} & 0 \\ \Delta \bar{E}_{12} & \Delta \bar{E}_{22} & 0 \\ 0 & 0 & \Delta E_3 \end{bmatrix} \quad (8.4)$$

where bared quantities are known and $\Delta E_3 = \ln \lambda_3$ is the unknown out-of-plane component of ΔE determined from the condition $\sigma_{33}|_{n+1} = 0$.

We write also

$$\Delta E = \Delta \bar{E} + \Delta E_3 \mathbf{a}, \quad \mathbf{a} \equiv \mathbf{e}_3 \mathbf{e}_3 = \mathbf{a}' + \frac{1}{3} \delta \quad (8.5)$$

where $\Delta \bar{E}$ is the known in-plane part of ΔE , and

$$\mathbf{a}' = \frac{1}{3} (-\mathbf{e}_1 \mathbf{e}_1 - \mathbf{e}_2 \mathbf{e}_2 + 2 \mathbf{e}_3 \mathbf{e}_3) \quad (8.6)$$

is the deviatoric part of \mathbf{a} .

Also, using (8.4), we conclude that $\hat{\sigma}_{33}|_{n+1} = \sigma_{33}|_{n+1} = 0$, where $\hat{\sigma}_{n+1} = \mathbf{R}_{n+1}^T \cdot \sigma_{n+1} \cdot \mathbf{R}_{n+1}$.

8.2 Integration of constitutive equations under plane stress conditions

Equations (7.18)-(7.29) are now written as

$$\hat{\sigma}_{n+1} = \sigma_n + \mathbf{L}^e : (\Delta E - \Delta E^m) = \sigma_n + \mathbf{L}^e : (\Delta \bar{E} + \Delta E_3 \mathbf{a} - \Delta E^m) = \bar{\sigma}^e - \mathbf{L}^e : (\Delta E^m - \Delta E_3 \mathbf{a}) \quad (8.7)$$

$$\Delta E^m = \frac{1}{3} \Delta \varepsilon_v^p \delta + \Delta \varepsilon_q \hat{\mathbf{N}}_{n+1}, \quad \hat{\mathbf{N}}_{n+1} = \frac{3}{2 \sigma_{eq}|_{n+1}} \hat{\mathbf{S}}_{n+1} \quad (8.8)$$

$$\Delta \varepsilon_v^p = \Delta_v \Delta f, \quad \Delta \varepsilon_q = \frac{1}{3} \sigma_{eq}|_{n+1} \theta^{\text{hom}}(\sigma_{eq}|_{n+1}) + A(\sigma_{eq}|_{n+1}) \Delta f \quad (8.9)$$

$$\Delta f = c_{n+1}^{(a)} \left(A_f|_{n+1} \dot{\varepsilon}_{n+1}^{p(a)} \Delta t + B_f|_{n+1} \Delta \Sigma \right) \quad (8.10)$$

$$c_{n+1}^{(3)} = c_n^{(3)} e^{-\Delta f}, \quad c_{n+1}^{(4)} = c_n^{(4)} e^{-\Delta f}, \quad c_{n+1}^{(a)} = 1 - f_{n+1} - c_{n+1}^{(3)} - c_{n+1}^{(4)} \quad (8.11)$$

where $\bar{\sigma}^e = \sigma_n + \mathbf{L}^e : \Delta \bar{E}$ = known is the elastic predictor that corresponds to the known part of ΔE .

It should be emphasized that the \mathbf{L}^e used in the definition of $\bar{\sigma}^e$ is the “full” elasticity tensor and

not the so-called “plane stress moduli” used in traditional small strain linear elastic finite element analysis.

Next, we substitute (8.8a) in (8.7) and set $\mathbf{a} = \mathbf{a}' + \frac{1}{3}\delta$ and $\mathbf{L}^e = 2\mu\mathbf{K} + 3\kappa\mathbf{J}$ to find

$$\hat{\boldsymbol{\sigma}}_{n+1} = \bar{\boldsymbol{\sigma}}^e - 2\mu(\Delta\varepsilon_q \hat{\mathbf{N}}_{n+1} - \Delta E_3 \mathbf{a}') - \kappa(\Delta\varepsilon_v^p - \Delta E_3)\delta \quad (8.12)$$

The deviatoric and spherical parts of $\hat{\boldsymbol{\sigma}}_{n+1}$ are

$$\hat{\mathbf{s}}_{n+1} = \bar{\mathbf{s}}^e - 2\mu(\Delta\varepsilon_q \hat{\mathbf{N}}_{n+1} - \Delta E_3 \mathbf{a}') \quad (8.13)$$

and

$$p_{n+1} = p^e - \kappa(\Delta\varepsilon_v^p - \Delta E_3) \quad (8.14)$$

Next, we substitute $\hat{\mathbf{N}}_{n+1} = \frac{3}{2\sigma_{eq}|_{n+1}}\hat{\mathbf{s}}_{n+1}$ in (8.13) and solve for $\hat{\mathbf{s}}_{n+1}$ to find

$$\hat{\mathbf{s}}_{n+1} = \frac{1}{1 + 3\Delta\varepsilon_q(\mu/\sigma_{eq}|_{n+1})}(\bar{\mathbf{s}}^e + 2\mu\Delta E_3 \mathbf{a}') \quad (8.15)$$

The last equation shows that $\hat{\mathbf{s}}_{n+1}$ and $\bar{\mathbf{s}}^e$ are **not** co-linear. Then, we use (8.15) to calculate

$\sigma_{eq}|_{n+1}$ as follows

$$\left(\sigma_{eq}|_{n+1}\right)^2 = \frac{3}{2}\mathbf{s}_{n+1}:\mathbf{s}_{n+1} = \frac{3/2}{\left[1 + 3\Delta\varepsilon_q(\mu/\sigma_{eq}|_{n+1})\right]^2}(\bar{\mathbf{s}}^e + 2\mu\Delta E_3 \mathbf{a}'):(\bar{\mathbf{s}}^e + 2\mu\Delta E_3 \mathbf{a}') \quad (8.16)$$

If we take into account that $\mathbf{a}':\mathbf{a}' = \frac{2}{3}$ and $\bar{\mathbf{s}}^e:\mathbf{a}' = \bar{\mathbf{s}}^e:\mathbf{a} = \bar{\mathbf{s}}^e:(\mathbf{e}_3\mathbf{e}_3) = \bar{s}_{33}^e$, we conclude that the last equation can be written as

$$\left(\sigma_{eq}|_{n+1}\right)^2 = \frac{1}{\left[1 + 3\Delta\varepsilon_q(\mu/\sigma_{eq}|_{n+1})\right]^2}(\bar{\sigma}_{eq}^e{}^2 + 6\mu\bar{s}_{33}^e\Delta E_3 + 4\mu^2\Delta E_3^2) \quad (8.17)$$

which can be solved for $\sigma_{eq}|_{n+1}$:

$$\sigma_{eq}|_{n+1} = -3\mu\Delta E_3 + \sqrt{\bar{\sigma}_{eq}^e{}^2 + 6\mu\bar{s}_{33}^e\Delta E_3 + 4\mu^2\Delta E_3^2} \quad (8.18)$$

where $\bar{\sigma}_{eq}^e = \sqrt{\frac{3}{2}\bar{\mathbf{s}}^e:\bar{\mathbf{s}}^e}$.

The plane stress condition $\hat{\sigma}_{33}|_{n+1} = 0$ can be written as $\hat{s}_{33}|_{n+1} + p_{n+1} = 0$, which, in view of (8.15), implies that

$$\frac{1}{1 + 3 \Delta \varepsilon_q \left(\mu / \sigma_{eq}|_{n+1} \right)} \left(\bar{s}_{33}^e + \frac{4}{3} \mu \Delta E_3 \right) + p_{n+1} = 0 \quad (8.19)$$

Summarizing, we note that we choose $\Delta \varepsilon_q$, Δf and ΔE_3 as the primary unknowns and treat the following as the basic equations:

$$\Delta \varepsilon_q = \frac{1}{3} \sigma_{eq}|_{n+1} \theta^{\text{hom}} \left(\sigma_{eq}|_{n+1} \right) + A \left(\sigma_{eq}|_{n+1} \right) \Delta f \quad (8.20)$$

$$\Delta f = c_{n+1}^{(a)} \left(A_f|_{n+1} \dot{\varepsilon}_{n+1}^{p(a)} \Delta t + B_f|_{n+1} \Delta \Sigma \right) \quad (8.21)$$

$$\frac{1}{1 + 3 \Delta \varepsilon_q \left(\mu / \sigma_{eq}|_{n+1} \right)} \left(\bar{s}_{33}^e + \frac{4}{3} \mu \Delta E_3 \right) + p_{n+1} = 0 \quad (8.22)$$

in which $\sigma_{eq}|_{n+1}$, p_{n+1} , $\Delta \varepsilon_v^p$, $c_{n+1}^{(3)}$, $c_{n+1}^{(4)}$ and $c_{n+1}^{(a)}$ are defined by equations (8.18), (8.14), (8.9a) and (8.11). Details of the calculations are presented in Appendix E. Also, $\theta_{n+1}^{\text{hom}}$ and $\dot{\varepsilon}_{n+1}^{p(a)}$ are determined by using the homogenization technique described in Chapter 4. Newton's method is used for the solution of (8.20)-(8.22).

Once $\Delta \varepsilon_q$, Δf and ΔE_3 are found, $\sigma_{eq}|_{n+1}$, p_{n+1} , $\Delta \varepsilon_v^p$, $c_{n+1}^{(3)}$, $c_{n+1}^{(4)}$, $c_{n+1}^{(a)}$ and $\hat{\sigma}_{n+1}$ are defined by equations (8.18), (8.14), (8.9a), (8.11) and (8.12). Finally, σ_{n+1} is computed from:

$$\sigma_{n+1} = \mathbf{R}_{n+1} \cdot \hat{\sigma}_{n+1} \cdot \mathbf{R}_{n+1}^T \quad (8.23)$$

which completes the integration process.

8.3 The linearization moduli

The linearization moduli are determined as discussed in section 7.3 and are of the form

$$\mathbf{C} = \mathbf{L}^e - g_1 \mathbf{K} + g_2 \mathbf{N} \mathbf{N} - g_3 \mathbf{N} \delta - g_4 \delta \mathbf{N} - g_5 \delta \delta \quad (8.24)$$

For a plane strain or plane stress problem, the last equation can be written in matrix form as

$$\begin{Bmatrix} d\sigma_{11} \\ d\sigma_{22} \\ d\sigma_{33} \\ d\sigma_{12} \end{Bmatrix} = \begin{bmatrix} C_{11} & C_{12} & C_{13} & C_{14} \\ C_{21} & C_{22} & C_{23} & C_{24} \\ C_{31} & C_{32} & C_{33} & C_{34} \\ C_{41} & C_{42} & C_{43} & C_{44} \end{bmatrix} \begin{Bmatrix} d\varepsilon_{11} \\ d\varepsilon_{22} \\ d\varepsilon_{33} \\ 2d\varepsilon_{12} \end{Bmatrix} \quad (8.25)$$

In plane stress problems, ABAQUS requires the linearization moduli \bar{C} in the form

$$\begin{Bmatrix} d\sigma_{11} \\ d\sigma_{22} \\ d\sigma_{12} \end{Bmatrix} = \begin{bmatrix} \bar{C}_{11} & \bar{C}_{12} & \bar{C}_{13} \\ \bar{C}_{21} & \bar{C}_{22} & \bar{C}_{23} \\ \bar{C}_{31} & \bar{C}_{32} & \bar{C}_{33} \end{bmatrix} \begin{Bmatrix} d\varepsilon_{11} \\ d\varepsilon_{22} \\ 2d\varepsilon_{12} \end{Bmatrix} \quad (8.26)$$

These are calculated from (8.25) as follows. The plane stress condition $\sigma_{33} = 0$ implies that $d\sigma_{33} = 0$, so that (8.25) implies $C_{31}d\varepsilon_{11} + C_{32}d\varepsilon_{22} + C_{33}d\varepsilon_{33} + 2C_{34}d\varepsilon_{12} = 0$ or

$$d\varepsilon_{33} = -\frac{1}{C_{33}}(C_{31}d\varepsilon_{11} + C_{32}d\varepsilon_{22} + 2C_{34}d\varepsilon_{12}) \quad (8.27)$$

Substituting the last equation in (8.25) and carrying out the algebra we conclude that

$$\bar{C}_{11} = C_{11} - \frac{C_{13}}{C_{33}}C_{31}, \quad \bar{C}_{12} = C_{12} - \frac{C_{13}}{C_{33}}C_{32}, \quad \bar{C}_{13} = C_{14} - \frac{C_{13}}{C_{33}}C_{34} \quad (8.28)$$

$$\bar{C}_{21} = C_{21} - \frac{C_{23}}{C_{33}}C_{31}, \quad \bar{C}_{22} = C_{22} - \frac{C_{23}}{C_{33}}C_{32}, \quad \bar{C}_{23} = C_{24} - \frac{C_{23}}{C_{33}}C_{34} \quad (8.29)$$

$$\bar{C}_{31} = C_{41} - \frac{C_{43}}{C_{33}}C_{31}, \quad \bar{C}_{32} = C_{42} - \frac{C_{43}}{C_{33}}C_{32}, \quad \bar{C}_{33} = C_{44} - \frac{C_{43}}{C_{33}}C_{34} \quad (8.30)$$

For example,

$$\begin{aligned} d\sigma_{11} &= C_{11}d\varepsilon_{11} + C_{12}d\varepsilon_{22} + C_{13}d\varepsilon_{33} + 2C_{14}d\varepsilon_{12} = \\ &= C_{11}d\varepsilon_{11} + C_{12}d\varepsilon_{22} - \frac{C_{13}}{C_{33}}(C_{31}d\varepsilon_{11} + C_{32}d\varepsilon_{22} + 2C_{34}d\varepsilon_{12}) + 2C_{14}d\varepsilon_{12} = \\ &= \left(C_{11} - \frac{C_{13}}{C_{33}}C_{31}\right)d\varepsilon_{11} + \left(C_{12} - \frac{C_{13}}{C_{33}}C_{32}\right)d\varepsilon_{22} + \left(C_{14} - \frac{C_{13}}{C_{33}}C_{34}\right)2d\varepsilon_{12} \end{aligned} \quad (8.31)$$

which implies (8.28).

CHAPTER NINE

FINITE ELEMENT RESULTS FOR TWO-PHASE TRIP STEELS

9.1 Introduction

The constitutive model developed in Chapter 6 for the two-phase TRIP steel is implemented in ABAQUS through the subroutine UMAT and is used for the analysis of model problems. In particular the problems of: i) uniaxial tension at different temperatures, ii) finite simple shear, and iii) plane strain tension are studied in detail.

9.2 Effect of temperature on martensitic transformation in uniaxial tension

Martensitic transformation is strongly affected by temperature. In order to study the dependence on temperature, we consider the problem of uniaxial tension for three different temperatures: $T_1 = -50^\circ\text{C}$, $T_2 = -10^\circ\text{C}$ and $T_3 = 23^\circ\text{C}$. We solve the problem using one four-node isoparametric axisymmetric finite element loaded in uniaxial tension in the vertical 2-direction. The element (CAX4H in ABAQUS) uses the so-called “B-bar” method for the numerical evaluation of the stiffness matrix $[k^e]$, i.e., 2×2 Gauss integration points for the numerical evaluation of the “deviatoric part” of $[k^e]$ and 1 Gauss integration point for the “volumetric part” (Hughes, 2000). All axisymmetric calculations in this Ph.D. thesis are carried out using CAX4H elements. A schematic representation of the problem is shown in Figure 9.1. The problem is solved incrementally: the displacement of the two “top” nodes is increased gradually until a final elongation of 30% is reached.

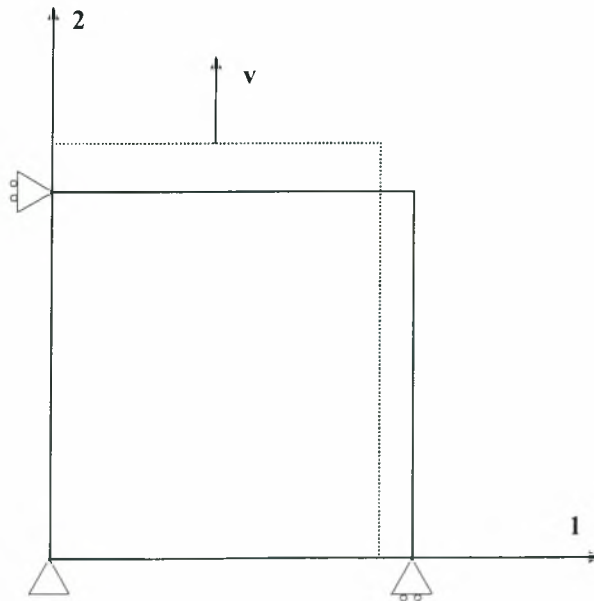


Figure 9.1: Schematic description of the uniaxial tension problem.

The values $E = 220$ GPa and $\nu = 0.3$ for the elastic Young's modulus and Poisson's ratio are used in the calculations. The curves $\sigma_y^{(a)}(\bar{\varepsilon}^{p(a)})$ and $\sigma_y^{(m)}(\bar{\varepsilon}^{p(m)})$ that define the variation of the flow stress of the austenitic and martensitic phases are those discussed in Chapter 6, i.e., Austenite:

$$\sigma_y^{(a)} = 323 + 2163 \bar{\varepsilon}^{p(a)} \quad (\text{MPa}) \quad \text{for } \bar{\varepsilon}^{p(a)} \leq 0.24365 \quad (9.1)$$

$$\sigma_y^{(a)} = 850 \quad (\text{MPa}) \quad \text{for } \bar{\varepsilon}^{p(a)} \geq 0.24365 \quad (9.2)$$

Martensite:

$$\sigma_y^{(m)} = 920 + 1000 \left(\bar{\varepsilon}^{p(m)} \right)^{0.15} \quad (\text{MPa}) \quad (9.3)$$

The values $\dot{\varepsilon}_0^{(a)} = \dot{\varepsilon}_0^{(r)} = 10^{-4} \text{ sec}^{-1}$ and $m = 20$ are used in the calculations; the macroscopic loading rate is also 10^{-4} sec^{-1} . The relative volume change associated with the martensitic transformation takes the value $\Delta_v = 0.02$. The transformation kinetics data are shown in Tables 9.1 and 9.2 and are those used by Naturani (1982) and Stringfellow et al. (1992). The values $M_{d,ut} = 52^\circ\text{C}$ and $M_{s,ut} = -63^\circ\text{C}$ are used in the calculations. The material is assumed to be fully austenitic initially, i.e., the initial volume fraction of martensite is $f_0 = 0$.

The variation of $\sigma_y^{(a)}(\bar{\varepsilon}^{p(a)})$ and $\sigma_y^{(m)}(\bar{\varepsilon}^{p(m)})$ with temperature is not taken into account; the differences in the macroscopic behavior at different temperatures reported below are due to the temperature-dependent parameters of the transformation kinetics model listed in Table 9.2.

β_0	r	g_0	g_1	g_2	\bar{g}	s_g	A_0
4.42	4	3400	4.7	493	3230	292	0.012

Table 9.1: Values used in the kinetics model

$T(^{\circ}\text{C})$	α	A_1	s_{α}^* (MPa)
-50	14.6	0.040	697
-10	7.0	0.030	581
23	4.7	0.028	496

Table 9.2: Values used in the kinetics model

The calculated variation of the volume fraction of martensite f is shown in Figure 9.2 for the three temperatures considered. The curves shown in Figure 9.2 have a "sigmoidal shape", in

agreement with experimental observation. At the lower temperature ($T_1 = -50^\circ\text{C}$), martensite is formed at smaller strains and at a higher rate. It should be noted also that, for the two lower temperatures $T_1 = -50^\circ\text{C}$ and $T_2 = -10^\circ\text{C}$, the volume fraction of the martensite f reaches the same “plateau” of about 100% in particular, the plateau is reached at a value of the nominal strain $\varepsilon \cong 0,13$ for $T_1 = -50^\circ\text{C}$, and at $\varepsilon \cong 0,30$ for $T_2 = -10^\circ\text{C}$. At room temperature ($T_3 = 23^\circ\text{C}$), the amount of martensite is about 75% at a nominal strain of $\varepsilon \cong 0,30$.

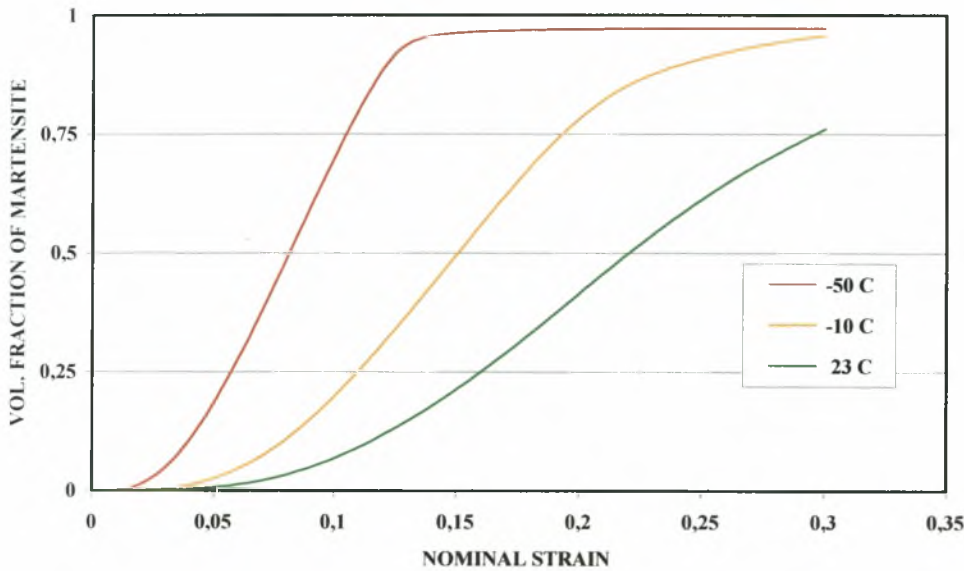


Figure 9.2: Volume fraction of martensite formed versus nominal strain for different temperatures in uniaxial tension.

The corresponding typical “S”-shaped stress-strain curves at the three temperatures are shown in Fig. 9.3, together with the stress-strain curves of the austenite (lower curve) and the martensite (top curve). The response of the TRIP steel at different temperatures lies between the aforementioned “limiting curves” as expected. The effects of the martensitic transformation are more pronounced at the lower temperature of ($T_1 = -50^\circ\text{C}$).

The variation of the equivalent plastic strain $\bar{\varepsilon}^p = \int \sqrt{\frac{2}{3} \mathbf{D}^p : \mathbf{D}^p} dt$ in the TRIP steel with the nominal strain is shown in Fig. 9.4. The corresponding variation of the TRIP “equivalent

strains” $\varepsilon_q^{TRIP} = \int \sqrt{\frac{2}{3} \mathbf{D}^{TRIP'} : \mathbf{D}^{TRIP'}} dt$ and $\varepsilon_p^{TRIP} = \int D_{kk}^{TRIP} dt = \int \dot{\varepsilon}_v^p dt = \varepsilon_v^p$ is shown in Fig. 9.5,

where a prime denotes the deviatoric part of a tensor. The volumetric TRIP strain ε_p^{TRIP} is

substantially smaller than the equivalent deviatoric TRIP strain ε_q^{TRIP} in all cases; the volumetric TRIP strain ε_p^{TRIP} saturates at the value of $\Delta_v = 0.02$ as expected.

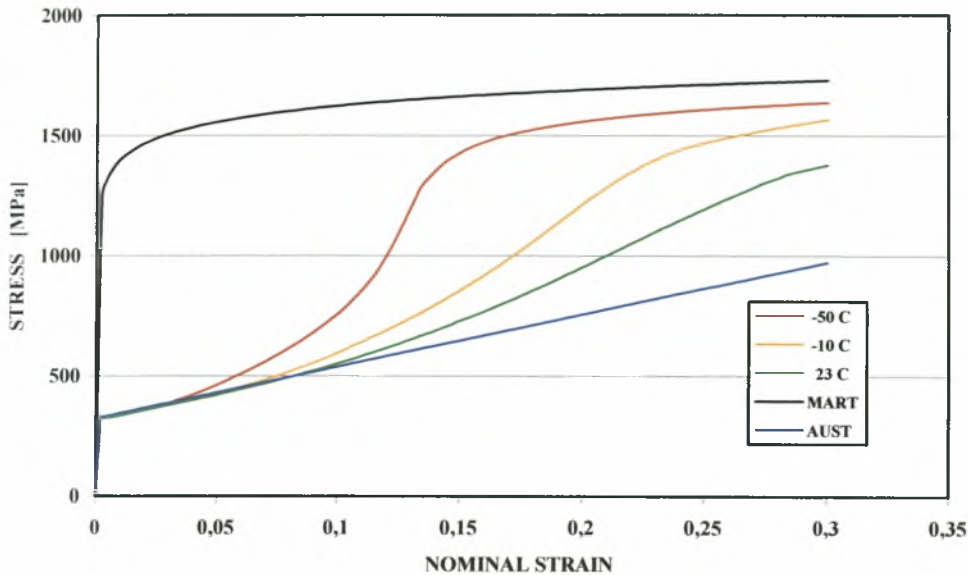


Figure 9.3: Stress-strain curves of austenite and martensite at different temperatures.

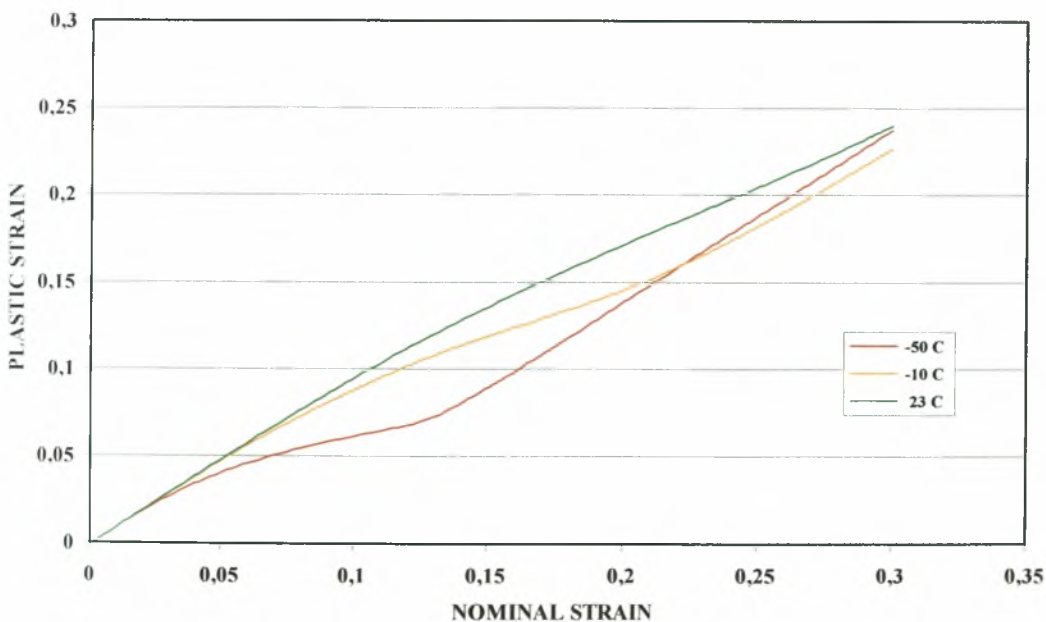


Figure 9.4: Equivalent plastic strain $\bar{\varepsilon}^p = \int \sqrt{\frac{2}{3} \mathbf{D}^p : \mathbf{D}^p} dt$ versus nominal strain for different temperatures in uniaxial tension.

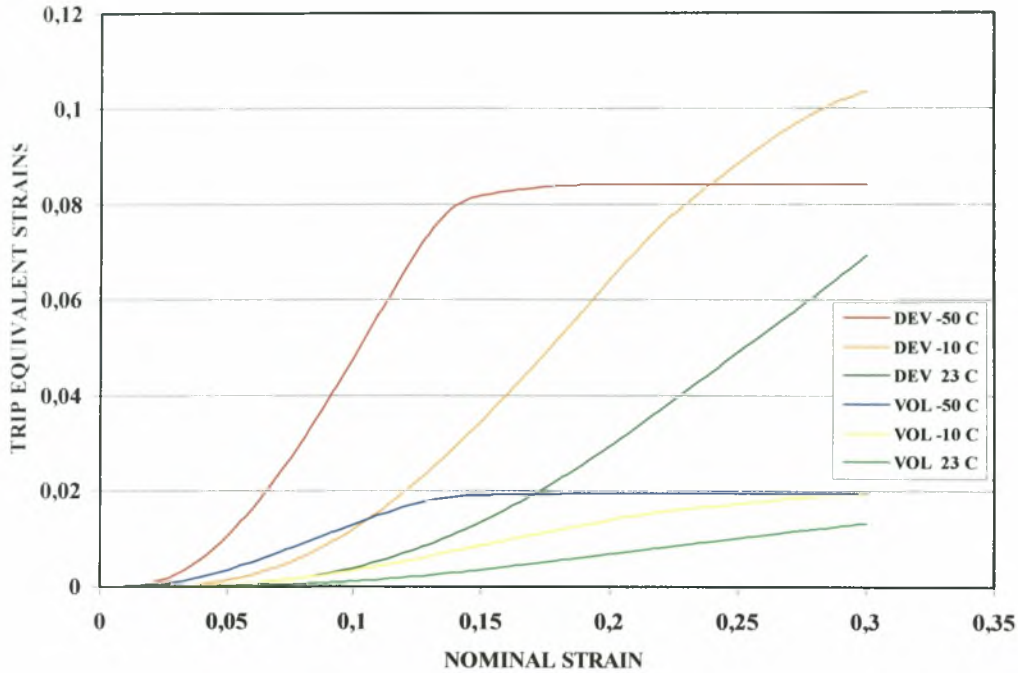


Figure 9.5: Variation of the TRIP “equivalent strains” ε_q^{TRIP} (DEV) and ε_p^{TRIP} (VOL) with the nominal strain for different temperatures in uniaxial tension.

The homogenization theory discussed in Chapter 6 provides estimates for the accumulated plastic strains $\bar{\varepsilon}^{p(a)}$ and $\bar{\varepsilon}^{p(m)}$ in the austenitic and martensitic phases. The variation of $\bar{\varepsilon}^{p(a)}$ and $\bar{\varepsilon}^{p(m)}$ with the nominal strain is shown in Figures 9.6 and 9.7. The accumulated plastic strain is always higher in the softer austenitic phase, i.e., $\bar{\varepsilon}^{p(a)} > \bar{\varepsilon}^{p(m)}$. It is interesting to note that for the lower temperature considered ($T_1 = -50^\circ\text{C}$) there is a sudden increase of the plastic strain rate; this is due to the fact that at $\varepsilon \cong 0.12$ the volume fraction of martensite reaches a plateau of $f \cong 90\%$, limiting the volume fraction of the austenite (which accommodates most of the strain from this point on) at about 10%.

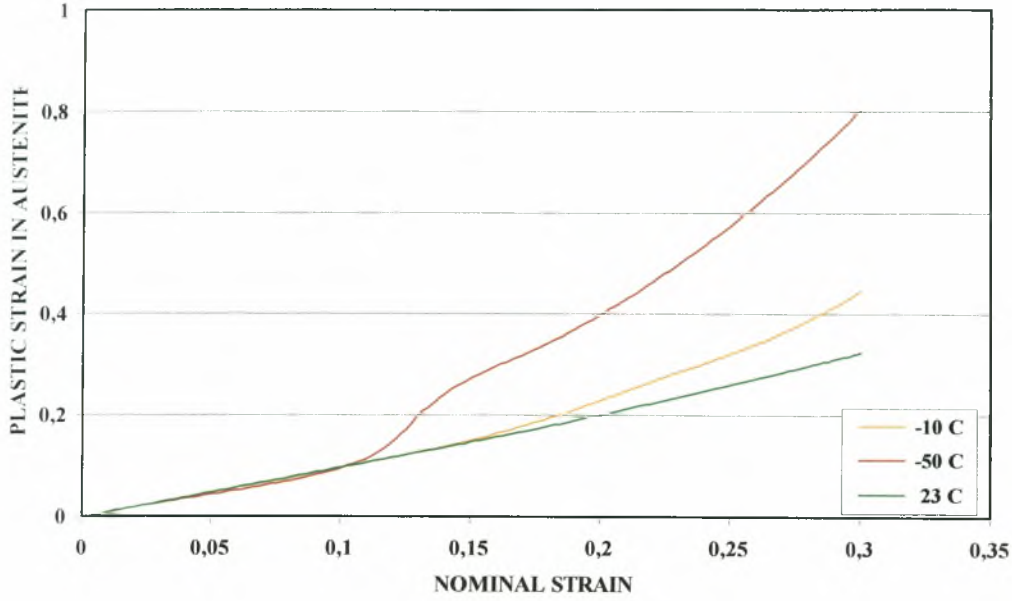


Figure 9.6: Plastic strain $\bar{\varepsilon}^{p(a)}$ in austenite versus nominal strain for different temperatures in uniaxial tension.

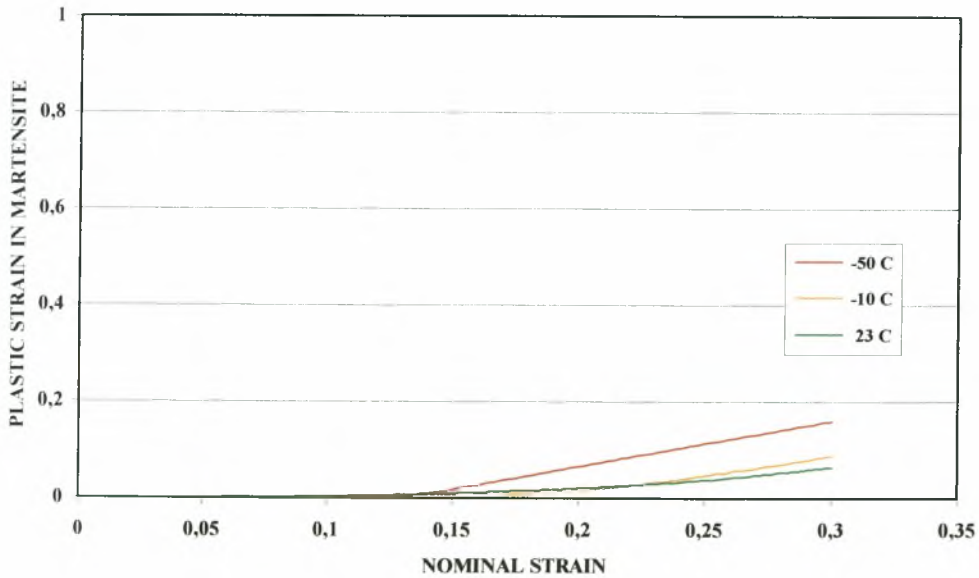


Figure 9.7: Plastic strain $\bar{\varepsilon}^{p(m)}$ in martensite versus nominal strain for different temperatures in uniaxial tension.

Figure 9.8 shows the variation of the equivalent plastic strain $\bar{\epsilon}^p = \int \sqrt{\frac{2}{3} \mathbf{D}^p : \mathbf{D}^p} dt$ in the TRIP steel with the nominal strain, together with the plastic strains $\bar{\epsilon}^{p(a)}$ and $\bar{\epsilon}^{p(m)}$ in the individual phases for the lower temperature $T_1 = -50^\circ\text{C}$. Initially, the equivalent plastic strain in the TRIP steel $\bar{\epsilon}^p$ equals that of the austenite since the volume fraction f of the martensite is very small; as the amount of the harder martensitic phase in the TRIP increases, most of the deformation is accommodated by the softer austenitic phase, and $\bar{\epsilon}^{p(a)}$ becomes larger than $\bar{\epsilon}^p$.

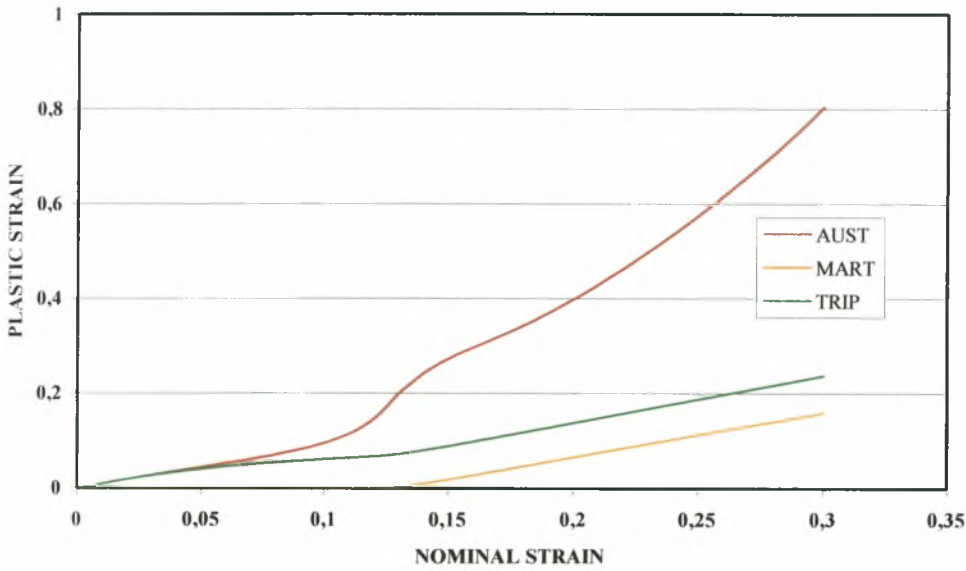


Figure 9.8: Variation of $\bar{\epsilon}^p$, $\bar{\epsilon}^{p(a)}$ and $\bar{\epsilon}^{p(m)}$ with nominal strain for $T_1 = -50^\circ\text{C}$.

9.3 Simple shear

In order to study the effect of the stress state in the behavior of TRIP steels, we consider the problem of finite simple shear. A schematic representation of the problem is shown in Fig. 9.9. The corresponding deformation gradient and the rate of deformation tensors are of the form

$$\mathbf{F}(t) = \boldsymbol{\delta} + \gamma(t)\mathbf{e}_1\mathbf{e}_2 \quad \text{and} \quad \mathbf{D}(t) = \frac{\dot{\gamma}(t)}{2}(\mathbf{e}_1\mathbf{e}_2 + \mathbf{e}_2\mathbf{e}_1) \quad (9.4)$$

where γ is the amount of shear. The von Mises “equivalent strain” $\bar{\epsilon}$ is defined as

$$\bar{\varepsilon} = \int \sqrt{\frac{2}{3} \mathbf{D}' : \mathbf{D}'} dt = \int \frac{\dot{\gamma}}{\sqrt{3}} dt = \frac{\gamma}{\sqrt{3}} \quad (9.5)$$

where a prime indicates the deviatoric part of a tensor.

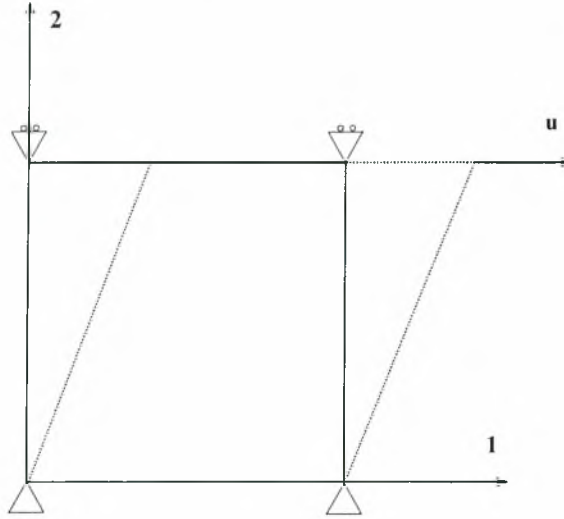


Figure 9.9: Schematic representation of the simple shear problem.

The problem is solved numerically using ABAQUS. One four-node plane strain isoparametric element is used. The element (CPE4H in ABAQUS) uses the so-called “B-bar” method for the numerical evaluation of the stiffness matrix $[k^e]$, i.e., 2×2 Gauss integration for the numerical evaluation of the “deviatoric part” of $[k^e]$ and 1 point Gauss integration for the “volumetric part” (Hughes, 2000). This element is equivalent to a “mixed” displacement-pressure four-node element with a constant pressure (Hughes, 1977; Malkus and Hughes, 1978). All plane strain calculations in this Ph.D. thesis are carried out using CPE4H elements.

The calculations are carried out for the case of room temperature $T = 23^\circ\text{C}$ and the material data used are the same as used for the problem of uniaxial tension.

Figure 9.10 shows the variation of the volume fraction of martensite f with the equivalent strain $\bar{\varepsilon}$. The amount of martensite formed in this case is substantially smaller than that of the uniaxial tension problem. This indicates the strong dependence of the plastic-strain-induced transformation on the stress state.

It should be noted also that substantial compressive hydrostatic stresses develop in the shear problem. This is due to the volumetric component of the transformation strain and the imposed constraint of zero displacement in the 2- and 3-directions. It well documented that the transformation of austenitic particles (FCC) to martensite (BCC) results in an increase in

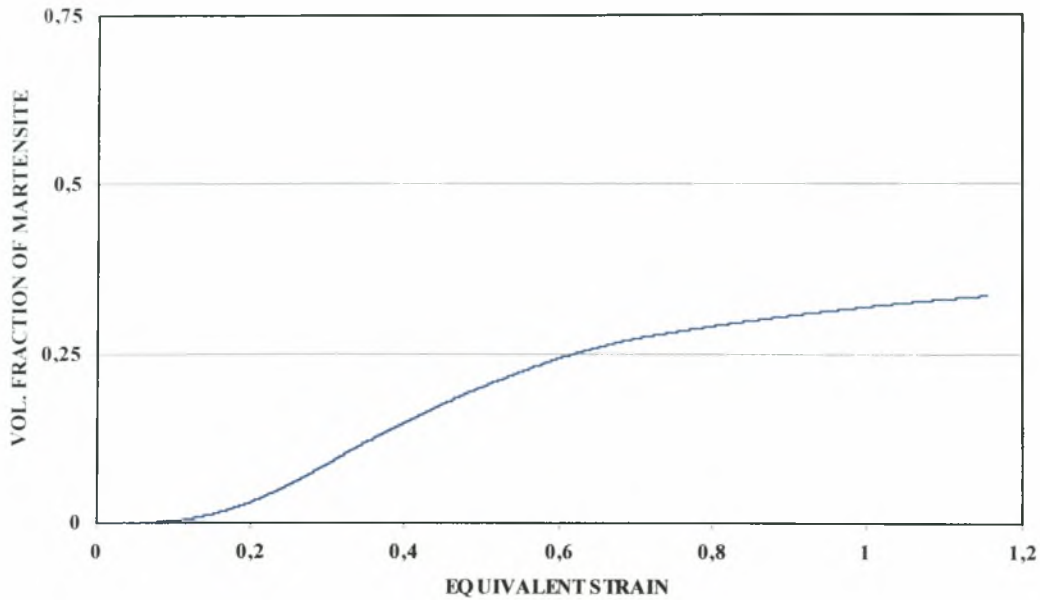


Figure 9.10: Volume fraction of martensite formed versus equivalent strain $\bar{\varepsilon} = \int \sqrt{\frac{2}{3} \mathbf{D}' : \mathbf{D}' } dt$ in simple shear at room temperature ($T = 23^\circ\text{C}$).

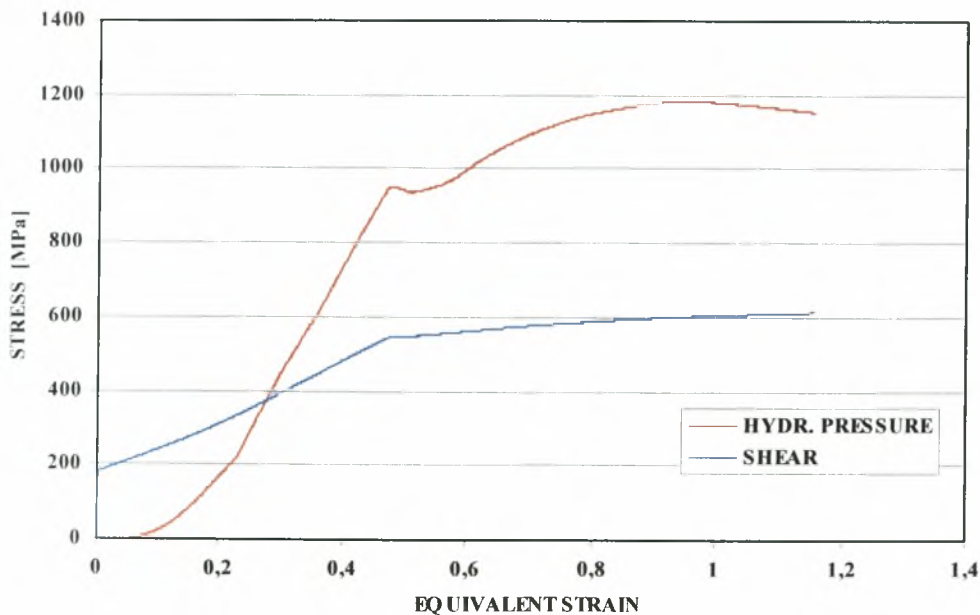


Figure 9.11: Hydrostatic pressure and shear component versus equivalent strain

$$\bar{\varepsilon} = \int \sqrt{\frac{2}{3} \mathbf{D}' : \mathbf{D}' } dt \text{ in simple shear at room temperature } (T = 23^\circ\text{C}).$$

volume of the order of 2-4% (Leal, 1984). Since the overall normal strains are forced to zero by the kinematics of the problem, substantial compressive normal stresses develop. Figure 9.11 shows the variation of the absolute value of the hydrostatic stress and the shear stress component σ_{12} with the equivalent strain. It should be noted that the compressive normal stresses that develop are all equal, and, therefore, equal to the hydrostatic stress.

9.4 Plane strain tension

The results presented in the two previous sections show the strong dependence of the martensitic transformation on the stress state. In order to study in more detail this stress dependence we study also the problem of plane strain tension.

Calculations similar to those described in section 9.1 are carried out at $T = 23^{\circ}\text{C}$ by using one four-node plane strain isoparametric element (CPE4H). Figure 9.12 shows the variation of the volume fraction of martensite formed for all three problems considered (uniaxial tension, simple shear, and plane strain tension) with the equivalent strain $\bar{\varepsilon} = \int \sqrt{\frac{2}{3} \mathbf{D}' : \mathbf{D}'} dt$. The amount of martensite formed in plane strain tension is very close to that of the uniaxial tension problem and substantially higher than that of the simple shear.

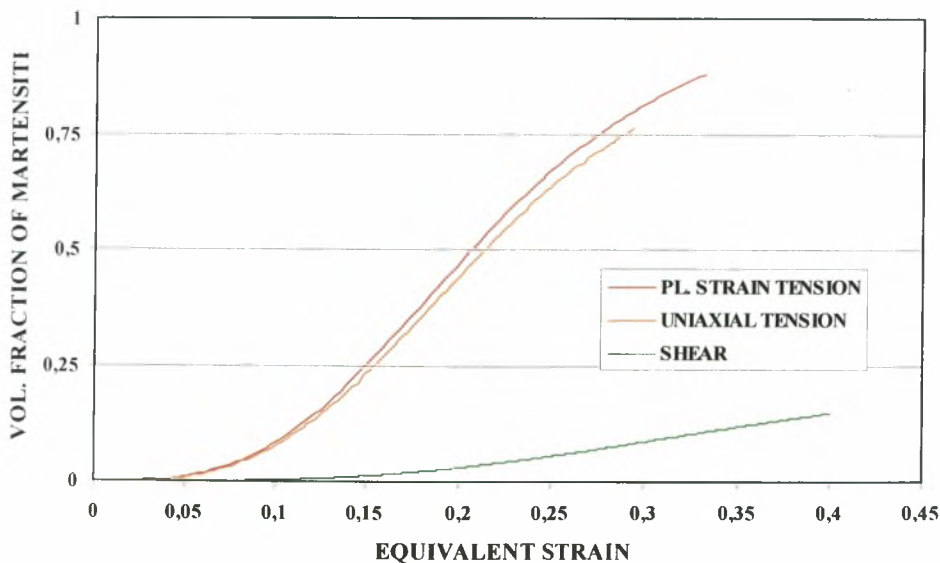
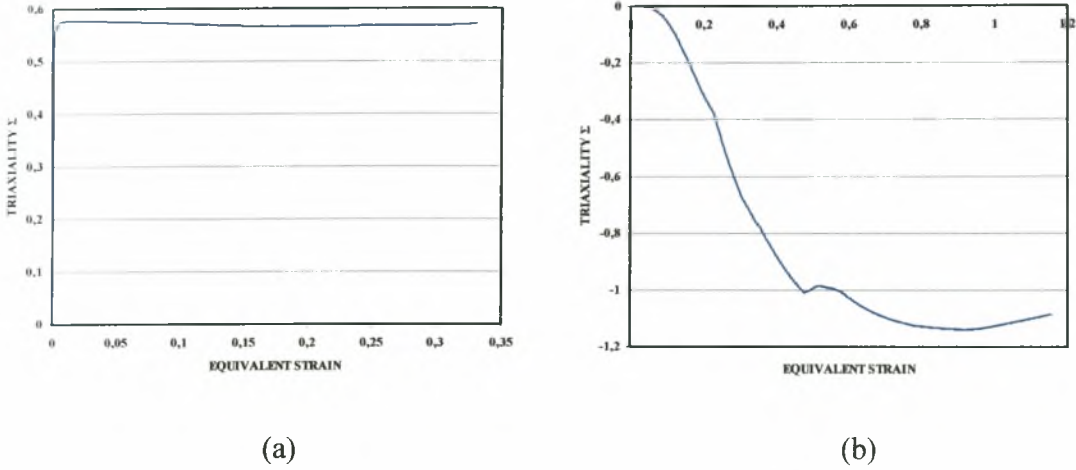


Figure 9.12: Volume fraction of martensite formed versus equivalent strain $\bar{\varepsilon} = \int \sqrt{\frac{2}{3} \mathbf{D}' : \mathbf{D}'} dt$

for the three problems considered at room temperature ($T = 23^{\circ}\text{C}$).



Figures 9.13: Triaxiality ratio Σ versus equivalent strain $\bar{\varepsilon} = \int \sqrt{\frac{2}{3} \mathbf{D}' : \mathbf{D}' } dt$ for plane strain tension (a) and simple shear (b) at room temperature ($T_3 = 23^\circ C$).

The response of TRIP steels depends on the values of the triaxiality ratio $\Sigma = \frac{p}{\sigma_{eq}} = \frac{\sigma_{kk}/3}{\sigma_{eq}}$. In

uniaxial tension the triaxiality takes the constant value of $\Sigma = \frac{1}{3} = 0.33$. The variation of Σ

with the equivalent strain $\bar{\varepsilon} = \int \sqrt{\frac{2}{3} \mathbf{D}' : \mathbf{D}' } dt$ is shown in Fig. 9.13 for the cases of simple shear

and plane strain tension. It should be noted that in all three problems analyzed $\dot{\Sigma} \leq 0$, so that $B_i = 0$ in the evolution equation for f (6.64). The triaxiality affects the solution only through the normalized thermodynamic driving force g (equation (6.59)) that enters the definition of the probability distribution function P in equation (6.58).

Figures 9.14 and 9.15 show the variation of the von Mises equivalent stress σ_{eq} and the equivalent plastic strain in the martensitic phase $\bar{\varepsilon}^{p(m)}$ with the equivalent strain strain in the

TRIP steel $\bar{\varepsilon} = \int \sqrt{\frac{2}{3} \mathbf{D}' : \mathbf{D}' } dt$. The results are very similar for the uniaxial and plane strain

tension problems. The equivalent stress σ_{eq} takes smaller values in simple shear and its variation with $\bar{\varepsilon}$ is almost linear.

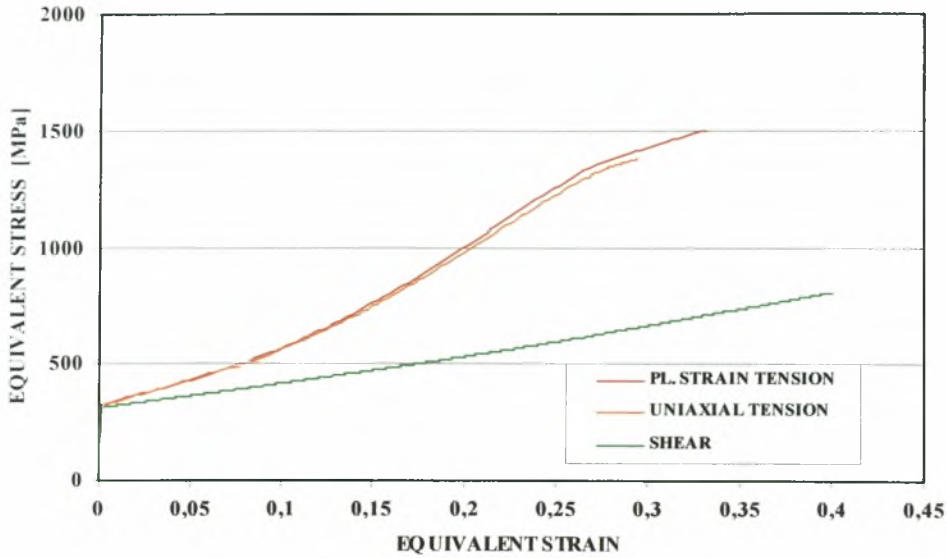


Figure 9.14: Equivalent stress versus equivalent strain $\bar{\varepsilon} = \int \sqrt{\frac{2}{3} \mathbf{D}' : \mathbf{D}' } dt$ for different stress states in room temperature ($T_3 = 23^\circ C$).

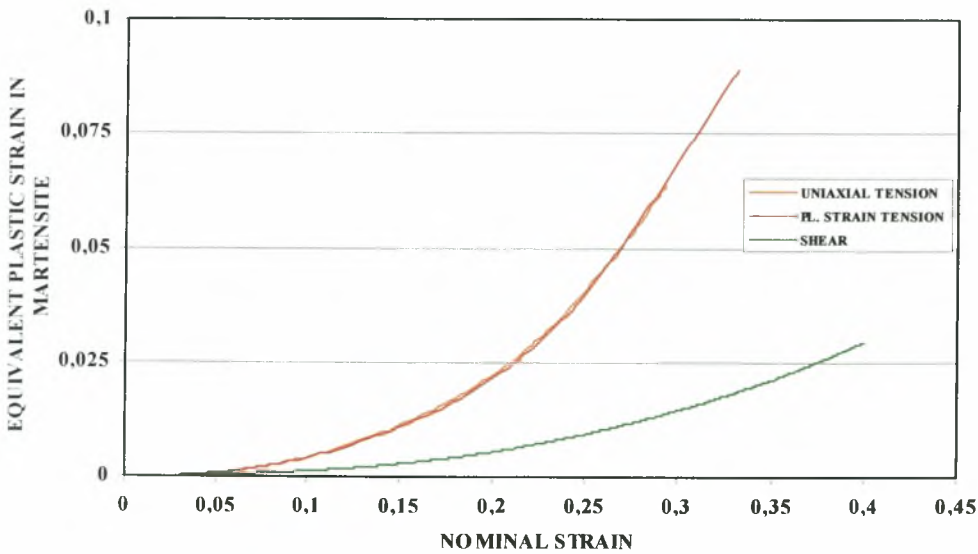


Figure 9.15: Equivalent plastic strain in the composite versus equivalent strain for different stress states in room temperature ($T_3 = 23^\circ C$).

CHAPTER TEN

FINITE ELEMENT RESULTS FOR FOUR-PHASE TRIP STEELS

10.1 Introduction

The constitutive model developed in Chapter 6 for the four-phase TRIP steel is implemented in ABAQUS through the subroutine UMAT and is used to calibrate the model. The model is used then to analyze the problems of uniaxial and plane-strain tension. The model is used also in the following chapters to study the problems of neck development in uniaxial and plane-strain tension and the problem of ductile fracture at a macroscopic blunt crack tip.

10.2 Experimental data used for the calibration of the model

A series of uniaxial tension tests on TRIP steels were carried out by the research group of Prof. Haidemenopoulos at the Laboratory of Materials of the Department of Mechanical and Industrial Engineering of the University of Thessaly. The tests were carried out at two different temperatures $T = 23^{\circ}\text{C}$ (room temperature) and 50°C in the context of an ECSC (2004) research program.

The tensile test specimens were designed according to DIN EN 10002 (Figure 10.1). The measuring range L_0 is 50 mm long. TRIP steel 52122 is used in the experiments; its chemical composition is shown in Table 10.1 and a schematic representation of its heat treatment is shown in Figure 10.2. At the end of the heat treatment, a triple phase microstructure of 50% ferrite, 38% bainite and 12% retained austenite is obtained. The retained austenite of 12% is transformed into martensite as the material deforms plastically. An electron microscopy picture of the corresponding microstructure is shown in Figure 10.3.

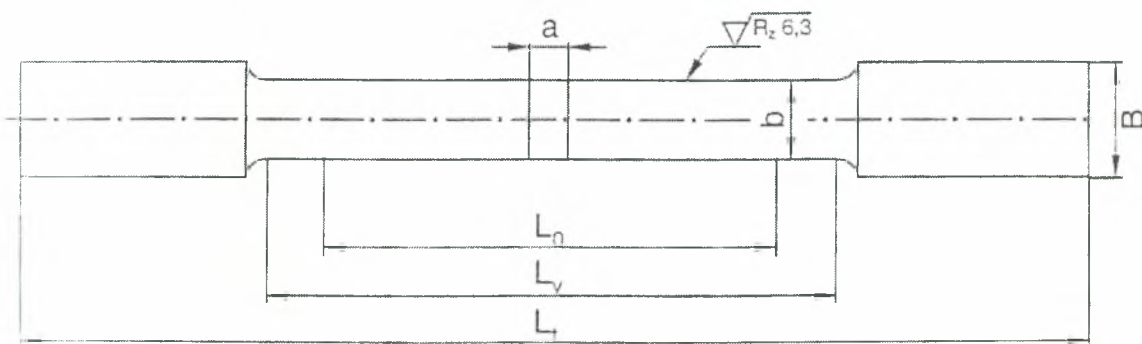


Figure 10.1: Tensile test specimen according to DIN EN 10002.

Steel	C	Mn	Si	Al	P
Lab 5	0.200	1.4	0.5	0.75	0.040

Table 10.1: Chemical composition of TRIP steel 52122.

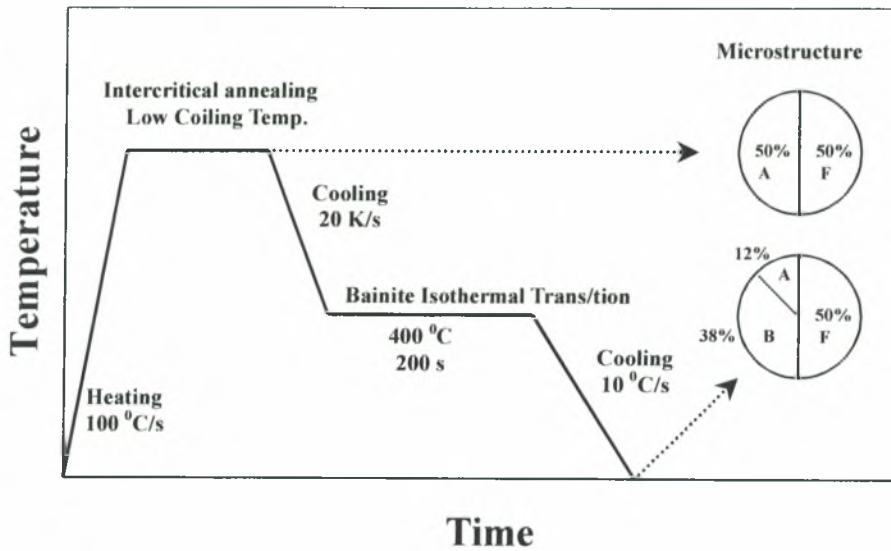


Figure 10.2: Schematic representation of the heat treatment performed for TRIP steel 52122 (A: austenite, B: bainite, F: ferrite).

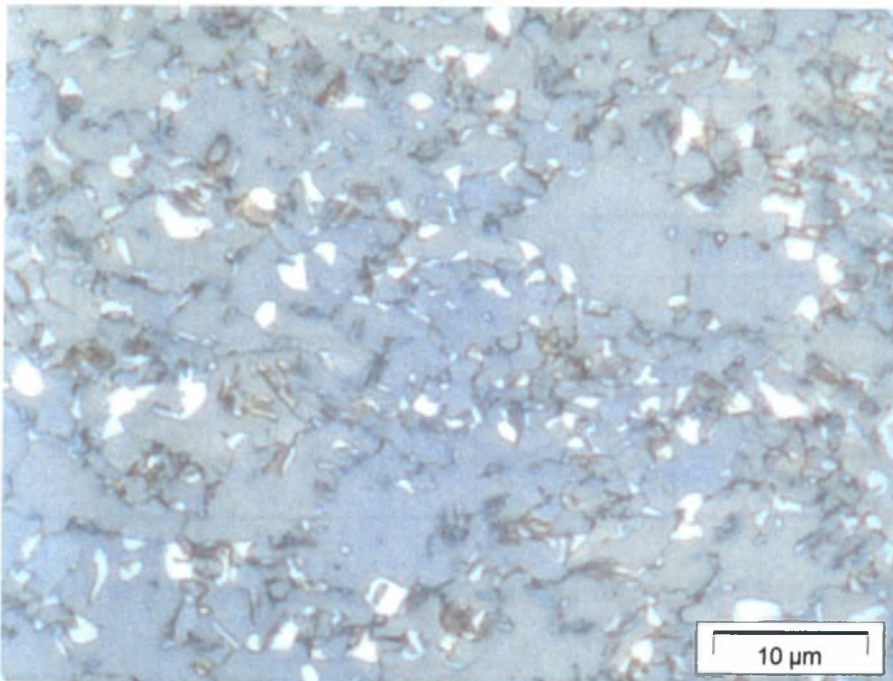


Figure 10.3: Microstructure of TRIP steel 52122.

The tensile tests were interrupted at different stages and the amount of retained austenite was measured (Table 10.2); the results are shown also in Figure 10.4. The corresponding stress-strain curves are shown in Figure 10.5.

The initial amount of martensite appears to be different from zero in Figure 10.4; this is due to the fact that “stress assisted transformation” takes place before macroscopic yielding occurs in the TRIP steel. It should be noted that the constitutive model developed in Chapter 6 accounts only for “plastic strain induced transformation”; therefore, in order to take into account the aforementioned “early transformation”, based on the experimental data, we choose the following initial values for the volume fraction of austenite and martensite: $f_0 = 0.017$, $c_0^{(a)} = 0.12 - f_0 = 0.103$ at room temperature, and $f_0 = 0.013$, $c_0^{(a)} = 0.12 - f_0 = 0.107$ at 50°C .

Test Temp. ($^\circ\text{C}$)	Strain (%)	Austenite (%)	Transf. Aust. (%)
Room temp.	2	10,0	2,0
	4	8,7	3,3
	7	7,6	4,4
	10	5,5	6,5
	15	4,3	7,7
	20	2,7	9,3
50 $^\circ\text{C}$	3	10,2	1,8
	6	9,3	2,7
	10	8,4	3,6
	15	7,1	4,9
	20	6,4	5,6

Table 10.2: Results of retained austenite measurements for TRIP steel 52122.

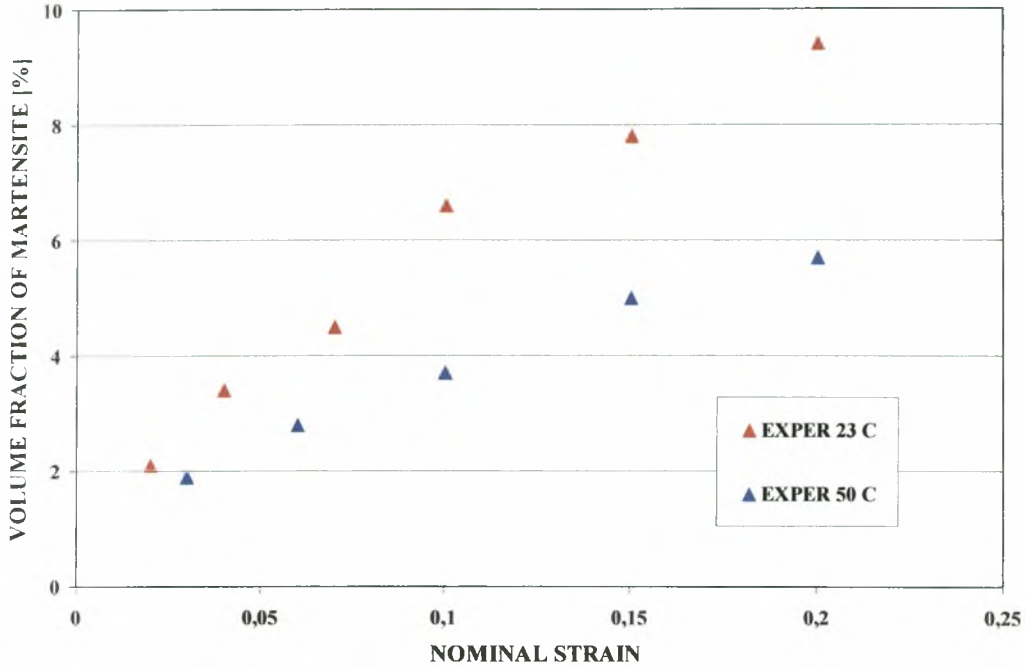


Figure 10.4: Experimental results for the $f - \varepsilon$ curve in TRIP steel 52122.

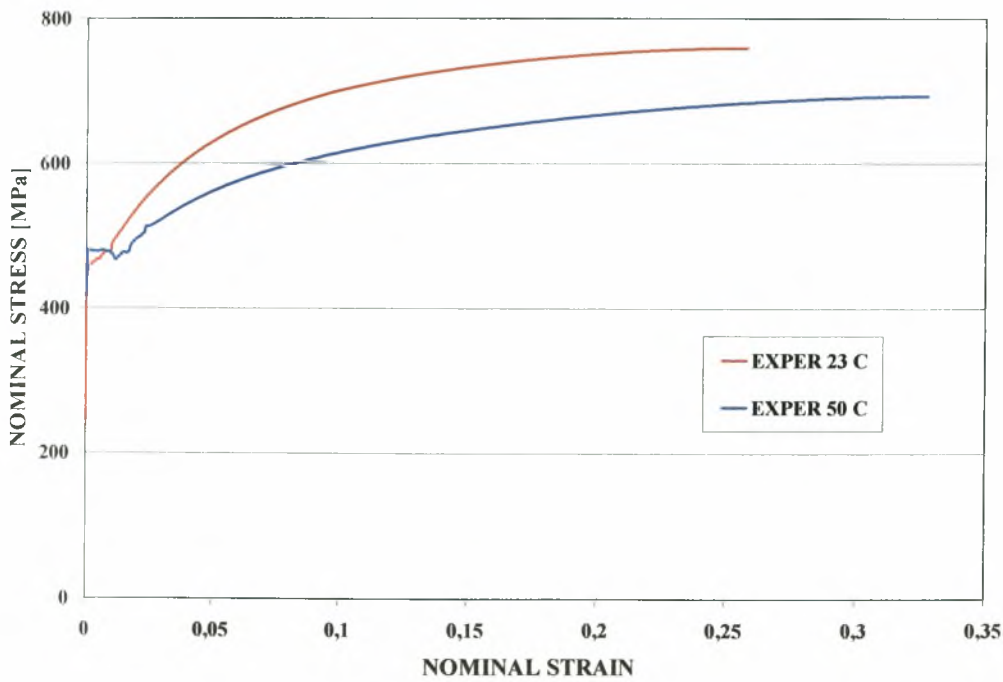


Figure 10.5: Experimental results for the $\sigma - \varepsilon$ curve of TRIP steel 52122.

10.3 A note on the integration scheme: backward vs. forward-backward Euler

As mentioned in Chapter 7, two different schemes were developed for the integration of the constitutive model: a standard backward Euler scheme (BE), and a combination of forward and backward Euler scheme (FBE). Before we proceed to the calibration of the model, we discuss briefly the performance of the two methods. The problem is the same as that described in Section 9.2 and shown in Figure 9.1. One axisymmetric four-node isoparametric element is used (CAX4H) and a total elongation of 30% is imposed in the 2-direction.

The values $E = 200$ GPa and $\nu = 0.3$ for the elastic Young's modulus and Poisson's ratio are used in the calculations. The curves $\sigma_y^{(r)}(\bar{\varepsilon}^{p(r)})$ (in MPa) that define the variation of the flow stress of the four individual phases are those discussed in Chapter 6, i.e.,

For Temperature 23°C :

$$\sigma_y^{(a)} = 300 + 500(\bar{\varepsilon}^{p(a)})^{0.25} \quad (10.1)$$

$$\sigma_y^{(m)} = 1200 + 1025(\bar{\varepsilon}^{p(m)})^{0.13} \quad (10.2)$$

$$\sigma_y^{(3)} = 810 + 753(\bar{\varepsilon}^{p(3)})^{0.25} \quad (10.3)$$

$$\sigma_y^{(4)} = 290 + 690(\bar{\varepsilon}^{p(4)})^{0.47} \quad (10.4)$$

For Temperature 50°C :

$$\sigma_y^{(a)} = 290 + 500(\bar{\varepsilon}^{p(a)})^{0.25} \quad (10.5)$$

$$\sigma_y^{(m)} = 1200 + 1025(\bar{\varepsilon}^{p(m)})^{0.13} \quad (10.6)$$

$$\sigma_y^{(3)} = 800 + 733(\bar{\varepsilon}^{p(3)})^{0.25} \quad (10.7)$$

$$\sigma_y^{(4)} = 265 + 590(\bar{\varepsilon}^{p(4)})^{0.47} \quad (10.8)$$

The values $\dot{\varepsilon}_0^{(a)} = \dot{\varepsilon}_0^{(r)} = \dot{\varepsilon}_0^{(3)} = \dot{\varepsilon}_0^{(4)} = 10^{-4} \text{ sec}^{-1}$ and $m = 60$ are used in the calculations; the macroscopic loading rate is also 10^{-4} sec^{-1} . The relative volume change associated with the martensitic transformation takes the value $\Delta_v = 0.02$. The values $M_{d,ut} = 80^\circ\text{C}$ and $M_{s,ut}^\sigma = 15^\circ\text{C}$ are used in the calculations. The initial values of the volume fractions of the four phases are: $f_0 = 0.017$, $c_0^{(a)} = 0.103$, $c_0^{(3)} = 0.38$ and $c_0^{(4)} = 0.50$ at room temperature, and $f_0 = 0.013$, $c_0^{(a)} = 0.107$, $c_0^{(3)} = 0.38$, $c_0^{(4)} = 0.50$ at 50°C . The parameters used for transformation kinetics model are those listed in Tables 10.4 and 10.5.

The comparison of the two methods is carried out for room temperature only. The analysis is carried out incrementally. First we impose constant displacement increments that correspond to nominal strain increments of $\Delta\varepsilon = 10^{-4}$ at a strain rate of 10^{-4} s^{-1} . Then, the problem is solved by using ten times larger constant strain increments, i.e., $\Delta\varepsilon = 10^{-3}$ at the same strain rate of 10^{-4} s^{-1} . The results are summarized in Figure 10.6: the curves marked BE and FBE correspond to backward-Euler and forward-backward-Euler with $\Delta\varepsilon = 10^{-3}$, whereas BEI and

FBEI indicate the results obtained by using the aforementioned small strain increment of $\Delta\varepsilon = 10^{-4}$. The BESI and FBESI curves coincide and can be thought of as the “exact” solution to the problem. The corresponding CPU times required for these analyses are shown in Table 10.3.

The results shown in Figure 10.6 and Table 10.3 make it clear that the backward Euler scheme is more accurate and more efficient; therefore, we choose to proceed with the backward Euler scheme.

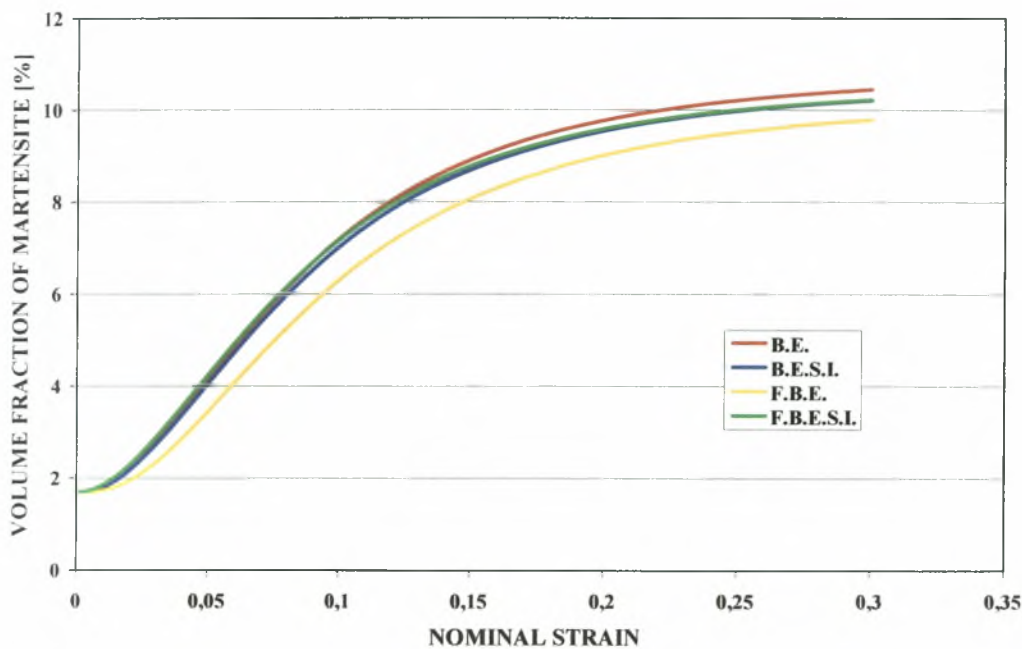


Figure 10.6: Comparison of $f - \varepsilon$ curves for BE and FBE integration schemes.

Integration procedure	INCREMENTS	CPU TIME
BESI	3000	845
FBESI	3000	779
BE	300	115
FBE	300	88

Table 10.3: CPU time required for the one-element uniaxial tension test.

10.4 Calibration of the model

In order to calibrate the constitutive model, we run various one-finite-element calculations and compare the predictions of the model to the experimental data. The experimental data for TRIP steel 52122 presented in section 10.2 are used for the calibration of the parameters that enter the transformation kinetics model for the two temperatures considered, i.e., room temperature and 50°C. The problem is the same as that described in Section 9.2 and shown in Figure 9.1. One axisymmetric four-node isoparametric element is used (CAX4H) and a total elongation of 30% is imposed in the 2-direction.

The values of the parameters listed in the previous section are used in the calculations.

The values of the parameters that enter the transformation kinetics model are chosen so that the predictions of the model agree with the $f - \varepsilon$ curves determined experimentally. The calibration of the model leads to the values shown in Tables 10.4 and 10.5.

r	g_0	g_1	g_2	\bar{g}	s_g	A_0	A_1	s_a^* (MPa)
2.0	3400	4.7	493	3230	292	0.012	0.057	496

Table 10.4: Values used in the kinetics model.

$T(^{\circ}C)$	α	β_0
23	8.7	1.8
50	5.2	1.5

Table 10.5: Values used in the kinetics model.

The values of the constants listed above are used in the calculations that are reported in the following. Figures 10.7 and 10.8 show the experimental and predicted $f - \varepsilon$ and $\sigma - \varepsilon$ curves for the two temperatures considered.

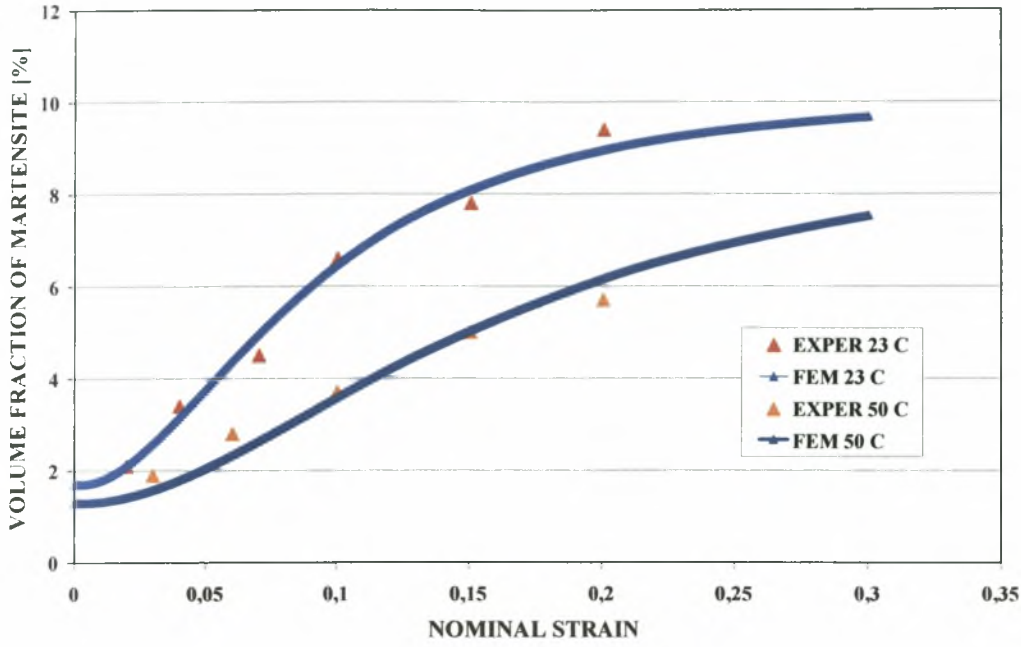


Figure 10.7: $f - \epsilon$ curves in uniaxial tension for room temperature and 50°C .

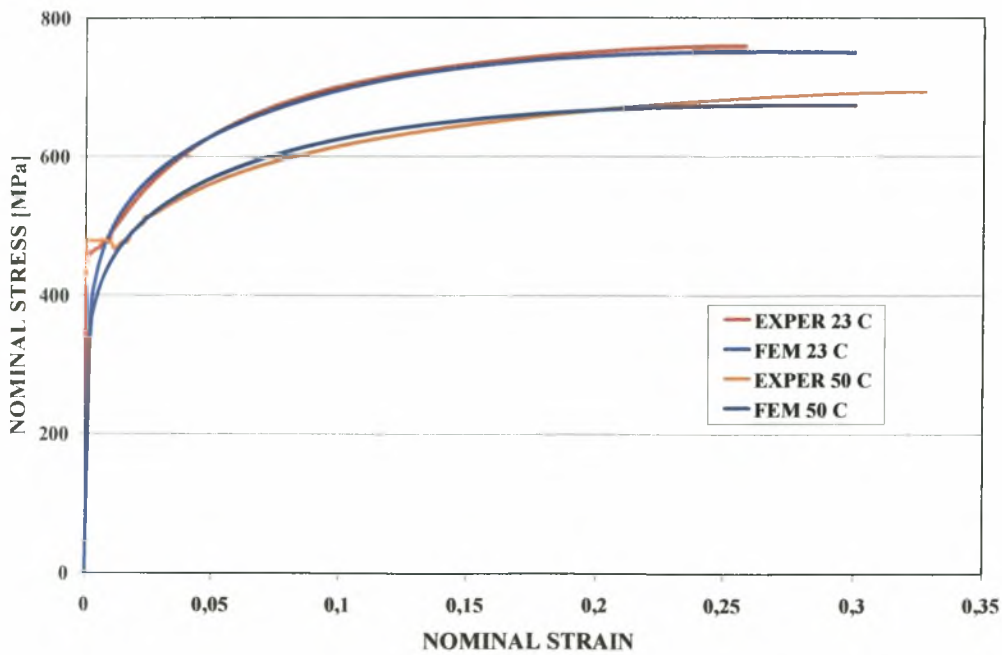


Figure 10.8: Stress-strain curves in uniaxial tension.

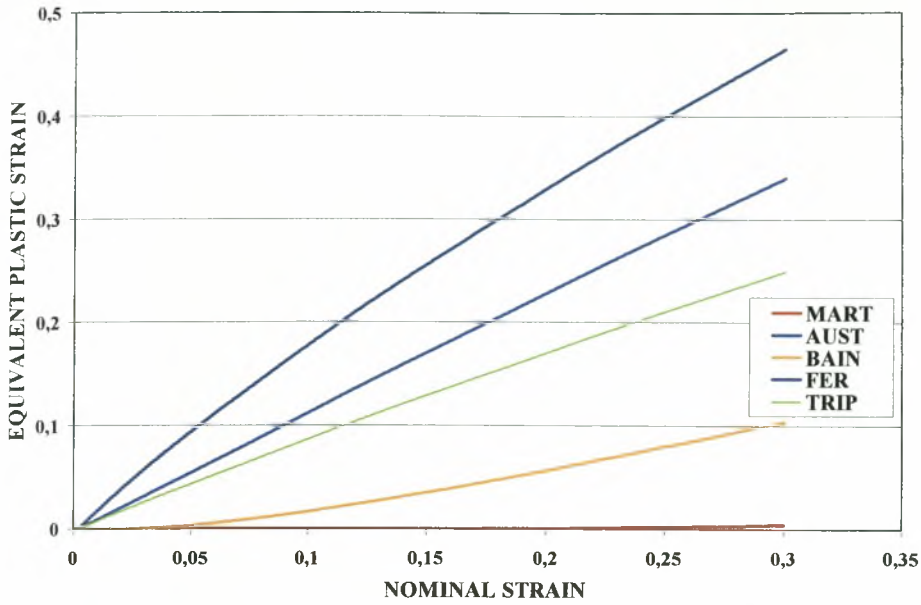


Figure 10.9: Equivalent plastic strain in the individual phases $\bar{\varepsilon}^{p(r)}$ together with equivalent

$$\text{plastic strain in the TRIP steel } \bar{\varepsilon}^p = \int \sqrt{\frac{2}{3} \mathbf{D}^p : \mathbf{D}^p} dt .$$

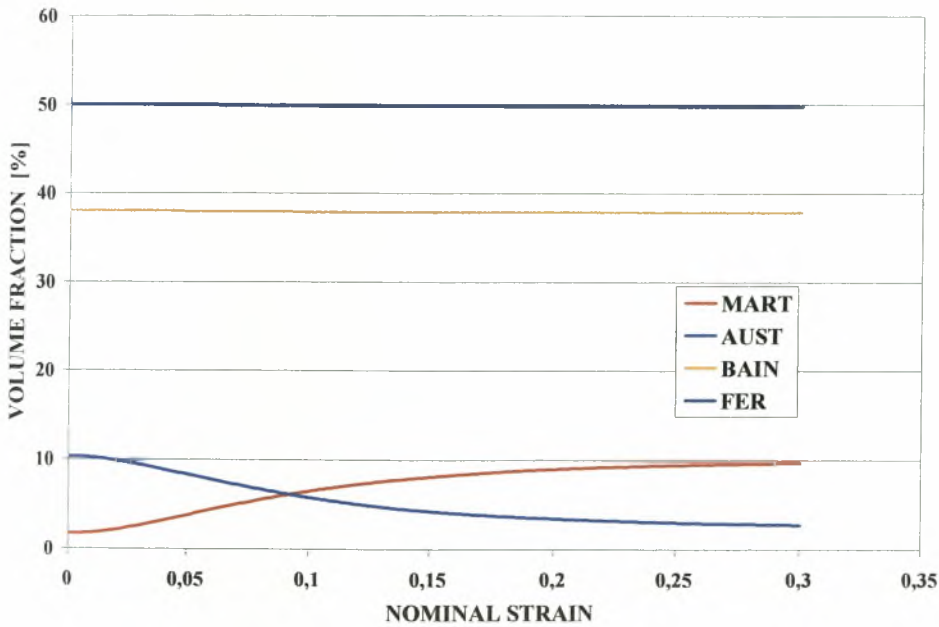


Figure 10.10: Evolution of volume fractions $c^{(r)}$ at room temperature.

Figure 10.9 shows the variation of the equivalent plastic strain $\bar{\varepsilon}^{p(r)}$ in the individual phases and the equivalent plastic strain in the TRIP steel $\bar{\varepsilon}^p = \int \sqrt{\frac{2}{3} \mathbf{D}^p : \mathbf{D}^p} dt$ with the nominal strain at room temperature. As expected, the plastic strain is higher in the “soft” phases (austenite, ferrite) and takes smaller values at the “harder” phases (bainite, martensite).

Figure 10.10 shows the variation of the volume fractions $c^{(r)}$ of the various phases with the nominal strain. It should be noted that the only volume fractions that change substantially are those of austenite and martensite, and this is due to the martensitic transformation that occurs. The corresponding changes are minimal in the non-transforming phases of bainite and ferrite; in these phases, the small change in the volume fraction is due to the increase of the total volume that is caused by the martensitic transformation. Therefore, we can write that $\dot{c}^{(a)} \cong -\dot{c}^{(m)} = -\dot{f}$ and $\dot{c}^{(3)} \cong \dot{c}^{(4)} = 0$.

10.4.1 Uniaxial versus plane-strain tension

In this section we study the problem of plane strain tension in a four-phase TRIP steel and compare the results with those of the uniaxial tension problem reported in the previous section. The material constants are the same as those used in the previous section and the problem formulation is the same as that described in section 9.4.

Figures 10.11-10.14 show the calculated $f - \varepsilon$ and $\sigma - \varepsilon$ curves in uniaxial and plane strain tension at the two temperatures considered.

Figures 10.15 and 10.16 show the variation of the von Mises equivalent stress σ_{eq} and the hydrostatic stress p with the nominal strain for the two problems at room temperature.

It is clear that the resulting f -values are always higher in plane strain. At the same time, the corresponding σ , σ_{eq} and p values are always higher in plane strain. Also the triaxiality Σ takes the values $\Sigma \cong 0.578$ in plane strain tension and $\Sigma \cong 0.333$ in uniaxial tension. The higher stress and triaxiality values that develop in plane strain tension are responsible for the observed higher f -values.

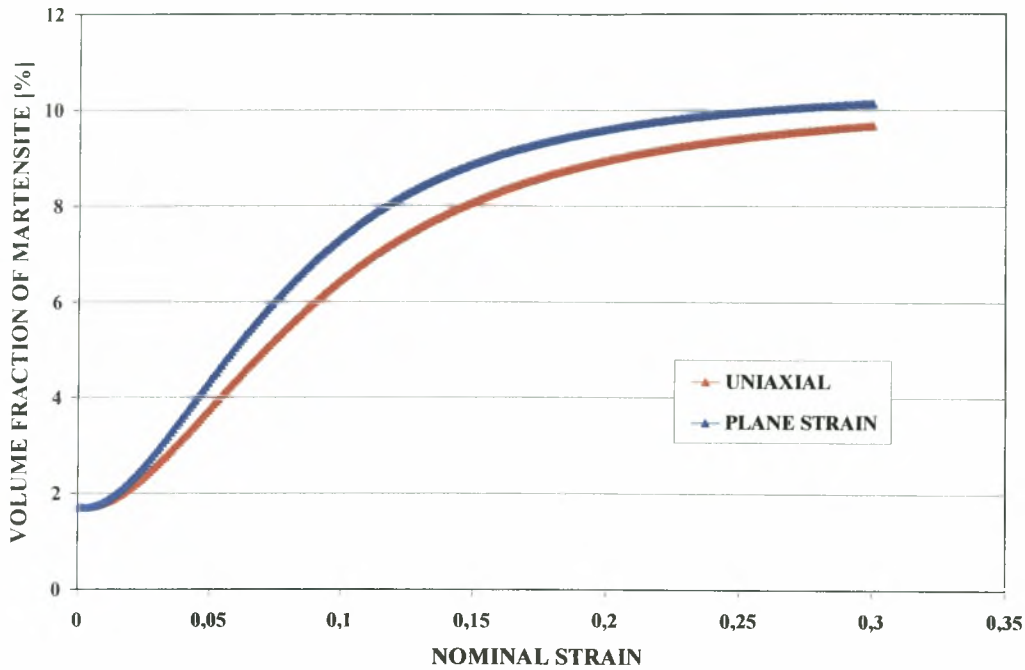


Figure 10.11: Comparison of model predictions for $f - \varepsilon$ curves in uniaxial and plane strain tension at room temperature.

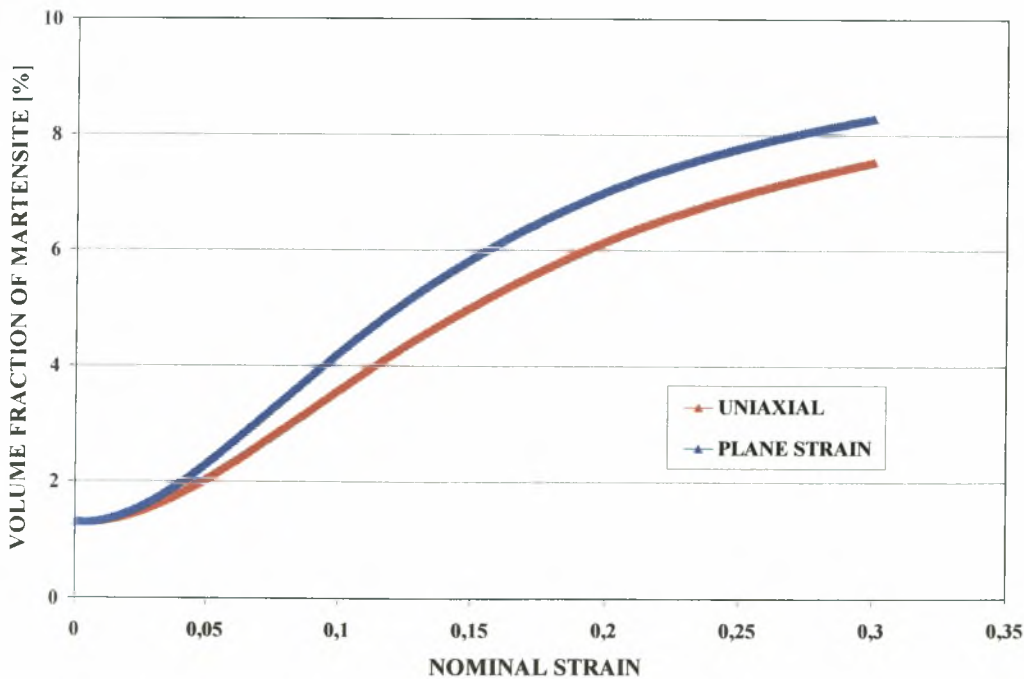


Figure 10.12: Comparison of model predictions for $f - \varepsilon$ curves in uniaxial and plane strain tension at 50°C .

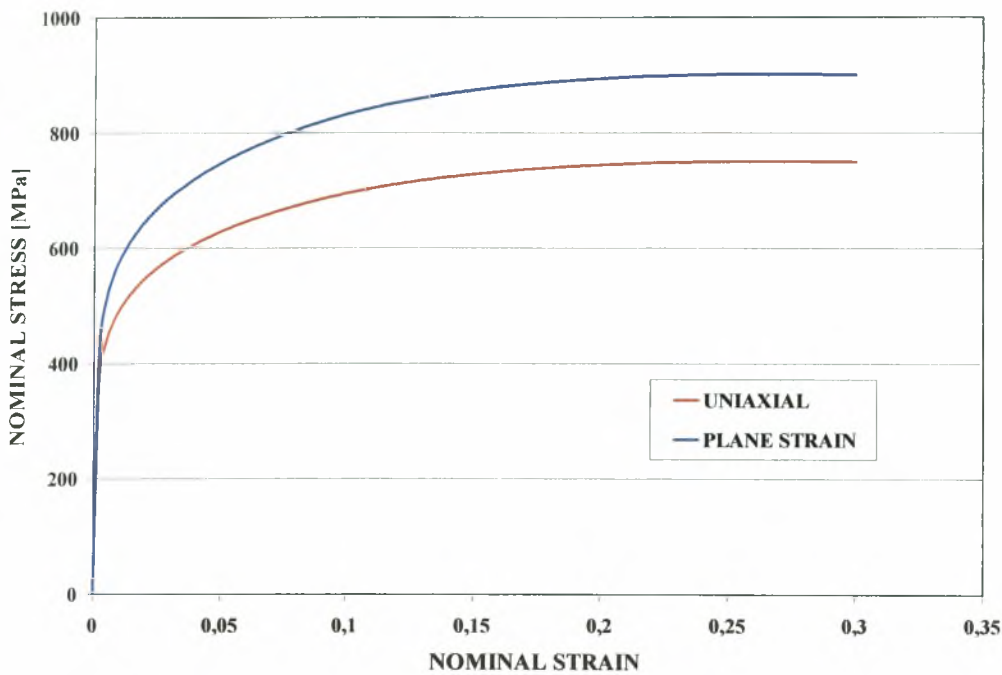


Figure 10.13: Comparison of model predictions for stress-strain curve in uniaxial and plane strain tension at room temperature.

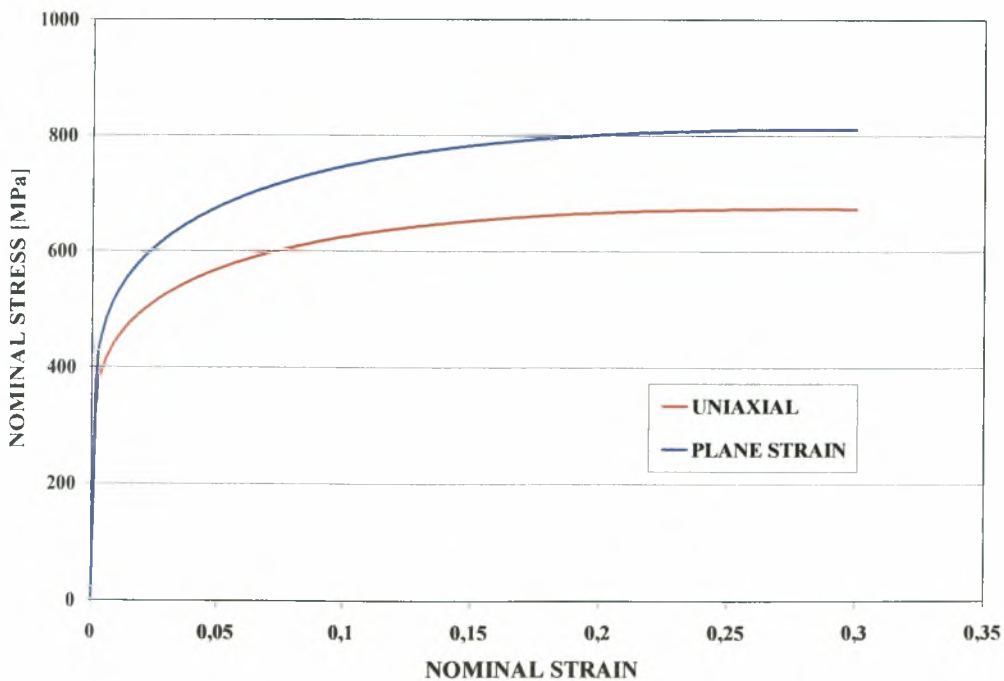


Figure 10.14: Comparison of model predictions for stress-strain curves in uniaxial and plane strain tension at 50°C .

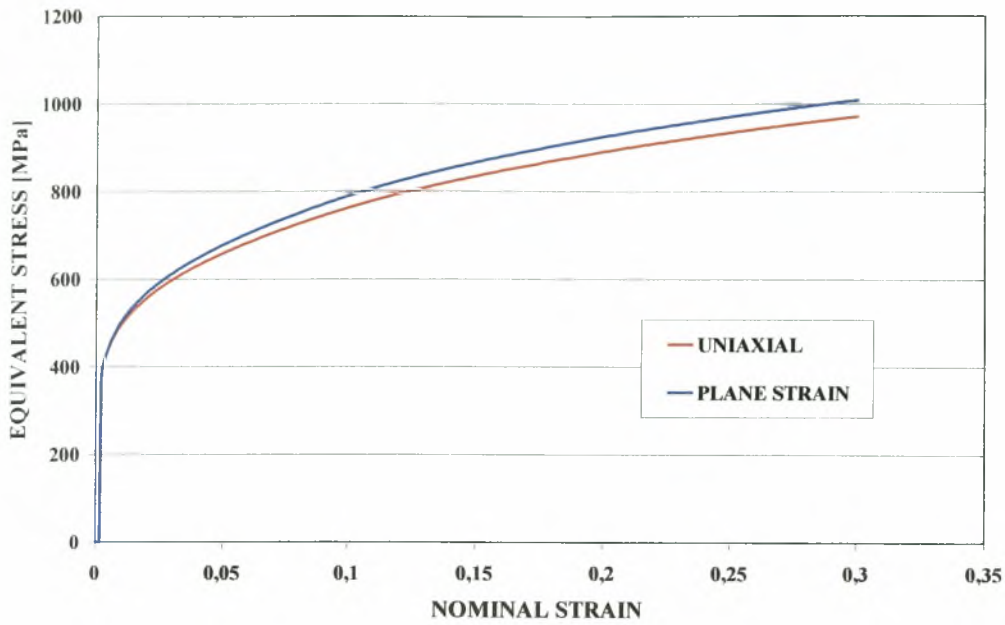


Figure 10.15: Comparison of model predictions for equivalent stress vs. nominal strain in uniaxial and plane strain tension at room temperature.

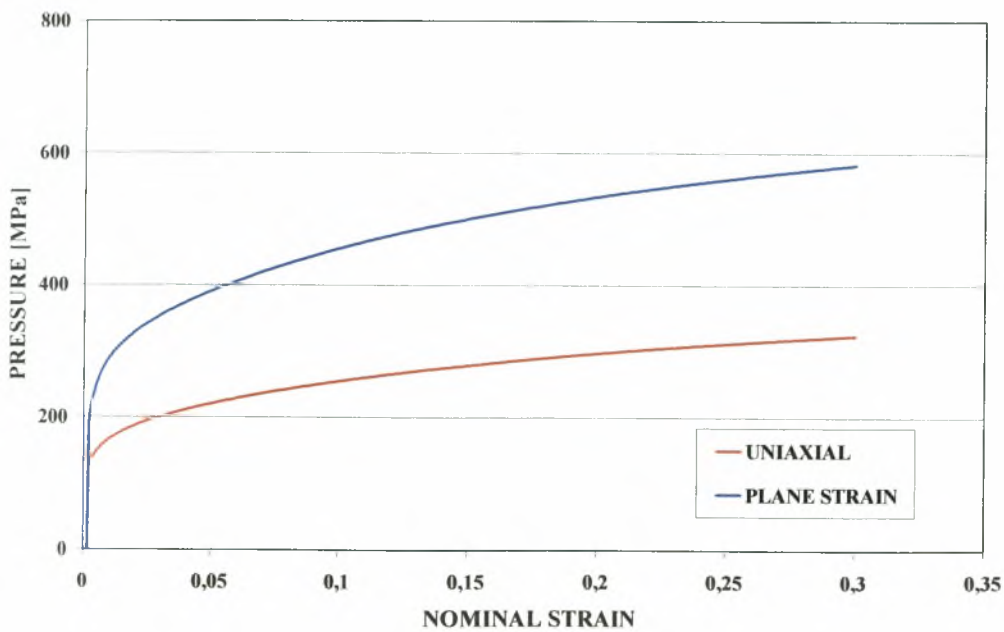


Figure 10.16: Comparison of model predictions for hydrostatic pressure vs. nominal strain tension in uniaxial and plane strain tension at room temperature.

CHAPTER ELEVEN

FINITE ELEMENT RESULTS OF NECKING PROBLEM FOR FOUR-PHASE TRIP STEELS

11.1 Introduction

In this chapter, we use the constitutive model developed for the four-phase TRIP steel to study the development of a neck in a tension specimen. Both uniaxial and plane strain tension are considered and the problem is solved at two different temperatures (room temperature and 50°C). Comparisons are made with the corresponding problems in which martensitic transformation is suppressed.

From a mathematical point of view, necking is a bifurcation of the uniform solution to the problem. It is well known (e.g., Tvergaard, 1985) that bifurcations cannot take place at realistic strain levels when elastic-viscoplastic (as opposed to rate-independent elastic-plastic) constitutive models are used. Therefore, in such problems, bifurcation analyses are replaced usually by studies of the sensitivity of the solution to small imperfections of some sort. Such an imperfection approach is used here in order to study the development of a neck in a tension specimen.

11.2 Simulation of necking in a uniaxial tension test

We consider a cylindrical specimen with aspect ratio $L_0/R_0 = 3$, where $2L_0$ is its initial length and R_0 its initial radius (Figure 11.1). We introduce the cylindrical system shown in Figure 11.2 and identify each material particle in the specimen by its position vector $\mathbf{X} = (r, z)$ in the undeformed configuration. Because of symmetry, only one half of the cylindrical specimen corresponding to $z \geq 0$ is analyzed. The problem is solved by using the ABAQUS general purpose finite element program. The finite element mesh used in the calculations is shown in Figure 11.2; it consists of 675 four-node isoparametric axisymmetric elements (CAX4H in ABAQUS) in a 15×45 grid. In order to promote necking, a geometric imperfection of the following form is introduced (see Figure 11.3):

$$R(z) = R_0 - \xi R_0 \cos \frac{\pi z}{2L_0},$$

where $R(z)$ is the perturbed radius of the specimen and the value $\xi = 0.005$ is used.

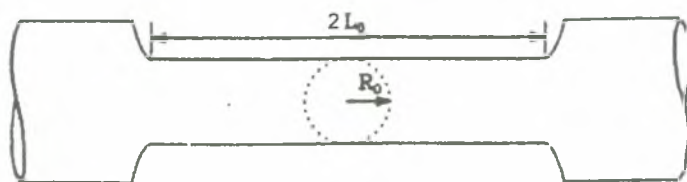


Figure 11.1: The cylindrical specimen analyzed.

All nodes along the midplane $z = 0$ are constrained to move only in the radial direction, and all nodes along the pole (z -axis) are constrained to have zero radial displacement. A schematic representation of the boundary conditions is shown in Figure 11.2.

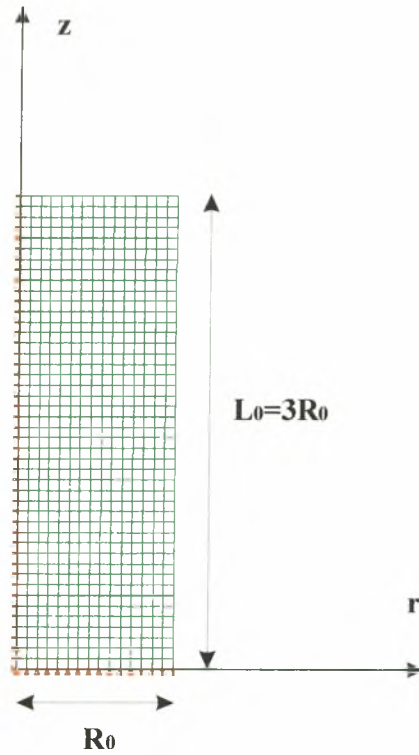


Figure 11.2: The finite element model used for the analysis and a schematic representation of the boundary conditions imposed.

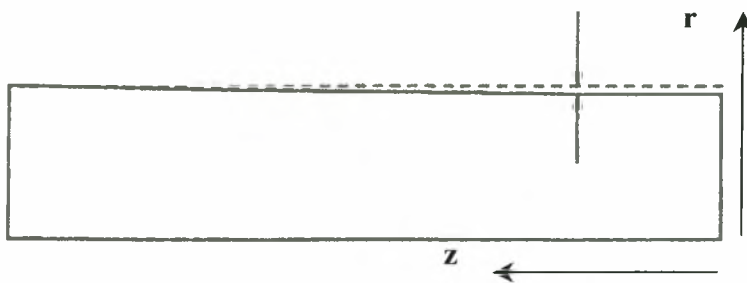


Figure 11.3: Schematic representation of the geometric imperfection.

The deformation is driven by the uniform prescribed end displacement in the z -direction on the shear free top end, while the lateral surface is kept traction free. The material data that resulted from the calibration discussed in Chapter 10 are used in the analysis. The initial values of the volume fractions of the four phases are: $f_0 = 0.017$, $c_0^{(a)} = 0.103$, $c_0^{(3)} = 0.38$ and

$c_0^{(4)} = 0.50$. The macroscopic strain rate imposed is 10^{-4} s^{-1} . The backward Euler method is used for the numerical integration of the constitutive equations. The finite element simulations are carried out in ABAQUS for two temperatures.

For comparison purposes, a separate set of calculations is carried out at room temperature for a “non-transforming” TRIP steel that consists of three phases, i.e., retained austenite, bainite and ferrite with constant volume fractions $f = 0$, $c^{(a)} = 0.12$, $c^{(3)} = 0.38$ and $c^{(4)} = 0.50$.

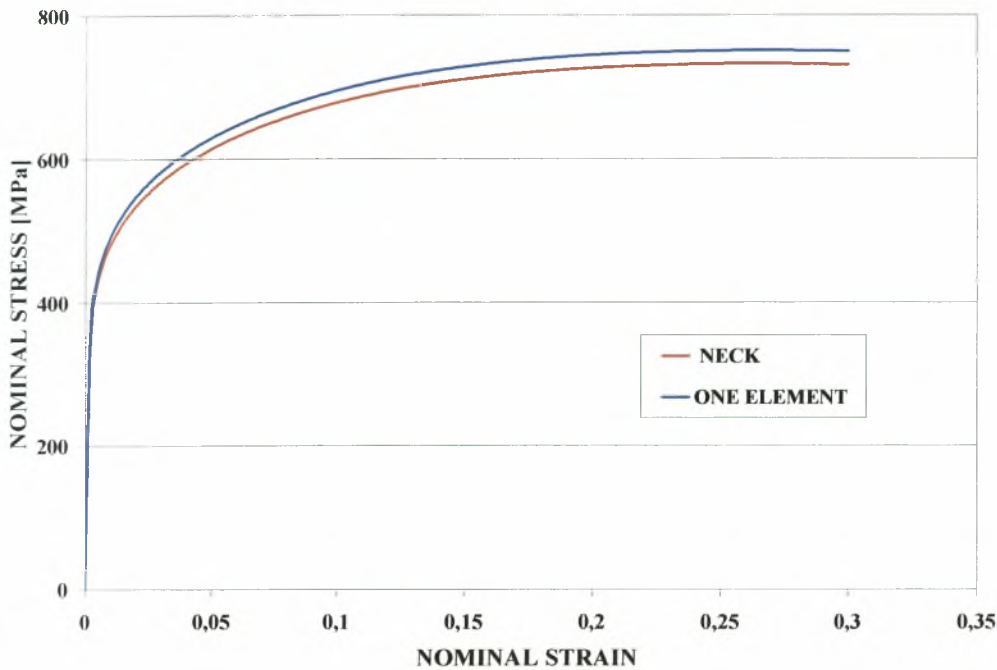


Figure 11.4: Stress-strain curves for the transforming TRIP steel predicted by a necking analysis and the corresponding uniform solution at room temperature.

Figure 11.4 shows the calculated $\sigma - \varepsilon$ curve for the transforming TRIP steel for the necking problem together with the corresponding uniform solution, obtained by carrying out an one-element calculation, at room temperature.

Figure 11.5 shows a three-dimensional representation of the specimen during the evolution of necking for the TRIP steel at room temperature.

Figure 11.6 shows the $\sigma - \varepsilon$ curves for both a transforming and a non-transforming material at room temperature. The arrows on the curves indicate the point of maximum load, which coincides with end of uniform elongation of the specimen. For the transforming (TRIP) steel the end of uniform elongation is observed at a nominal strain of 26.3% and 732 MPa stress, whereas for the non-transforming steel at 20.8% and 677 MPa. Figure 11.6 makes it clear that

the TRIP effect not only hardens the material but also increases substantially the range of uniform elongation.

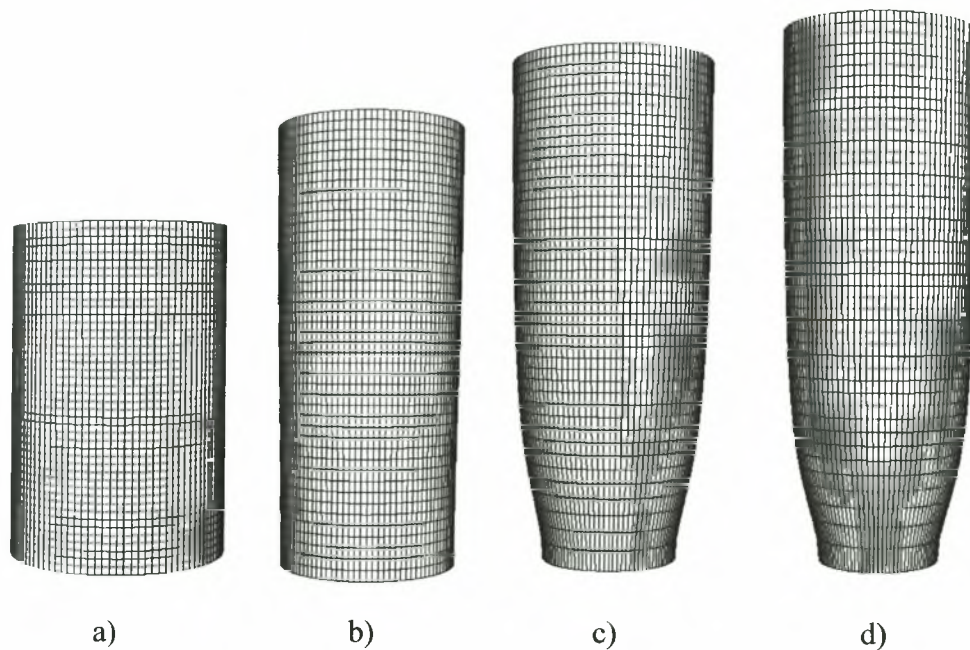


Figure 11.5: 3D representation of the specimen during the evolution of necking for a TRIP steel at room temperature: a) undeformed, b) 40%, c) 50%, d) 57% nominal strain.

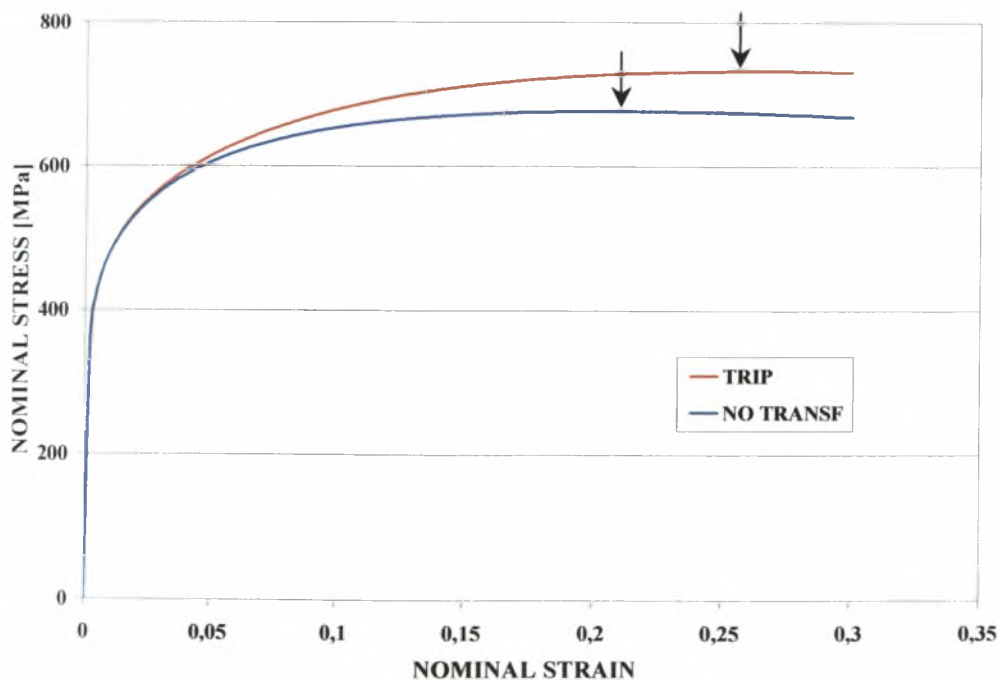


Figure 11.6: Stress-strain curves for a TRIP steel and a “non-transforming” steel at room temperature. Arrows indicate maximum-load position.

Figure 11.7 shows the deformed configurations for the transforming and non-transforming materials. The formation of martensite stabilizes the neck and leads to its propagation down the length of the specimen. At a nominal strain of 50%, the non-transforming material exhibits a 41.3% reduction of its minimum cross section; the corresponding reduction for the TRIP steel is 31.4%.

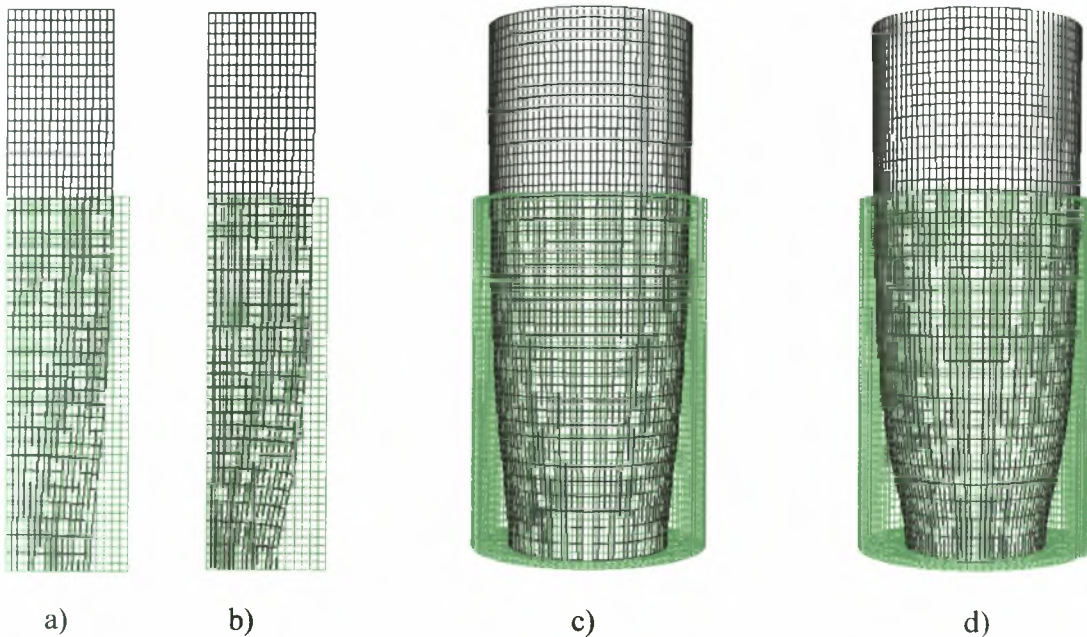


Figure 11.7: Deformed configurations for a nominal strain of 50% at room temperature: (a,c) transforming, (b,d) non-transforming steel.

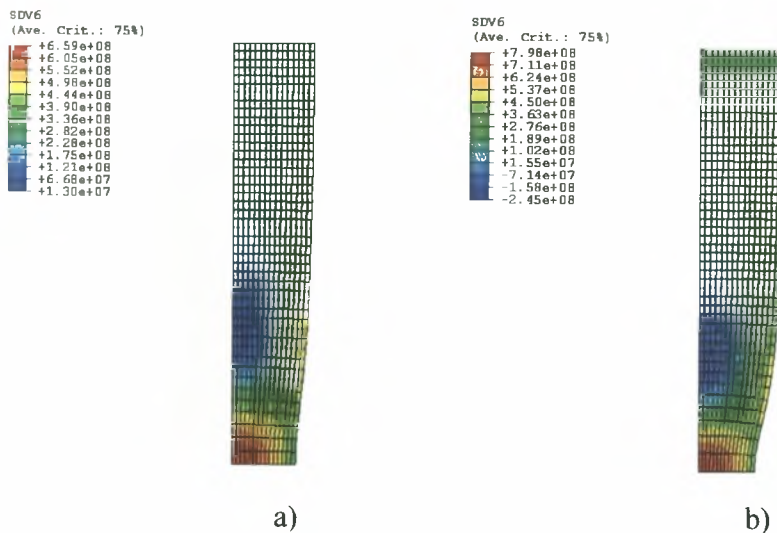


Figure 11.8: Contours of hydrostatic stress $p = \sigma_{kk} / 3$ (in Pa) for a nominal strain of 50% at room temperature: a) transforming, b) non-transforming steel.

Figure 11.8 shows contours of the hydrostatic stress $p = \sigma_{kk} / 3$ for a nominal strain of 50% at room temperature. The contours of the triaxiality ratio $\Sigma = p / \sigma_{eq}$ are similar to those of the hydrostatic stress with Σ taking higher values in the non-transforming case (Figure 11.9). It should be noted that in the case of uniform elongation $\Sigma = 1/3 = 0.333$ everywhere, whereas $\Sigma_{max} \cong 0.520$ for the transforming and $\Sigma_{max} \cong 0.646$ for the non-transforming steel at a nominal strain of 50%; the maximum Σ -value occurs at the center of the neck. Figures 11.10 and 11.11 show contours of the volume fraction of the individual phases $c^{(r)}$ and the corresponding equivalent plastic strains $\bar{\epsilon}^{p(r)}$ for a nominal strain of 50% at room temperature.

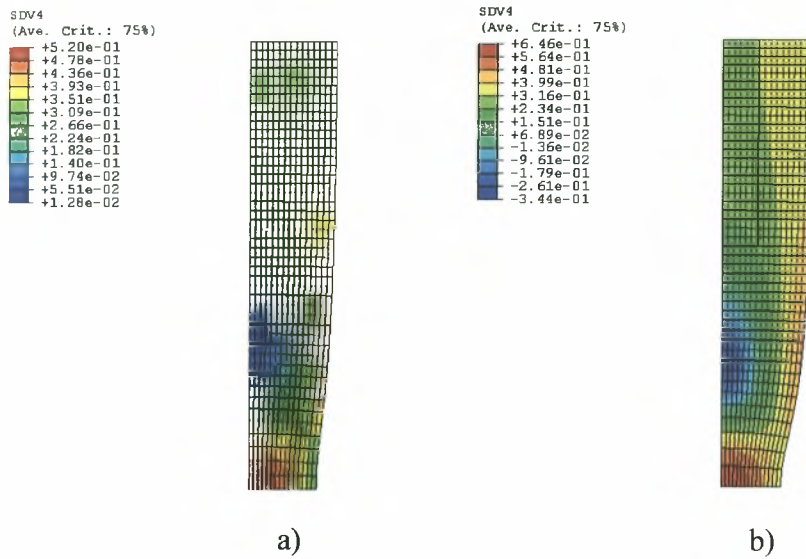


Figure 11.9: Contours of triaxiality ratio $\Sigma = p / \sigma_{eq}$ for a nominal strain of 50% at room temperature: a) transforming, b) non-transforming steel.

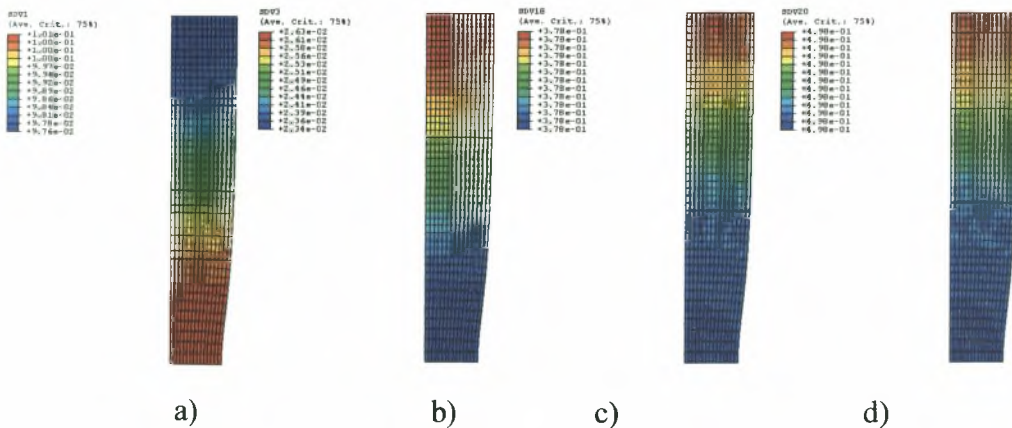


Figure 11.10: Contours of volume fraction of phases for a nominal strain of 50% at room temperature: a) martensite f , b) austenite $c^{(a)}$, c) bainite $c^{(3)}$, d) ferrite $c^{(4)}$.

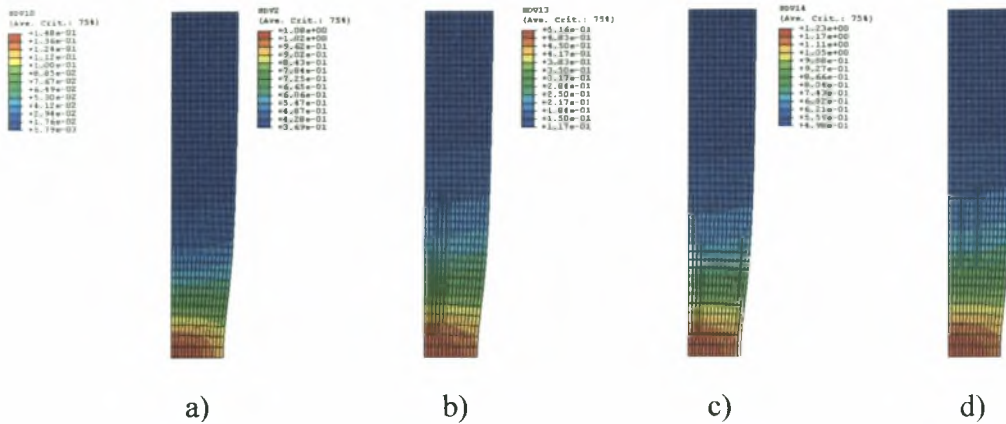


Figure 11.11: Contours of equivalent plastic strain of the phases $\bar{\varepsilon}^{p(r)}$ for a nominal strain of 50% at room temperature: a) martensite, b) austenite, c) bainite, d) ferrite.

The formation of the neck is accompanied by a concentration of strain and an increase in triaxiality (over its level in uniform tension) at the center of the neck. The increased triaxiality at the neck leads to an enhanced driving force for transformation resulting in higher levels of volume fraction of martensite in that region (Figure 11.9).

Close examination of the hydrostatic stress contours of Figure 11.8 shows that p at the center of the neck is higher in the non-transforming specimen. There are two main reasons for this: a) the reduction of the minimum cross section is higher in the non-transforming case, thus causing a higher level of hydrostatic stress (Bridgman, 1952), and b) the transformation of austenite to martensite is accompanied by a local increase in volume which, in turn, lowers the local hydrostatic tension.

The value of the triaxiality ratio $\Sigma = p/\sigma_{eq}$ also takes a lower value at the center of the TRIP specimen relative to the non-transforming case. This is because p is lower locally for the TRIP specimen and, at the same time, the transformation of retained austenite to martensite causes a higher level of hardening in the neck region, i.e., increases σ_{eq} locally in the TRIP steel.

In the following we study the necking problem at 50°C. Figure 11.12 shows the stress-strain curves for a necking TRIP specimen at room temperature and 50°C. The two arrows on the curves indicate again the point of maximum load. For the case of room temperature the end of uniform elongation is observed at a nominal strain of 26.3% and 732 MPa stress, whereas at 50°C the corresponding values are 28% and 657 MPa. The neck formation is more

pronounced at room temperature (Figure 11.13). The predicted lower level of uniform elongation at room temperature is in agreement with experimental observations.

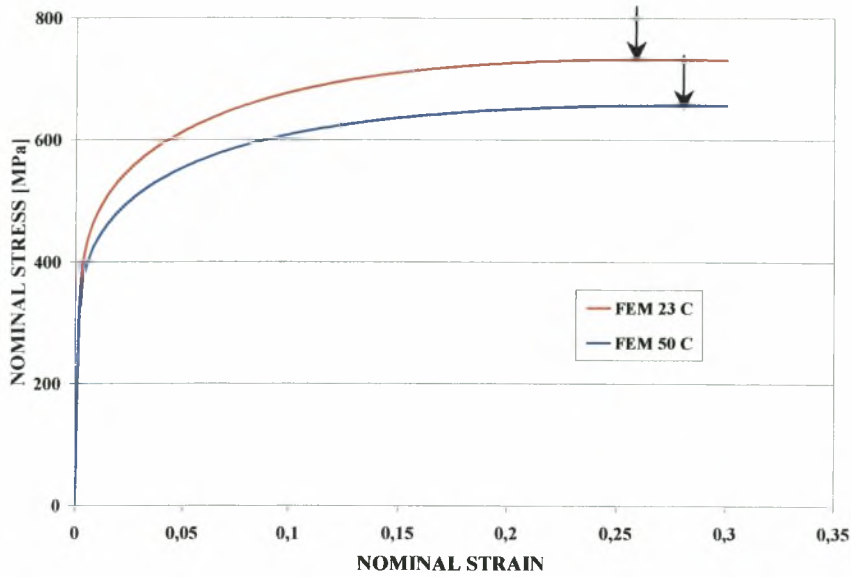


Figure 11.12: Stress-strain curves for room temperature and 50°C in uniaxial tension.

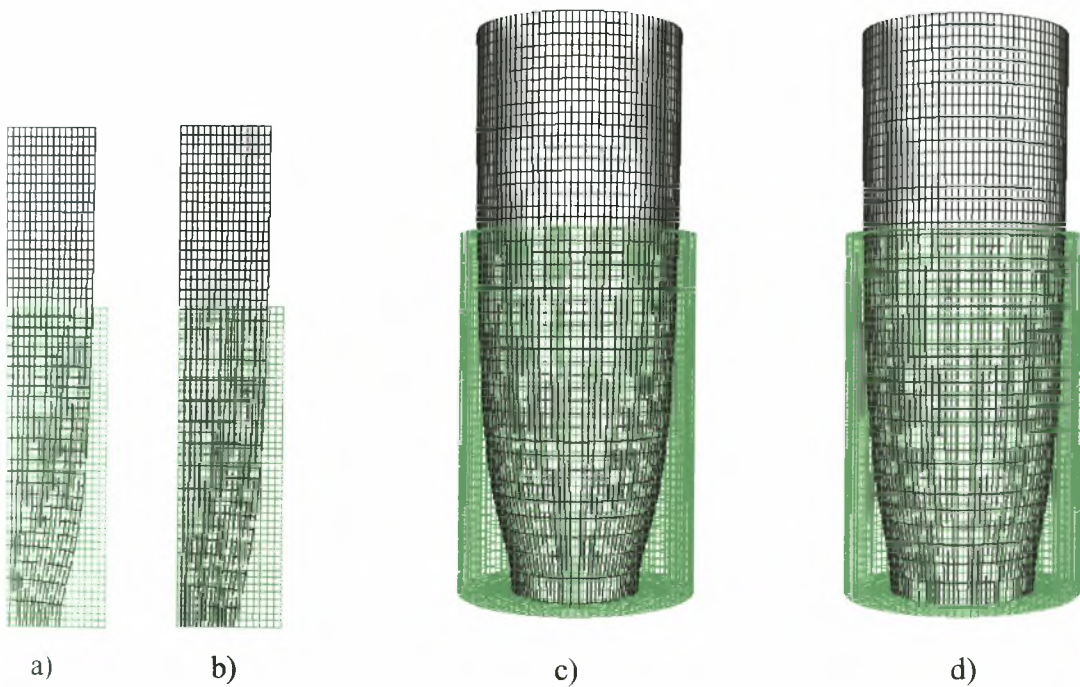


Figure 11.13: Deformed configurations of TRIP specimens for a nominal strain of 57% at (a,c) room temperature, (b,d) 50°C .

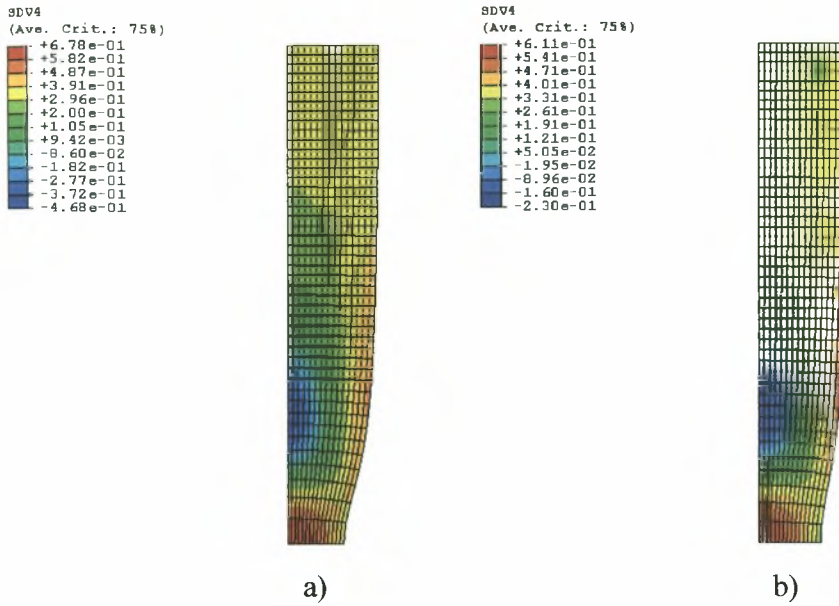


Figure 11.14: Contours of triaxiality ratio for nominal strain of 57% at: a) room temperature, b) 50°C.

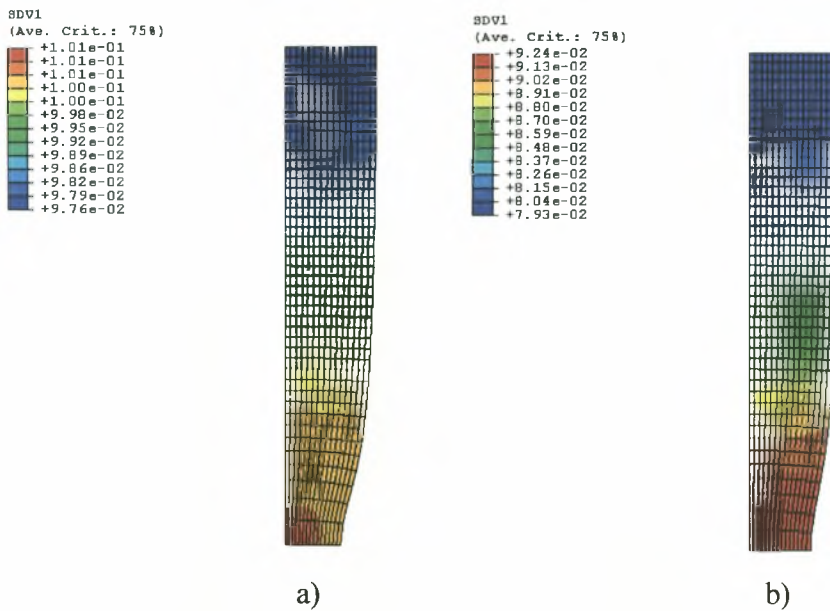


Figure 11.15: Contours of volume fraction f of martensite for a nominal strain of 57% at: a) room temperature, b) 50°C.

Figures 11.14 and 11.15 show contours of the triaxiality ratio $\Sigma = p/\sigma_{eq}$ and the martensite volume fraction f at the two temperatures analyzed for a nominal strain of 57%. Both Σ and f at the center of the neck take higher values at room temperature. The higher f -value at room temperature is due to the fact that the driving force for martensitic transformation

increases with decreasing temperature. In fact, the lower level of uniform elongation observed at room temperature is a result of the increased martensitic formation at this temperature.

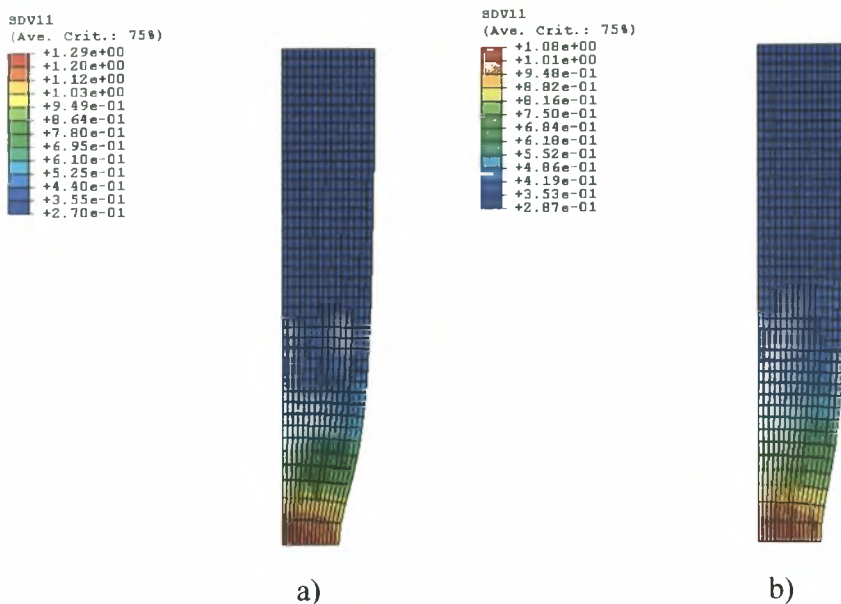


Figure 11.16: Contours of equivalent plastic strain $\bar{\epsilon}^p = \int \sqrt{\frac{2}{3} \mathbf{D}^p : \mathbf{D}^p} dt$ for a nominal strain of 57% at: a) room temperature, b) 50°C .

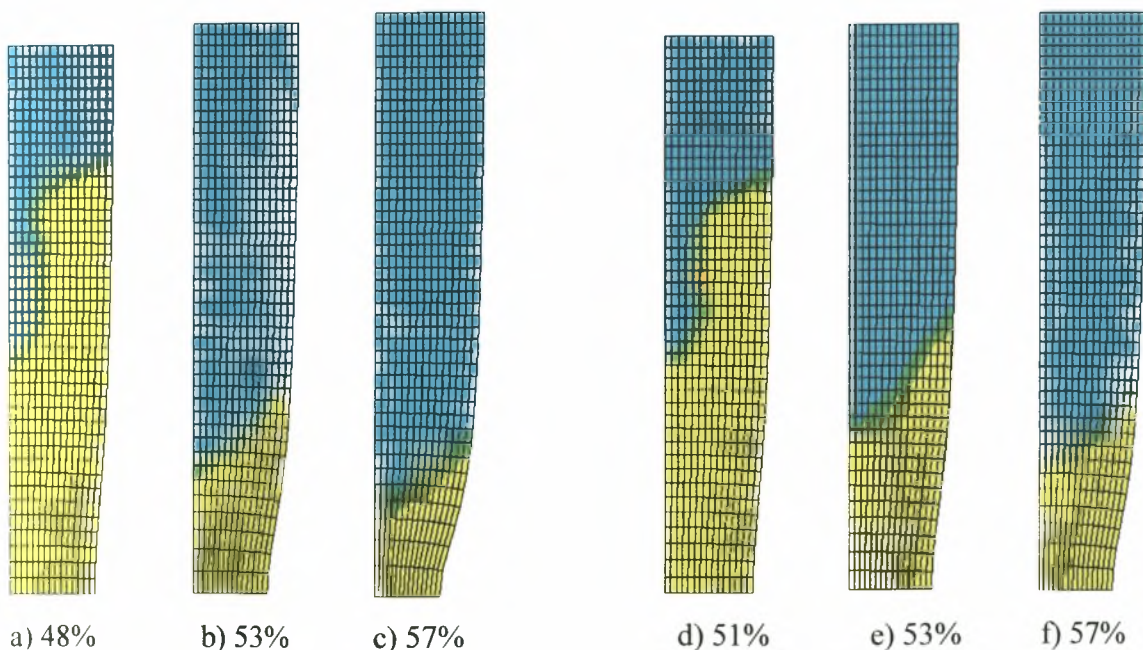


Figure 11.17: Plastic zones (yellow regions) for different strain levels: (a,b,c) room temperature, and (d,e,f) 50°C .

Figure 11.16 shows contours of the equivalent plastic strain $\bar{\varepsilon}^p = \int \sqrt{\frac{2}{3} \mathbf{D}^p : \mathbf{D}^p} dt$ for a nominal strain of 57% at room temperature and at 50⁰C . Higher plastic strains occur at room temperature.

Figure 11.17 shows the evolution of the plastic zone in the specimens after the necks have been formed. In all cases, the neck develops gradually and the first elastic unloading appears at the upper-left corner of the mesh at 48% nominal strain for room temperature; the corresponding value at 50⁰C is 51%.

11.3 Simulation of necking in a plane strain tension test

A similar finite element analysis of necking of a bar is carried out under plane strain conditions. A schematic representation of the plane strain specimen is shown in Figure 11.18. The initial imperfection, the finite element mesh, the loading rate and the material properties used are identical to those of the axisymmetric problem discussed in the previous sections. The analysis is carried out by using CPE4H elements in ABAQUS at room temperature and 50⁰C . The backward Euler method is used for the integration of all the constitutive equations.

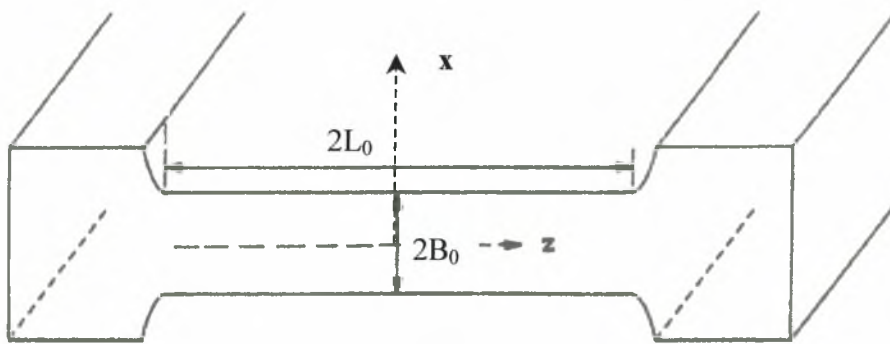


Figure 11.18: The rectangular specimen analyzed.

Figure 11.19 shows the $\sigma - \varepsilon$ curves for a transforming and a non-transforming material at room temperature and at 50⁰C for plane strain conditions. Figure 11.20 shows the $\sigma - \varepsilon$ curves for the TRIP steel at room temperature and at 50⁰C . Again, the two arrows on the curves indicate the point of maximum load, which coincides with end of uniform elongation of the specimen. At room temperature, for the transforming (TRIP) steel the end of uniform

elongation is observed at a nominal strain of 26.4% and 882 MPa stress, whereas for the non-transforming steel at 20% and 808 MPa. The corresponding values at 50°C are 28.5% and 793 MPa for the transforming, and 26.4% and 882 MPa for the non-transforming steel.

The conclusions are the same as those of the case of uniaxial tension: the TRIP effect hardens the material and increases substantially the range of uniform elongation. The TRIP effect is more pronounced at room temperature.

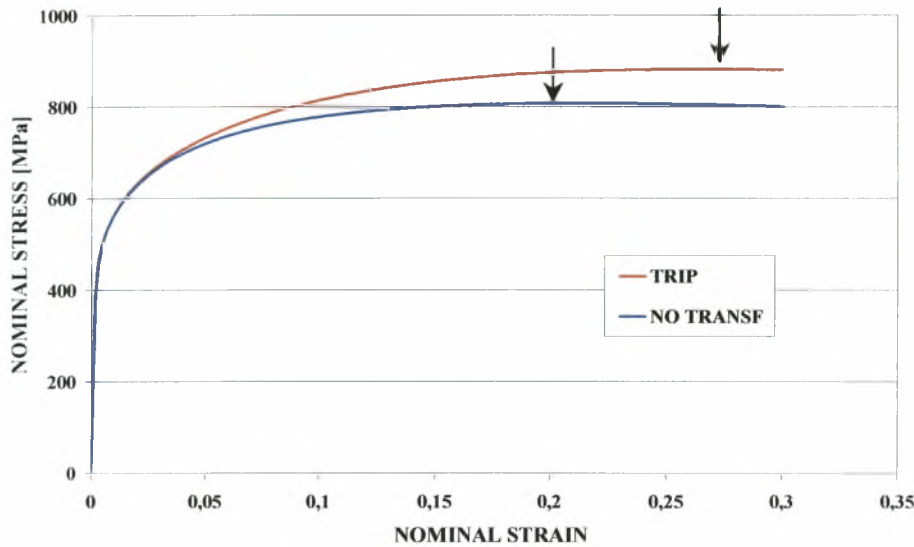


Figure 11.19: Stress-strain curves for a TRIP steel and a “non-transforming” steel in plane strain tension at room temperature.

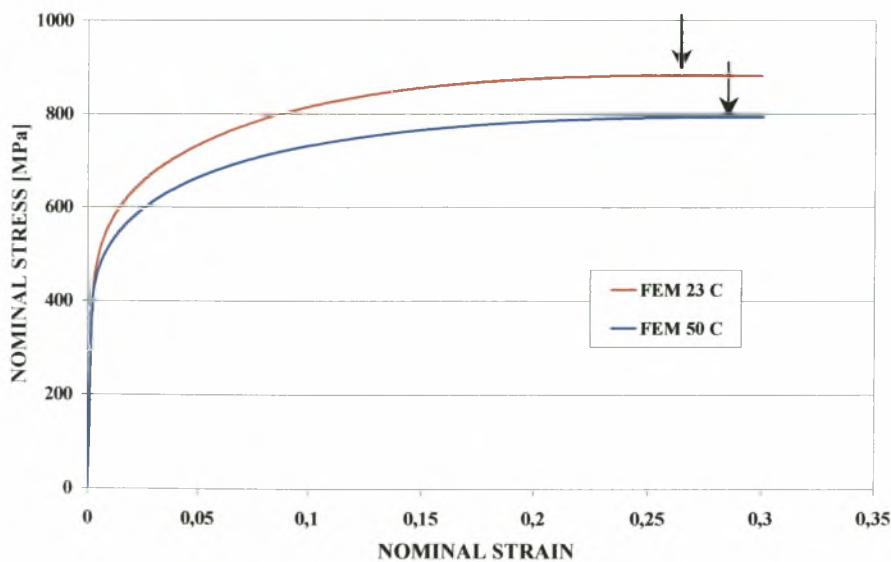


Figure 11.20: Stress-strain curves for room temperature and 50°C in plane strain tension.

11.4 Comparison of neck formation in uniaxial and plane strain tension

Figure 11.21 shows the undeformed and deformed configurations at a nominal strain of 50% for the cases of uniaxial and plane strain tension at room temperature. The neck in plane strain tension is much less developed and the deformed configuration reminds us of cold drawing rather than necking. A similar behavior has been observed by Stringfellow (1990) for two-phase TRIP steels.

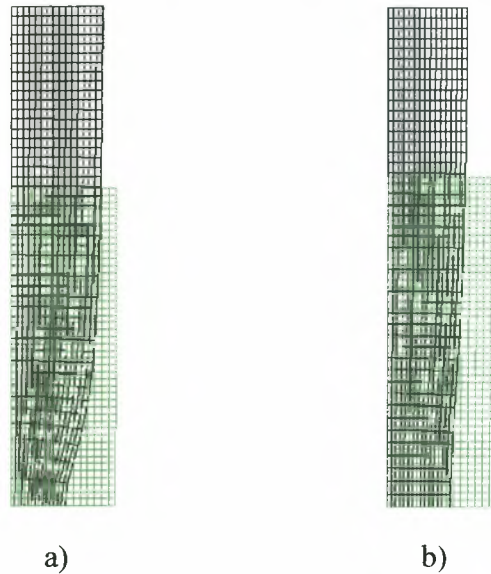


Figure 11.21: Deformed and undeformed configurations for a nominal strain of 50% at room temperature: a) uniaxial tension, b) plane strain tension.

Before the neck develops, the state of stress in plane strain tension is uniform and is given approximately by

$$\sigma_{zz} \cong \sigma, \quad \sigma_{yy} \cong \frac{\sigma}{2}, \quad \text{all other components } \sigma_{ij} = 0,$$

so that

$$\sigma_{eq} = \sqrt{\frac{3}{2} s_{ij} s_{ij}} \cong \frac{\sigma\sqrt{3}}{2}, \quad p = \frac{\sigma_{kk}}{3} \cong \frac{\sigma}{2} \quad \text{and} \quad \Sigma = \frac{p}{\sigma_{eq}} \cong \frac{1}{\sqrt{3}} = 0,577,$$

where the stress components are referred to the coordinate axes shown in Figure 11.18. The corresponding uniform triaxiality is lower in uniaxial tension and takes the value $\Sigma = 1/3 = 0,333$.

Figure 11.22 shows triaxiality contours **after** the neck develops in uniaxial and plane strain tension. At a nominal strain of 57%, in plane strain tension a small fluctuation of the triaxiality ratio from $\Sigma = 0,565$ to $0,611$ is observed; at the same nominal strain in a uniaxial

tension test the triaxiality takes a high value in the neck region ($\Sigma = 0,520$) and much lower values in the rest specimen ($\Sigma = 0,182$ to $0,350$). The larger triaxiality value in plane strain results in an enhanced driving force for transformation and a larger amount of martensite (Figure 11.23). The uniform and rapid evolution of martensite through the specimen in plane strain tension is responsible for the uniform raise in the hardening level of the specimen, which results in a diffusion of the neck as indicated by the much smoother specimen profile.

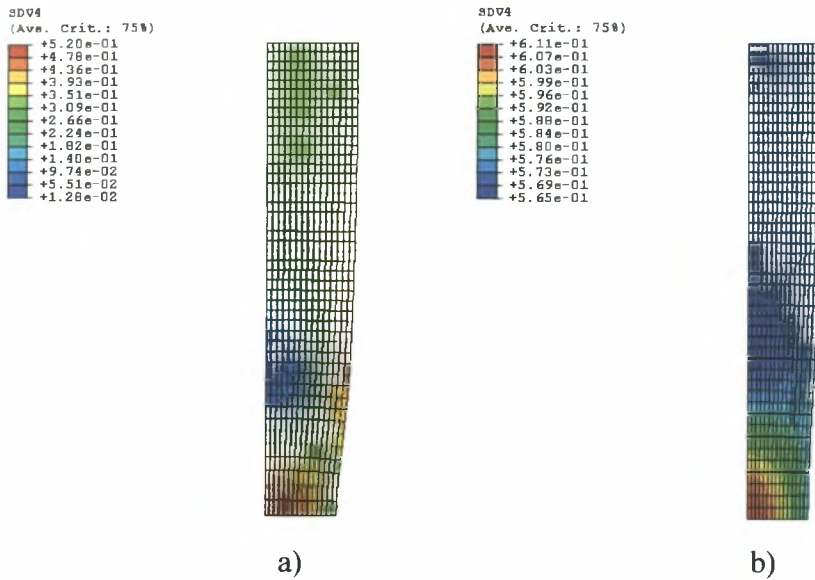


Figure 11.22: Contours of triaxiality ratio Σ for a nominal strain of 57% at room temperature: a) uniaxial tension, b) plane strain tension.

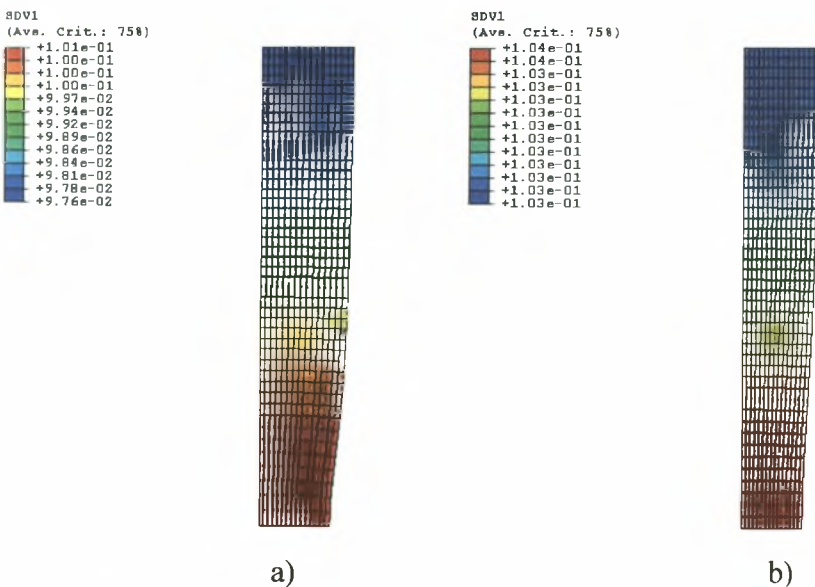


Figure 11.23: Contours of volume fraction of martensite f for a nominal strain of 57% at room temperature: a) uniaxial tension, b) plane strain tension.

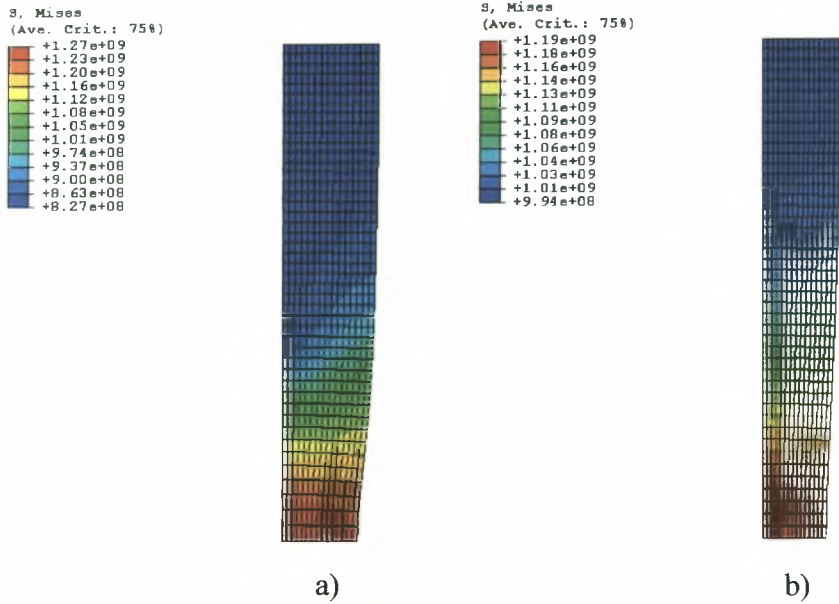


Figure 11.24: Contours of von Mises equivalent stress (in Pa) for a nominal strain of 57% at room temperature: a) uniaxial tension, b) plane strain tension.

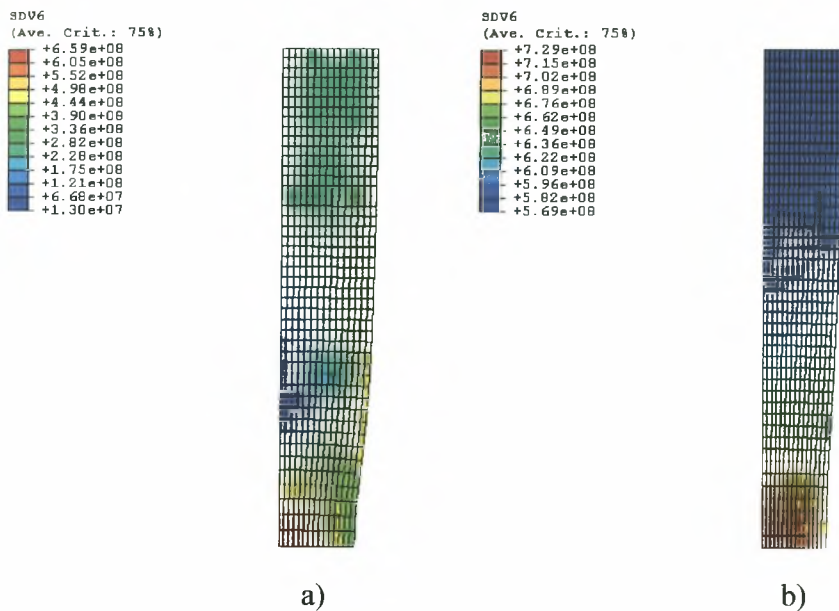


Figure 11.25: Contours of hydrostatic stress (in Pa) for a nominal strain of 57% at room temperature: a) uniaxial tension, b) plane strain tension.

Under plane strain conditions the deformation is constrained in the out-of-plane direction leading to a more intense 3D stress field relative to the uniaxial tension case where no constraint is imposed. Figures 11.24-11.26 show contours of the von Mises equivalent stress

σ_{eq} , the hydrostatic stress p , and the equivalent plastic strain $\bar{\epsilon}^p = \int \sqrt{\frac{2}{3} \mathbf{D}^p : \mathbf{D}^p} dt$ for

uniaxial and plane strain tension tests at a nominal strain of 57% at room temperature. In uniaxial tension, the development of neck leads to a high value of the von Mises equivalent stress in the neck; in plane strain tension, a more uniform distribution of σ_{eq} is observed, with the maximum value appearing in the region near the minor neck. The higher value of hydrostatic pressure in plane strain tension relative to uniaxial tension is a result of the constraint in deformation in the-out-of plane direction. The contours of the equivalent plastic strain shown in Figure 11.26 are similar to those of σ_{eq} .

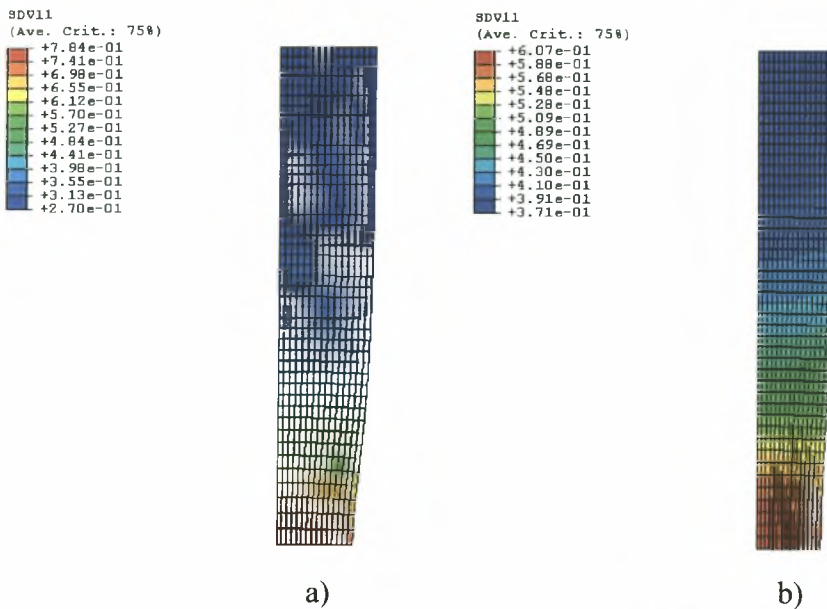


Figure 11.26: Contours of equivalent plastic strain $\bar{\epsilon}^P = \int \sqrt{\frac{2}{3} \mathbf{D}^P : \mathbf{D}^P} dt$ for a nominal strain of 57% at room temperature: a) uniaxial tension, b) plane strain tension.

11.5 Summary of necking analysis

The comparison of transforming and non-transforming steels leads to the conclusion that the TRIP effect leads to stabilization of necking, causes propagation of the neck down the length of the specimen, and increases substantially the uniform elongation and hardening of the steel. The driving force for martensitic transformation increases with decreasing temperature. Therefore, the TRIP effect is more pronounced at room temperature and leads to higher levels of hardening. The lower level of uniform elongation observed at room temperature is a result of the massive martensitic formation at this temperature. This observation agrees with experimental results.

Comparison of the neck formation under uniaxial and plane strain tension conditions leads to the conclusion that the uniform and rapid evolution of martensite through the plane strain specimen is responsible for the uniform raise of the hardening level, which causes, in turn, a diffusion of the neck as indicated by the much smoother specimen profile shown in Figure 11.21.

CHAPTER TWELVE

FINITE ELEMENT RESULTS OF A MODE-I CRACK PROBLEM FOR FOUR-PHASE TRIP STEELS

12.1 Introduction

In this chapter, we use the constitutive model developed for the four-phase TRIP steel to study the problem of a plane strain mode-I blunt crack under small scale yielding conditions. The fracture properties of a material depend upon the state of stress and strain in the vicinity of the crack tip. Therefore, we examine the crack problem in order to better understand how martensitic transformation affects the fracture resistance of TRIP steels. The concept of small scale yielding implies that the size of the plastic deformation zone is small in comparison to any other relevant length scales, i.e. the length of the crack, or the width of the specimen.

The problem of crack is solved for two temperatures and comparisons are made with corresponding problems in which martensitic transformation is suppressed.

12.2 FEM simulation of crack

We consider the problem of a plane strain mode-I blunt crack in a four-phase TRIP steel under small scale yielding conditions. A schematic representation of the boundary value problem considered is shown in Figures 12.1(a) and (b). We consider a fan-shaped area around the crack in the infinite body shown in Figure 12.1(a). Only one half of the region (i.e., $0 \leq \theta \leq \pi$) needs to be modeled due to symmetry about the plane of the crack. Thus, symmetry conditions are applied at the mid-plane, while traction-free conditions are imposed along the free surface of the crack. The mode-I load is applied by imposing the linear elastic, asymptotic crack tip (K_I) displacement field along the outer boundary of the model as shown in Figure 12.1(b), i.e., displacement boundary conditions remote from the tip are applied incrementally:

$$\begin{Bmatrix} u_1 \\ u_2 \end{Bmatrix} = \frac{K_I}{2\mu} \sqrt{\frac{r}{2\pi}} (3 - 4\nu - \cos\theta) \begin{Bmatrix} \cos(\theta/2) \\ \sin(\theta/2) \end{Bmatrix}$$

where u_i are the displacement components, K_I is the mode-I stress intensity factor, x_1 and x_2 are the crack-tip Cartesian coordinates with the x_1 being the axis of symmetry and x_2 the direction of the mode-I loading, and (r, θ) are crack-tip polar coordinates.

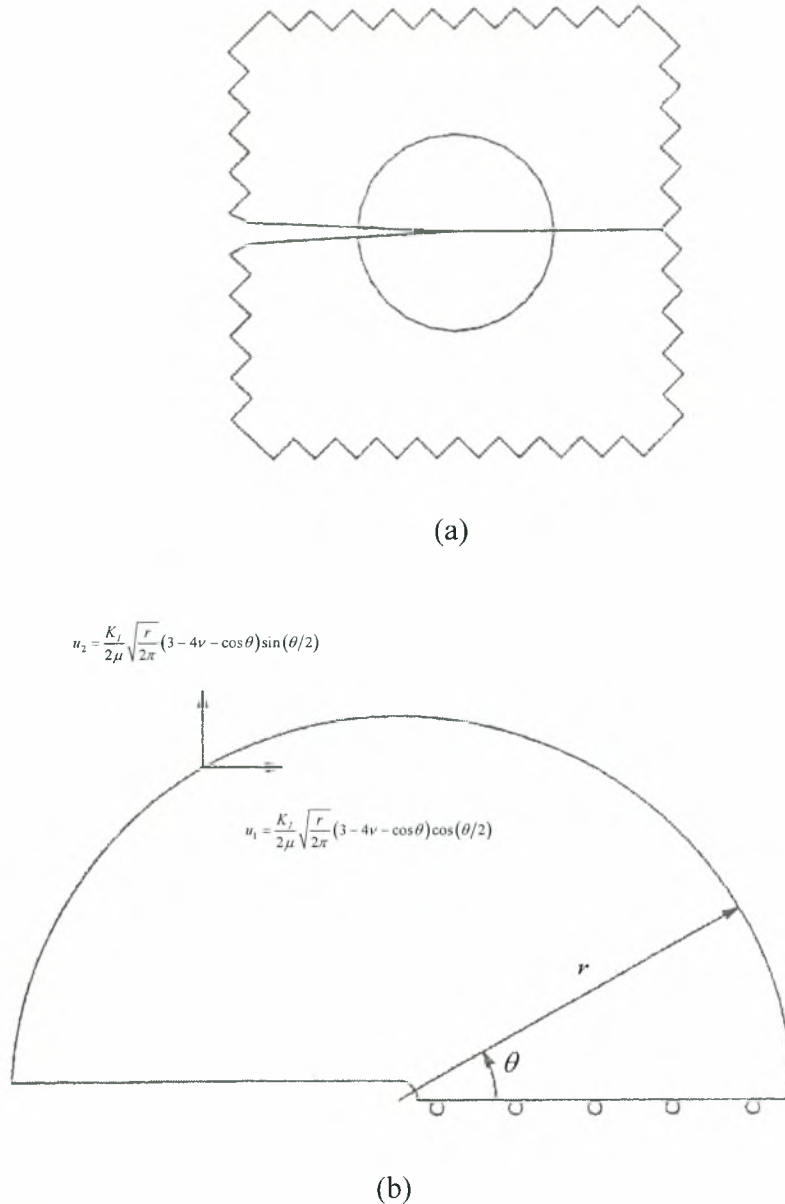


Figure 12.1: Schematic description of the crack blunting problem: (a) the circular near-tip region modeled, (b) schematic representation of the near-tip small-scale-yielding boundary value problem.

The calculations are carried out in ABAQUS for room temperature and 50°C. Four-node isoparametric plane strain elements (CPE4H) with 2×2 Gauss integration stations are used in the calculations. A total number of 1658 elements are used in the computations. The outermost radius of the finite element mesh, where the elastic asymptotic displacement field is imposed, is $R \cong 1.2 \times 10^3 b_0$, where b_0 is the initial radius of the semicircular notch at the tip of

the blunt crack. The finite element mesh used in the calculations is presented in Figure 12.2; details of the mesh in the region near the crack tip is shown in Figure 12.3.

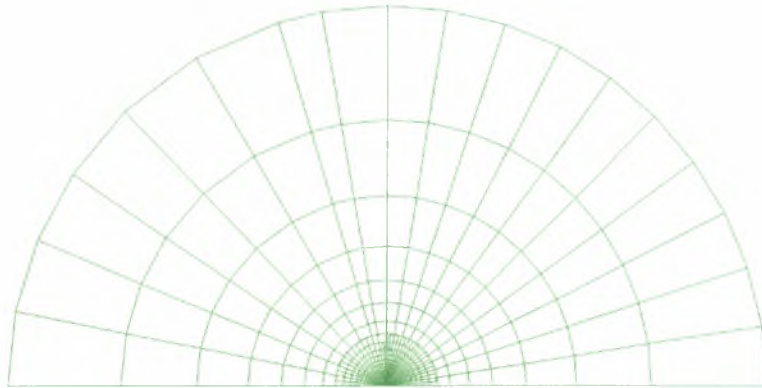


Figure 12.2: The finite element mesh used in the calculations.

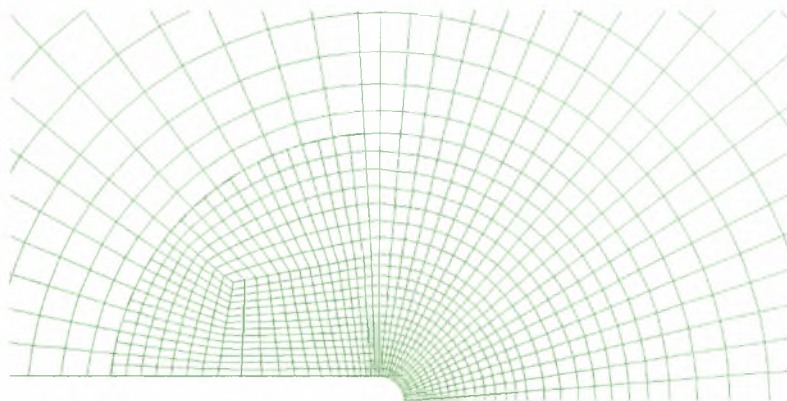


Figure 12.3: The finite element mesh in the region near the crack tip.

The values for the parameters presented for one element test are used for the new calculations at room temperature and at 50°C. Furthermore, we simulate the crack problem for a “non-transforming” steel analogous to that simulated in the problem of necking. This steel consists of three phases (retained austenite, bainite and ferrite), with the mechanical behavior of these phases defined in Chapter 6 from equations (6.22) to (6.29). The simulation is carried out for room temperature and all the parameters used are the same with the transforming case. Therefore, we can compare the behavior of a TRIP steel with that of a “non-transforming” steel in the crack problem.

Figure 12.4 shows the deformed finite element mesh superposed on the undeformed at a load level $K_I \equiv K_I / (\sigma_0 \sqrt{b_0}) = 50$ for the transforming case at room temperature, where the reference stress $\sigma_0 = 480$ MPa is used in the definition of K_I and for the normalization of various quantities for the rest of this chapter.

Figures 12.5 to 12.8 show the variation of the opening stress σ_{22} , the hydrostatic pressure $p = \sigma_{kk} / 3$, the triaxiality ratio $\Sigma = p / \sigma_{eq}$, and the equivalent plastic strain

$$\bar{\epsilon}^p = \int \sqrt{\frac{2}{3} \mathbf{D}^p : \mathbf{D}^p} dt$$

ahead of the crack tip at different load levels for both the transforming and the non-transforming steels. In these figures “ x ” is the distance of a material point in the undeformed configuration from the root of the semicircular notch.

Since the blunt crack tip is traction free, the maximum of σ_{22} and p appear at some distance ahead of the crack and this peak point moves away from the crack tip for higher values of load imposed. The stress fields that develop in both materials are very similar, with the stresses in the transforming steel being slightly higher due to the formation of the harder martensitic phase in that steel.

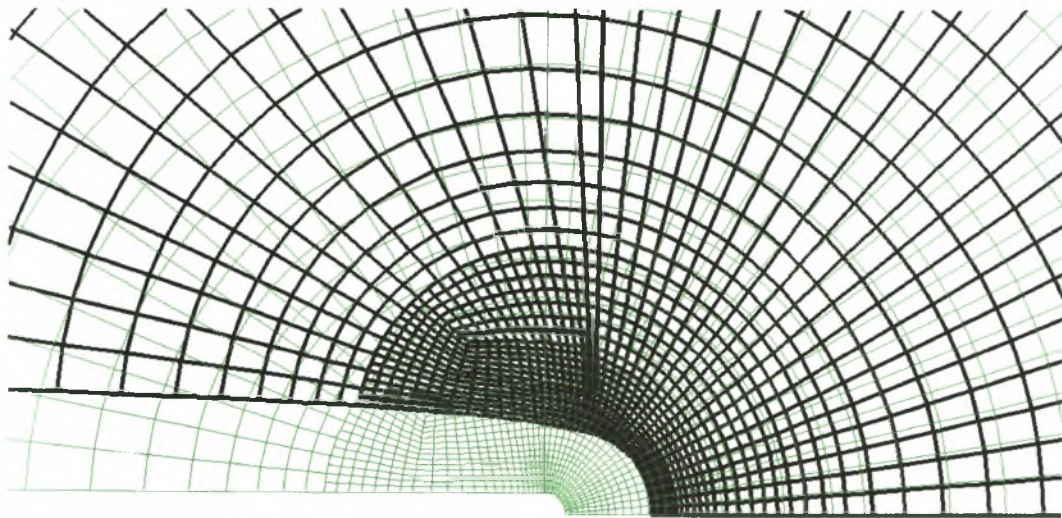


Figure 12.4: Deformed finite element mesh superposed on the undeformed mesh (green lines) in the region near the blunt crack tip at a load level $K_I \equiv K_I / (\sigma_0 \sqrt{b_0}) = 50$ for the transforming steel at room temperature.

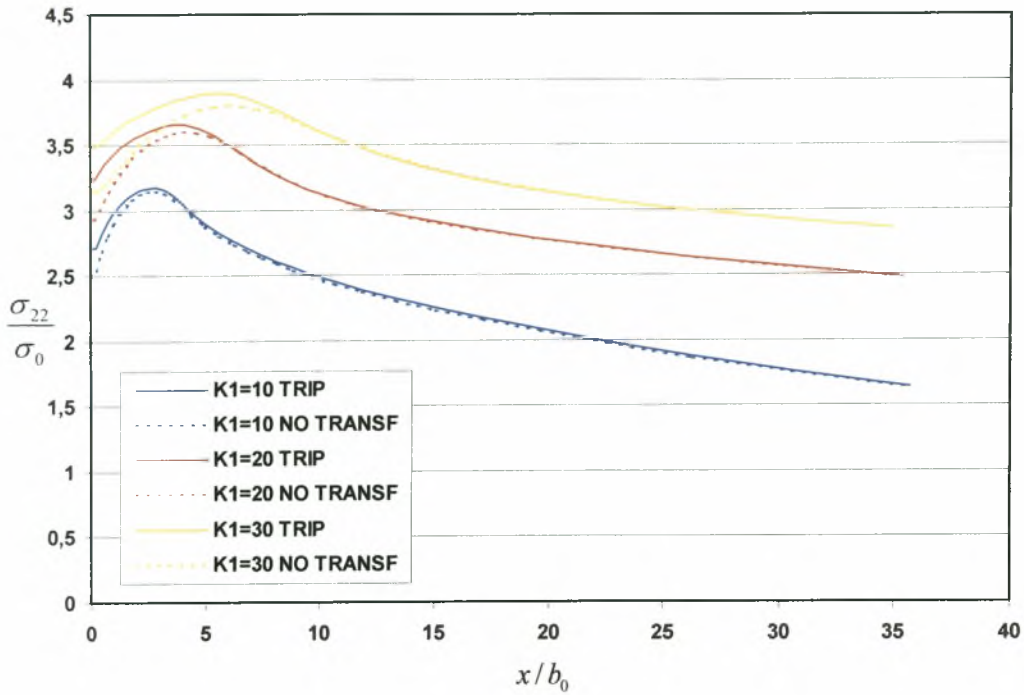


Figure 12.5: Opening stress ahead of the crack tip at different load levels for a TRIP steel and a non-transforming steel at room temperature.

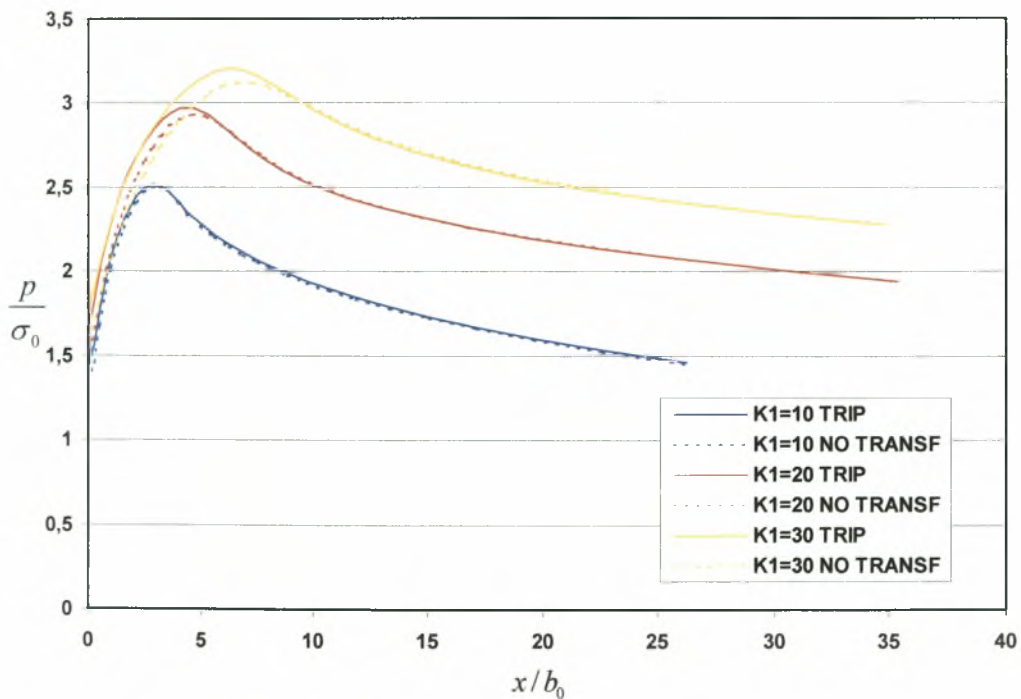


Figure 12.6: Variation of the hydrostatic pressure ahead of the crack tip at different load levels for a TRIP steel and a non-transforming steel at room temperature.

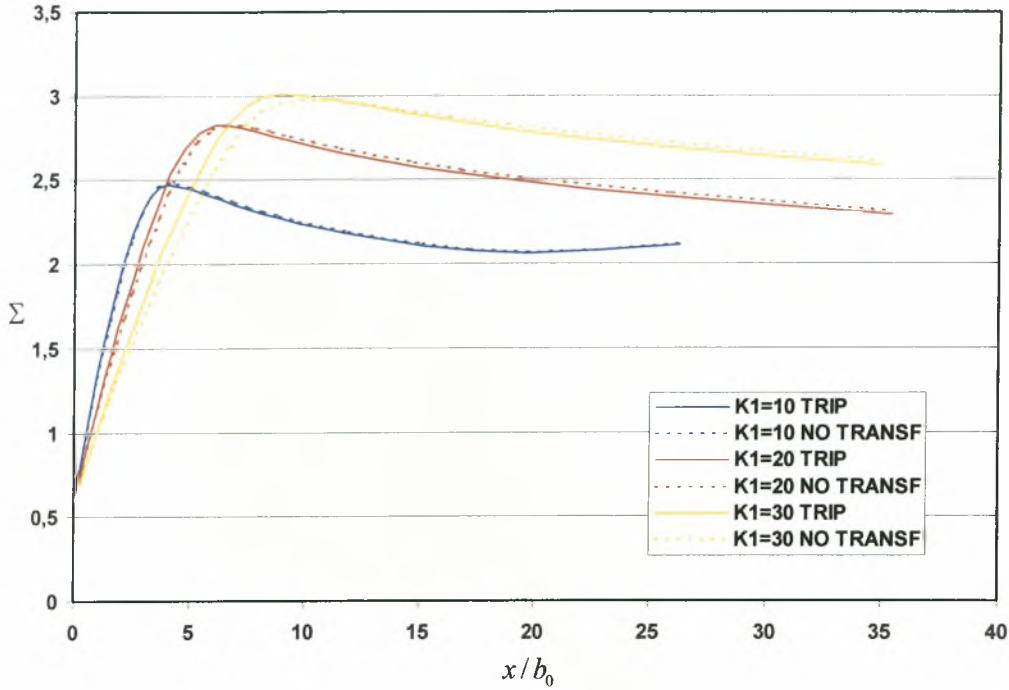


Figure 12.7: Variation of the triaxiality ratio ahead of the crack tip at different load levels for a TRIP steel and a non-transforming steel at room temperature.

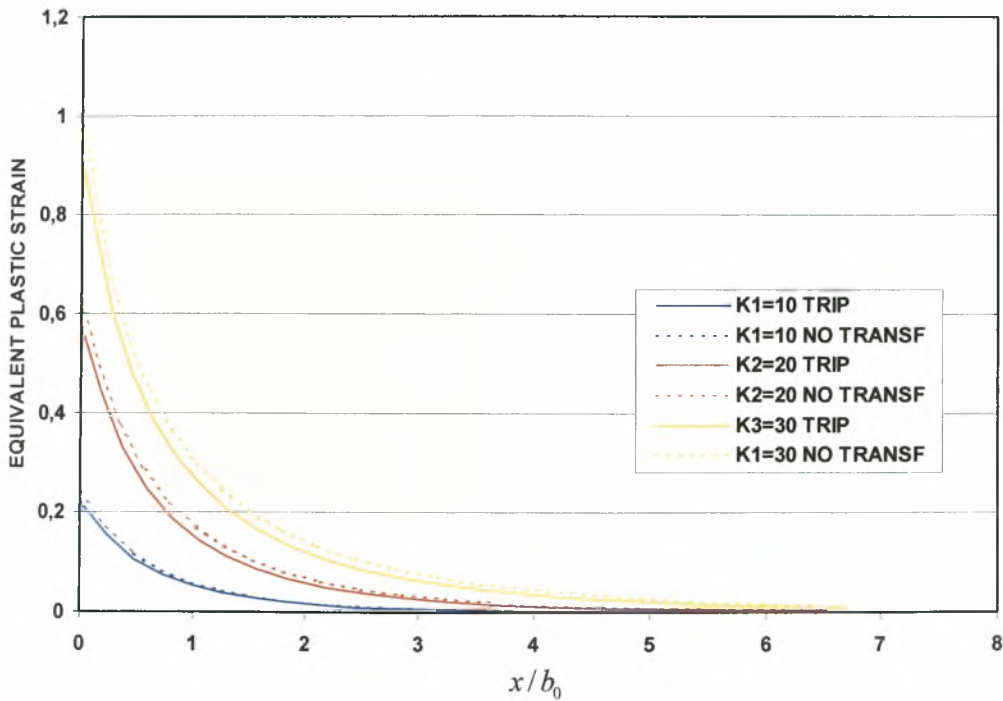


Figure 12.8: Variation of equivalent plastic strain $\bar{\epsilon}^P = \int \sqrt{\frac{2}{3}} \mathbf{D}^P : \mathbf{D}^P dt$ ahead of the crack tip at different load levels for a TRIP steel and a non-transforming steel at room temperature.

Figures 12.9 and 12.10 show contours of the equivalent plastic strain $\bar{\varepsilon}^p = \int \sqrt{\frac{2}{3} \mathbf{D}^p : \mathbf{D}^p} dt$ ahead of the crack tip at a load level of $K_I \equiv K_I / (\sigma_0 \sqrt{b_0}) = 50$ for a TRIP and non-transforming steels at room temperature.

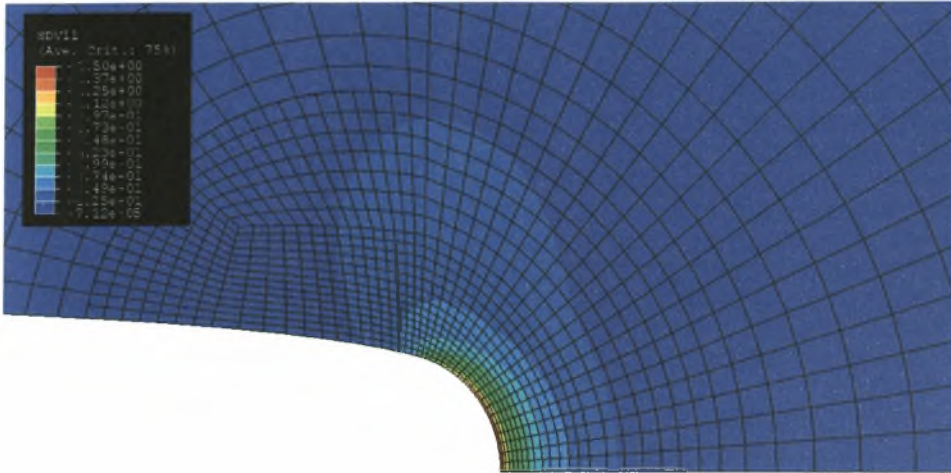


Figure 12.9: Contour of equivalent plastic strain $\bar{\varepsilon}^p = \int \sqrt{\frac{2}{3} \mathbf{D}^p : \mathbf{D}^p} dt$ ahead of the crack tip at a load level of $K_I \equiv K_I / (\sigma_0 \sqrt{b_0}) = 50$ for a TRIP steel at room temperature.

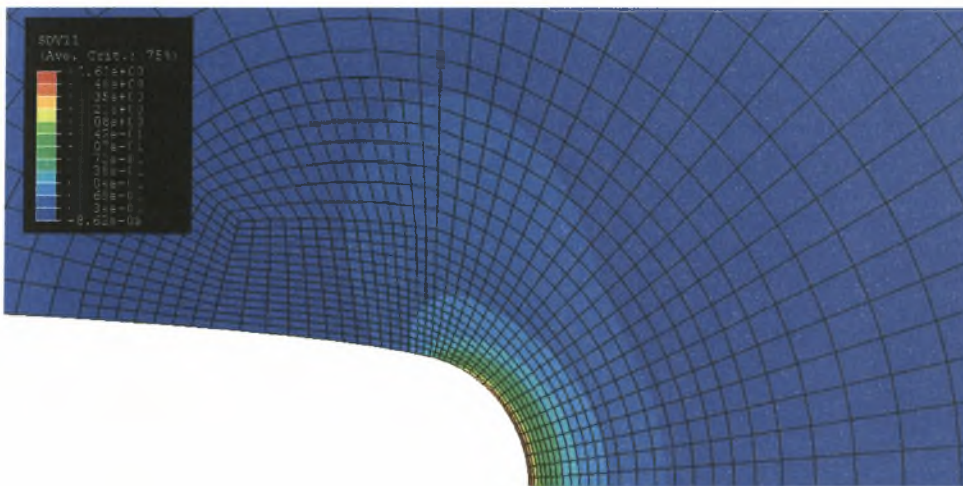


Figure 12.10: Contour of equivalent plastic strain $\bar{\varepsilon}^p = \int \sqrt{\frac{2}{3} \mathbf{D}^p : \mathbf{D}^p} dt$ ahead of the crack tip at a load level of $K_I \equiv K_I / (\sigma_0 \sqrt{b_0}) = 50$ for the non-transforming steel at room temperature.

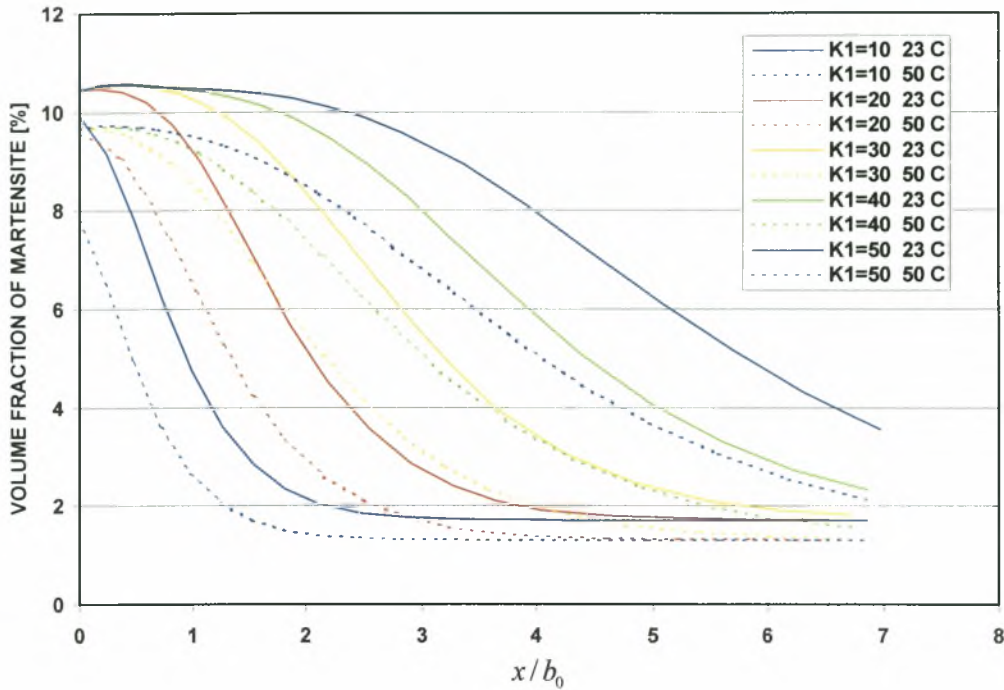


Figure 12.11: Distribution of volume fraction of martensite ahead of the crack tip at different load levels for room temperature and 50°C.

Martensitic transformation is highly affected by temperature as stated in former chapters. Figure 12.11 shows the variation of the volume fraction of martensite f formed ahead of the crack tip at different load levels for room temperature (23°C) and 50°C. The martensitic transformation is taking place in the region near the crack tip where substantial stresses and plastic strains develop. At the tip of the blunted crack the volume fraction of martensite is maximum and as long as we move away from the crack martensite reduces and finally we reach an area that no transformation takes place.

Figure 12.12 shows the variation of the opening stress σ_{22} ahead of the crack tip at different load levels $K1$ for 23°C and 50°C. A higher level of hardening appears at room temperature (23°C) due to the higher amount of martensite formed.

Figure 12.13 shows the variation of the equivalent plastic strain $\bar{\epsilon}^p = \int \sqrt{\frac{2}{3} \mathbf{D}^p : \mathbf{D}^p} dt$ ahead of the crack tip at different load levels for room temperature (23°C) and 50°C.

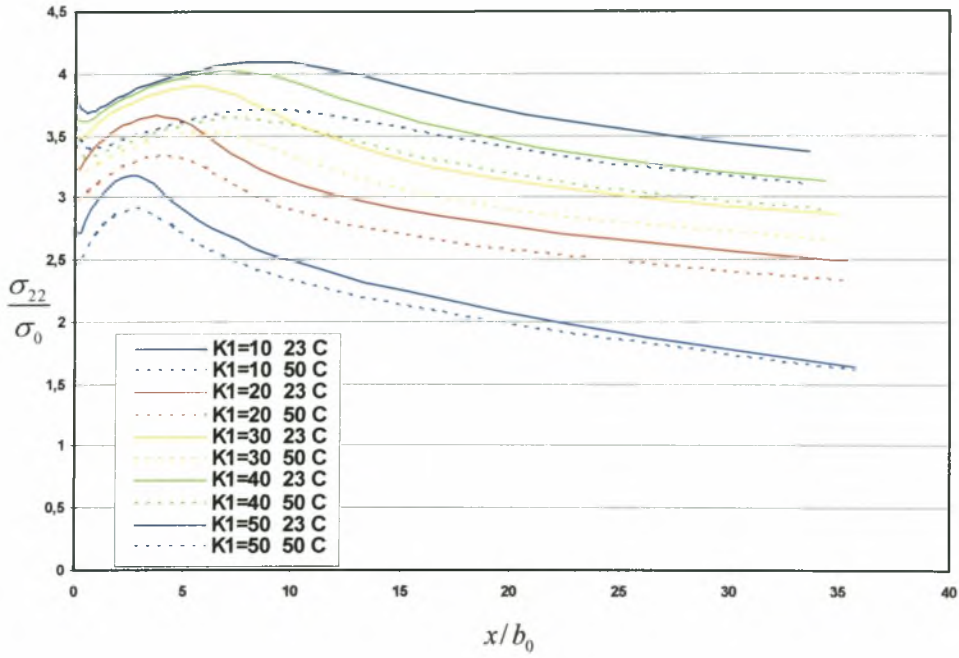


Figure 12.12: Normal stress distribution ahead of the crack tip at different load levels for room temperature and 50°C.

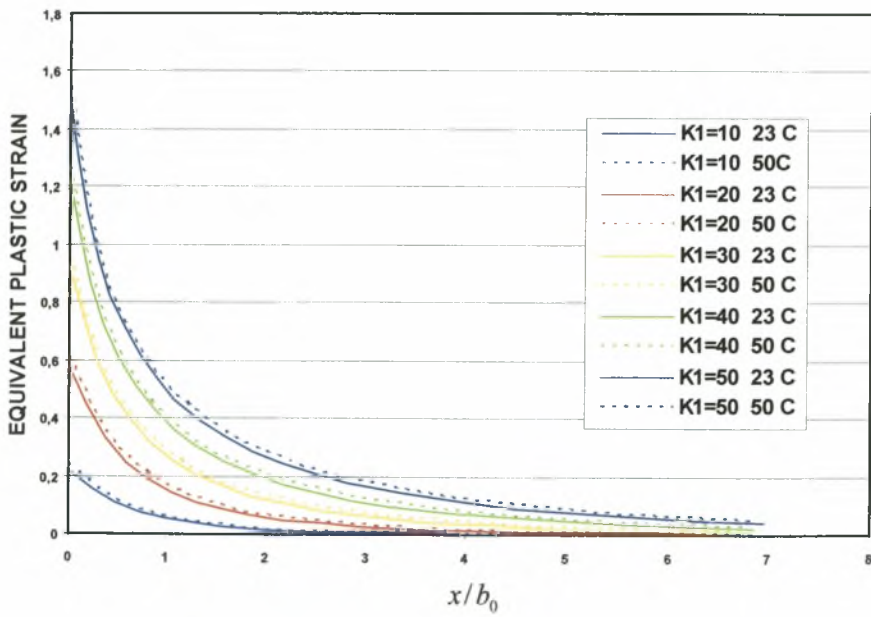


Figure 12.13: Variation of equivalent plastic strain $\bar{\epsilon}^p = \int \sqrt{\frac{2}{3} \mathbf{D}^p : \mathbf{D}^p} dt$ ahead of the crack tip at different load levels for room temperature and 50°C.

CHAPTER THIRTEEN

FORMING LIMIT DIAGRAMS FOR TRIP STEELS

13.1 Introduction

In this chapter, we use the constitutive model developed for the four-phase TRIP steel to calculate “forming limit diagrams” for sheets made of TRIP steels. The predictions of the analytical model are compared with experimental data. Comparisons are made with the corresponding problems in which martensitic transformation is suppressed.

13.2 Problem formulation

We consider a sheet made of TRIP steel that is deformed uniformly on its plane in such a way that the in-plane principal strain increments increase in proportion. We study the possibility of the formation of a neck in the form of a narrow straight band (Figure 13.1) and construct the corresponding “forming limit diagram”. The problem of necking in biaxially stretched viscoplastic sheets has been studied by Hutchinson and Neal (1978), Tvergaard (1978, 1980) and Needleman and Tvergaard (1984).

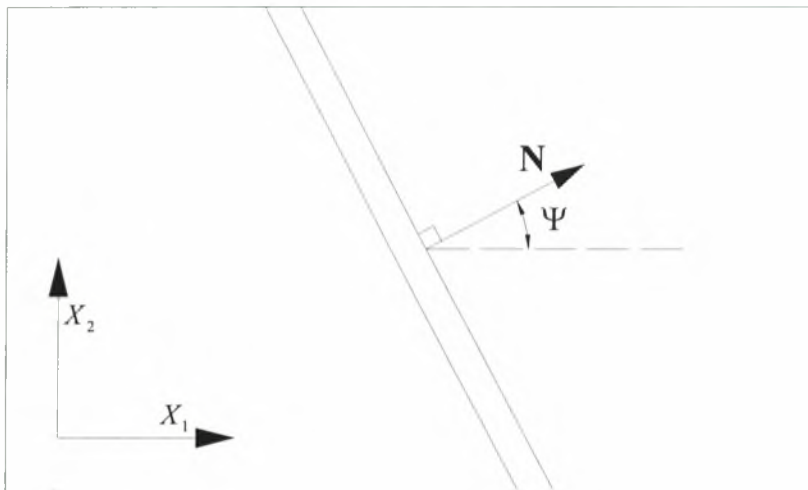


Figure 13.1: Narrow band in biaxially stretched sheet.

As discussed in Chapter Six, the constitutive equations of the TRIP steel can be written in the form:

$$\overset{\nabla}{\boldsymbol{\sigma}} = \mathbf{L} : \mathbf{D} + \mathbf{P} \quad (13.1)$$

It turns out that the formulation of the problem is simpler, if one works with “nominal” quantities. Let $\mathbf{t} = J \mathbf{F}^{-1} \cdot \boldsymbol{\sigma}$ be the nominal (1st Piola-Kirchhoff) stress tensor, where $J = \det \mathbf{F}$; then, it can be shown readily that

$$\dot{\mathbf{t}} = J \mathbf{F}^{-1} \cdot \left(\overset{\nabla}{\boldsymbol{\sigma}} + D_{kk} \boldsymbol{\sigma} - \boldsymbol{\sigma} \cdot \mathbf{W} - \mathbf{D} \cdot \boldsymbol{\sigma} \right) \quad (13.2)$$

Substituting (13.1) into the last equation, we find that

$$\dot{\mathbf{t}} = \mathbf{C} : \dot{\mathbf{F}}^T + \mathbf{B} \quad (13.3)$$

where

$$C_{ijkl} = J F_{im}^{-1} F_{kn}^{-1} (L_{mjnl} + V_{mjnl}), \quad \mathbf{B} = J \mathbf{F}^{-1} \cdot \mathbf{P} \quad (13.4)$$

$$V_{ijkl} = \frac{1}{2} (\sigma_{ik} \delta_{jl} - \delta_{ik} \sigma_{jl} - \sigma_{il} \delta_{jk} - \delta_{il} \sigma_{jk}) + \sigma_{ij} \delta_{kl} \quad (13.5)$$

In the following, we examine the possibility of the formation of a neck as shown in Figure 13.1; both inside and outside the band a state of uniform plane stress is assumed. Since the in-plane displacements are continuous, their spatial derivatives parallel to the band remain uniform. The only discontinuities in the displacement gradient are restricted kinematically to the form (Hadamard (1903), Hill (1961), Rice (1976))

$$\left[\frac{\partial u_a}{\partial X_\beta} \right] = G_\alpha N_\beta \quad (13.6)$$

where \mathbf{X} is the position vector of a material point in the undeformed configuration, $[]$ denotes the difference (jump) of the field within the band and the field outside the band, \mathbf{N} is the unit vector normal to the band in the undeformed configuration, and \mathbf{G} is the jump in the normal derivative of \mathbf{u} , i.e., $[\partial \mathbf{u} / \partial N] \equiv [(\partial \mathbf{u} / \partial \mathbf{X}) \cdot \mathbf{N}] = \mathbf{G}$. The vector \mathbf{G} takes a constant value within the band and depends on the imposed uniform deformation gradient outside the band; a method for the determination of \mathbf{G} is discussed in the following. In equation (13.6) and for the rest of this section, Greek indices take values in the range (1,2) where $X_1 - X_2$ is the plane of the sheet.

In view of (13.6), the in-plane components of the uniform deformation gradient inside the band takes the form

$$F_{\alpha\beta}^b = F_{\alpha\beta} + G_\alpha N_\beta \quad (13.7)$$

where the superscript b denotes quantities within the band, and quantities with no superscript correspond to the uniform field outside the band. The corresponding matrix form of the deformation gradients is

$$[F] = \begin{bmatrix} \lambda_1 & 0 & 0 \\ 0 & \lambda_2 & 0 \\ 0 & 0 & \lambda_3 \end{bmatrix} \quad \text{and} \quad [F^b] = \begin{bmatrix} \lambda_1 + G_1 N_1 & G_1 N_2 & 0 \\ G_2 N_1 & \lambda_2 + G_2 N_2 & 0 \\ 0 & 0 & \lambda_3^b \end{bmatrix} \quad (13.8)$$

The plane stress condition $\sigma_{33} = 0$ implies that $t_{33} = 0$ as well. Using the equation $\dot{t}_{33} = 0$ to solve for \dot{F}_{33} , we arrive at the in-plane constitutive relations needed for the sheet necking analysis:

$$\dot{t}_{\alpha\beta} = \hat{C}_{\alpha\beta\gamma\delta} \dot{F}_{\delta\gamma} + \hat{B}_{\alpha\beta} \quad (13.9)$$

where the plane stress moduli and initial stress term are given in terms of their three-dimensional counterparts by

$$\hat{C}_{\alpha\beta\gamma\delta} = C_{\alpha\beta\gamma\delta} - C_{\alpha\beta 33} \frac{C_{33\gamma\delta}}{C_{3333}} \quad \text{and} \quad \hat{B}_{\alpha\beta} = B_{\alpha\beta} - C_{\alpha\beta 33} \frac{B_{33}}{C_{3333}} \quad (13.10)$$

Equilibrium across the band requires that

$$T_{\alpha} \equiv H N_{\beta} t_{\beta\alpha} = H^b N_{\beta} t_{\beta\alpha}^b \equiv T_{\alpha}^b \quad (13.11)$$

where H^b and H , respectively, denote the initial thickness of the sheet inside and outside the band. The rate form of this equilibrium relation is

$$\dot{T}_{\alpha} = H N_{\beta} \dot{t}_{\beta\alpha} = H^b N_{\beta} \dot{t}_{\beta\alpha}^b = \dot{T}_{\alpha}^b \quad (13.12)$$

Substituting (13.9) into the last equation and using (13.8) for \mathbf{F} and \mathbf{F}^b , we obtain

$$A_{\alpha\beta} \dot{G}_{\beta} = b_{\alpha} \quad (13.13)$$

where

$$A_{\alpha\beta} = N_{\gamma} \hat{C}_{\gamma\alpha\delta\beta} N_{\delta} \quad \text{and} \quad b_{\alpha} = N_{\beta} \left[\left(\frac{H}{H^b} \hat{C}_{\beta\alpha\gamma\delta} - \hat{C}_{\beta\alpha\gamma\delta}^b \right) \dot{F}_{\delta\gamma} - \frac{H}{H^b} \hat{B}_{\beta\alpha} - \hat{B}_{\beta\alpha}^b \right] \quad (13.14)$$

In a perfect sheet ($H^b = H$), before necking occurs we have that $\mathbf{C}^b = \mathbf{C}$ and $\mathbf{B}^b = \mathbf{B}$, the right hand side of (13.13) vanishes, and the deformation remains homogenous ($\dot{\mathbf{G}} = \mathbf{0}$) until at some stage the determinant of the coefficient matrix $[A]$ vanishes, and this is the condition of a local necking bifurcation. In most rate-dependent plasticity models the instantaneous moduli \mathbf{L} are the elastic moduli \mathbf{L}^e . In the constitutive model for TRIP steels presented in Chapter Six, the components L_{ijkl} are of order “elastic modulus”, and $\mathbf{L} = \mathbf{L}^e$ when $\dot{\Sigma} \leq 0$. In such cases, the first bifurcation point in a perfect specimen ($H^b = H$) is that predicted by linear hypoelasticity and occurs at unrealistically large strains. In the context of a rate sensitivity formulation the most important feature is the very strong sensitivity to small imperfections, whereas bifurcation plays no central role (Tvergaard (1985a, 1985b)). Therefore, in order to

carry out a necking analysis for a rate dependent solid it is always necessary to introduce some small inhomogeneity (imperfection).

We follow the approach of Marciniak and Kuzyski (1967), known as the “M-K” model, in which the sheet is assumed to contain a small initial inhomogeneity and necking results from a gradual localization of the strains at the inhomogeneity. The inhomogeneity is in the form of straight narrow band (neck) of reduced thickness $H^b < H$, as can be seen in Figure 13.1. Both inside and outside the band a state of uniform plane stress is assumed, and the analysis consists in determining the uniform state of deformation inside the band that is consistent kinematically and statically with the prescribed uniform state outside the band (Tvergaard (1978, 1980), Needleman and Tvergaard (1984)). In the presence of an initial thickness imperfection, the right hand side of (13.13) does not vanish and these equations provide a system that defines the two unknowns \dot{G}_1 and \dot{G}_2 . Given the initial sheet thickness inside and outside the band and the imposed uniform deformation history outside the band, equations (13.13) are solved incrementally for $\Delta \mathbf{G} = \dot{\mathbf{G}} \Delta t$ to obtain the deformation history inside the band. Localization is said to occur when the ratio of some scalar measure of the amount of incremental straining inside the band to the corresponding value outside the band becomes unbounded.

In our calculations, an initial thickness imperfection is introduced and the deformation gradient outside the band \mathbf{F} is prescribed in such a way that the corresponding principal logarithmic strains ε_1 and ε_2 outside the band increase in proportion, i.e. $(d\varepsilon_2/d\varepsilon_1 = \varepsilon_2/\varepsilon_1 = \rho = \text{const.})$. The uniform solution outside the band is determined incrementally by using the plane stress algorithm presented in Chapter 8. At the end of every increment, equations (13.13) are used to determine $\Delta \mathbf{G}$ and this defines the corresponding deformation gradient inside the band \mathbf{F}^b . Then, the uniform solution inside the band is determined by using again the algorithm presented in Chapter 8. Necking localization is assumed to occur, when the ratio of some scalar measure of the amount of incremental straining inside the band to the corresponding value outside the band becomes very large; in particular, the calculations are terminated when either one of the two conditions $|\Delta G_1|/\Delta \lambda_1 > 30$ or $|\Delta G_2|/\Delta \lambda_1 > 30$ is satisfied. In order to improve the accuracy of the calculations and be able to use increments of reasonable size, “equilibrium correction” is used in (13.13), i.e., instead of the rate of equilibrium equation (13.12), we use equilibrium itself

$$\mathbf{T}_{n+1} = \mathbf{T}_{n+1}^b \quad (13.15)$$

where the subscript $n+1$ denotes values at the end of the increment. Then, we set $\mathbf{T}_{n+1} \simeq \mathbf{T}_n + \dot{\mathbf{T}}_n \Delta t$ and $\mathbf{T}_{n+1}^b \simeq \mathbf{T}_n^b + \dot{\mathbf{T}}_n^b \Delta t$ in the last equation to find

$$A_{\alpha\beta}|_n \Delta G_\beta = b_\alpha|_n \Delta t + \frac{1}{H^b} (\mathbf{T}_n - \mathbf{T}_n^b), \quad (13.16)$$

which is used instead of (13.13). In the last equation, Δt is the time increment, the subscript n denotes values at the start of the increment, and the last term on the right hand side accounts for any unbalanced forces at the end of the previous increment.

13.3 Results

The material constants reported in Chapter 10 are used in the calculations. The initial volume fractions of the four phases in the TRIP steel are assumed to be $f_0 = 0.017$, $c_0^{(a)} = 0.103$, $c_0^{(3)} = 0.38$ and $c_0^{(4)} = 0.50$. For comparison purposes, a separate set of calculations is carried out for a non-transforming steel that consists of the three phases, i.e., retained austenite, bainite and ferrite with constant volume fractions $f_0 = 0$, $c_0^{(a)} = 0.12$, $c_0^{(3)} = 0.38$ and $c_0^{(4)} = 0.50$. In all cases, a constant strain rate outside the band $\dot{\varepsilon}_1 = 10^{-4} \text{ sec}^{-1}$ is imposed.

For every value of $\rho = d\varepsilon_2/d\varepsilon_1$, we set $\mathbf{N} = \cos\Psi \mathbf{e}_1 + \sin\Psi \mathbf{e}_2$, where Ψ is the angle of inclination of the band relative to the X_1 -axis in the undeformed configuration, and calculations are carried out for values of Ψ that cover the range $0 \leq \Psi \leq 90^\circ$; the critical value Ψ^{cr} for each ρ is determined as that giving the minimum localization strain.

Figure 13.2 shows “forming limit curves” obtained for imposed proportional straining ρ for two different values of the initial thickness imperfection, namely $H^b/H = 0.999$ and $H^b/H = 0.99$. The two solid curves correspond to the TRIP steel, whereas the dashed curves are for the non-transforming steel.

The TRIP phenomenon increases the necking localization strains. In particular, for an initial thickness imperfection of $H^b/H = 0.99$ and $\rho = 0$ (plane strain), the critical strain ε_{11}^{cr} increases from 0.2145 for the non-transforming steel to 0.2541 for the TRIP steel; the corresponding values of ε_{11}^{cr} for $H^b/H = 0.999$ and $\rho = 0$ are 0.3179 for the non-transforming steel and 0.3567 for the TRIP steel. A comparison of the model predictions with available experimental data is also presented in Figure 13.2. The experimental points on the forming

limit diagram were determined for the same TRIP steel used for the calibration of the model. An “Erichsen” universal sheet metal testing machine was employed for the experiments. A hemispherical punch with a diameter of 50 mm was used and the punch velocity was set to 1 mm/s (ECSC Final Report (2004)). The agreement between the model predictions and the experimental data is reasonable.

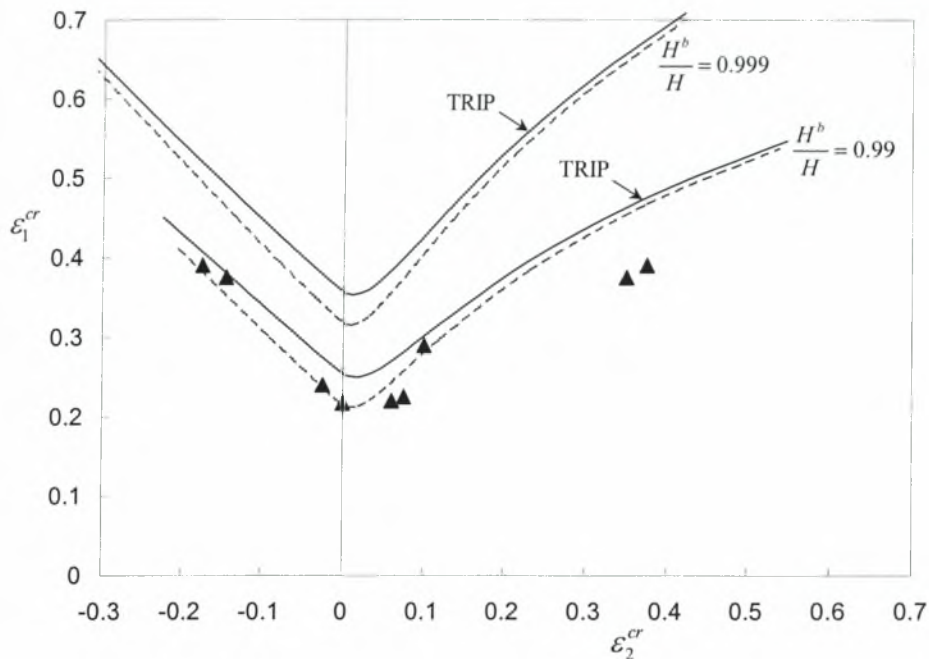


Figure 13.2: Forming limit curves for two different values of initial thickness inhomogeneities $H^b/H = 0.999$ and 0.99 . The solid lines correspond to the TRIP steel, whereas the dashed lines are for a non-transforming steel. The dark triangles are experimental data.

It should be noted also that an initial thickness inhomogeneity is one of the options to be used in the M-K model. Alternatively, a geometrically perfect sheet can be used and the initial inhomogeneity can be in the form of band of “softer” material. Further work in this direction is now underway in order to better understand the predictions of the model vs. the experimental data.

The necking development, leading to the forming limit curves of Figure 13.2, is illustrated in Figure 13.3 where the ratio of the maximum principal logarithmic strain inside (ε_f^b) and outside the neck (ε_f) are plotted versus ε_f for the TRIP steel for $\rho = 0$. Figure 13.4 shows the

corresponding evolution of thickness of the band h^b normalized by the thickness outside the band h as ε_1 increases.

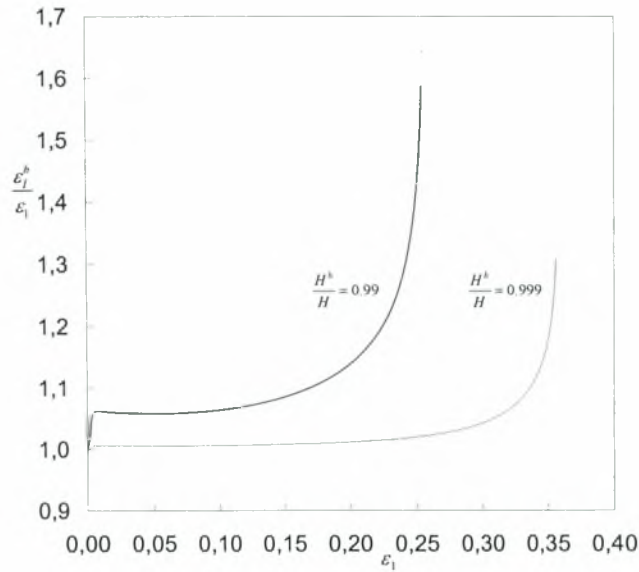


Figure 13.3: Growth of maximum principal logarithmic strain inside the band ε_1^b for the TRIP steel and $\rho = 0$.

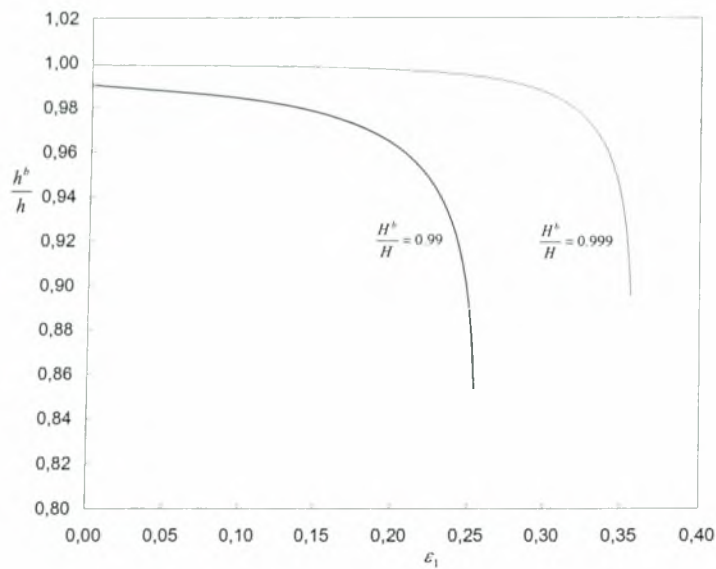


Figure 13.4: Evolution of band thickness h^b for the TRIP steel and $\rho = 0$.

In the analysis so far we used $m = 60$ for the exponent of the viscoplasticity models as stated in chapter ten. In Figure 13.5 we examine the effect of the exponent m on the forming limit diagram for the case of initial thickness inhomogeneity $H^b / H = 0.99$. Calculations for $m = 50$ and $m = 70$ are carried out and the results are compared with the case of $m = 60$. As can be seen, the three curves are almost identical implying that the dependence on m is negligible and does not affect the results.

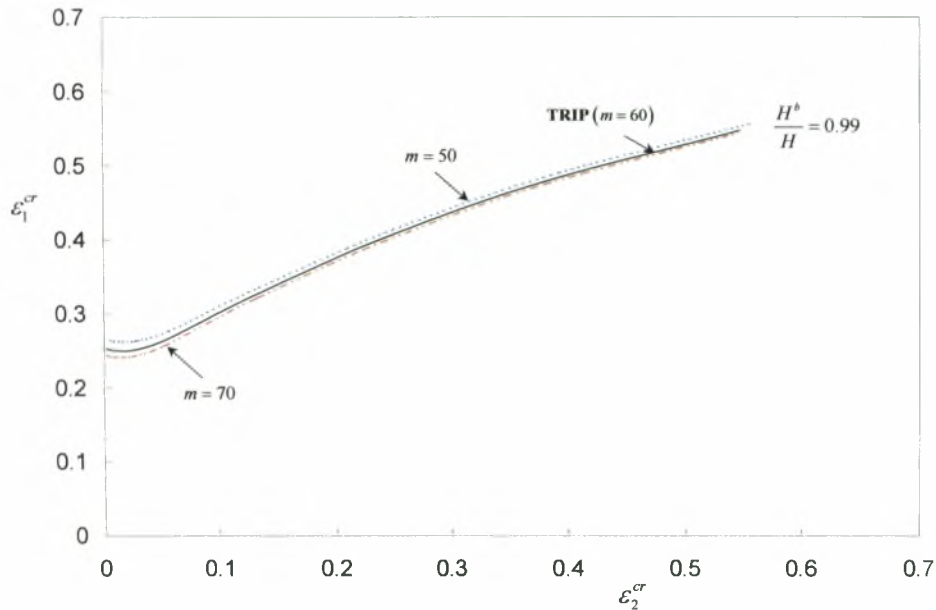


Figure 13.5: Forming limit curves for three different values of m ($m = 50, 60, 70$) for initial thickness inhomogeneity $H^b / H = 0.99$. The solid line corresponds to the value of m we use in the calculations for TRIP steel, whereas the dashed lines are for the comparison curves.

CHAPTER FOURTEEN

PROPOSALS FOR FUTURE RESEARCH ON TRIP STEELS

Modeling the mechanical behavior of multiphase TRIP steels using Finite Elements is a complicated task depending on a variety of parameters. In our research we developed a constitutive model that simulates with success multiphase TRIP steels. Nevertheless, further research can be made in this area. Some proposals for future work can be:

1. As stated, after thermal treatment, a four-phase TRIP steel obtains a substructure consisting of a dispersion of retained austenite islands and bainite in a ferritic matrix. The dispersed islands of retained austenite transform, with straining, into martensite leading to a substructure of martensitic islands dispersed in the matrix of TRIP steel. It is believed, that the transformation of the dispersed austenitic islands affects the kinetics behavior and creates the need of the implementation of the grain size of the initially austenitic islands as an important parameter to the model.
2. The experimental data for the hardening curves of the individual phases presented in Chapter six derived from a detailed bibliographic search. An experimental method can be developed in order to measure experimentally the hardening of the individual phases of the corresponding TRIP steel. Therefore, precise input data for the hardening curves of the phases would lead to a further improved simulation of the mechanical behavior of TRIP steels.
3. Transformation can occur by two distinct mechanisms, i.e. stress-assisted and strain-induced transformation of retained austenite to martensite. The stress-assisted mechanism dominates at stresses lower than the yield strength of the retained austenite, whereas the strain-induced mechanism prevails after the yield strength has been surpassed. In our research we focused on the strain-induced transformation where plasticity appears. However, experiments show that, in uniaxial tension, some amount of martensite appears before yielding takes place originating from the stress-assisted transformation. Therefore, an experimental method of measuring the initial value of martensite formed, during stress-assisted transformation, should be developed.
4. Finally, in order to develop the forming limit diagrams for TRIP steels an initial thickness inhomogeneity was used. Alternatively, a geometrically perfect sheet can be used and the initial inhomogeneity can be in the form of band of “softer” material.

REFERENCES

1. ABAQUS, Analysis User's Manual, Version 6.4, ©ABAQUS, Inc., 2003.
2. Aravas, N., On the numerical integration of a class of pressure-dependent plasticity models, *Int. J. Numer. Methods Engrg.* **24** (1987) 1395-1416.
3. Aravas, N. and Ponte Castañeda, P., Numerical methods for porous metals with deformation-induced anisotropy, *Comput. Methods Appl. Mech. Engrg.* **193** (2004) 3767-3805.
4. Bridgman, P. W., Studies in large plastic flow and fracture with special emphasis on the effects of hydrostatic pressure, McGraw-Hill Book Co., 1952.
5. ECSC Final Report, Optimization of Microstructure in Multiphase Steels Containing Retained Austenite, contract No. 7210-PR/161, European Commission, (2004).
6. Hadamard, J., *Leçons sur la propagation des ondes et les équations de l'hydrodynamique*, Librairie Scientifique A, Hermann, Paris (1903).
7. Hill, R., Discontinuity relations in mechanics of solids, in: I. N. Sneddon and R. Hill (Eds.), *Progress in Solid Mechanics*, Vol. II, Chapt. 6, North Holland Publ. Co., Amsterdam, 1961, pp. 247-276.
8. Hughes, T. J. R., Equivalence of finite elements for nearly incompressible elasticity, *J. Appl. Mech.* **44** (1977) 181-183.
9. Hughes T. J. R., *The Finite Element Method*, Dover Publications, 2000.
10. Hutchinson, J. W., Neal, K.W. and Needleman, A., Sheet necking-I. Validity of plane stress assumptions of the long-wavelength approximation, in: D.P. Koistinen, N.-M. Wang (Eds), *Mechanics of Sheet Metal Forming*, Plenum Press, New York, London, 1978, pp. 111-126.
11. Hutchinson, J. W. and Tvergaard, V., Softening due to void nucleation in metals, *ASTM STP 1020* (1989) 61-83.
12. Kreher, W., Residual stresses and stored elastic energy of composites and polycrystals, *J. Mech. Phys. Solids* **38** (1990) 115-128.
13. Leal, R. H., Transformation toughening of metastable austenitic steels, Ph.D. thesis, MIT, Cambridge, MA, 1984.
14. Malkus, D. S. and Hughes T. J. R., Mixed finite element methods-reduced and selective integration techniques: A unification of concepts, *Comp. Methods Appl. Mech. Engrg.* **15** (1978) 63-81.
15. Marciniak, Z. and Kuczynski, K., Limit strains in the process of stretch forming sheet metal, *Int. J. Mech. Sciences* **9** (1967) 609-620.

16. Naturani, T., Olson, G. B. and Cohen, M., Constitutive flow relations for austenitic steels during strain-induced martensitic transformation, *J. de Phys.* **43** (1982) 429-434.
17. Needleman, A., On finite element formulations for large elastic-plastic deformations, *Comput. Struct.* **20** (1985) 247-257.
18. Needleman, A. and Tvergaard, V., Limits to formability in rate-sensitive metal sheets, in: J. Carlsson and N. G. Ohlson (Eds.), *Mechanical Behavior of Materials – IV*, Pergamon Press, Oxford and New York, London, 1984, pp. 51-65.
19. Olson, G. B. and Azrin, M., Transformation Behavior of TRIP steels, *Metall. Trans. A* **9A** (1978) 713-721.
20. Olson, G. B. and Cohen, M., A general mechanism of martensitic nucleation, *Metall. Trans. A* **7A** (1976) 1897-1923.
21. Olson, G. B. and Cohen, M., Kinetics of strain-induced martensitic nucleation, *Metall. Trans. A* **7A** (1975) 791-795.
22. Olson, G. B., Tsuzaki, K. and Cohen, M., Statistical aspects of martensitic nucleation, in: G.S. Cargill, F. Spaepen, K.N. Tu (Eds.), *Phase transformations in condensed systems (Turnball Symposium)*, MRC Proc., vol. 57, 1987, pp. 129-148.
23. Ponte Castañeda, P., Exact second-order estimates for the effective mechanical properties of nonlinear composites materials, *J. Mech. Phys. Solids* **44** (1996) 827-862.
24. Ponte Castañeda, P., New variational principles in plasticity and their application to composite materials, *J. Mech. Phys. Solids* **40** (1992) 1757-1788.
25. Ponte Castañeda, P., The effective mechanical properties of nonlinear isotropic solids, *J. Mech. Phys. Solids* **39** (1991) 45-71.
26. Ponte Castañeda, P. and Suquet, P., *Nonlinear composites*, Advances in Applied Mechanics, Academic Press, vol. 34, 1998, pp. 171-302.
27. Qiu, Y. P. and Weng, G. J., A theory of plasticity for porous materials and particle-reinforced composites, *J. Appl. Mech.* **59** (1992) 261-268.
28. Ramaswamy, S. and Aravas, N., Finite element implementation of gradient plasticity models -- Part I: Gradient-dependent yield functions, *Comp. Methods Appl. Mech. Engrg.* **163** (1998) 11-32.
29. Rice, J. R., The localization of plastic deformation, in: W. T. Koiter (Ed.), *Proceedings of the 14th International Congress on Theoretical and Applied Mechanics*, North-Holland Publishing Corporation, Amsterdam, 1976, pp. 207-220.
30. Stringfellow, R. G., *Mechanics of strain-induced transformation toughening in metastable austenitic steels*, Ph.D. Thesis, MIT, Cambridge, MA, 1990.

31. Stringfellow, R. G., Parks, D. M. and Olson, G. B., A constitutive model for transformation plasticity accompanying strain-induced martensitic transformations in metastable austenitic steels, *Acta Metall.* **40** (1992) 1703-1716.
32. Suquet, P., Overall potentials and flow stresses of ideally plastic or power law materials, *J. Mech. Phys. Solids* **41** (1993) 981-1002.
33. Suquet, P., Overall properties of nonlinear composites: A modified secant moduli theory and its link with Ponte Castañeda's nonlinear variational procedure, *C. R. Acad. Sci. Paris, II b* **320** (1995) 563-571.
34. Suquet, P., Overall properties of nonlinear composites: Remarks on secant and incremental formulations, in: A. Pineau, A. Zaoui (Eds.), *Micromechanics of plasticity and damage of multiphase materials (IUTAM Symposium)*, Kluwer, Dordrecht, The Netherlands, 1996, pp. 149-156.
35. Suquet, P., Overall properties of nonlinear composites: Secant moduli theories and variational bounds, in: K.Z. Markov (Ed.), *Continuum models of discrete systems (CMDS8 Symposium)*, World Scientific, Singapore, 1996, pp. 290-299.
36. Technical Steel Research: Modeling of mechanical properties and local deformation of high-strength multi-phase steels, Final Report, European Commission, Contract No. 7210-PR/044, 2002.
37. Tvergaard, V., Effect of kinematic hardening on localized necking in biaxially stretched sheets, *Int. J. Mech. Sci.* **20** (1978) 651-658.
38. Tvergaard, V., Bifurcation and imperfection sensitivity at necking instabilities, *Zeits. ang. Math. Mech.* **60** (1980) T26-T34.
39. Tvergaard, V., On bifurcation and stability under elastic-plastic deformation, in: A. Sawczuck, G. Bianchi (Eds.), *Plasticity Today: Modelling, Methods and Applications*, Elsevier, London, 1985, pp. 377-398.
40. Tvergaard, V., Rate-sensitivity in elastic-plastic panel buckling, in: D. J. Dawe, R. W. Horsington, A. G. Kamtekar and G. H. Little (Eds.), *Aspects of the Analysis of Plate Structures*, A volume in honor of W. H. Wittrick, Clarendon Press, Oxford, 1985, pp. 293-308.
41. Walpole, L. J., On bounds for the overall elastic moduli of inhomogeneous systems, *J. Mech. Phys. Solids* **14** (1966) 151-162.
42. Wayman, C. M., Phase transformations, non-diffusive, in: *Physical Metallurgy*, R.W. Cahn, P. Haasen, Elsevier Science Publishers, 1983.

43. Willis, R., Elasticity Theory of Composites, in: H.G. Hopkins, M.J. Sewell (Eds.), Mechanics of Solids, The Rodney Hill 60th Anniversary Volume, Pergamon Press, 1980, pp. 653-686.

APPENDICES

APPENDIX A

In the following, we discuss the solution procedure of equations (4.50)

$$H(\mathbf{x}) = x^{(i)} - D^{(i)} \left(\frac{\bar{b}^{(i)}}{\bar{b}^{(4)}} \right)^{m-1} = 0 \quad i=1,2,3. \quad (1.1)$$

where

$$\bar{b}^{(i)}(\mathbf{x}) = \left[\frac{2}{(2+3x^{(i)})^2} \frac{2\Pi(\mathbf{x})+3A(\mathbf{x})}{[\Pi(\mathbf{x})]^2} \right]^{1/2} \quad \text{for } i=1,2,3, \quad (1.2)$$

and

$$\bar{b}^{(4)}(\mathbf{x}) = \left[\frac{1}{c^{(4)}} \frac{B(\mathbf{x})\Pi(\mathbf{x})-A(\mathbf{x})C(\mathbf{x})}{[\Pi(\mathbf{x})]^2} \right]^{1/2}, \quad (1.3)$$

with

$$A(\mathbf{x}) = \sum_{r=1}^4 \frac{2c^{(r)}x^{(r)}}{2+3x^{(r)}}, \quad \Pi(\mathbf{x}) = \sum_{r=1}^4 \frac{2c^{(r)}}{2+3x^{(r)}}, \quad (1.4)$$

$$B(\mathbf{x}) = -\sum_{r=1}^3 \frac{4c^{(r)}x^{(r)}}{(2+3x^{(r)})^2}, \quad C(\mathbf{x}) = -\frac{2c^{(4)}}{5} - \sum_{r=1}^3 \frac{4c^{(r)}}{(2+3x^{(r)})^2}, \quad (1.5)$$

where $x^{(4)} = 1$.

The Jacobian that corresponds to (1.1) is

$$J_{ij} = \frac{\partial H^{(i)}}{\partial x^{(j)}} = \delta_{ij} - (m-1)D^{(i)} \left(\frac{\bar{b}^{(i)}}{\bar{b}^{(4)}} \right)^{m-2} \left[\frac{\partial \bar{b}^{(i)}}{\partial x^{(j)}} \frac{1}{\bar{b}^{(4)}} - \frac{\bar{b}^{(i)}}{(\bar{b}^{(4)})^2} \frac{\partial \bar{b}^{(4)}}{\partial x^{(j)}} \right] \Rightarrow$$

$$J_{ij} = \delta_{ij} - (m-1)D^{(i)} \left(\frac{\bar{b}^{(i)}}{\bar{b}^{(4)}} \right)^{m-1} \left(\frac{1}{\bar{b}^{(i)}} \frac{\partial \bar{b}^{(i)}}{\partial x^{(j)}} - \frac{1}{\bar{b}^{(4)}} \frac{\partial \bar{b}^{(4)}}{\partial x^{(j)}} \right) \quad i, j = 1, 2, 3.$$

The derivatives involved in that last equation are determined as follows:

$$(1.2) \Rightarrow \left[\bar{b}^{(i)}(\mathbf{x}) \right]^2 = \frac{2}{(2+3x^{(i)})^2} \frac{2\Pi(\mathbf{x})+3A(\mathbf{x})}{[\Pi(\mathbf{x})]^2} \Rightarrow$$

$$2\bar{b}^{(i)} \frac{\partial \bar{b}^{(i)}}{\partial x^{(j)}} = \frac{2 \times (-2) \times 3 \delta_{ij}}{(2+3x^{(i)})^3} \frac{2\Pi+3A}{\Pi^2} + \frac{2}{(2+3x^{(i)})^2} \left[\frac{2 \frac{\partial \Pi}{\partial x^{(j)}} + 3 \frac{\partial A}{\partial x^{(j)}}}{\Pi^2} + (2\Pi+3A) \frac{-2}{\Pi^3} \frac{\partial \Pi}{\partial x^{(j)}} \right] \Rightarrow$$

$$\frac{\partial \bar{b}^{(i)}}{\partial x^{(j)}} = \frac{1}{\bar{b}^{(i)} \Pi^2 (2+3x^{(i)})^2} \left(-6\delta_{ij} \frac{2\Pi+3A}{2+3x^{(i)}} + 2 \frac{\partial \Pi}{\partial x^{(j)}} + 3 \frac{\partial A}{\partial x^{(j)}} - 2 \frac{2\Pi+3A}{\Pi} \frac{\partial \Pi}{\partial x^{(j)}} \right) \quad i, j = 1, 2, 3.$$

Also,

$$(1.3) \Rightarrow \left[\bar{b}^{(4)}(\mathbf{x}) \right]^2 = \frac{1}{c^{(4)}} \frac{B(\mathbf{x})\Pi(\mathbf{x}) - A(\mathbf{x})C(\mathbf{x})}{[\Pi(\mathbf{x})]^2} \Rightarrow$$

$$2\bar{b}^{(4)} \frac{\partial \bar{b}^{(4)}}{\partial x^{(j)}} = \frac{1}{c^{(4)}} \left[\frac{\frac{\partial B}{\partial x^{(j)}} \Pi + B \frac{\partial \Pi}{\partial x^{(j)}} - \frac{\partial A}{\partial x^{(j)}} C - A \frac{\partial C}{\partial x^{(j)}}}{\Pi^2} + (B\Pi - AC) \frac{-2}{\Pi^3} \frac{\partial \Pi}{\partial x^{(j)}} \right] \Rightarrow$$

$$\frac{\partial \bar{b}^{(4)}}{\partial x^{(j)}} = \frac{1}{2c^{(4)} \bar{b}^{(4)} \Pi^2} \left(\frac{\partial B}{\partial x^{(j)}} \Pi + B \frac{\partial \Pi}{\partial x^{(j)}} - \frac{\partial A}{\partial x^{(j)}} C - A \frac{\partial C}{\partial x^{(j)}} - 2 \frac{B\Pi - AC}{\Pi} \frac{\partial \Pi}{\partial x^{(j)}} \right) \quad j=1,2,3.$$

Finally, (1.4) and (1.5) imply that

$$\frac{\partial A}{\partial x^{(j)}} = \frac{4c^{(j)}}{(2+3x^{(j)})^2} \quad j=1,2,3,$$

$$\frac{\partial B}{\partial x^{(j)}} = -4c^{(j)} \frac{2-3x^{(j)}}{(2+3x^{(j)})^3} \quad j=1,2,3,$$

$$\frac{\partial C}{\partial x^{(j)}} = \frac{24c^{(j)}}{(2+3x^{(j)})^3} \quad j=1,2,3,$$

and

$$\frac{\partial \Pi}{\partial x^{(j)}} = -\frac{6c^{(j)}}{(2+3x^{(j)})^2} \quad j=1,2,3.$$

APPENDIX B

We consider the probability parameter P

$$P(g) = \frac{1}{\sqrt{2\pi} s_g} \int_{-\infty}^g \exp\left[-\frac{1}{2} \left(\frac{g' - \bar{g}}{s_g}\right)^2\right] dg', \quad (2.1)$$

and introduce the transformation

$$x = -\frac{g' + \lambda - 2g}{g' - \lambda} \quad \Leftrightarrow \quad g' = \frac{\lambda x - \lambda + 2g}{x + 1}, \quad (2.2)$$

where the parameter λ is chosen to be $\lambda > g$, so that the singularity of the transformation at $g' = \lambda$ is outside the integration region $(-\infty, g)$. Then (2.1) can be written as

$$P(g) = \int_{-1}^1 F(x) dx, \quad F(x) = \frac{2(\lambda - g)}{\sqrt{2\pi} s_g} \frac{1}{(x + 1)^2} \exp\left\{-\frac{1}{2} \left[\frac{(\lambda - \bar{g})x - \lambda + 2g - \bar{g}}{(x + 1) s_g}\right]^2\right\}. \quad (2.3)$$

Note that $\lim_{x \rightarrow -1} F(x) = 0$, i.e., the integrand in (2.3) is nowhere singular. In the calculations we choose $\lambda = g + s_g > g$ so that

$$F(x) = \sqrt{\frac{2}{\pi}} \frac{1}{(x + 1)^2} \exp\left[-\frac{1}{2} \left(\frac{g - \bar{g}}{s_g} + \frac{x - 1}{x + 1}\right)^2\right], \quad (2.4)$$

and use a 64-point Gauss integration scheme in order to evaluate numerically the integral on the right hand side of (2.4).

Calculation of the linearization moduli $\hat{\mathbf{C}} = d\hat{\boldsymbol{\sigma}}_{n+1} / d\mathbf{E}_{n+1}$

Starting with the derivative of the elasticity equation $\hat{\boldsymbol{\sigma}}_{n+1} = \hat{\boldsymbol{\sigma}}^e - 2G \Delta \varepsilon_q \hat{\mathbf{N}}_{n+1} - K \Delta \varepsilon_p \boldsymbol{\delta}$ we find

$$d\hat{\boldsymbol{\sigma}} = \mathbf{L}^e : d\varepsilon - 2G \Delta \varepsilon_q d\hat{\mathbf{N}} - 2G d\varepsilon_q \hat{\mathbf{N}} - K d\varepsilon_p \boldsymbol{\delta}, \quad (3.1)$$

where for simplicity we drop the subscripts $n+1$. We can show easily that

$$d\hat{\mathbf{N}} = \frac{3G}{\sigma_{eq}} \left(\mathbf{K} - \frac{2}{3} \hat{\mathbf{N}} \hat{\mathbf{N}} \right) : d\mathbf{E} \quad \text{and} \quad d\varepsilon_p = \Delta_v df. \quad (3.2)$$

Therefore, (3.1) can be written as

$$d\hat{\boldsymbol{\sigma}} = \mathbf{L}^e : d\mathbf{E} - \frac{6G^2 \Delta \varepsilon_q}{\sigma_{eq}} \left(\mathbf{K} - \frac{2}{3} \hat{\mathbf{N}} \hat{\mathbf{N}} \right) : d\mathbf{E} - 2G d\varepsilon_q \hat{\mathbf{N}} - K \Delta_v df \boldsymbol{\delta}. \quad (3.3)$$

In order to determine $d\hat{\boldsymbol{\sigma}}$ we need to define $d\varepsilon_q$ and df .

We start with the calculation of $d\sigma_{eq}$, dp and $d\Sigma$ in terms of $d\varepsilon$, $d\varepsilon_q$ and df . Equation

$\sigma_{eq} = \sigma_{eq}^e - 3G \Delta \varepsilon_q$ implies that

$$d\sigma_{eq} = 2G \hat{\mathbf{N}} : d\mathbf{E} - 3G d\varepsilon_q = 2G \hat{\mathbf{N}} : d\mathbf{E} - 3G d\varepsilon_q. \quad (3.4)$$

Also, $p = p^e - K \Delta \varepsilon_p$ implies that

$$dp = dp^e - K d\varepsilon_p = K \boldsymbol{\delta} : d\mathbf{E} - K \Delta_v df. \quad (3.5)$$

Finally, the definition $\Sigma = p / \sigma_{eq}$ implies that

$$d\Sigma = \frac{dp - \Sigma d\sigma_{eq}}{\sigma_{eq}} = \frac{1}{\sigma_{eq}} \left(K \boldsymbol{\delta} - 2\Sigma G \hat{\mathbf{N}} \right) : d\mathbf{E} + \frac{3\Sigma G}{\sigma_{eq}} d\varepsilon_q - \frac{K \Delta_v}{\sigma_{eq}} df. \quad (3.6)$$

We proceed with the calculation of $d\varepsilon_q$ and df . We start with the equations that define $\Delta \varepsilon_q$

and Δf

$$\Delta \varepsilon_q = \frac{1}{3} \sigma_{eq} \Big|_{n+1} \theta_{n+1}^{\text{hom}}(\sigma_{eq}, f) \Delta t + A_{n+1}(\sigma_{eq}) \Delta f, \quad (3.7)$$

$$\Delta f = c_{n+1}^{(a)} \left[A_f \Big|_{n+1}(\sigma_{eq}, f, \Sigma) \dot{\varepsilon}_{n+1}^{(a)}(\sigma_{eq}, f) \Delta t + B_f \Big|_{n+1}(\sigma_{eq}, f, \Sigma) \Delta \Sigma(\sigma_{eq} \Big|_{n+1}, p_{n+1}) H(\Delta \Sigma) \right]. \quad (3.8)$$

Now, (3.7) implies

$$d\varepsilon_q = \frac{\Delta t}{3} \left(d\sigma_{eq} \theta^{\text{hom}} + \sigma_{eq} d\theta^{\text{hom}} \right) \sigma_{eq} + (dA \Delta f + A df), \quad (3.9)$$

where

$$d\theta^{\text{hom}} = \frac{\partial\theta^{\text{hom}}}{\partial\sigma_{eq}} d\sigma_{eq} + \frac{\partial\theta^{\text{hom}}}{\partial f} df, \quad (3.10)$$

$$\text{and} \quad A(\sigma_{eq}) = A_0 + \frac{A_1}{s_a} \sigma_{eq} \quad \Rightarrow \quad dA = \frac{A_1}{s_a} d\sigma_{eq}. \quad (3.11)$$

Substituting (3.10) and (3.11) into (3.9) we find

$$d\varepsilon_q = c_1 d\sigma_{eq} + c_2 df, \quad (3.12)$$

where

$$c_1 = \frac{\Delta t}{3} \left(\theta^{\text{hom}} + \sigma_{eq} \frac{\partial\theta^{\text{hom}}}{\partial\sigma_{eq}} \right) + \frac{A_1}{s_a} \Delta f \quad \text{and} \quad c_2 = \left(\frac{\Delta t}{3} \sigma_{eq} \frac{\partial\theta^{\text{hom}}}{\partial f} + A \right). \quad (3.13)$$

Also, substituting $d\sigma_{eq}$ from (3.4) we find that

$$\boxed{(1 + 3Gc_1)d\varepsilon_q - c_2 df = 2c_1 G \hat{\mathbf{N}} : d\mathbf{E}}. \quad (3.14)$$

Next, we use (3.8) to find

$$df = dc^{(a)} \left[A_f \dot{\varepsilon}^{p^{(a)}} \Delta t + B_f \Delta\Sigma H \right] + c^{(a)} \left[\Delta t \left(dA_f \dot{\varepsilon}^{p^{(a)}} + A_f d\dot{\varepsilon}^{p^{(a)}} \right) + H \left(dB_f \Delta\Sigma + B_f d\Sigma \right) \right]. \quad (3.15)$$

In order to simplify the calculations, we assume that $dc^{(3)} \cong dc^{(4)} \cong 0$, so that

$$dc^{(a)} \cong -df. \quad (3.16)$$

Next, we evaluate dA_f , $d\dot{\varepsilon}^{p^{(a)}}$ and dB_f as follows

$$dA_f = \frac{\partial A_f}{\partial\sigma_{eq}} d\sigma_{eq} + \frac{\partial A_f}{\partial f} df + \frac{\partial A_f}{\partial\Sigma} d\Sigma, \quad (3.17)$$

$$d\dot{\varepsilon}^{p^{(a)}} = \frac{\partial\dot{\varepsilon}^{p^{(a)}}}{\partial\sigma_{eq}} d\sigma_{eq} + \frac{\partial\dot{\varepsilon}^{p^{(a)}}}{\partial f} df, \quad (3.18)$$

$$dB_f = \frac{\partial B_f}{\partial\sigma_{eq}} d\sigma_{eq} + \frac{\partial B_f}{\partial f} df + \frac{\partial B_f}{\partial\Sigma} d\Sigma. \quad (3.19)$$

The calculation of the derivatives $\frac{\partial A_f}{\partial\sigma_{eq}}$, $\frac{\partial A_f}{\partial f}$, $\frac{\partial A_f}{\partial\Sigma}$, $\frac{\partial B_f}{\partial\sigma_{eq}}$, $\frac{\partial B_f}{\partial f}$, $\frac{\partial B_f}{\partial\Sigma}$ is presented at the end

of this section; the derivatives $\frac{\partial\dot{\varepsilon}^{p^{(a)}}}{\partial\sigma_{eq}}$, $\frac{\partial\dot{\varepsilon}^{p^{(a)}}}{\partial f}$ are calculated easily in the process of the

homogenization.

Substituting (3.16), (3.17), (3.18) and (3.19) into (3.15) we find that

$$df = d_1 d\sigma_{eq} + d_2 d\Sigma, \quad (3.20)$$

where

$$d_1 = \frac{1}{\Delta} \left[c^{(a)} \Delta t \left(\frac{\partial A_f}{\partial \sigma_{eq}} \dot{\varepsilon}^{p(a)} + A_f \frac{\partial \dot{\varepsilon}^{p(a)}}{\partial \sigma_{eq}} \right) + c^{(a)} H \frac{\partial B_f}{\partial \sigma_{eq}} \Delta \Sigma \right], \quad (3.21)$$

$$d_2 = \frac{1}{\Delta} \left[c^{(a)} \Delta t \frac{\partial A_f}{\partial \Sigma} \dot{\varepsilon}^{p(a)} + c^{(a)} H \left(\frac{\partial B_f}{\partial \Sigma} \Delta \Sigma + B_f \right) \right], \quad (3.22)$$

$$\Delta = 1 + A_f \dot{\varepsilon}^{p(a)} \Delta t + B_f \Delta \Sigma H - c^{(a)} \Delta t \left(\frac{\partial A_f}{\partial f} \dot{\varepsilon}^{p(a)} + A_f \frac{\partial \dot{\varepsilon}^{p(a)}}{\partial f} \right) - c^{(a)} H \frac{\partial B_f}{\partial f} \Delta \Sigma. \quad (3.23)$$

Finally, substituting $d\sigma_{eq}$ and $d\Sigma$ from (3.4) and (3.6) into (3.20) we find that

$$\boxed{3G \left(d_1 - \frac{d_2 \Sigma}{\sigma_{eq}} \right) d\varepsilon_q + \left(1 + \frac{d_2 K \Delta_v}{\sigma_{eq}} \right) df = \left[2G \left(d_1 - \frac{d_2 \Sigma}{\sigma_{eq}} \right) \hat{\mathbf{N}} + \frac{d_2 K}{\sigma_{eq}} \boldsymbol{\delta} \right] : d\mathbf{E}}. \quad (3.24)$$

Summarizing, we note that we can write equations (3.14) and (3.24) in a matrix form as

$$\begin{bmatrix} A_{11} & A_{12} \\ A_{21} & A_{22} \end{bmatrix} \begin{Bmatrix} d\varepsilon_q \\ df \end{Bmatrix} = \begin{Bmatrix} (b_{11} \hat{\mathbf{N}} + b_{12} \boldsymbol{\delta}) : d\mathbf{E} \\ (b_{21} \hat{\mathbf{N}} + b_{22} \boldsymbol{\delta}) : d\mathbf{E} \end{Bmatrix}, \quad (3.25)$$

where

$$A_{11} = 1 + 3G c_1, \quad A_{12} = -c_2, \quad b_{11} = 2c_1 G, \quad b_{12} = 0, \quad (3.26)$$

$$A_{21} = 3G \left(d_1 - \frac{d_2 \Sigma}{\sigma_{eq}} \right), \quad A_{22} = 1 + \frac{d_2 K \Delta_v}{\sigma_{eq}}, \quad b_{21} = 2G \left(d_1 - \frac{d_2 \Sigma}{\sigma_{eq}} \right), \quad b_{22} = \frac{d_2 K}{\sigma_{eq}}. \quad (3.27)$$

Equation (3.25) implies that

$$\begin{Bmatrix} d\varepsilon_q \\ df \end{Bmatrix} = \begin{bmatrix} A_{11} & A_{12} \\ A_{21} & A_{22} \end{bmatrix}^{-1} \begin{Bmatrix} (b_{11} \hat{\mathbf{N}} + b_{12} \boldsymbol{\delta}) : d\mathbf{E} \\ (b_{21} \hat{\mathbf{N}} + b_{22} \boldsymbol{\delta}) : d\mathbf{E} \end{Bmatrix} \equiv \begin{bmatrix} B_{11} & B_{12} \\ B_{21} & B_{22} \end{bmatrix} \begin{Bmatrix} (b_{11} \hat{\mathbf{N}} + b_{12} \boldsymbol{\delta}) : d\mathbf{E} \\ (b_{21} \hat{\mathbf{N}} + b_{22} \boldsymbol{\delta}) : d\mathbf{E} \end{Bmatrix},$$

or

$$\boxed{\begin{Bmatrix} d\varepsilon_q \\ df \end{Bmatrix} = \begin{Bmatrix} (c_{11} \hat{\mathbf{N}} + c_{12} \boldsymbol{\delta}) : d\mathbf{E} \\ (c_{21} \hat{\mathbf{N}} + c_{22} \boldsymbol{\delta}) : d\mathbf{E} \end{Bmatrix}}, \quad (3.28)$$

where $[B] = [A]^{-1}$ and

$$c_{11} = B_{11} b_{11} + B_{12} b_{21}, \quad c_{12} = B_{11} b_{12} + B_{12} b_{22}, \quad c_{21} = B_{21} b_{11} + B_{22} b_{21}, \quad c_{22} = B_{21} b_{12} + B_{22} b_{22}. \quad (3.29)$$

Finally, we substitute $d\varepsilon_q$ and df from (3.28) into (3.3) for $d\boldsymbol{\sigma}$ to find

$$d\hat{\boldsymbol{\sigma}} = \mathbf{L}^\varepsilon : d\mathbf{E} - \frac{6G^2 \Delta \varepsilon_q}{\sigma_{eq}} \left(\mathbf{K} - \frac{2}{3} \hat{\mathbf{N}} \hat{\mathbf{N}} \right) : d\mathbf{E} - 2G \left[(c_{11} \hat{\mathbf{N}} + c_{12} \boldsymbol{\delta}) : d\mathbf{E} \right] \hat{\mathbf{N}} - K \Delta_v \left[(c_{21} \hat{\mathbf{N}} + c_{22} \boldsymbol{\delta}) : d\mathbf{E} \right] \boldsymbol{\delta},$$

or

$$d\hat{\boldsymbol{\sigma}} = \left\{ \mathbf{L}^e - \frac{6G^2 \Delta \varepsilon_q}{\sigma_{eq}} \left(\mathbf{K} - \frac{2}{3} \hat{\mathbf{N}} \hat{\mathbf{N}} \right) - 2G \hat{\mathbf{N}} (c_{11} \hat{\mathbf{N}} + c_{12} \boldsymbol{\delta}) - K \Delta_v \boldsymbol{\delta} (c_{21} \hat{\mathbf{N}} + c_{22} \boldsymbol{\delta}) \right\} : d\mathbf{E}. \quad (3.30)$$

Therefore the linearization moduli are determined from

$$\hat{\mathbf{C}} = \mathbf{L}^e - \frac{6G^2 \Delta \varepsilon_q}{\sigma_{eq}} \mathbf{K} + 2G \left(\frac{2G \Delta \varepsilon_q}{\sigma_{eq}} - c_{11} \right) \hat{\mathbf{N}} \hat{\mathbf{N}} - K \Delta_v c_{22} \boldsymbol{\delta} \boldsymbol{\delta} - 2G c_{12} \hat{\mathbf{N}} \boldsymbol{\delta} - K \Delta_v c_{21} \boldsymbol{\delta} \hat{\mathbf{N}}. \quad (3.31)$$

Calculation of $\partial A_f / \partial \sigma_{eq}$, $\partial A_f / \partial f$, $\partial A_f / \partial \Sigma$, $\partial B_f / \partial \sigma_{eq}$, $\partial B_f / \partial f$ and $\partial B_f / \partial \Sigma$.

The parameter A_f is determined from:

$$A_f(\sigma_{eq}, f, \Sigma) = A_f(f_{sb}(\sigma_{eq}, f), P) = \alpha \beta_0 r(f_{sb}^{r-1} - f_{sb}^r) P(\Sigma), \quad (3.32)$$

where

$$f_{sb}(\sigma_{eq}, f) = f_{sb}(\bar{\varepsilon}^{p(a)}(\sigma_{eq}, f)) = 1 - e^{-\alpha \bar{\varepsilon}^{p(a)}}, \quad \bar{\varepsilon}^{p(a)} = \bar{\varepsilon}^{p(a)}(\sigma_{eq}, f), \quad (3.33)$$

$$P(\Sigma) = P(g) = \frac{1}{\sqrt{2\pi} s_g} \int_{-\infty}^{g(\Sigma)} \exp \left[-\frac{1}{2} \left(\frac{g' - \bar{g}}{s_g} \right)^2 \right] dg', \quad (3.34)$$

$$g(\Sigma) = g_0 - g_1 \Theta + g_2 \Sigma. \quad (3.35)$$

The derivative of P with respect to Σ is given by

$$\frac{\partial P}{\partial \Sigma} = \frac{\partial P}{\partial g} \frac{\partial g}{\partial \Sigma}, \quad (3.36)$$

where

$$\frac{\partial P}{\partial g} = \frac{1}{\sqrt{2\pi} s_g} \exp \left[-\frac{1}{2} \left(\frac{g - \bar{g}}{s_g} \right)^2 \right], \quad (3.37)$$

$$\frac{\partial g}{\partial \Sigma} = g_2. \quad (3.38)$$

The derivatives of A_f with respect to σ_{eq} , f and Σ are determined as follows

$$\frac{\partial A_f}{\partial \sigma_{eq}} = \frac{\partial A_f}{\partial f_{sb}} \frac{\partial f_{sb}}{\partial \sigma_{eq}} + \frac{\partial A_f}{\partial P} \frac{\partial P}{\partial \Sigma} \frac{\partial \Sigma}{\partial \sigma_{eq}}, \quad (3.39)$$

$$\frac{\partial A_f}{\partial f} = \frac{\partial A_f}{\partial f_{sb}} \frac{\partial f_{sb}}{\partial f} + \frac{\partial A_f}{\partial P} \frac{\partial P}{\partial \Sigma} \frac{\partial \Sigma}{\partial f}, \quad (3.40)$$

$$\frac{\partial A_f}{\partial \Sigma} = \frac{\partial A_f}{\partial P} \frac{\partial P}{\partial \Sigma}, \quad (3.41)$$

where

$$\frac{\partial A_f}{\partial f_{sb}} = \alpha \beta_0 r \left[(r-1) f_{sb}^{r-2} - r f_{sb}^{r-1} \right] P, \quad (3.42)$$

$$\frac{\partial A_f}{\partial P} = \alpha \beta_0 r \left(f_{sb}^{r-1} - f_{sb}^r \right), \quad (3.43)$$

$$\frac{\partial f_{sb}}{\partial \bar{\varepsilon}^{p(a)}} = \alpha e^{-\alpha \bar{\varepsilon}^{p(a)}}, \quad (3.44)$$

$$\frac{\partial f_{sb}}{\partial \sigma_{eq}} = \frac{\partial f_{sb}}{\partial \bar{\varepsilon}^{p(a)}} \frac{\partial \bar{\varepsilon}^{p(a)}}{\partial \sigma_{eq}} = \frac{\partial f_{sb}}{\partial \bar{\varepsilon}^{p(a)}} \frac{\partial \dot{\bar{\varepsilon}}^{p(a)}}{\partial \sigma_{eq}} \Delta t, \quad (3.45)$$

$$\frac{\partial f_{sb}}{\partial f} = \frac{\partial f_{sb}}{\partial \bar{\varepsilon}^{p(a)}} \frac{\partial \bar{\varepsilon}^{p(a)}}{\partial f} = \frac{\partial f_{sb}}{\partial \bar{\varepsilon}^{p(a)}} \frac{\partial \dot{\bar{\varepsilon}}^{p(a)}}{\partial f} \Delta t. \quad (3.46)$$

The parameter B_f is determined from

$$B_f(\sigma_{eq}, f, \Sigma) = B_f(f_{sb}, g) = \frac{g_2}{\sqrt{2\pi} s_g} \beta_0 f_{sb}^r(\sigma_{eq}, f) \exp \left[-\frac{1}{2} \left(\frac{g(\Sigma) - \bar{g}}{s_g} \right)^2 \right]. \quad (3.47)$$

The derivatives of B_f with respect to σ_{eq} , f , and Σ are determined as follows

$$\frac{\partial B_f}{\partial \sigma_{eq}} = \frac{\partial B_f}{\partial f_{sb}} \frac{\partial f_{sb}}{\partial \sigma_{eq}} + \frac{\partial B_f}{\partial g} \frac{\partial g}{\partial \Sigma} \frac{\partial \Sigma}{\partial \sigma_{eq}}, \quad (3.48)$$

$$\frac{\partial B_f}{\partial f} = \frac{\partial B_f}{\partial f_{sb}} \frac{\partial f_{sb}}{\partial f} + \frac{\partial B_f}{\partial g} \frac{\partial g}{\partial \Sigma} \frac{\partial \Sigma}{\partial f}, \quad (3.49)$$

$$\frac{\partial B_f}{\partial \Sigma} = \frac{\partial B_f}{\partial g} \frac{\partial g}{\partial \Sigma}, \quad (3.50)$$

where

$$\frac{\partial B_f}{\partial f_{sb}} = \frac{g_2}{\sqrt{2\pi} s_g} \beta_0 r f_{sb}^{r-1} \exp \left[-\frac{1}{2} \left(\frac{g - \bar{g}}{s_g} \right)^2 \right], \quad (3.51)$$

$$\frac{\partial B_f}{\partial g} = -\frac{g_2}{\sqrt{2\pi} s_g^3} \beta_0 f_{sb}^r (g - \bar{g}) \exp \left[-\frac{1}{2} \left(\frac{g - \bar{g}}{s_g} \right)^2 \right]. \quad (3.52)$$

APPENDIX D

Let $\mathbf{A} = \frac{1}{2}(d\mathbf{L} - d\mathbf{L}^T) \cdot \boldsymbol{\sigma} - \frac{1}{2}\boldsymbol{\sigma} \cdot (d\mathbf{L} + d\mathbf{L}^T)$. We write the matrix form of $\boldsymbol{\sigma}$ and $d\mathbf{L}$ as

$$[\boldsymbol{\sigma}] = \begin{bmatrix} \sigma_{11} & \sigma_{12} & \sigma_{13} \\ \sigma_{21} & \sigma_{22} & \sigma_{23} \\ \sigma_{31} & \sigma_{32} & \sigma_{33} \end{bmatrix} \quad \text{and} \quad [d\mathbf{L}] = \begin{bmatrix} dL_{11} & dL_{12} & dL_{13} \\ dL_{21} & dL_{22} & dL_{23} \\ dL_{31} & dL_{32} & dL_{33} \end{bmatrix}.$$

Then, the matrix form of \mathbf{A} is given by

$$[A] = \frac{1}{2}([d\mathbf{L}] - [d\mathbf{L}]^T)[\boldsymbol{\sigma}] - \frac{1}{2}[\boldsymbol{\sigma}]([d\mathbf{L}] + [d\mathbf{L}]^T) \equiv \begin{bmatrix} A_{11} & A_{12} & A_{13} \\ A_{21} & A_{22} & A_{23} \\ A_{31} & A_{32} & A_{33} \end{bmatrix},$$

where

$$A_{11} = -\sigma_{11}dL_{11} - \sigma_{12}dL_{21} - \sigma_{13}dL_{31}, \quad (4.1)$$

$$A_{22} = -\sigma_{12}dL_{12} - \sigma_{22}dL_{22} - \sigma_{32}dL_{23}, \quad (4.2)$$

$$A_{33} = -\sigma_{33}dL_{33} - \sigma_{13}dL_{13} - \sigma_{23}dL_{23}, \quad (4.3)$$

$$A_{12} = -\sigma_{12}dL_{22} + \frac{\sigma_{22} - \sigma_{11}}{2}dL_{12} - \frac{\sigma_{11} + \sigma_{22}}{2}dL_{21} + \frac{\sigma_{23}}{2}dL_{13} - \frac{\sigma_{23}}{2}dL_{31} - \frac{\sigma_{13}}{2}dL_{23} - \frac{\sigma_{13}}{2}dL_{32}, \quad (4.4)$$

$$A_{21} = -\sigma_{12}dL_{11} - \frac{\sigma_{11} + \sigma_{22}}{2}dL_{12} + \frac{\sigma_{11} - \sigma_{22}}{2}dL_{21} - \frac{\sigma_{23}}{2}dL_{13} - \frac{\sigma_{23}}{2}dL_{31} + \frac{\sigma_{13}}{2}dL_{23} - \frac{\sigma_{13}}{2}dL_{32}, \quad (4.5)$$

$$A_{13} = -\sigma_{13}dL_{33} + \frac{\sigma_{23}}{2}dL_{12} - \frac{\sigma_{23}}{2}dL_{21} + \frac{\sigma_{33} - \sigma_{11}}{2}dL_{13} - \frac{\sigma_{11} + \sigma_{33}}{2}dL_{31} - \frac{\sigma_{12}}{2}dL_{23} - \frac{\sigma_{12}}{2}dL_{32}, \quad (4.6)$$

$$A_{31} = -\sigma_{13}dL_{11} - \frac{\sigma_{23}}{2}dL_{12} - \frac{\sigma_{23}}{2}dL_{21} - \frac{\sigma_{11} + \sigma_{33}}{2}dL_{13} + \frac{\sigma_{11} - \sigma_{33}}{2}dL_{31} - \frac{\sigma_{12}}{2}dL_{23} + \frac{\sigma_{12}}{2}dL_{32}, \quad (4.7)$$

$$A_{23} = -\sigma_{23}dL_{33} - \frac{\sigma_{13}}{2}dL_{12} + \frac{\sigma_{13}}{2}dL_{21} - \frac{\sigma_{12}}{2}dL_{13} - \frac{\sigma_{12}}{2}dL_{31} + \frac{\sigma_{33} - \sigma_{22}}{2}dL_{23} - \frac{\sigma_{22} + \sigma_{33}}{2}dL_{32}, \quad (4.8)$$

$$A_{32} = -\sigma_{23}dL_{22} - \frac{\sigma_{13}}{2}dL_{12} - \frac{\sigma_{13}}{2}dL_{21} - \frac{\sigma_{12}}{2}dL_{13} + \frac{\sigma_{12}}{2}dL_{31} - \frac{\sigma_{22} + \sigma_{33}}{2}dL_{23} + \frac{\sigma_{22} - \sigma_{33}}{2}dL_{32}. \quad (4.9)$$

Next, we introduce the notation

$$[A] = [A_{11} \ A_{22} \ A_{33} \ A_{12} \ A_{21} \ A_{13} \ A_{31} \ A_{23} \ A_{32}],$$

$$[d\mathbf{L}] = [dL_{11} \ dL_{22} \ dL_{33} \ dL_{12} \ dL_{21} \ dL_{13} \ dL_{31} \ dL_{23} \ dL_{32}],$$

$$[\boldsymbol{\sigma}] = [\sigma_{11} \ \sigma_{22} \ \sigma_{33} \ \sigma_{12} \ \sigma_{21} \ \sigma_{13} \ \sigma_{31} \ \sigma_{23} \ \sigma_{32}].$$

Then, using (4.1)-(4.9) we can write

$$\{A\} = [A] \{d\mathbf{L}\},$$

where

$$[\Sigma] = \begin{bmatrix} -\sigma_{11} & 0 & 0 & 0 & -\sigma_{12} & 0 & -\sigma_{13} & 0 & 0 \\ & -\sigma_{22} & 0 & -\sigma_{12} & 0 & 0 & 0 & 0 & -\sigma_{23} \\ & & -\sigma_{33} & 0 & 0 & -\sigma_{13} & 0 & -\sigma_{23} & 0 \\ & & & \frac{\sigma_{22} - \sigma_{11}}{2} & -\frac{\sigma_{11} + \sigma_{22}}{2} & \frac{\sigma_{23}}{2} & -\frac{\sigma_{23}}{2} & -\frac{\sigma_{13}}{2} & -\frac{\sigma_{13}}{2} \\ & & & & \frac{\sigma_{11} - \sigma_{22}}{2} & -\frac{\sigma_{23}}{2} & -\frac{\sigma_{23}}{2} & \frac{\sigma_{13}}{2} & -\frac{\sigma_{13}}{2} \\ & & & & & \frac{\sigma_{33} - \sigma_{11}}{2} & -\frac{\sigma_{11} + \sigma_{33}}{2} & -\frac{\sigma_{12}}{2} & -\frac{\sigma_{12}}{2} \\ & & & & & & \frac{\sigma_{11} - \sigma_{33}}{2} & -\frac{\sigma_{12}}{2} & \frac{\sigma_{12}}{2} \\ & & & & & & & \frac{\sigma_{33} - \sigma_{22}}{2} & -\frac{\sigma_{22} + \sigma_{33}}{2} \\ & & & & & & & & \frac{\sigma_{22} - \sigma_{33}}{2} \end{bmatrix}$$

symmetric

Alternatively, we can write $\mathbf{A} = \frac{1}{2}(d\mathbf{L} - d\mathbf{L}^T) \cdot \boldsymbol{\sigma} - \frac{1}{2}\boldsymbol{\sigma} \cdot (d\mathbf{L} + d\mathbf{L}^T) = \boldsymbol{\Sigma} : d\mathbf{L}$, where

$$\Sigma_{ijkl} = \Sigma_{klij} = \frac{1}{2}(\delta_{ik}\sigma_{jl} - \delta_{il}\sigma_{jk} - \sigma_{ik}\delta_{jl} - \sigma_{il}\delta_{jk}),$$

and the components of $[\Sigma]$ can be calculated using the above expression.

APPENDIX E

Calculation of the derivatives for the non-linear problem of plane stress

The basic equations are

$$F_1(\Delta\varepsilon_q, \Delta f, \Delta\varepsilon_3) \equiv \Delta\varepsilon_q - \frac{1}{3}\sigma_{eq}|_{n+1} \theta_{n+1}^{\text{hom}} \Delta t - A(\sigma_{eq}|_{n+1}) \Delta f = 0,$$

$$F_2(\Delta\varepsilon_q, \Delta f, \Delta\varepsilon_3) \equiv \Delta f - c_{n+1}^{(a)} \left(A_f|_{n+1} \Delta\bar{\varepsilon}_{n+1}^{(a)} + B_f|_{n+1} \Delta\Sigma \right) = 0,$$

$$F_3(\Delta\varepsilon_q, \Delta f, \Delta\varepsilon_3) \equiv p_{n+1} \left(\sigma_e|_{n+1} + 3G \Delta\varepsilon_q \right) + \left(s_{33}^e + \frac{4}{3}G \Delta\varepsilon_3 \right) \sigma_e|_{n+1} = 0.$$

We need to determine the Jacobian matrix

$$[J] = \begin{pmatrix} \partial F_1 / \partial \Delta\varepsilon_q & \partial F_1 / \partial \Delta f & \partial F_1 / \partial \Delta\varepsilon_3 \\ \partial F_2 / \partial \Delta\varepsilon_q & \partial F_2 / \partial \Delta f & \partial F_2 / \partial \Delta\varepsilon_3 \\ \partial F_3 / \partial \Delta\varepsilon_q & \partial F_3 / \partial \Delta f & \partial F_3 / \partial \Delta\varepsilon_3 \end{pmatrix}.$$

For simplicity, we drop the indices $n+1$ in the following.

The derivatives of F_1 with respect to the unknowns $\Delta\varepsilon_q$, Δf and $\Delta\varepsilon_3$ are

$$\frac{\partial F_1}{\partial \Delta\varepsilon_q} = 1 - \frac{\Delta t}{3} \left(\frac{\partial \sigma_{eq}}{\partial \Delta\varepsilon_q} \theta^{\text{hom}} + \sigma_{eq} \frac{\partial \theta^{\text{hom}}}{\partial \Delta\varepsilon_q} \right) - \Delta f \frac{\partial A}{\partial \Delta\varepsilon_q},$$

$$\frac{\partial F_1}{\partial \Delta f} = -\frac{\Delta t}{3} \sigma_{eq} \frac{\partial \theta^{\text{hom}}}{\partial \Delta f} - A,$$

$$\frac{\partial F_1}{\partial \Delta\varepsilon_3} = 1 - \frac{\Delta t}{3} \left(\frac{\partial \sigma_{eq}}{\partial \Delta\varepsilon_3} \theta^{\text{hom}} + \sigma_{eq} \frac{\partial \theta^{\text{hom}}}{\partial \Delta\varepsilon_3} \right) - \Delta f \frac{\partial A}{\partial \Delta\varepsilon_3}.$$

The derivatives $\frac{\partial \theta^{\text{hom}}}{\partial \Delta\varepsilon_q}$, $\frac{\partial A}{\partial \Delta\varepsilon_q}$, $\frac{\partial \theta^{\text{hom}}}{\partial \Delta\varepsilon_3}$ and $\frac{\partial A}{\partial \Delta\varepsilon_3}$ are determined as follows

$$\frac{\partial \theta^{\text{hom}}}{\partial \Delta\varepsilon_q} = \frac{\partial \theta^{\text{hom}}}{\partial \sigma_e} \frac{\partial \sigma_e}{\partial \Delta\varepsilon_q},$$

$$\frac{\partial A}{\partial \Delta\varepsilon_q} = \frac{\partial A}{\partial \sigma_{eq}} \frac{\partial \sigma_{eq}}{\partial \Delta\varepsilon_q} = \frac{A_1}{s_a^*} \frac{\partial \sigma_{eq}}{\partial \Delta\varepsilon_q},$$

$$\frac{\partial \theta^{\text{hom}}}{\partial \Delta\varepsilon_3} = \frac{\partial \theta^{\text{hom}}}{\partial \sigma_e} \frac{\partial \sigma_e}{\partial \Delta\varepsilon_3},$$

$$\frac{\partial A}{\partial \Delta\varepsilon_3} = \frac{\partial A}{\partial \sigma_{eq}} \frac{\partial \sigma_{eq}}{\partial \Delta\varepsilon_3} = \frac{A_1}{s_a^*} \frac{\partial \sigma_{eq}}{\partial \Delta\varepsilon_3}.$$

The derivatives $\frac{\partial \theta^{\text{hom}}}{\partial \Delta f}$, $\frac{\partial \theta^{\text{hom}}}{\partial \sigma_e}$ are determined in the process of homogenization. Finally, we

the derivatives $\frac{\partial \sigma_{eq}}{\partial \Delta \varepsilon_q}$, $\frac{\partial \sigma_{eq}}{\partial \Delta \varepsilon_3}$ are found as follows. The equivalent stress is given by

$$\sigma_{eq}(\Delta \varepsilon_q, \Delta \varepsilon_3) = -3G \Delta \varepsilon_q + \left[(\sigma_{eq}^e)^2 + 6G \Delta \varepsilon_3 s_{33}^e + 4G^2 (\Delta \varepsilon_3)^2 \right]^{1/2}.$$

Therefore

$$\frac{\partial \sigma_{eq}}{\partial \Delta \varepsilon_q} = -3G, \text{ and } \frac{\partial \sigma_{eq}}{\partial \Delta \varepsilon_3} = \frac{1}{2} \left[6G s_{33}^e + 8G^2 \Delta \varepsilon_3 \right] \left[(\sigma_{eq}^e)^2 + 6G \Delta \varepsilon_3 s_{33}^e + 4G^2 (\Delta \varepsilon_3)^2 \right]^{1/2}.$$

The derivatives of function F_2 with respect to the unknowns $\Delta \varepsilon_q$, Δf and $\Delta \varepsilon_3$ are

$$\frac{\partial F_2}{\partial \Delta \varepsilon_q} = -c^{(a)} \left[\Delta t \left(\frac{\partial A_f}{\partial \Delta \varepsilon_q} \dot{\bar{\varepsilon}}^{p^{(a)}} + A_f \frac{\partial \dot{\bar{\varepsilon}}^{p^{(a)}}}{\partial \Delta \varepsilon_q} \right) + \left(\frac{\partial B_f}{\partial \Delta \varepsilon_q} \Delta \Sigma + B_f \frac{\partial \Delta \Sigma}{\partial \Delta \varepsilon_q} \right) \right],$$

$$\frac{\partial F_2}{\partial \Delta f} = 1 - \frac{\partial c^{(a)}}{\partial \Delta f} \left(A_f \Delta \bar{\varepsilon}^{p^{(a)}} + B_f \Delta \Sigma \right) - c^{(a)} \left[\Delta t \left(\frac{\partial A_f}{\partial \Delta f} \dot{\bar{\varepsilon}}^{p^{(a)}} + A_f \frac{\partial \dot{\bar{\varepsilon}}^{p^{(a)}}}{\partial \Delta f} \right) + \left(\frac{\partial B_f}{\partial \Delta f} \Delta \Sigma + B_f \frac{\partial \Delta \Sigma}{\partial \Delta f} \right) \right],$$

$$\frac{\partial F_2}{\partial \Delta \varepsilon_3} = -c^{(a)} \left[\Delta t \left(\frac{\partial A_f}{\partial \Delta \varepsilon_3} \dot{\bar{\varepsilon}}^{p^{(a)}} + A_f \frac{\partial \dot{\bar{\varepsilon}}^{p^{(a)}}}{\partial \Delta \varepsilon_3} \right) + \left(\frac{\partial B_f}{\partial \Delta \varepsilon_3} \Delta \Sigma + B_f \frac{\partial \Delta \Sigma}{\partial \Delta \varepsilon_3} \right) \right].$$

We use the chain rule to determine the values of $\frac{\partial A_f}{\partial \Delta \varepsilon_q}$, $\frac{\partial \dot{\bar{\varepsilon}}^{p^{(a)}}}{\partial \Delta \varepsilon_q}$, $\frac{\partial B_f}{\partial \Delta \varepsilon_q}$, $\frac{\partial A_f}{\partial \Delta f}$, $\frac{\partial B_f}{\partial \Delta f}$, $\frac{\partial A_f}{\partial \Delta \varepsilon_3}$,

$$\frac{\partial \dot{\bar{\varepsilon}}^{p^{(a)}}}{\partial \Delta \varepsilon_3}, \frac{\partial B_f}{\partial \Delta \varepsilon_3}:$$

$$\frac{\partial A_f}{\partial \Delta \varepsilon_q} = \frac{\partial A_f}{\partial f_{sb}} \frac{\partial f_{sb}}{\partial \sigma_{eq}} \frac{\partial \sigma_{eq}}{\partial \Delta \varepsilon_q} + \frac{\partial A_f}{\partial P} \frac{\partial P}{\partial \Sigma} \frac{\partial \Sigma}{\partial \Delta \varepsilon_q},$$

$$\frac{\partial \dot{\bar{\varepsilon}}^{p^{(a)}}}{\partial \Delta \varepsilon_q} = \frac{\partial \dot{\bar{\varepsilon}}^{p^{(a)}}}{\partial \sigma_{eq}} \frac{\partial \sigma_{eq}}{\partial \Delta \varepsilon_q},$$

$$\frac{\partial B_f}{\partial \Delta \varepsilon_q} = \frac{\partial B_f}{\partial f_{sb}} \frac{\partial f_{sb}}{\partial \sigma_{eq}} \frac{\partial \sigma_{eq}}{\partial \Delta \varepsilon_q} + \frac{\partial B_f}{\partial g} \frac{\partial g}{\partial \Sigma} \frac{\partial \Sigma}{\partial \Delta \varepsilon_q},$$

$$\frac{\partial A_f}{\partial \Delta f} = \frac{\partial A_f}{\partial f_{sb}} \frac{\partial f_{sb}}{\partial \Delta f} + \frac{\partial A_f}{\partial P} \frac{\partial P}{\partial \Sigma} \frac{\partial \Sigma}{\partial \Delta f},$$

$$\frac{\partial B_f}{\partial \Delta f} = \frac{\partial B_f}{\partial f_{sb}} \frac{\partial f_{sb}}{\partial \Delta f} + \frac{\partial B_f}{\partial g} \frac{\partial g}{\partial \Sigma} \frac{\partial \Sigma}{\partial \Delta f},$$

$$\frac{\partial A_f}{\partial \Delta \varepsilon_3} = \frac{\partial A_f}{\partial f_{sb}} \frac{\partial f_{sb}}{\partial \sigma_{eq}} \frac{\partial \sigma_{eq}}{\partial \Delta \varepsilon_3} + \frac{\partial A_f}{\partial P} \frac{\partial P}{\partial \Sigma} \frac{\partial \Sigma}{\partial \Delta \varepsilon_3},$$



$$\frac{\partial \dot{\varepsilon}^{p^{(a)}}}{\partial \Delta \varepsilon_3} = \frac{\partial \dot{\varepsilon}^{p^{(a)}}}{\partial \sigma_{eq}} \frac{\partial \sigma_{eq}}{\partial \Delta \varepsilon_3},$$

$$\frac{\partial B_f}{\partial \Delta \varepsilon_3} = \frac{\partial B_f}{\partial f_{sb}} \frac{\partial f_{sb}}{\partial \sigma_{eq}} \frac{\partial \sigma_{eq}}{\partial \Delta \varepsilon_3} + \frac{\partial B_f}{\partial g} \frac{\partial g}{\partial \Sigma} \frac{\partial \Sigma}{\partial \Delta \varepsilon_3}.$$

The derivatives $\frac{\partial \dot{\varepsilon}^{p^{(a)}}}{\partial \sigma_{eq}}$, $\frac{\partial \dot{\varepsilon}^{p^{(a)}}}{\partial \Delta f}$ are calculated in the process of homogenization and the

quantities $\frac{\partial A_f}{\partial f_{sb}}$, $\frac{\partial f_{sb}}{\partial \sigma_{eq}}$, $\frac{\partial A_f}{\partial P}$, $\frac{\partial P}{\partial \Sigma}$, $\frac{\partial B_f}{\partial f_{sb}}$, $\frac{\partial B_f}{\partial g}$, $\frac{\partial g}{\partial \Sigma}$ and $\frac{\partial f_{sb}}{\partial \Delta f}$ are estimated in APPENDIX B.

In the following, we calculate the derivatives $\frac{\partial \Delta \Sigma}{\partial \Delta \varepsilon_q}$, $\frac{\partial \Delta \Sigma}{\partial \Delta f}$ and $\frac{\partial \Delta \Sigma}{\partial \Delta \varepsilon_3}$. The definition

$\Sigma = p / \sigma_{eq}$ implies that

$$\frac{\partial \Delta \Sigma}{\partial \Delta \varepsilon_q} = -\frac{\Sigma}{\sigma_{eq}} \frac{\partial \sigma_{eq}}{\partial \Delta \varepsilon_q}, \quad \frac{\partial \Delta \Sigma}{\partial \Delta f} = \frac{-K \Delta_v}{\sigma_{eq}} \quad \text{and} \quad \frac{\partial \Delta \Sigma}{\partial \Delta \varepsilon_3} = \frac{1}{\sigma_{eq}} \frac{\partial p}{\partial \Delta \varepsilon_3} - \frac{\Sigma}{\sigma_{eq}} \frac{\partial \sigma_{eq}}{\partial \Delta \varepsilon_3}.$$

We also recall that $p = p^e + K \Delta \varepsilon_3 - K \Delta_v \Delta f \Rightarrow$

$$\frac{\partial p}{\partial \Delta \varepsilon_3} = K, \quad \frac{\partial p}{\partial \Delta f} = -K \Delta_v \quad \text{and} \quad \frac{\partial p}{\partial \Delta \varepsilon_q} = 0.$$

We also assume that the the variation of the volume fractions of bainite and ferrite are negligible, i.e., $\frac{\partial c^{(3)}}{\partial \Delta f} \cong \frac{\partial c^{(4)}}{\partial \Delta f} \cong 0$. Then the relationship $c^{(a)} + f + c^{(3)} + c^{(4)} = 1$ implies that

$$\frac{\partial c^{(a)}}{\partial \Delta f} = -1.$$

Finally, the derivatives of function F_3 with respect to the unknowns $\Delta \varepsilon_q$, Δf and $\Delta \varepsilon_3$ are

$$\frac{\partial F_3}{\partial \Delta \varepsilon_q} = p \left(\frac{\partial \sigma_{eq}}{\partial \Delta \varepsilon_q} + 3G \right) + \left(s_{33}^e + \frac{4}{3} G \Delta \varepsilon_3 \right) \frac{\partial \sigma_{eq}}{\partial \Delta \varepsilon_q},$$

$$\frac{\partial F_3}{\partial \Delta f} = -K \Delta_v (\sigma_{eq} + 3G \Delta \varepsilon_q),$$

$$\frac{\partial F_3}{\partial \Delta \varepsilon_3} = K (\sigma_{eq} + 3G \Delta \varepsilon_q) + P \frac{\partial \sigma_{eq}}{\partial \Delta \varepsilon_3} + \left[\frac{\partial \sigma_{eq}}{\partial \Delta \varepsilon_3} \left(s_{33}^e + \frac{4}{3} G \Delta \varepsilon_3 \right) + \frac{4}{3} G \sigma_{eq} \right].$$

ΠΑΝΕΠΙΣΤΗΜΙΟ
ΘΕΣΣΑΛΙΑΣ



004000091231